Controlled molecular beam deposition of hybrid inorganic/organic semiconductor structures

Dissertation
zur Erlangung des akademischen Grades

doctor rerum naturalium
(Dr. rer. nat.)
im Fach Physik
Spezialisierung: Experimentalphysik

eingereicht an der
Mathematisch-Naturwissenschaftlichen Fakultät
Institut für Physik
Humboldt-Universität zu Berlin

von M.Sc. Mino Sparenberg

Präsidentin der Humboldt-Universität zu Berlin:
Prof. Dr-Ing. habil. Dr. Sabine Kunst

Dekan der Mathematisch-Naturwissenschaftlichen Fakultät:
Prof. Dr. Elmar Kulke

Gutachter:

1. Prof. Dr. Oliver Benson
2. Prof. Dr. Stefan Kowarik
3. Prof. Dr. Gregor Witte

Tag der mündlichen Prüfung: 24.04.2018

Abstract

Hybrid inorganic/organic systems (HIOS) are investigated in this thesis with a focus on the specific processes at the interface between the two material classes. Organic molecules used together with inorganic semiconductors have a great potential for future opto-electronic applications in hybrid components by combining the advantages of two dissimilar worlds. Crucial for the functionality of hybrid structures is the understanding of the growth processes and the interaction at the interface between organic and inorganic material. To achieve this, the growth of the hybrid structures is conducted and observed in an all Ultra-High Vacuum (UHV)[1] environment, where growth conditions of the inorganic semiconductor and the organic molecules can be controlled and analyzed *in situ* by various investigation methods. Those include electron diffraction techniques, scanning probe microscopy as well as optical investigation during growth of the molecules by differential reflectance spectroscopy (DRS). The inorganic semiconductor is epitaxially overgrown ZnO, which has been proven for its suitability in hybrid structures due to its exceptional properties, as for example strong light-matter coupling and the ability of crystalline growth at temperatures as low as 50 °C.

As model system for growth studies the linear conjugated organic molecule sexiphenyl (6P) and its fluorinated derivatives are used in the first part of the thesis. Hereby, the growth behavior under utilization of different surface terminations of ZnO, variation of the temperature and functionalization of the molecule is exemplarily elucidated. It is found by *in situ* atomic force microscopy (AFM) that the morphology of the ZnO-6P system is strongly dependent on the balance between inter-molecular and molecule-substrate interaction. This leads to the formation of either islands composed of upright standing molecules or needles built of flat-lying ones. By changing the face of ZnO or the substrate temperature, a control over the prevailing molecular orientation can be achieved. Kelvin probe force microscopy (KPFM) measurements further confirm a different energy-level alignment for standing/lying molecules and the substrate. Eventually, the effect of chemical modification is investigated. It is shown that fluorination of 6P drastically alters the growth mode from rough, three-dimensional towards a smooth, crystalline layer-by-layer growth as is demanded for efficient opto-electronic devices. By a comparative KPFM study of symmetrically and asymmetrically fluorinated 6P-F_4 and 6P-F_2 a further growth control is demonstrated by the introduction of a permanent dipole moment on one side of the molecules, which leads to a general preferential orientation of the molecular head group.

Subsequently, hybrid stacks consisting of embedded 6P nanocrystals in ZnO are studied for differently terminated substrate surfaces and analyzed in depth by high resolution transmission electron microscopy (HRTEM). It is found that the 6P layer can be overgrown without impairment of the molecule's crystal structure, with all interfaces defined on an atomic/molecular level, showing no interdiffusion of the ZnO. By investigation of the ZnO top layer, a distinct columnar structure with preferred c-axis orientation atop the organic inclusion becomes apparent, while aside the inclusions the ZnO top layer is single crystalline.

1 UHV is defined by pressures in the range of $10^{-7} - 10^{-12}$ mbar

The last part addresses the optical observations during the organic growth by analyzing the change in reflectance spectra. Thereby it is possible to determine changes of structural properties and interactions between molecules and the substrate non-destructively in real-time during deposition. Properties reflected in the spectra are absorption of substrate and adsorbed molecule, a spectral '*gas-to-crystal*' shift due to aggregation of the molecules and charge transfer resulting in band bending of ZnO. Four molecules are selected to exemplary demonstrate and analyze the respective effects. First, as proof of principle, the structural development on an inert non-absorbing substrate (KBr) is observed using the organic molecule PTCDI. By using the extended dipole approximation the structural evolution of the PTCDI growth can be identified. In the next step the dielectric function is determined for L4P on ZnO, which is spectrally resonant to the exciton transition of ZnO. A negligible interaction between molecules and the ZnO substrate arises, *i.e.* no significant charge transfer or chemisorption is detected. The thesis is concluded by an investigation of molecules showing a considerable interaction with the substrate in form of charge transfer. This becomes apparent in the spectra by a characteristic feature in the proximity of the ZnO band gap, attributed to a change in the band bending.

Conclusively, this work can hopefully stimulate future studies to further improve growth control at the interface between conjugated organic molecules and inorganic semiconductor to realize efficient optoelectronic structures.

Zusammenfassung

Anorganisch/organische Hybridsysteme (HIOS) werden in dieser Arbeit mit besonderem Fokus auf die speziellen Prozesse an der Grenzfläche beider Materialklassen untersucht. Organische Moleküle, in Verbindung mit anorganischen Halbleitern haben ein großes Potenzial für Anwendungen in zukünftigen optoelektronischen Hybridbauteilen, indem sie Vorteile zweier unterschiedlicher Welten kombinieren. Entscheidend für die Herstellung von hybriden Strukturen ist das Verständnis der Wechselwirkungen an der Grenzfläche zwischen organischem und anorganischem Material. Um dies zu erreichen, wird das Wachstum der Hybridstrukturen im Ultrahochvakuum (UHV)[2] durchgeführt und beobachtet. Hierbei können Wachstumsbedingungen des anorganischen Halbleiters und der organischen Moleküle präzise *in situ* kontrolliert und mit verschiedenen Untersuchungsmethoden analysiert werden. Diese beinhalten Elektronenbeugungstechniken, Rastersondenmikroskopie sowie optische Untersuchungen während des Wachstums mittels differentieller Reflektivitätsspektroskopie (DRS). Bei dem hier untersuchten anorganischen Halbleiter handelt es sich um epitaktisch überwachsenes ZnO, das sich aufgrund seiner außergewöhnlichen Eigenschaften für Hybridstrukturen bewährt hat, wie beispielsweise eine starke Licht-Materie Kopplung und die Möglichkeit von kristallinem Wachstum bei Temperaturen von lediglich 50 °C.
Als Modellsystem für Wachstumsstudien wird im ersten Teil der Arbeit das lineare konjugierte organische Molekül Sexiphenyl (6P) und dessen fluorierten Derivate verwendet. Hiermit wird exemplarisch das Wachstumsverhalten unter Nutzung verschiedener Oberflächenterminierungen des Substrates, Variation der Temperatur und Funktionalisierung des Moleküls ermittelt. Mithilfe der Rasterkraftmikroskopie (AFM) zeigt sich, dass die Morphologie des ZnO-6P-Systems stark vom Gleichgewicht zwischen der intermolekularen und Molekül-Substrat-Wechselwirkung abhängt. Dies führt zum einen zur Bildung von Inseln aus aufrecht stehenden oder Nadeln aus flach liegenden Molekülen. Durch Änderung der Oberflächenterminierung von ZnO oder der Substrattemperatur kann die vorherrschende Orientierung der Moleküle kontrolliert werden. Messungen mittels Kelvin-Sondenkraftmikroskopie (KPFM) bestätigen des Weiteren eine Veränderung in der Anordnung der Energieniveaus für stehende/liegende Moleküle und dem Substrat. Schließlich wird der Effekt von chemischer Modifikation der Moleküle untersucht. Es ergibt sich, dass die Fluorierung von 6P den Wachstumsmodus von rau und dreidimensional hin zu einem glattem, kristallinen Lage-für-Lage-Wachstum ändern kann, wie es für effiziente optoelektronische Bauteile erforderlich ist. Durch eine vergleichende KPFM-Untersuchung von symmetrisch und asymmetrisch fluorierten 6P-F_4 und 6P-F_2 wird eine weitere Möglichkeit der Wachstumskontrolle durch die Einführung eines permanenten Dipolmoments auf einer Seite der Moleküle aufgezeigt. Hierbei wird eine allgemeine Vorzugsorientierung der molekularen Kopfgruppe erreicht.
Anschließend werden Hybridstapel aus eingebetteten 6P-Nanokristallen in ZnO auf unterschiedlich terminierten Substratoberflächen untersucht und mittels hochauflösender Transmissionselektronenmikroskopie (HRTEM) eingehend analysiert. Es zeigt sich, dass 6P ohne Beeinträchtigung der Kristallstruktur, mit definierten Grenzflächen bis hin zur atom-

2 UHV ist definiert bei Drücken im Bereich von $10^{-7} - 10^{-12}$ mbar

aren/molekularen Ebene, überwachsen werden kann ohne einen Hinweis auf Interdiffusion von ZnO. Bei Untersuchung der ZnO-Deckschicht wird eine ausgeprägte Säulenstruktur mit bevorzugter c-Achsen-Orientierung über dem organischen Einschluss sichtbar, während die ZnO-Deckschicht neben den Einschlüssen einkristallin ist.
Der letzte Teil der Arbeit befasst sich mit der optischen Beobachtung während des organischen Wachstums durch Analyse von Änderungen der Reflexionsspektren. Dadurch ist es möglich Veränderungen von Struktureigenschaften und Wechselwirkungen zwischen Molekülen und dem Substrat zerstörungsfrei zu bestimmen während diese aufgewachsen werden. Eigenschaften, die sich in den Spektren widerspiegeln, sind die Absorption von Substrat und adsorbiertem Molekül, eine spektrale '*Gas-zu-Kristall*'-Verschiebung aufgrund der Aggregation der Moleküle und Ladungstransfer, der zu einer Bandverbiegung des ZnO führt. Vier Moleküle werden ausgewählt, um die jeweiligen Effekte beispielhaft zu demonstrieren und zu analysieren. Zunächst wird als prinzipieller Nachweis die Strukturentwicklung auf einem inerten nicht-absorbierenden Substrat (KBr) und dem organischen Molekül PTCDI untersucht. Unter Verwendung der erweiterten Dipolnäherung kann hier die strukturelle Entwicklung während des Wachstums identifiziert werden. Im nächsten Schritt wird die dielektrische Funktion für L4P auf ZnO bestimmt, welches spektral resonant gegenüber dem Exzitonenübergang von ZnO ist. Es zeigt sich eine vernachlässigbare Wechselwirkung zwischen Molekülen und dem ZnO-Substrat und es wird kein signifikanter Ladungstransfer oder Chemisorption nachgewiesen. Die Arbeit schließt mit der Untersuchung von Molekülen, die eine erhebliche Wechselwirkung mit dem Substrat in Form von Ladungstransfer aufweisen. Dies wird in den Spektren durch ein charakteristisches Merkmal in der Nähe der ZnO-Bandlücke offenbart, das der Bandverbiegung zugeschrieben wird.

Abschließend kann diese Arbeit hoffentlich zukünftige Studien anregen, um die Wachstumskontrolle an der Grenzfläche zwischen konjugierten organischen Molekülen und anorganischem Halbleiter weiter zu verbessern, damit effiziente optoelektronische Bauteile realisiert werden können.

Contents

Glossary

Notation	Description
5A	Pentacene
6P	*para*-Sexiphenyl
AFM	Atomic Force Microscope
ALA	Attachment Limited Aggregation
AM	Amplitude Modulation
BL	Bottom Layer
CB	Conduction Band
CPD	Contact Potential Difference
CT	Charge Transfer
CTF	Contrast Transfer Function
CVD	Chemical Vapor Deposition
CVT	Chemical Vapor Transport
CZD	Capture Zone Distribution
DFT	Density Functional Theory
DLA	Diffusion Limited Aggregation
DRS	Differential Reflectance Spectroscopy
EMT	Effective Medium Theory
ESB	Ehrlich-Schwoebel Barrier
F_6TCNNQ	1,3,4,5,7,8-hexafluorotetracyano-naphthoquinodimethane
FIB	Focussed Ion Beam
FM	Frequency Modulation
FT	Fourier Transform
FvdM	Frank-van-der-Merwe
FWHM	Full Width at Half Maximum
GWS	Generalized Wigner Surmise

Notation	Description
HIOS	Hybrid Inorganic/Organic Systems
HOMO	Highest Occupied Molecular Orbital
HRTEM	High Resolution Transmission Electron Microscopy
HT	Hydrothermal
IC	Internal Conversion
ISC	Intersystem Crossing
ISD	Island Size Distribution
KPFM	Kelvin Probe Force Microscopy
L4P	Ladder-type Quaterphenyl
LBL	Layer-By-Layer
LDOS	Local Density of States
LEED	Low Energy Electron Diffraction
LMA	Long Molecular Axis
LUMO	Lowest Unoccupied Molecular Orbital
MBE	Molecular Beam Epitaxy
MCP	Microchannel Plate
MD	Molecular Dynamics
ML	Monolayer
NTCDA	1,4,5,8-Naphthalenetetracarboxylic dianhydride
OLEDs	Organic Light Emitting Devices
OMBD	Organic Molecular Beam Deposition
OTFTs	Organic Thin-Film Transistors
PL	Photoluminescence
PLD	Pulsed Layer Deposition
PTCDI	3,4,9,10-Perylenetetracarboxylic diimide

Notation	Description
RF	Radiofrequency
RHEED	Reflection High Energy Electron Diffraction
RMS	Root Mean Square
RT	Room Temperature
SK	Stranski-Krastanov
SNBD	Scanning Nanobeam Diffraction
STM	Scanning Tunneling Microscope
TEM	Transmission Electron Microscope
TL	Top Layer
TPA	Two-Photon Absorption
UHV	Ultra-High Vacuum
UPS	Ultraviolet Photoemission Spectrocscopy
UV-Vis	Ultraviolet–Visible
VB	Valence Band
VR	Vibrational Relaxation
VW	Volmer-Weber
WL	Wetting Layer
XRD	X-ray Diffraction
XRR	X-ray Reflectivity
ZnO	Zinc Oxide

Physical constants

Notation	Description
$\hbar$	$\simeq 6.626 \cdot 10^{-34}$ Js: Planck's constant
c	$\simeq 2.998 \cdot 10^{8}$ $\frac{\mathrm{m}}{\mathrm{s}}$: Speed of light in vacuum
ε_0	$\simeq 8.859 \cdot 10^{-12}$ $\frac{\mathrm{As}}{\mathrm{Vm}}$: Permittivity of vacuum

Notation	Description
e	$\simeq 1.602 \cdot 10^{-19}\ \frac{\mathrm{kgm}^2}{\mathrm{s}^2}$: Elementary charge
k_B	$8.617 \cdot 10^{-5}$ eV/K: Boltzmann constant
μ_0	$\simeq 4\pi \cdot 10^{-7}\ \frac{\mathrm{Vs}}{\mathrm{Am}}$: Permeability of vacuum
m_e	$\simeq 9.109 \cdot 10^{-31}$ kg: Mass of electron

"Nature's imagination is so much greater than man's,
she's never going to let us relax."
— Richard Feynman

CHAPTER 1

Introduction

Historical ages in human history have been denoted according to their dominant working material as stone, bronze and iron age. The use and processing of the respective materials was associated with a great technological leap forward and advance in human civilization from hunter-gatherers to the modern society we now have. Today, every area of our life is deeply interwoven with the use of inorganic semiconducting materials, especially silicon. Accordingly, our current digital era has been frequently referred to as silicon age. This semiconductor is used in almost every electronic device as transistor material, but has also promoted the rise of the photovoltaic technique. From the invention of the first transistor in the middle of the last century, the capabilities of electronic devices today have been strongly enhanced. The scientific progress stimulated the development of micro-electronics and led to more efficient, less power consuming and smaller electronic devices. For instance, the whole computational power used to bring mankind to the moon is nowadays exceeded thousandfold by every smartphone. However, the silicon age is drawing near physical limits as nanometer scales are reached. Furthermore, devices based on silicon show poor light coupling due to silicon's indirect band gap and are therefore rather unsuited for opto-electronic devices. Hence, the development of novel materials for a new age are due. A candidate for a new class of materials has recently been arising by using organic molecules in optoelectronic devices. For one, they exhibit an efficient light-matter coupling, being reflected in the colorfulness of nature. Flowers and animals show vibrant colors as signal for attraction or defense, leaves build green chlorophyll and convert sun light into energy. The strong light-matter coupling, high quantum yield and variety in color are outstanding properties of organic molecules. The variety is achieved by the vast amount of different organic molecules which can be tailored for their respective use. Atoms or functional groups can be added to change electronic properties, the color can be tuned by changing the length of the conjugated system or the structure can be modified to mediate certain growth processes. Still another property makes them attractive for application: Organic molecules show a semiconducting character. Furthermore, this property is intrinsic to the single molecule rather than a property of a crystal structure as is the case for inorganic material. This makes molecular semiconductors more tolerant to impurities or defects.

Those properties have basically been known for a long time, the conductivity of anthracene was already investigated in the early 20th century,[1] and electroluminescence was found in the 1960s.[2] But practical problems hindered the development of efficient devices until in the late 1980s, when Tang and Van Slyke were able to engineer an organic electroluminescent diode with high emission efficiency and low operating voltage.[3] Intense research led to the establishment of organic semiconductors and enabled the development of Organic Thin-Film Transistors (OTFTs) as well as Organic Light Emitting Devices (OLEDs) and organic photovoltaic cells with respectable efficiencies.[4–7] However, low charge carrier mobilities and difficulties in the charge carrier injection still limit the application of those organic devices.

On the other hand the well-investigated inorganic semiconductors show exceptional charge carrier mobilities and densities with efficient electrical charge injection mechanisms. Furthermore, structural control is achieved down to the atomar level, assuring high crystalline perfection. The downside of inorganic semiconductors is a comparably small optical absorption cross-section and little spectral flexibility.

However, if the single constituents are brought together, their respective unique features could be exploited in heterostructures with novel characteristics. The foundation for those Hybrid Inorganic/Organic Systems (HIOS) were first laid in the late 1990s, where Agranovich et al. showed the theoretical possibility for electronic coupling and hybridization of the quantum states between inorganic and organic materials.[8,9] First experimental evidence for non-radiative energy transfer at the hybrid interface was then given for ZnO and GaN.[10,11] Possible applications for HIOS are high brightness light emitters or lasers covering a wide spectral range, as well as light absorbing photovoltaic devices, exploiting the high absorption cross section of the organic and superior charge carrier mobilities of the inorganic material. By this, the advantages of both worlds could be synergistically improved. However, a crucial point is the understanding of the processes taking place at the interface between the inorganic layer and deposited organic molecules. For eventual applications in optoelectronic devices it is furthermore mandatory to be able to prepare structures of designated structural order. Therefore, the present work focuses on the characterization of growth processes under controlled conditions and by this illustrates ways of monitoring and controlling the structure and morphology of hybrid systems composed of an inorganic semiconductor and conjugated organic molecules. While growth of inorganic structures based on single atoms is well-understood, the underlying growth processes of organic molecules are far more complex than for inorganic film growth. This is due to structural characteristics: The mostly anisotropic geometry of the molecules and many degrees of freedom make their movement hard to predict. Furthermore, weak intermolecular and molecule-substrate interactions compete between molecule-intrinsic or substrate-induced structures. Common parameters as substrate temperature, growth rate, but also the nature of the underlying substrate and deposited molecule itself influence the growth modes additionally and also have to be considered for the aggregation on inorganic surfaces.

Object of this work is to study the fundamental processes of hybrid systems between the inorganic semiconductor ZnO and various organic molecules, chosen by their respective specific properties. ZnO as a transparent wide band-gap material with notable light-matter coupling and high charge carrier mobility is highly available and non-toxic and therefore especially suitable for future applications. All the more as it can be grown with high crystalline perfection at substrate temperatures as low as 50 °C it is compatible with organic growth conditions.[12] Moreover, the choice of different faces of the ZnO crystal poses an additional control mechanism as *e.g.* ZnO($10\bar{1}0$) features a significant electrostatic surface field, modifying the molecular growth mode. All the growth experiments in this work take place in inorganic/organic all Ultra-High Vacuum (UHV) environment, which enables growth far from equilibrium and makes it possible to create materials in a highly controlled environment with unique properties which otherwise cannot be found in nature. After the utilized molecules are introduced in Sec. 4.1 and epitaxial overgrown ZnO surfaces are presented in Sec. 4.2, fundamental growth properties will be investigated with the aid of the prototypical rod-like organic model system *para*-sexiphenyl (6P) in Sec. 4.3. The rod-like structure of the molecule leads to a strong anisotropy in opto-electronic properties as well as in the growth. The anisotropy in the optical properties originates from the transition dipole moment, which is oriented along the long molecular axis of 6P. In contrast to this, the charge carrier mobility is greatest when the π-π overlap is maximal, which is perpendicular to the long molecular axis for 6P. Furthermore, diffusion and aggregation are defined by the anisotropic shape of the molecule. Consequently, the orientation of the molecules is crucial for the design of optoelectronic devices. For OLEDs flat-lying molecules are required for efficient charge injection and light emission, whereas for OTFTs the molecules should be standing upright to transport the charges from source to drain.[13] It will be shown how the orientation and nucleation of 6P can be controlled by different growth conditions. Additionally, the morphology and roughness of the molecular layer are of great importance and an alternative way to improve the growth from a rough three-dimensional towards a smooth, crystalline layer-by-layer growth by chemical modification will be demonstrated. After control over the molecular growth is obtained, a hybrid stack consisting of a 6P film overgrown with an additional ZnO layer is prepared. The result will be investigated by Transmission Electron Microscopy (TEM) in Sec. 4.4. Subsequently, an optical *in situ* method for the observation of the molecular layers during growth, which was implemented in this work, is introduced in Sec. 4.5. The so-called Differential Reflectance Spectroscopy (DRS) is highly sensitive to monitor minor changes in optical properties. Due to the high absorption coefficient of organic molecules and strong dependence of the absorption on the morphology ultrathin films of molecular layers can be investigated. The DR spectra can be modified by intermolecular interactions, changing the spectrum from monomer to aggregate spectrum. Using the example of the molecule PTCDI, it is shown how the change of the optical spectra is indicative for the structural development during growth. Furthermore, the ladder-type quaterphenyl L4P, known for its energy transfer with ZnO is used to extract dielectric properties of the molecule on an absorbing substrate. Eventually, charge transfer processes at the interface are spectrally observed during growth using the acceptor molecules NTCDA and F_6TCNNQ.

"The beauty of a living thing is not the atoms that go into it,
but the way those atoms are put together."
— Carl Sagan

CHAPTER 2

Fundamentals

In the following chapter a general overview over physical fundamentals of the experiments performed in the context of this thesis is given. The main focus will be the growth processes of thin films, treating especially the characteristic features of the growth of organic molecules on inorganic substrates. The individual components of an HIOS will be introduced and their respective properties, which make them particularly suitable for applications, will be presented. On the side of the inorganic semiconductors as a representative the wide-band gap material Zinc Oxide (ZnO) is chosen. Its crystal structure, different growth techniques, as well as the role of different crystal faces will be discussed. On the organic side, the outstanding diversity of organic molecules will be exploited by using molecules with tailored properties to modify optoelectronic properties as well as altering growth processes. General electronic and optical properties in the single molecule and in a crystal are illustrated. The chapter is concluded with an overview of the physics of thin films used to describe optical properties of molecules at the interface of the HIOS.

2.1 Growth of Hybrid Inorganic/Organic Systems

In this section, growth processes of hybrid structures are discussed. The outline follows the growth of those structures on a substrate surface. Therefore, first the general mechanisms for atoms/molecules are described, from arriving at the surface, diffusing and interacting, up to nucleation. Here thin film growth far-from-equilibrium is considered, making a kinetic description necessary. Moreover, features of organic molecular growth are highlighted which arise to a large extend from the anisotropy and additional degrees of freedom that molecules possess as well as the weak van der Waals interaction in the organic matter. Finally the processes that exceed the first Monolayer (ML) are discussed and different epitaxial growth mechanisms are defined.

2.1.1 Crystal Growth: Adsorption, Diffusion and Nucleation

This subsection follows the description of crystal growth in the book 'Islands, Mounds and Atoms' by Michely and Krug.[14] Crystal growth depends crucially on the thermodynamic state of the system, as this defines the underlying processes. Thus, it is essential to distinguish growth at or near equilibrium from growth proceeding in the non-equilibrium regime. In contrast to the natural crystal growth near equilibrium, which can be described in a thermodynamic framework, the thin film deposition in the vapor phase is a far-from-equilibrium process. For crystal growth close to equilibrium, the difference in the chemical potential between the deposit and the substrate is small and accordingly the deposit is adsorbed in the energetically favorable binding sites. Whereas far-from-equilibrium, large differences in the chemical potentials exist, making metastable binding sites accessible. Hence, the description of thin film growth far-from-equilibrium is mostly governed by kinetics.

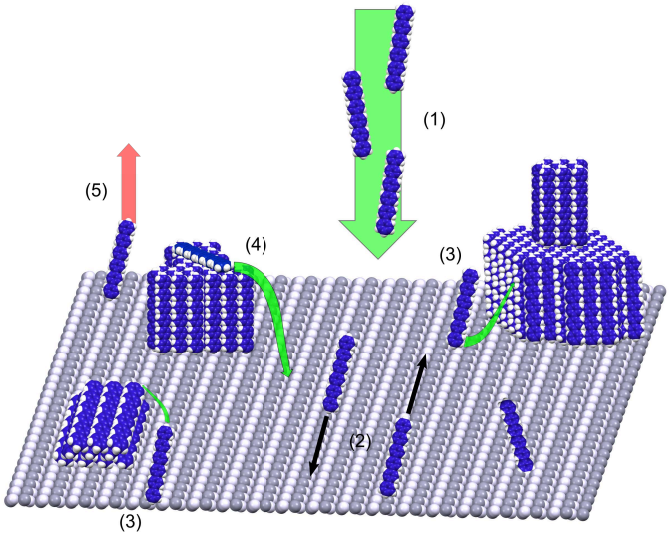

Figure 2.1: Surface processes, schematically shown for the exemplarily HIOS 6P/ZnO. The processes include adsorption of the molecules (1), intralayer diffusion (2) nucleation (3), interlayer diffusion (4) and re-desorption (5).

A schematic illustration of the different growth processes on the surface of a HIOS is shown in Fig. 2.1. Growth begins with the deposition of an atom/molecule on a surface. The deposit has a certain kinetic energy and, for Molecular Beam Epitaxy (MBE)[3], hits the sample in a focused beam of atoms/molecules (1). The flux F of the deposit towards the surface is one key parameter for the following growth processes.

3 This is the prevailing growth method used in this work, the general aspects of this growth technique will be introduced in Sec. 2.2.3, more technical aspects will be introduced in Sec. 3.1

The flux is defined through velocity and amount of deposited material:

$$F = N/SAt, \tag{2.1}$$

with the number of atoms/molecules N deposited per time t and surface area SA. As deposition drives the system from equilibrium, the flux determines the time that the system has to equilibrate before further material adsorbs and thus strongly determines the growth morphology.
When the deposit hits the surface, it either adsorbs and transfers its kinetic energy to the lattice or it is reflected. The probability for the deposit to adsorb is given by the sticking coefficient. The product of sticking coefficient and flux defines the growth rate.
If the deposit is adsorbed, the next crucial phase of growth begins: diffusion on the substrate (2). During diffusion, the adsorbate has to overcome energy barriers which is enabled through the remaining kinetic energy of the adsorbate, as well as the substrates' thermal energy. Thus, flux and substrate temperature are the two key parameters for growth in Ultra-High Vacuum (UHV). Diffusion is defined by the jump rate ν between adjacent adsorption sites. Those can only be accessed by overcoming the energy barrier E_D for surface diffusion between those sites with a certain attempt frequency ν_0. Conclusively for assuming a simple random walk, the jump rate ν is given by an Arrhenius law, which is proportional to the diffusion coefficient D:

$$D \propto \nu = \nu_0 \cdot exp(-E_D/k_BT) \tag{2.2}$$

The condition for this law, however, is that the attempt frequency is considerably higher than the jump rate, so that equilibrium is reached in the adsorption site. While diffusion of atoms can be described rather straightforward, different diffusion routes for molecules emerge due to the anisotropy of the molecules and their internal degrees of freedom. This results in attempt frequencies that are much higher for molecules. Whereas typical values for atoms are in the order of $1 \cdot 10^{13}$ s^{-1} values of up to $1 \cdot 10^{25}$ s^{-1} are reported for molecules.[15] Following diffusion, the next central phase in the growth process is the transition from a number of individually diffusing atoms/molecules to a stable nucleus (3), which crucially depends on the critical nucleus size i^*, which is defined as the largest unstable nucleus which still can disassemble, while a cluster of $i^* + 1$ particles will grow on average.[4] The stable clusters are important because they are the initial seeds that determine the island density. In Layer-By-Layer (LBL) growth, the nucleation forms the first of three regimes that arise for each layer: nucleation, aggregation and coalescence. In the nucleation regime, the density of nuclei increases as new islands form. The aggregation regime is defined by lateral growth of the existing islands, accompanied by a constant island density as newly deposited atoms/molecules land near or on top of an island and are immediately incorporated. This is followed by the coalescent regime, associated with a decrease of the island density as islands edges meet and merge. Eventually, on top of

4 For growth of molecules on an inorganic substrate the critical nucleus size can change for subsequent monolayers.

the first island of atoms/molecules another layer will start to grow, which also enables interlayer transport (4) as discussed below. Additionally, some adsorbed particles can be re-desorbed again (5), which is, however, neglected in the simple model considered below.

Aggregation mechanisms during Island Nucleation

The formation of clusters from particles is described through rate equations. These determine the change in the cluster density n_s with s particles using the rate Γ_s by which an $s+1$-cluster forms when a particle is added to the system

$$\frac{dn_s}{dt} = \Gamma_{s-1} - \Gamma_s \quad (s \geq 2). \tag{2.3}$$

The formation rate Γ_s is defined through the diffusion coefficient D of the monomer, a capture number σ_s, giving the diffusional flow of an s-cluster to adsorb and the rate Δ_s of an s-cluster to lose particles

$$\Gamma_s = \sigma_s D n_1 n_s - \Delta_{s+1} n_{s+1}. \tag{2.4}$$

Providing the substrate with the flux F of molecules, the resulting rate equation for the density of monomers is as follows

$$\frac{dn_1}{dt} = F - 2\Gamma_1 - \sum_{s \geq 2} \Gamma_s, \tag{2.5}$$

where the incoming flux feeds the density of monomers, while formation of dimers and larger clusters reduces it. Although Eqns. 2.3-2.5 describe nucleation pretty well, the parameters defining them are generally not experimentally accessible. Here the concept of critical nucleus size comes in. As previously mentioned, clusters with $s \geq i^* + 1$ are considered stable and are assumed to not decay anymore, hence $\Delta_s = 0$ for $s > i^*$. The total density N of stable clusters is defined as the sum of islands from $s = i^* + 1$ to infinity. Then Eqn. 2.3 becomes

$$\frac{dN}{dt} = \sigma_{i^*} D n_1 n_{i^*}. \tag{2.6}$$

In order to determine the island density of stable islands, Venables et al. first formulated a scale invariant power law, which depends on flux and surface temperature and holds for complete condensation[5] during growth stages before the coalescence regime.[16]

$$\frac{N}{N_0} = \eta\left(\Theta, i^*\right) \left(\frac{F}{D N_0}\right)^{\chi} e^{E_{n,i^*}/k_B T}, \tag{2.7}$$

here η is a weakly varying function of the coverage Θ and the critical nucleus i^*.[14] The constant N_0 is the number of possible adsorption sites per unit area, while E_{n,i^*} is the nucleation binding energy and χ is an exponent which depends on both i^* and the

5 In this case no desorption of the admolecules is assumed.

aggregation mechanism. For constant T, Eqn. 2.7 can basically be reduced to $N \sim (F/D)^{\chi}$. This shows that with increased flux the molecules are not able to move fast enough leading to a higher island density, while for greater diffusion rates D the molecules form fewer, bigger islands. For the aggregation various additional mechanisms are known, which are not included by rate equations. Those are for example limited by diffusion, attachment barriers, impurities or desorption.[17]
If an adsorbate diffuses to a stable aggregate and sticks to its edge with a probability of unity, the model of Diffusion Limited Aggregation (DLA) introduced by Witten and Sander gives a suitable description.[18] Their Monte Carlo simulations result in island morphologies of dendrite or fractal nature. For the power law, given in Eqn. 2.7 DLA yields analytical exponents which are:[16]

$$\chi_{DLA} = \frac{i^*}{i^*+2} \quad \text{and} \quad E_{DLA,n,i^*} = \frac{i^* E_d + E_{i^*}}{i^*+2}. \tag{2.8}$$

Here the activation energy for monomer diffusion is E_d and the binding energy of critical clusters is E_i^*. Crucial for the nucleation regime is the concept of the capture number σ of an island. This depends on the diffusion and attachment barrier of the island, whose respective capture numbers add inversely ($1/\sigma = 1/\sigma_D + 1/\sigma_A$). For a much larger diffusion barrier capture number $\sigma_D \gg \sigma_A$ the DLA can be applied. The other limit, $\sigma_A \gg \sigma_D$, is called Attachment Limited Aggregation (ALA) and was first studied by Kandel[19]

$$\chi_{ALA} = \frac{2i^*}{i^*+3} \quad \text{and} \quad E_{ALA,n,i^*} = \frac{2[i^*(E_d+E_a)+E_{i^*}]}{i^*+3}. \tag{2.9}$$

This model includes an additional attachment barrier E_a of the islands, meaning that the attachment probability is distinct from unity. ALA is especially relevant for growth of organic molecules, which exhibit a pronounced anisotropic shape. The anisotropy leads to an orientation dependent attachment barrier of the nucleus, since a single molecule diffuses in a lying state, however mostly forms standing equilibrium structures for high densities. This reorientation was for example shown for pentacene and para-sexiphenyl on mica.[17,20–22] For the different aggregation regimes Eqn. 2.7 implies that there is a direct relationship between the critical nucleus size i^* and the Island Size Distribution (ISD), through N, giving an experimentally measurable quantity to determine i^*. Transferring Eqn. 2.7 to the scaled ISD $n_s = (\Theta/S^2) f(s/S)$ indicates that n_s should only depend on the coverage Θ, the mean island size S and the ratio $u = s/S$. In the limit of DLA, Amar and Family gave an empirical formula for f by using kinetic Monte Carlo simulations and showed that the scaling function is:[23]

$$f_p(u) = C_{i^*} u^{i^*} exp(-i^* a_{i^*} u^{1/a_{i^*}}), \tag{2.10}$$

with C_{i^*}, u^{i^*} being implicit geometrical equations

$$C_{i^*} = \frac{(i a_i^*)^{(i^*+1)a_{i^*}}}{a_{i^*}\Gamma[(i^*+1)a_{i^*}]}, \quad (i^* a_{i^*})^{a_{i^*}} = \frac{\Gamma[(i^*+2)a_{i^*}]}{\Gamma[(i^*+1)a_{i^*}]}. \tag{2.11}$$

Pimpinelli and Einstein follow a different approach to obtain an experimentally accessible way to determine i^*. Instead of using ISD, they employ the Capture Zone Distribution (CZD). Here, not the island size is measured directly, but the capture zone around it is used. This idea dates back to Mulheran and Blackman, who used Voronoi polygons to approximate the areas that capture the adatoms within the capture zone.[24] Those polygons are areas, where the corresponding lines of the polygon are created by midpoints between the centers of the surrounding islands, as seen in Fig. 2.2.

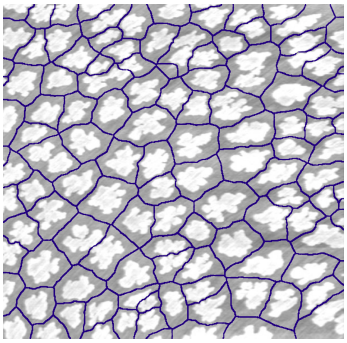

Figure 2.2: Voronoi tesselation of a sub-monolayer of *para*-sexiphenyl molecules on a ZnO substrate.

Pimpinelli and Einstein proposed to use the generalized Wigner surmise to extract i^* from the CZD. Wigner gives a probability distribution, which they extended for any aggregation mechanism.[17,25]

$$P_\beta(s) = a_\beta \cdot s^\beta \cdot \exp(-b_\beta s^2), \tag{2.12}$$

containing only one parameter β, where $s = A/\langle A \rangle$, A is the Voronoi polygon size, $\langle A \rangle$ the mean value of A and a_β and b_β are constants assuring normalization and unit mean respectively.

$$a_\beta = 2\Gamma\left(\frac{\beta+2}{2}\right)^{\beta+1} / \Gamma\left(\frac{\beta+1}{2}\right)^{\beta+2}, \quad b_\beta = \left[\Gamma\left(\frac{\beta+2}{2}\right) / \Gamma\left(\frac{\beta+1}{2}\right)\right]^2. \tag{2.13}$$

To describe different aggregation mechanisms β has different values for the various mechanisms. For DLA and ALA it is determined as $\beta_{DLA} = i^* + 2$ and $\beta_{ALA} = (i^* + 3)/2$.[17] Using these limits, Eqn. 2.12 forms the basis for coverage dependent growth studies evaluating the critical islands size independent of the growth regime. This will be demonstrated in Sec. 4.3 for *para*-sexiphenyl derivatives.

Beyond the first Monolayer

For growth processes that go beyond the 1st ML, not only the diffusion on the substrate is of importance but it is also critical how interlayer diffusion proceeds. For this situation Eqn. 2.2 has to be customized, since the molecules experience an additional energy barrier on top of an island that exists between adjacent crystal planes, as seen in Fig. 2.3. This additional barrier keeps atoms from overcoming the step edges, leading to the growth of stepped surfaces.

In the case of step-edge diffusion the jump rate from Eqn. 2.2 is altered to

$$\nu = \nu_0' \cdot \exp(-(E_D + E_{ES})/k_B T), \tag{2.14}$$

with the new attempt frequency ν_0' and E_{ES} being the Ehrlich-Schwoebel Barrier (ESB), which describes the additional step-edge barrier.[26,27] This step edge barrier is the result of the broken 2D crystal lattice, due to missing 'neighbors' below the step edge. It dominates interlayer transport, since the hopping rate can be significantly reduced if the barrier is sufficiently high. Therefore, the step edge barrier is crucial for the morphology of the films, as it can suppress interlayer mass transport, leading to a strongly corrugated surface and the formation of 'wedding cake' like mounds. For an infinite step-edge barrier the mound shape approximately follows a Poisson distribution.[14] Fig. 2.3 depicts a strongly simplified model of the ESB.

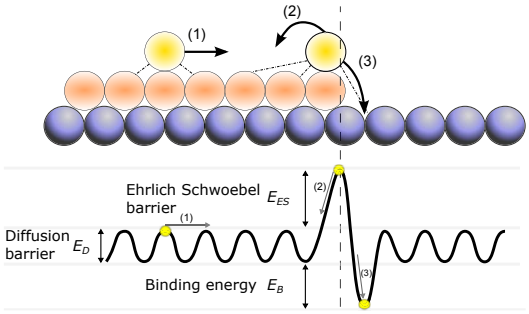

Figure 2.3: Diffusing particle in the energetic landscape of a step edge. Relevant parameters are the diffusion barrier E_D between adjacent adsorption sites for in-plane diffusion (1). The Ehrlich-Schwoebel barrier at the step edge E_{ES} has to be overcome to prevent reflection (2), while leap of the step results in energy gain due to the binding energy E_B (3).

For molecules, the model becomes more complicated and no general rules can be applied since the energetic landscape is altered by the possibility of the molecule to twist, rotate and bend over the edge. These edge-crossing modes have been shown for the rod-like but flexible *para*-sexiphenyl in Refs. [20, 28, 29]. Another difference to inorganic growth is the dependency of the ESB on the tilt angle of the molecules to the surface normal. The ESB reduces with increasing tilt angle of the molecules, because molecules crossing the island edge need to bend less to get to the underlying layer.[20,28]

Epitaxial Growth Mechanisms

Thin film growth of a crystalline layer on a likewise crystalline substrate is denoted as epitaxy originating from the Greek terms *epi* for above and *taxis* for ordered. In epitaxial growth the deposit is influenced by the substrate in such a way that an order is imposed onto the growing layer. Epitaxy is subdivided into homo- and heteroepitaxy according to whether grown layer and substrate are chemically identical or not. For thin film growth of organic molecules the terms van der Waals epitaxy and quasiepitaxy are used. These describe physisorption of molecules in an epitaxial relationship and growth with a defined orientational order evoked by the substrate respectively.[30] For near equilibrium crystal growth three scenarios are distinguished according to a criterion introduced 1958 by Bauer,

which each have distinctive morphologies.[31,32] The three growth scenarios only hold true for growth near thermodynamic equilibrium, meaning that morphologies that arise at far-from-equilibrium are not generally covered within the scope of this description.[14,31] The scenarios differ in the surface energies γ_s, γ_a of substrate and adsorbate, as well as the interface energy γ_i between them. They are schematically depicted in Fig. 2.4.

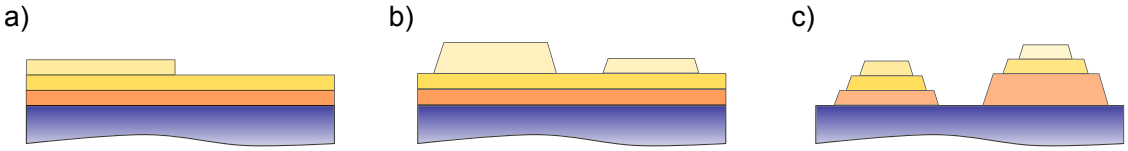

Figure 2.4: Schematic representation of the three epitaxial growth modes: (a) Frank-van-der-Merwe (b) Stranski-Krastanov (c) Volmer-Weber

Crucial for thin film growth is the ratio of the lateral adsorbate-adsorbate and the adsorbate-substrate interaction. The first scenario is growth in a layer-by-layer fashion, denoted as Frank-van-der-Merwe (FvdM) growth (Fig. 2.4a),[33–35] where one layer grows on the proceeding one until the surface is completely covered. Here, the adsorbates are more strongly bound to the substrate than to each other and the surface energy is reduced, so that the system gains energy by completely covering the substrate. This is the case when the sum of free energy of adsorbate and interface is less or equal than the surface free energy of the substrate. For homoepitaxial growth, γ_s and γ_a are equal, while per definition the interface energy is zero, making FM growth the natural growth mode if kinetic processes can be neglected. For both hetero- and homoepitaxy, FM growth fulfills

$$\gamma_s \geq \gamma_{a,k} + \gamma_{i,k} \tag{2.15}$$

for all layers k. The second scenario (Stranski-Krastanov (SK), see Fig.2.4b) arises, if Eqn. 2.15 holds only up to a critical layer k_c and breaks down for subsequent layers.[36] This phenomenon can arise if there is strain due to a difference in the lattice constants of substrate and adsorbate. The strain accumulates with the layer, which leads to an increase of $\gamma_{i,k}$ with increasing k. Above k_c this results in a dewetting of the adsorbate, which then forms islands. Finally, if the self-adhesion of the adsorbates is initially higher than the attachment to the substrate, the adsorbates instantly pile up in 3D islands (Fig. 2.4c), which is denoted as the Volmer-Weber (VW) growth mode.[37] In this case the surface energy of adsorbate and interface is bigger than the substrate right from the onset of growth:

$$\gamma_s < \gamma_a + \gamma_i \tag{2.16}$$

Conclusively, structures grown under near equilibrium conditions can be well-described through three growth scenarios which take into account surface and interface energies. Nonetheless, as mentioned before, the conditions for MBE growth are often determined by kinetic processes, which is why emerging structures are not necessarily dominated by the surface or interface energies but could arise due to differences in energy barrier heights, such as EBSs.

2.2 Zinc oxide

ZnO is used as the main substrate for the experiments in this work and the main inorganic component of the HIOS, hence, it is introduced in the subsequent section. For a more thorough overview reference is made to several reviews and other literature focusing on ZnO.[38–41]

As material, different forms of ZnO have been used in various fields for centuries. The first applications date back to around 500 BC, where a healing salve referred to as pushpanjan is mentioned in Indian medical texts. It was fabricated by "heating a metal in air",[42] believed to be zinc considering the medical effects zinc oxide has. Later on, it was even described by Marco Polo on his journey to Persia, where he observed the preparation of a solution to treat eye diseases.[43] For those medical purposes zinc oxide is still used today, especially in skin and wound treatment due to its antiseptic effects.[44] Zinc oxide also played a part in first brass production, where calamine, a compound of zinc oxide, was used already from at least the 1st century BC.[45] It became widely known as pigment in paint called zinc white. Today it is mainly used in the rubber fabrication and ceramic industry, but also in a more specialized field exploiting the pronounced piezoelectric properties, although the full potential of zinc oxide is far from being developed due to its favorable properties, which could be employed in transparent electronics, transistors or diodes.

Scientific descriptions of ZnO trace back to the beginning of the twentieth century. However, the use of naturally occurring material, powder and sintered ZnO with different quality grades, resulted in a wide spread in measured properties.[46] Sound measurements were first acquired around 1935 by Fritsch, who evaporated ZnO to perform conductivity measurements,[46] by Bunn, who resolved the structural properties of ZnO "condensed from the smoke" and was the first to determine the lattice parameters with high accuracy,[47] as well as by Yearian who did first electron diffraction measurements.[48] Extensive studies of optical properties were performed in the 1950s and 1960s, starting with investigations of the luminescence by Mollwo[49] and followed up with absorption and reflection spectra, focusing on the excitonic structure of the crystal.[50–53] Light-emitting diodes were first realized in 1968 using Cu_2O as p-type material.[54] Further research on ZnO addressed the defect structure and growth to enable the fabrication of ZnO based optoelectronic devices in the blue and near UV spectral range. These investigations culminated in the awareness of two major problems for further developments: First, the high defect density of intrinsic donors attributed to oxygen vacancies (V_O), Zn interstitials (Zn_i), as well as hydrogen impurities[38] cause an "intrinsically" n-type doping of nominally undoped material. This leads to the second major problem for the development of efficient optoelectronic devices made out of ZnO: The problem of ambipolar doping with the easily achievable n-type doping but the hurdle of obtaining reliable p-type doping.[55] Associated with this issue are self-compensating donor defects, deep acceptors with a high activation energy, and low solubility of possible p-type dopants.[41]
This bottleneck to efficiently p-dope a II-VI semiconductor also applies to the very similar wide band gap semiconductors GaN, which exhibits the same problem of growing

high-quality substrates with a controllable p-type doping. The breakthrough for p-doping of GaN was to implement a low temperature buffer layer that was honored with the Nobel Prize due to the "invention of efficient blue light-emitting diodes, which has enabled bright and energy-saving white light sources".[6][56] Although the same obstacle for ZnO is still a central problem, ZnO has fundamental advantages over the established GaN. High-quality single crystalline bulk ZnO is relatively easy to generate and homoepitaxial growth techniques without the need of highly toxic metalorganica are advantageous aspects. Further, important considerations for device production are easily possible wet chemical etching and nanostructuring. The strong polar character of ZnO make it attractive for piezoelectric applications. Finally, a high exciton binding energy of 60 meV makes laser operation well above room temperature (thermal energy of $k_BT = 26$ meV) with low thresholds possible, already successfully demonstrated by Bagnall et al.[57] However, despite repeated reports that claim successful p-doping or methods to achieve it, the development of p-doping strategies still stays the pivotal point of further ZnO development.[41,58–60]

What now follows is a summary of the basic properties of ZnO and of the most common growth methods.

2.2.1 Crystal structure

The primary crystal structures of ZnO are the hexagonal wurtzite and cubic zinc blende, as for most of the II-VI binary semiconductors. While the wurtzite structure is the thermodynamically stable phase at ambient conditions, the cubic zinc blende structure can only be grown on cubic substrates.[38] The bonding between Zn and O is partly covalent but exhibits a significant polar character due to the very strong electronegativity of oxygen and low zinc electronegativity. This leads to a substantial ionic character of 0.616 on the Phillips scale with ionized Zn^{2+}-O^{2-}.[40] Due to a sp^3 hybridization, the atoms are tetrahedrically coordinated where every Zn cation is surrounded by four O anions, and vice versa, forming the two interpenetrating hexagonal sub-lattices of the wurtzite structure. The two lattices are displaced by the internal parameter $u = 3/8 = 0.375$, corresponding to the bonding length parallel to the c-axis.

The primitive translation vectors $\boldsymbol{a} = \boldsymbol{b}$ form an angle of 120° and are defined in the x-y-plane with reported values ranging around $3.2475 - 3.2501$ Å, while the $\boldsymbol{c}$-vector is parallel to the z-axis with values ranging from 5.2042 to 5.2075 Å.[39] The hexagonal wurtzite structure of ZnO is shown in Fig. 2.5a. While the ideal wurtzite structure exhibits a $\boldsymbol{c}/\boldsymbol{a}$-ratio of $\sqrt{8/3} = 1.633$, the ZnO crystal differs by about 2% from this value. This is the largest known deviation for a wurtzite-type semiconductor resulting in an even stronger polarity due to the missing inversion symmetry. The unusually high polarity is accountable for the favoring of the wurtzite crystal structure, as is shown by theoretical calculations.[40] The growth and several physical properties of ZnO are strongly influenced by the polarity of the chosen surface, while the strong bond polarity additionally leads to a distinctive

6 Nobel committee of the Royal Swedish Academy of Sciences in 2014.

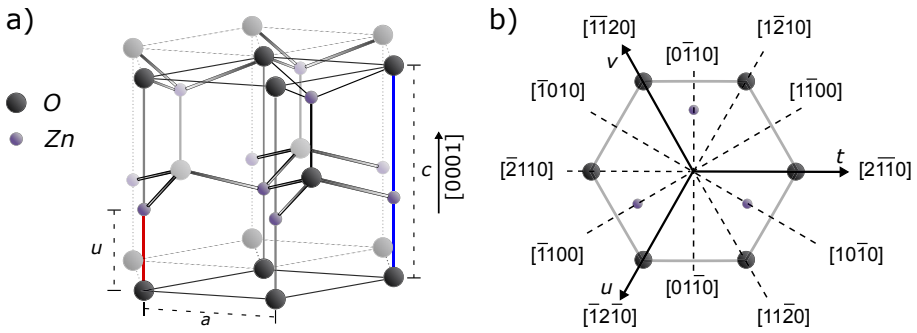

Figure 2.5: (a) Wurtzite crystal structure of ZnO with highlighted unit cell where (b) shows the top view with the corresponding facet orientations in the (tuvw) coordinate system. Adapted from Ref. [39].

piezoelectric behavior. As the polarity of the crystal leads to the formation of two faces with different polarity, they are unambiguously denoted in crystallography by two planes. To describe the hexagonal wurtzite crystal system and its plane orientations not the usual three-digit Miller index notation but four-digit Miller-bravais indices $hkil$ are used where the value of i is linear dependent of two other components:

$$i = -(h + k) \tag{2.17}$$

using this notation crystallographically equivalent planes are identified unambiguously. This can be seen for common orientations of the wurtzite crystal in Fig. 2.5b. For ZnO the c-axis is denoted by [0001] with corresponding perpendicular planes (0001) and (000-1). Those two planes originate from Zn- and O-terminated faces. The positive [0001] direction is therefore called Zn-polar, while the downwards pointing [000-1] direction is called O-polar. Moreover the [10-10] direction with equal numbers of Zn and O ions in alternating rows perpendicular to the c-axis should be particularly mentioned, since special properties of this orientation are employed in this work.

2.2.2 Band structure

The electronic band structure is essential for optical properties of a semiconductor. ZnO is a direct semiconductor, implying that the maximum of the Valence Band (VB) and the minimum of the Conduction Band (CB) are both located at the Γ-point of the Brillouin zone. ZnO exhibits a wide band gap, with a value of $E_g = 3.36\ eV$ at room temperature.[39] This wide band gap makes an application as transparent electrode and replacement for the toxic indium tin oxide possible. The CB of ZnO is formed by empty $4s$ states of Zn^{2+}, while the VB stems mainly from the $2p$ states of O^{2-}. The VB states, however, are split due to spin-orbit coupling in two multiple degenerated states at $\boldsymbol{k} = 0$, while crystal field interaction in wurtzite ZnO induces a further splitting of the lower lying band in two bands. The three resulting bands are labeled from higher to lower energy as A, B, C as shown in Fig. 2.6. A local approximation of the wave vector dependent energy $E(\boldsymbol{k})$ can be made by assuming a free electron in a box that is under the influence of a crystal field which

results in a parabolic dispersion relation, where the curvature of the parabola is given by the effective mass m^*:

$$E(\boldsymbol{k}) = E_0 + \frac{\hbar^2 \boldsymbol{k}}{2m*}, \tag{2.18}$$

with the offset of the energy E_0. The effective mass accounts for the change in movement due to external forces when compared to a free particle. The valence bands A, B and C are referred to as heavy hole, light hole and crystal field split band respectively.

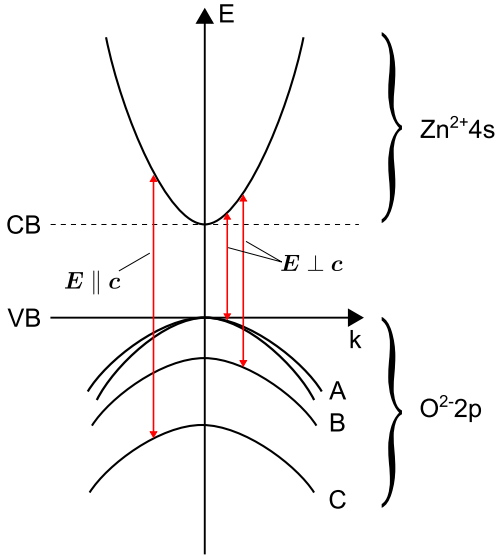

Figure 2.6: Schematic band structure at the Γ-point of ZnO. Adapted from Ref. [61].

A prerequisite for optoelectronic application is the ability to tune the band gap by using appropriate alloy materials. In the case of ZnO by cationic substitution of Zn with Mg, Cd or Be the band gap can be tuned between 2.5-4.3 eV, where phase separation stays the limiting factor.[40] For anionic substitution large electronegativity and size differences of the substituents lead to high bowing parameters, hindering an effective tuning.

2.2.3 Growth Techniques

Several techniques exist to grow ZnO bulk crystals, though it is still a challenge to grow high-quality structures. There are three main methods, namely Chemical Vapor Deposition (CVD), Pulsed Layer Deposition (PLD) and MBE to obtain epitaxial ZnO layers, grown either homoepitaxially on ZnO substrates or heteroepitaxially, *e.g.* on sapphire (Al_2O_3). Each of these techniques have its merits and disadvantages concerning the structural, electrical and optical properties of the resulting ZnO crystals.

Bulk Growth

The quality of the underlying substrate is crucial for ZnO growth and the resulting properties of potential ZnO devices. Homoepitaxial growth and the use of high-quality ZnO single crystals is naturally advantageous over foreign substrates like the often used Al_2O_3. Compared to ZnO Al_2O_3 exhibits a large lattice and thermal expansion mismatch and therefore produces a high dislocation density. However, the availability of ZnO substrates

cannot be taken for granted and its growth is hard to control and difficult to achieve on a large scale. Substrate growth uses the Chemical Vapor Transport (CVT) technique, growth from the melt, as well as primarily the Hydrothermal (HT) technique.

Chemical Vapor Transport (CVT)

CVT takes place in a horizontal tube with two temperature zones. The hot zone, where highly pure ZnO powder is placed, has temperatures of 800-1200 °C. The temperature difference to the cooler zone ranges from 20-200 °C.[62] ZnO is reduced with the assistance of a carrier gas, normally H_2, following the reaction $ZnO(s)+H_2(g) \rightarrow Zn(g)+H_2O(g)$. The carrier gas then transports the products to the cooler end of the tube, where the gaseous Zn reoxidizes at a ZnO crystal seed. Additional water vapor helps to maintain the proper stoichiometry. The crystallinity of the resulting ZnO is determined by the Full Width at Half Maximum (FWHM) of the (0002) X-ray Diffraction (XRD) rocking curve. Those indicate high-quality bulk crystals. Low FWHM-values of about 30 arcsec are observed for CVT grown samples, while the total impurity level was measured to be very low with < 0.5 ppm.[63] A drawback of this technique, is that it exhibits a low growth rate and hence is not suited for large scale production

Growth from the melt

This is rather uncomplicated for growth from the melt. Here zinc oxide powder is heated to the melting point. The high melting point for ZnO of 1975 °C and the decomposition in atomic components close to this melting point makes this process challenging.[64] To achieve the high temperatures, a Radiofrequency (RF) coil outside a cooled crucible is used, while the crucible itself is under pressure to avoid decomposition. When ZnO is melted it is slowly pulled into cooler areas, where it crystallizes. This method can achieve growth rates in the range of 5-20 mm/h and crystals with sizes of 5.5 inches, making this technique attractive due to the very high growth rate and scalability to large-sized crystals.[65,66]

Hydrothermal Technique (HT)

The prevalent method to commercially grow high-quality substrates is the hydrothermal technique. The HT growth occurs in an autoclave that is located in a two-zone furnace. In the autoclave sintered ZnO is solved in an alkaline-metal chloride mineralizer (mostly KOH/LiOH base) at elevated temperature and pressure until super-saturation is reached. This nutrient is placed in the higher temperature zone. Growth is then controlled by pulling ZnO seeds out of the solution to the colder zone in synchronization with the growth rate of the ZnO crystal. This is about 0.25 mm/day in the [0001] direction, while the growth proceeds anisotropically faster in the [0001] as in the [000-1] direction. By this crystals of up to 3 in. diameter can be grown.[39] The resulting ZnO crystals are of high quality, and samples with a very narrow FWHM of 8 arcsec in the (0002) reflection peak were achieved.[67] However, due to the growth from solution, an incorporation of impurities from the alkali metals is nearly impossible to avoid, and concentrations of up to several ppm for Li and tenths of ppm for K are observed, while also other impurities like Si, Fe, Al, present in the mineralizer and raw material are found. Those impurities influence the electric properties of the substrate and lead to unintentional doping, so that

hydrothermal substrates are highly n-type, while mobilities of ≈ 200 cm$^2V^{-1}s^{-1}$ are still observed. Additionally, comparably slow growth rates make this technique rather expensive. Nonetheless all substrates in this work are hydrothermally grown by CrysTec GmbH and further processed *in situ* in an MBE machine as described in Sec. 3.1

Epitaxial Growth

Pulsed Laser Deposition (PLD)

For PLD a high-power laser pulse in the nano- or picosecond regime is focused on a target composed of the depositing material. For ZnO excimer or Nd:YAG laser with pulses in the near-UV range are usually used. The laser evaporates ZnO and a plasma plume is created and directed to the heated substrate surface, where the material condenses. For ZnO this process takes place in an oxygen atmosphere at ambient oxygen pressures of $10^{-5}-10^{-1}$ mbar. Pulse energy of the laser, background pressure and substrate temperature control the growth and determine optical as well as electrical properties of the resulting film. Using this technique, the evaporated material keeps in principle its composition due to the high peak energy, although one has to consider that the sticking and incorporation coefficients on the surface are not necessarily the same for all elements of the compound. However, this method allows to process materials with a high melting point rather easily. The critical parameter is the ambient gas pressure that can ensure the right stoichiometry of the film.[68] Generally, films of high quality can be grown (FWHM of ≤ 18 arcsec and mobilities of 72 cm^{2}V^{-1} s^{-1} are achieved[39]). The challenges of this method lie in the often occurring clustering of particles on the surface and a limitation of the homogeneity to a rather small area of the sample.

Chemical Vapor Deposition (CVD)

Another technique to control epitaxial thin film growth on a molecular level is the chemical vapor deposition. Here, growth takes place in the gas phase at low pressure, where volatile compounds that contain the key material, the precursors, are transported by an inert carrier gas to the heated substrate surface. Often metalorganics are used, so that the technique is also denoted as MOCVD. The precursors chemically react with the surface and optimally decompose such that only the layer-forming elements adsorb and are built onto the substrate to gradually form layers, while the residuals of the compound desorb. The choice of the precursor is essential for the quality of the growth. The challenge lies in choosing a precursor that is volatile enough and only reacts on the substrate, which is difficult for compounds containing the reactive oxygen. Nonetheless, it is possible nowadays to grow abrupt interfaces and precisely control the growth, making it possible to produce heterostructures with multiple quantum wells. Furthermore, self-organizing processes can lead to the formation of nanowires. While the structural quality is comparable to other homoepitaxial techniques, a great advantage over other techniques is the principal possibility of production on a large-scale with a high throughput rate. Today's CVD apparatuses can grow several wafers of up to 8 inch in diameter in parallel with growth rates of up to several µm/h. Two major drawbacks of CVD, however, are that the produced layers can barely be investigated *in situ* and, due to the growth conditions, only structures near thermodynamic equilibrium can be created.

Molecular Beam Epitaxy (MBE)

Molecular beam epitaxy is the third common technique used to produce high-quality epitaxial thin films. Hereby the structures in this work are grown. The major difference to the other methods is that the deposition takes place in UHV chambers, making the technique sophisticated but also high in maintenance. However, it is the method of choice for the growth of high quality epitaxial samples, as UHV conditions make samples of the highest purity possible and achieve a precise control of the crystalline layers down to the atomic level. To obtain ultra-high vacuum, a combination of different pumping systems is used, like the mechanical turbomolecular pumps, ion pumps, which ionize residual gas and cryopumps that use helium with a temperature of ≈ 10 K to condense gases. Additionally, MBE chambers have a cooling shroud that can be filled with liquid nitrogen, making the chamber wall a sink for impurities. For the growth of different atomic species, elements of high purity are kept in separate effusion cells. They are sublimated out of the cells as an atomic/molecular beam. Varying the cell temperature leads to a change in the vapor pressure, which determines the growth rate. The special evaporation cells are called Knudsen cells. They assure an atomic/molecular beam with a particle density following a cosine distribution by using a considerably smaller orifice than the mean free path of the vapor. Additionally, the material is deposited in a pyrolitic boron nitride crucible that can withstand high temperatures. This allows to set the temperature suitable for the use of a great number of elements either as dopant or for ternary compounds. For the growth of oxides, an additional oxygen radical beam is provided by a RF plasma source, which is more reactive than it would be in the molecular form. Control over the growth is given by shutters in front of the cells to precisely switch off the atomic/molecular beam. Essential for MBE growth is the possibility to directly investigate the quality of the grown films, enabled by the Reflection High Energy Electron Diffraction (RHEED) technique (→ Sec. 3.2.1) which provides an extensive investigation tool to determine structure and morphology as well as the growth rate *in situ*. RHEED is the most common technique used during the growth process, but the UHV conditions also allow several other methods to investigate the pristine surface and structure of the film. These include LEED, PEEM, PES, XRD, AFM/STM (→ Sec. 3.2.2), but also optical spectroscopy during growth is possible (→ Sec. 3.2.5). The growth itself is governed by kinetics rather than thermodynamics, allowing growth far-from-equilibrium and the creation of naturally not existing metastable compounds. The parameters that control the growth process are the substrate temperature and the flux of impinging matter, where the substrate temperature controls diffusion, ad-/desorption and nucleation/dissociation, while the flux sets a time scale for impinging species to find an energetically favorable site. As mentioned before, ZnO epitaxy has been and still is mainly conducted on foreign substrates such as Al_2O_3. This is due to their low cost and high availability, while ZnO substrates are still expensive. However, in this work epitaxially overgrown ZnO substrates are used due to their exceptional surface properties that are especially interesting for the interaction with molecular adsorbates. Another great advantage of molecular beam epitaxy, particularly for hybrid inorganic/organic structures is the possibility to deposit not only atomic species but also molecules, especially organic molecules. This is then denoted as Organic Molecular Beam Deposition (OMBD).[30]

Here, the inorganic/organic structures can be grown without interruption of the UHV. Furthermore, due to the possibility to grow ZnO at temperatures as low as 50 °C,[12] inorganic overgrowth of the organic molecules layer without impairment becomes feasible. These aspects and advantages make MBE an excellent technique for this work.

2.2.4 ZnO Surfaces

For homoepitaxial growth as well growth of hybrid inorganic/organic structures the surface orientation of ZnO plays a significant role. The ZnO used in this work is exclusively of wurtzite structure. Hence, it lacks inversion symmetry, leading to crystallographic polarity, referred to as either Zn polar or O polar surfaces, according to the (0001) and (000$\bar{1}$) basal planes. The polarity affects the growth mode and defect formation as well as physical properties in general as for example doping or piezoelectricity. At growth this manifests itself in the surface morphology defined especially by the Zn/O ratio. Smooth films for the O polar surface can be achieved in a Zn-rich regime, while excess O supply is required for the Zn polar surface (differing by a factor of around 3.7).[39] This is due to the high equilibrium vapor pressure of Zn, making a high oxygen flux necessary to avoid 3D growth on the Zn polar surface, as well as different dangling bond configurations of the surfaces as seen in Fig. 2.7a. On the Zn polar surface terminal O atoms exhibit three dangling bonds, while for the O polar surface the O atoms have only a single dangling bond. Therefore, the Zn migration length for the O-terminated surface of Zn polar ZnO is smaller than the corresponding O polar surface.[39] This has to be kept in mind for epitaxial overgrowth since well-defined smooth surfaces with broad monoatomar terraces without defects are desired for the controlled growth of smooth conjugated organic molecules films. Another property of the polar surfaces is a finite dipole moment, making the structure electrostatically unstable. Stabilization of the surface can be obtained by charge transfer between the polar surfaces, reconstruction or adsorbtion of atoms/molecules, which can be depending on the rest gas composition, adsorption of hydrogen/hydroxy or water layers.[69] Furthermore, the non-polar ZnO(10$\bar{1}$0) surface is used in this work (cf. Fig. 2.7b). This surface is characterized by alternating rows of Zn and O ions perpendicular to the c-axis. Owing to the Zn-O dimers of opposite charge a pronounced electrostatic potential landscape with a locally structured electric dipolar field emerges. This exhibits strengths of several V/nm, which plays an essential role in the alignment of molecules on the surface.[70]

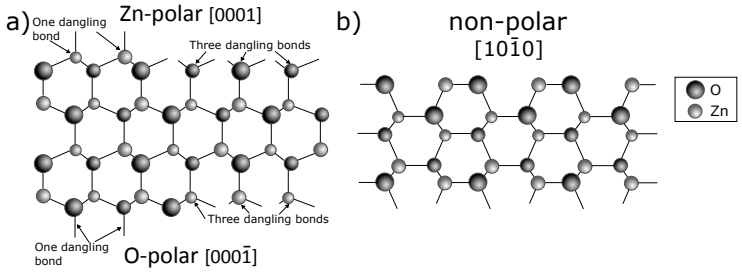

Figure 2.7: a) Schematic ZnO structure of the polar surfaces, showing also dangling bonds. View direction is a-plane. b) Surface structure of the non-polar ZnO(10$\bar{1}$0) surface.

2.3 Organic Molecules

The second component of the hybrid inorganic/organic systems, the organic molecules themselves, stands out due to their strong light-matter coupling and optical/electrical properties. By combining conjugated organic molecules with the inorganic semiconductor, novel heterostructures with new optoelectronic properties can be created. One of the biggest advantages is the great variety of different organic materials to choose from, which makes it possible to tailor their properties for the desired application. The characteristic properties of organic semiconductors are based on the π-bonding in the molecules, which create delocalized orbitals over the organic conjugated molecular system. Just like their inorganic counterpart this creates a semiconducting behavior. Similar to the energy bands of an inorganic semiconductor, the organic semiconductor posses a Highest Occupied Molecular Orbital (HOMO) and a Lowest Unoccupied Molecular Orbital (LUMO), denoting the highest orbital of the molecule containing electrons and the next higher energy orbital respectively. The optical gap between those are typically in the Ultraviolet–Visible (UV-Vis) range. However, unlike in the band model of inorganic semiconductors, the electrons of organic semiconductors are localized in the single organic molecule and conductivity happens as a hopping transport between overlapping π orbitals of molecules. This results in a strongly temperature dependent properties and comparably low mobilities of organic semiconductors. In the following an introduction to the basic properties of organic semiconductors and an overview of the molecules used in this work will be given. For a more thorough introduction, the reader is referred to extensive literature for example by Pope and Swenberg, Schwörer and Wolf.[71,72]

2.3.1 Conjugated aromatic hydrocarbons

Hydrocarbons are organic molecules that are composed of hydrogen atoms bonded to carbon chains. In hydrocarbons with alternating double and single bonds between the carbon atoms orbitals can conjugate. Then, the carbon has sp^2 hybridized orbitals, where the three degenerated coplanar bonds to hydrogen and carbon atoms form strong localized σ bonds. Since the carbon binds to only three surrounding atoms, a fourth unbound valence electron of p_z character remains, oriented perpendicularly to the molecular plane. Those protruding p_z orbitals overlap between adjacent carbon atoms across σ bonds. As a result they form π bonds that can be delocalized over the whole molecule.

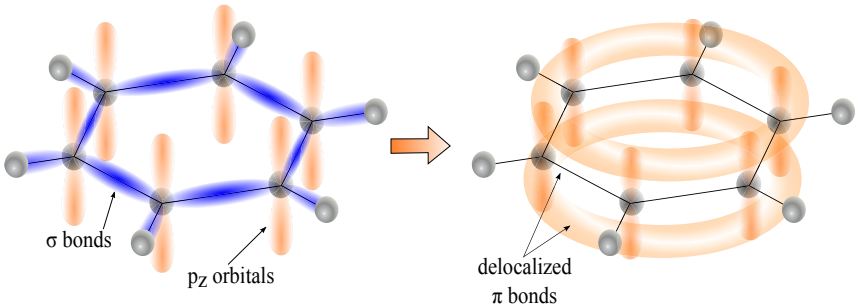

Figure 2.8: Benzene molecule with a sketch of the transition of p_z orbitals to a delocalized π system above and below the molecule.

This delocalization becomes apparent in the length of the bonds between the carbon atoms. Single and double bonds normally have different lengths, nonetheless the π bonds are equidistant. Conjugated hydrocarbons are aromatic in coplanar configuration, cyclically arranged and particularly stable. Coplanar conjugated hydrocarbons follow Hückel's rule, which states that the number of π-electrons has to be $4n + 2$ with $n \in \mathbb{N}$. The prime example for a conjugated aromatic hydrocarbon is the benzene molecule (C_6H_6), where the six carbon atoms are arranged in a ring, as is shown in Fig. 2.8 with the delocalization of the π system. The benzene molecule serves as a base unit for a great class of organic molecules. The delocalization between the different carbon bonds can be described within the molecule orbital (MO) theory, where the respective wave functions of the atomic orbitals are linearly combined. The resulting MOs are either of bonding (π), non-bonding n or antibonding (π^*) character, depending if they are additive, non-interacting or subtractive. For benzene this results in three bonding orbitals. Bonding and non-bonding orbitals are energetically lower, so that they are occupied first. Correspondingly benzene has 3 bonding orbitals occupied with the six π-electrons and 3 antibonding orbitals as can be seen in Fig. 2.9. The energy gap between bonding and antibonding orbitals is denoted as HOMO-LUMO gap in analogy to the band gap in inorganic semiconductors. The HOMO-LUMO gap describes the optical transitions in organic molecules. Notably, if molecules consist of polycyclic building blocks, but differ in the number of rings, chemical and electronic properties are similar, while the transition energies of HOMO-LUMO decrease with increasing length of the molecule.[72] The transition processes between HOMO and LUMO, are described in the following chapter.

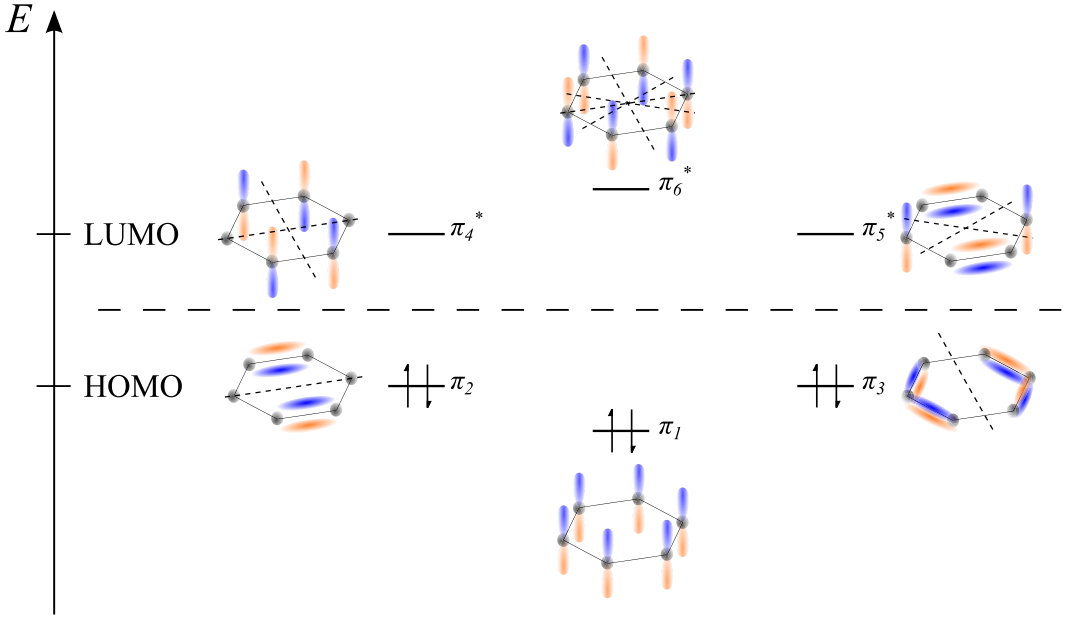

Figure 2.9: Schematic energy diagram for the six π orbitals in the benzene molecule. The π orbitals of lowest energy up to the HOMO are occupied and of bonding character, while orbitals above the LUMO are antibonding and unoccupied in the unexcited state.

2.3.2 Electronic States of Molecules

Molecules can be excited through electromagnetic waves, where basically three excitations are distinguished, namely rotation, rotational–vibrational and electronic excitations. These are described through the Schrödinger equation. To solve the equation for molecules, the total molecular wave function $\Psi_{mol}(\mathbf{r_i},\mathbf{R_j})$ is separated according to the Born-Oppenheimer approximation into nuclear (vibrational χ_{vib}, rotational ϕ_{rot}) and electronic ψ_{el} component:

$$\Psi_{mol} = \psi_{el}(\mathbf{r_i},\mathbf{R_j}) \cdot \chi_{vib}(\mathbf{R_j} \cdot \phi_{rot}(\mathbf{R_j})), \tag{2.19}$$

with the electronic coordinates $\mathbf{r_i}$ and the nuclear coordinates $\mathbf{R_j}$. The separation is justified as the mass of the nucleus is approximately 1870 greater than the electron mass and therefore the transition between electronic states takes place in the time scale of $\lesssim 10^{-15}$ s, whereas the nuclear motion occurs in 10^{-13} s.[71] Applying the Schrödinger equation to Eqn. 2.19, the total excitation energy is found to be $E_T = E_{el}+E_{vib}+E_{rot}$. Here, the rotation excitations are a result of transitions between rotational states defined by the quantum number J. Rotational-vibrational excitations additionally exhibit a change of the rotational-vibrational states denoted with the quantum number ν. Ultimately, transitions between electronic states, can change both quantum numbers of the system. For electronic transitions all excitation processes play a role so that an electronic band is the entirety of transitions between two electron states with all corresponding changes in rotational and vibrational states yielding the characteristic electromagnetic spectrum of a molecule. The transition energies are then determined by $E_t = \Delta E_{el} + \Delta E_{vib} + \Delta E_{rot}$, whereby in general $\Delta E_{el} \gg \Delta E_{vib} \gg \Delta E_{rot}$.[73] The electronic bands of conjugated molecules are usually in the UV-Vis range due to their weakly bound π orbitals that need a lower excitation energy than σ bonded electrons.[71] In a solid state, where the molecules are restricted in their freedom of movement, and where additional broadening processes are present, rotational transitions can be neglected.[71,73] Additionally they are not resolved by most measuring instruments since the energetic spacing between the respective excitation energies for conjugated molecules is in the order of $E_e : E_{vib} : E_r = (1 : 0.1 : 0.001)$ eV.[71] The electronic, together with vibrational transitions result in vibronic transitions. To denote a transition between ground and excited state double and single prime are used respectively: $E''_{el}(\nu'') \rightarrow E'_{el}(\nu')$.

2.3.3 Optical Properties of Monomers

Franck-Condon Principle

To understand the different possible transitions, radiative as well as non-radiative, and their probabilities, a very comprehensible picture is given by the Franck-Condon principle, shown schematically in the diagram in Fig. 2.10 for a diatomic molecule.[74,75] The depicted ground electronic E''_{el} and excited electronic states E'_{el} are represented by a Morse like potential, that contains the dissociation energy E_{Diss} of the potential, a as constant characteristic for the molecules' interaction, as well as R and R_e as nuclear coordinate and equilibrium nuclear coordinate:

$$V(R) = E_{Diss}(1 - e^{a(R-R_e)})^2. \tag{2.20}$$

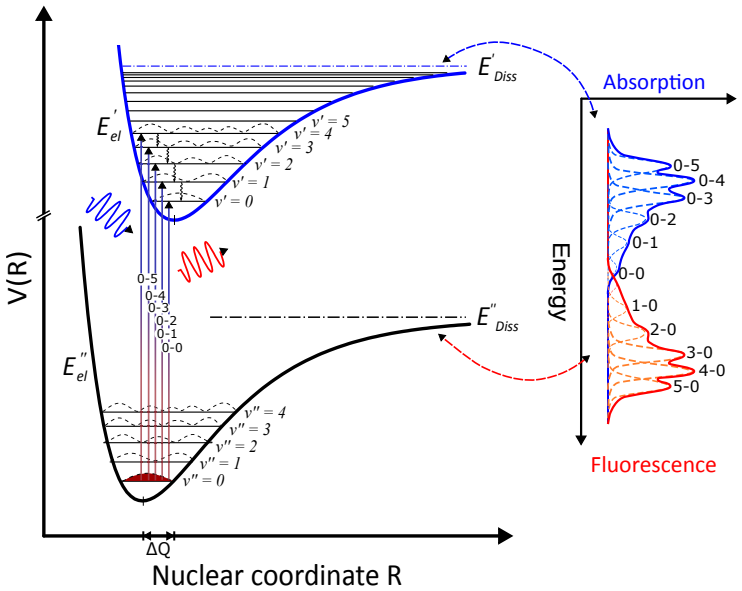

Figure 2.10: Franck-Condon principle energy diagram depicting two electronic states for a diatomic molecule. The nuclear coordinate corresponds to the distance between the atoms. The two electronic states E''_{el} and E'_{el} with vibrational levels ν'' and ν' and corresponding wave functions are shown for the first five vibrational levels. The energy levels are shifted by the configuration al coordinate displacement ΔQ upon excitation. Additionally the absorption from the ground in the excited state for selected transitions as well as radiationless relaxations between the vibrational levels can be seen, while on the right schematically a resulting absorption spectra and the mirror-inverted fluorescence is shown.

It accounts for both the anharmonicity in the real potential due to repulsion at low nuclear distances and the dissociation of the molecule at higher distances. Also, contrary to the picture of the quantum mechanical harmonic oscillator, the eigenstates in the potential are only approximately equidistant, devolving into a continuum at the dissociation energy. The eigenstates represent the respective vibrational states ν'' and ν' of the molecule with the associated wave functions. Starting with the Born-Oppenheimer approximation that the electronic transition does not affect the nucleus movement based on the great mass difference between nuclear particles and electron, an optical transition between two vibrational states in the different electronic states is given through a vertical transition in the Franck-Condon energy diagram. The probability of an excitation is not solely limited by the amount of energy needed for the transition but also by two other factors: The transition probability and the selection rules between the states. The probability of a transition between two vibrational states is given by the overlap integral of the wave functions of ground and excited state, also called the Franck-Condon factor:[74–76]

$$q_{\nu''\nu'} = \int \psi^*_{\nu'} \psi_{\nu''} \, \mathrm{d}V. \tag{2.21}$$

The intensity of the transition is proportional to the absolute square $I \propto |q_{\nu''\nu'}|^2$ of Eqn. (2.21). The so-called transition rules describe the coupling of the electric dipole of the molecule to the electromagnetic field and determine if a transition is allowed at all. The optical selection rules are however softened by different effects. Hence, '*forbidden*' transitions are still possible, but their rates are much smaller. The forbidden states are associated with a specific value of the transition dipole moment $M_{\nu''\nu'}$ and are defined for the states that yield a value of zero for the integral

$$M_{\nu''\nu'} = \int \psi^*_{e'} \mu_e \psi_{e''} \, \mathrm{d}V, \tag{2.22}$$

with the dipole moment μ_e. Furthermore the transition between two spin states is only allowed if the multiplicity $2S+1$ is preserved. Here, S is the total spin angular momentum S. In total, the transition probability between two states (not considering rotational transitions) is given as:

$$P = \int \psi^*_{\nu'} \psi_{\nu''} \, \mathrm{d}V_n \int \psi^*_{e'} \mu \psi_{e''} \, \mathrm{d}V_e \int \psi^*_{s'} \psi_{s''} \, \mathrm{d}V_s \tag{2.23}$$

Anisotropic molecules, that are for example elongated, exhibit an orientation dependent transition dipole moment (see Sec. 2.3.4). Attributable to the transition probability and selection rules, characteristic vibronic bands with certain intensity ratios arise from the interaction of light, denoted as vibronic progression. Typically the excitation takes place from the ground vibrational state, since the thermal energy $k_B T$ at room temperature is not sufficient for the excitation between different states.[7] The excited electronic state is, however, generally shifted to a higher equilibrium Q'_e than for the ground state Q''_e, due to the changed charge distribution and weaker bonding in the excited state. As a consequence, the transition probability also depends on the displacement $\Delta Q = Q'_e - Q''_e$ between ground and excited state. When in the excited state, the molecule relaxes quickly, phonon assisted, into the energetically more favorable lowest vibrational state $\nu' = 0$ before it decays under emission of light in the ground electronic state. This is known as Kasha's rule, which is also associated with a greater overlap integral between neighboring vibrational states than between the vibrational electronic states, making the transition between vibrational states faster.[78,79] In consequence of this the emission spectrum is nearly a mirror image of the absorption spectrum, as seen in Fig. 2.10. Generally, however, the emission spectrum is energetically shifted to lower energies due to the so-called Stokes shift, which describes the transition to a new equilibrium configuration in the electronic excited state, accompanied by a loss of energy. For a single molecule at low temperature and vanishing Stokes shift, an overlapping spectrum with the $\nu'' = 0 \leftrightarrow \nu' = 0$ transition as the mirror plane, also called the zero-phonon line is observed. The measured spectra are, as described before, not discrete line spectra but broadened by homogeneous and inhomogeneous effects.

7 According to the Boltzmann distribution $f_m = exp(-mE_\nu/k_B T)$, the thermal energy at room temperature of around 20 meV is not enough to excite the fundamental vibrational modes that are in the range of 100 meV.[71,77]

The homogeneous broadening influences the spectral linewidth for all molecules of the same kind in the same way, resulting in a Lorentzian profile. Contrary to homogeneous broadening, the inhomogeneous broadening originates from molecules that show slightly differing optical transition energies due to a different environment for every single molecule. Overlapping of the shifted zero-phonon lines and phonon side bands broadens the absorption and emission spectra, while the phonon sideband is shifted to higher energy in absorption and to lower energy in emission. This broadening is strongly temperature dependent, as for the higher temperatures the phonon energy increases. More energy creates more excited phonons, leading to a broadening of the phonon band while the zero-phonon transition decreases.[77]

Jabłoński Diagram

Up to now the excited states of the molecule were not further specified. They can, however, be of either singlet (denoted by S_0, S_1, S_2,...) or triplet (denoted by T_1, T_2,...) character, defined by the alignment of the spins in the respective states. While for the singlet states the total spin adds up to $S = 0$, the total spin for the triplet state is $S = 1$. Generally, the energy levels of the triplet states are lower than those of the corresponding singlet states according to Hund's rule. The different processes taking place in a system possessing singlet and triplet states are depicted in Fig. 2.11 as a Jabłoński diagram. Usually, organic molecules posses an even electron number so that the ground state is of singlet S_0 character.[72] Interaction with light results in absorption, exciting the molecule out of the ground state into the different singlet states S_n, following the transition probabilities. Transitions that change the multiplicity of the spin are '*forbidden*' in the Born-Oppenheimer approximation, so that a $S_0 \Rightarrow T_1$ transition is generally not observed. However, for molecules with certain properties the $S_0 \Rightarrow T_1$ transition probability can be drastically increased, due to spin-orbit coupling. From the excited singlet state of the molecule can now either decay directly radiatively by fluorescence from the lowest electronic states or it decays non-radiatively. A number of possible non-radiative decay mechanisms are possible. First, the energy can be transmitted to the surrounding crystal lattice as transition across the vibrational levels. Then the molecule rapidly decays to the lowest states of the corresponding S_n states through Vibrational Relaxation (VR) within $10^{-10} - 10^{-12}$ s.[77] Transitions between two levels of the same multiplicity are denoted as Internal Conversion (IC) and occur in $10^{-11} - 10^{-14}$ s, after which a further decay into the vibronic ground state happens. In Two-Photon Absorption (TPA) a second photon of sufficient energy is absorbed and excite the molecule in a higher state. Alternatively, the non-radiative Intersystem Crossing (ISC) with change of the multiplicity is possible. The probability of this process is enhanced by overlapping vibrational levels of the excited states. This overlap arises for heavy atoms where the spin-orbit coupling is increased.[80] In the triplet state VR and IC or, with a much smaller rate, ISC will occur. Being in the lowest level of the triplet state T_1, the transition to the ground singlet state is spin forbidden so that the lifetimes can last up to 100 s for molecules with a fluorescence lifetime in the range of $10^{-7} - 10^{-9}$ s.[77] This subsequent radiative transition is of lower energy than the corresponding singlet transitions and is denoted as phosphorescence.

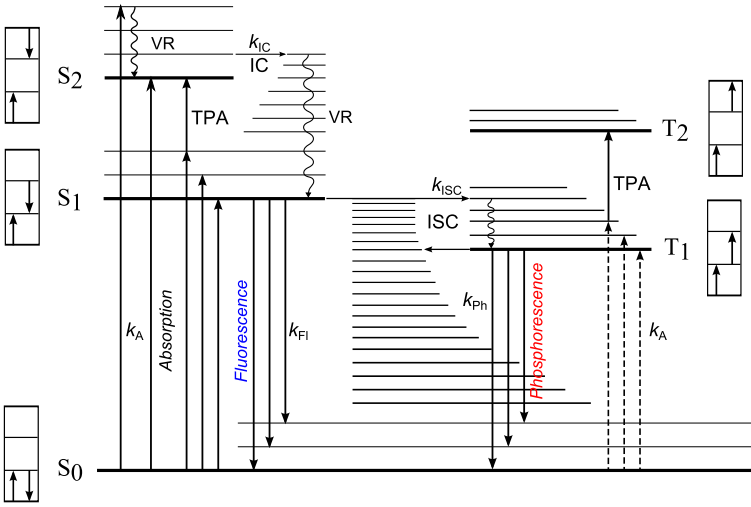

Figure 2.11: Jabłoński energy diagram with the possible optical and thermal processes between the different states present in a molecule for singlet and triplet states. k_{IC}, k_{ISC}, k_A, k_{Fl} and k_{Ph} respectively denote the transition rates for IC, ISC, Absorption, Fluorescence and Phosphorescence (Adapted from Ref. [72]).

2.3.4 From Molecule to Crystal

First observations for changes in the optical spectra in the transition from gas phase to crystalline organic molecules were obtained from investigations on benzene.[81] It was shown that organic crystals only show a comparably small difference to the gas phase or liquid spectra. This is unlike inorganic crystals, which exhibit a strongly deviating spectrum to their respective composing materials. The observation is explained through the relatively weak intramolecular binding forces compared to intermolecular forces, resulting in optical spectra that are still dominated by the features of the single molecule. Most notably, a '*solvent shift*' of the respective transition peaks arises when comparing gas state and solution spectra. This solvent shift generally results in lower energies in solution and an additional shift for the transition from solution to crystal, adding up to a '*gas-to-crystal*' shift. Depending on the crystal structure, a splitting of the peaks is observed as well as a general broadening of the spectrum. To explain this, a dimer system is considered, which consists of two identical molecules that are closer to each other than to surrounding molecules, but are not chemically bonded. Instead the dimer is held together by weak van der Waals forces. The molecules of the dimer are denoted with the subscript 1 and 2, with corresponding ground-state wave functions ψ_1 and ψ_2 and the energies $E_1 = E_2 = E_0$. The Hamiltonian describing this system is given by:

$$\hat{H} = \hat{H}_1 + \hat{H}_2 + V_{int}, \tag{2.24}$$

where V_{int} accounts for the intermolecular interactions. For a non-coupled pair of molecules V_{int} is zero. Then with the ground-state $\Psi_G = \psi_1\psi_2 = |0\rangle$ the energy for the system is

calculated as:

$$E_G = \left\langle \Psi_G | \hat{H} | \Psi_G \right\rangle = E_1 + E_2 = 2E_0 \tag{2.25}$$

The excited states of the molecules are ψ_1^*, ψ_2^* with the energies $E_1^* = E_2^* = E^*$. For one molecule in the singly excited state and the other one in the ground state, the respective states $\psi_1^*\psi_2 = \left|1^1\right\rangle$ and $\psi_1\psi_2^* = \left|1^2\right\rangle$ are degenerated (see Fig. 2.12, left side). If the interaction between them, however, is $V_{int} \neq 0$, the wave function for the excited dimer is given as a linear combination of the indistinguishable components:

$$\Psi_\pm^* = \frac{1}{\sqrt{2}} \left(\psi_1^*\psi_2 \pm \psi_1\psi_2^*\right), \tag{2.26}$$

where $\frac{1}{\sqrt{2}}$ ensures that the normalization condition is fulfilled (while antisymmetrization is neglected).
The corresponding energy yields:

$$\begin{aligned} E_\pm^* = \left\langle \Psi_\pm^* | \hat{H} | \Psi_\pm^* \right\rangle &= E_0 + E^* + \left\langle \Psi_\pm^* | V_{int} | \Psi_\pm^* \right\rangle \\ &= E_0 + E^* + \left\langle 1^1 \left| V_{int} \right| 1^1 \right\rangle \pm \left\langle 1^1 \left| V_{int} \right| 1^2 \right\rangle \\ &= E_0 + E^* + W^* \pm \beta \end{aligned} \tag{2.27}$$

Here W^* accounts for the Coulomb coupling between the excited molecule 1 and molecule 2 in the ground state (or vice versa) corresponding to van der Waals forces.[8] The resonant interaction energy labeled as β describes how the excitation energy is transferred from one molecule to another. This parameter lifts degeneration and the states split up into two energies, resulting in dimer exciton states. These are experimentally observed and schematically seen as depicted in Fig. 2.12.
To decide if a transition is allowed, one has to consider the respective dipole moments of the molecules and determine the transition dipole moment for the dimer. Here one assumes the transition point dipoles $\mathbf{M}_1$ and $\mathbf{M}_2$ for the molecules with different possible configurations. The dimer transition dipole moment $\mathbf{M}^\pm$ is

$$\begin{aligned} \mathbf{M}^\pm &= \left\langle \Psi_G | \mathbf{p} | \Psi_\pm^* \right\rangle \\ &= \frac{1}{\sqrt{2}} \left(\left\langle 0 \left| \mathbf{p} \right| 1^1 \pm 1^2 \right\rangle \right) \\ &= \frac{1}{\sqrt{2}} \left(\left\langle 0 \left| \mathbf{p} \right| 1^1 \right\rangle \pm \left\langle 0 \left| \mathbf{p} \right| 1^2 \right\rangle \right) \\ &= \frac{1}{\sqrt{2}} \left(\mathbf{M}^1 \pm \mathbf{M}^2 \right) \end{aligned} \tag{2.28}$$

For translationally equivalent molecules, the geometric interpretation of the transition dipole moment follows the exciton theory of Kasha.[82] For the parallel and head-to-tail configuration (→ Fig. 2.13), one transition dipole moment is dipole forbidden, since they

8 Accordingly for the ground state a shift of W_0 can be determined.

either add up to $\mathbf{M}^+ = \frac{2}{\sqrt{2}}\mathbf{M}^{\mathbf{1(2)}}$ or $\mathbf{M}^- = 0$. For a dimer consisting of two molecules parallel to each other, only the transition to the E_-^* state takes place, which creates a blue shift of the spectrum (→ Fig. 2.13). In contrast, for molecules in a head-to-tail configuration only a transition to the lower state E_+^* is possible, resulting in a red shift. The respective configurations are called H- and J-aggregates. For oblique molecules, however, there is always a non-vanishing transition moment, as can be seen exemplarily in Fig. 2.13 by vector addition.

The simple dimer model also describes the optical properties of a crystal with a periodic lattice, consisting of N identical molecules. For simplicity a one-dimensional lattice with equally oriented molecules in a periodical linear array and periodic boundary conditions is assumed, where the interaction between molecules is weak compared to intramolecular interactions. The total ground-state and state of molecules with a singly excited state of the ith molecule is given by:

$$\begin{aligned} \Psi_0 &= \mathcal{A} \prod_{m=1}^{N} \psi_m^0 \\ \Psi_n^* &= \mathcal{A}\psi_n^* \prod_{m\neq n}^{N} \psi_m^0, \end{aligned} \tag{2.29}$$

similar to the expressions given for the non-interacting dimer. This means that there is now a degeneracy of N excited states for the crystal, which again is lifted if the

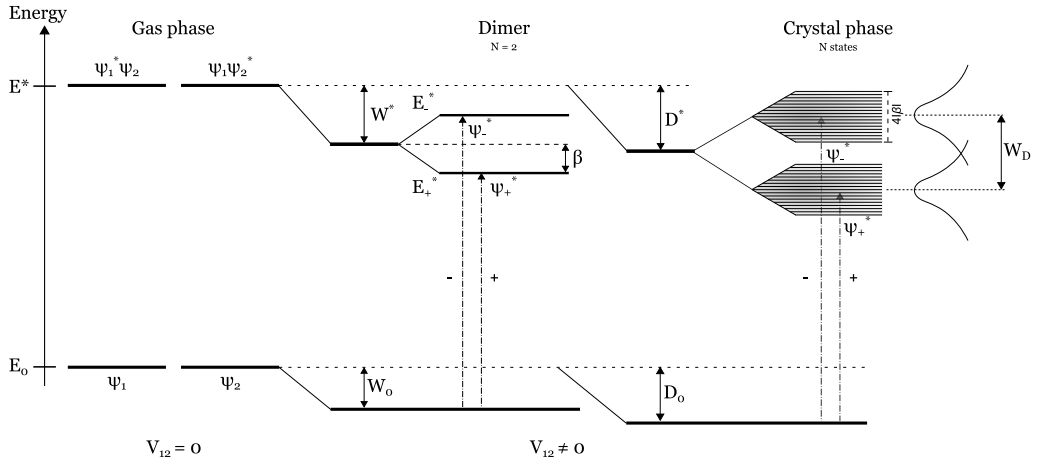

Figure 2.12: Energy states for a system of two molecules (Dimer) and corresponding crystal phase in the ground and excited states. In the case of non-interacting molecules the excited states are degenerated. For an interaction between them, an energy shift of $(W^* - W_0)$ and a splitting of 2β in two states E_+^* and E_-^* can be observed. Whereas for the crystal with N molecules and 2 inequivalent molecules in the unit cell there are 2 bands with N states. Here a shift D^* of the center of the excited states is observed as well as a shift D_0 of the ground state (Adapted from Ref. [71]).

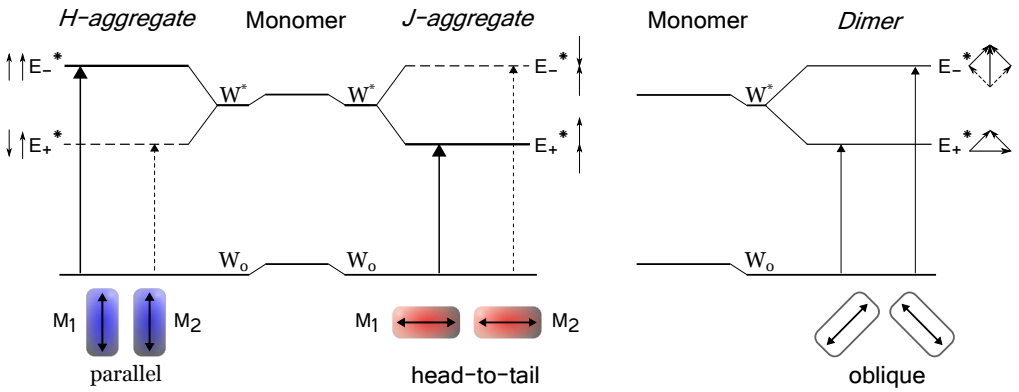

Figure 2.13: Splitting of exciton states in the case of non-translationally equivalent molecules in a dimer with corresponding transitions for different geometries. Forbidden transitions are denoted by dotted lines. For parallel (H-aggregate) or head-to-tail (J-aggregate) orientations of the molecules there is only one dipole-allowed transition possible, while for an oblique orientation both states are allowed (adapted from Ref. [71]).

intermolecular interaction is included, leading to N independent states and a band-like structure with delocalized excitons. To account for the antisymmetry of the wave function for identical fermions, the antisymmetrization operator $\mathcal{A}$ is introduced. The antisymmetric wave functions are not eigenfunctions of the crystals Hamiltonian. To obtain the crystal eigenfunctions the wave function can be described with the Bloch-wave ansatz:

$$\Psi(\mathbf{r}+\mathbf{R}) = f(\mathbf{R}) \cdot \Psi(\mathbf{r}) = e^{i\mathbf{k}\cdot\mathbf{r}} u(\mathbf{r}), \tag{2.30}$$

where $u(\mathbf{r})$ denotes for a periodic function with periodicity $\mathbf{R}$, while $\mathbf{k}$ is the crystal wave vector with the wavenumber:

$$k = 2\pi s/Na, \quad s = -N/2, -N/a+1...,N/2. \tag{2.31}$$

The distance a is the nearest-neighbor separation. Eqn. 2.31 results in eigenfunctions that are delocalized over the whole crystal:[72]

$$\Psi(k) = \frac{1}{\sqrt{N}} \sum_{l=1}^{N} e^{ilka} \Psi_l^*. \tag{2.32}$$

This wave function and the Hamiltonian for a linear molecular crystal with N states results in band like exciton eigenvalues:

$$E(k) = E_{Mol}^* + E_0 + D^* + 2\beta\cos(ka), \tag{2.33}$$

where D^* accounts for the solvent shift, or the shift of the center of the exciton band in respect to the free singly excited electron. D^* is generally smaller than 0 leading to a red-shift in the spectrum.[72] The width of the N states is given by $2\beta\cos(ka)$, as can be

seen in Fig. 2.12 for the crystal phase on the right. These exciton states, which occur mainly in molecular crystals, are tightly bound to energy levels below the band gap. The concept of those bound electron-hole states were first introduced in 1931 by Frenkel and are therefore called Frenkel excitons.[71,83] In addition to Frenkel states, Davydov showed that the N bands can be further split. This is dependent on the number of translationally inequivalent molecules m in the unit cell, due to an exchange of energy between them. This yields m bands with N states, denoted as Davydov-splitting W_D.[84] The splitting can be in the order of $10 - 100$ meV for singlet states.[71] See Fig. 2.12 for the example of two inequivalent molecules in the unit cell, which exhibit different polarizations. The effect of the gas-to-crystal shift with a Davydov-splitting can exemplarily be well-observed for an anthracene molecule, and becomes visible when comparing crystal and solution spectra.[85]

2.4 Thin Film Optics

In this work thin films of molecules are grown on substrates as well as in multilayer systems. To receive additional information of the growth processes those films are experimentally investigated with optical *in situ* measurements. The fundamentals of the underlying thin film optics are presented below.

2.4.1 Maxwell's Equations

From a classical physics point of view all electromagnetic and optical phenomena can be derived from the description of electromagnetic waves given by a set of four partial differential equations that relate the electric field $\boldsymbol{E}$ with the magnetic field $\boldsymbol{H}$ in a medium with charge and current density ρ and $\boldsymbol{j}$. The electric displacement field $\boldsymbol{D} = \varepsilon_0 \boldsymbol{E} + \boldsymbol{P}$ additionally accounts for a polarization $\boldsymbol{P}$ in a dielectric medium induced by the electric field due to a displacement of charges that creates a dipole in the single atom or molecule. The factor ε_0 in the equation stands for the permittivity of free space. In the case of small electric fields and an isotropic, non-conducting medium (a dielectric), the displacement field can be linearly approximated (defining the branch of linear optics) by $\boldsymbol{D} = \varepsilon_r \varepsilon_0 \boldsymbol{E}$, accounting for the polarization with the medium dependent relative permittivity ε_r[9].
Similarly, the magnetic field leads to a permeability induced magnetization in a medium according to $\boldsymbol{H} = \frac{\boldsymbol{B}}{\mu_0 \mu_r}$, with the vacuum permeability μ_0, relative permeability μ_r[10] and the magnetic induction $\boldsymbol{B}$. The complete set of equations which connect the different fields were in a condensed form first written down by James Clerk Maxwell, and are known as Maxwell's equations. In the macroscopic form they are as follows:

$$\nabla \cdot \boldsymbol{D} = \rho \qquad \nabla \cdot \boldsymbol{B} = 0 \tag{2.34a}$$

$$\nabla \times \boldsymbol{E} = -\frac{\partial \boldsymbol{B}}{\partial t} \qquad \nabla \times \boldsymbol{H} = \boldsymbol{j} + \frac{\partial \boldsymbol{D}}{\partial t} \tag{2.34b}$$

9 The relative permittivity is a function of the wavelength λ. In the case of an anisotropic medium ε_r is additionally a tensor of second order, depending on the direction of incidence of the light

10 Here only non-magnetic materials are considered, so that the relative permeability μ_r can be set to 1

These equations further simplify in the case of a dielectric and a negligible magnetic contribution, where the charge and current density vanish. By forming the curl of equation Eqn. (2.34b) without a polarizing medium in vacuum, one obtains the wave equations for electromagnetic waves in space and time:

$$\Delta \boldsymbol{F}(\boldsymbol{r},t) = \varepsilon_0 \mu_0 \frac{\partial^2 \boldsymbol{F}(\boldsymbol{r},t)}{\partial t^2} \tag{2.35}$$

With $\boldsymbol{F} = \{\boldsymbol{E},\boldsymbol{H}\}$ representing electric and magnetic fields respectively. Eqn. (2.35) is a second-order linear partial differential equation with the second derivative of space connecting the second derivative of time by the phase velocity of the wave

$$v_{Ph} = \frac{1}{\sqrt{\varepsilon_0 \mu_o}} = c. \tag{2.36}$$

Here, the speed of light in vacuum c is introduced. Using Eqn. (2.34a) and Eqn. (2.34b) one finds that: $\nabla \cdot \boldsymbol{F} \propto \nabla \cdot \boldsymbol{k}$, respectively $\nabla \times \boldsymbol{F} \propto \nabla \times \boldsymbol{k}$, implying that $\boldsymbol{k}$ is orthogonal to $\boldsymbol{D}$ and $\boldsymbol{B}$ as well as the fields being perpendicular to each other

$$\boldsymbol{D} \perp \boldsymbol{k} \perp \boldsymbol{B} \perp \boldsymbol{D}.$$

To describe the propagation of the wave in a medium, also polarization $\boldsymbol{P}$ in form of the displacement field has to be considered. By forming the time derivative of the Maxwell equation **rot H** in Eqn. (2.34b) with $\mathbf{j} = 0$ and $\mu_r = 1$ it becomes evident that the velocity defined in Eqn. (2.36) reduces in dielectric media due to the polarization:

$$\Delta \boldsymbol{E}(\boldsymbol{r},t) = \varepsilon_0 \mu_0 \frac{\partial^2 \boldsymbol{E}(\boldsymbol{r},t)}{\partial t^2} + \mu_0 \frac{\partial^2 \boldsymbol{P}(\boldsymbol{r},t)}{\partial t^2} \tag{2.37}$$

$$= \frac{1}{c^2} \frac{\partial^2 \boldsymbol{E}(\boldsymbol{r},t)}{\partial t^2} + \frac{1}{\varepsilon_0 c^2} \frac{\partial^2 \boldsymbol{P}(\boldsymbol{r},t)}{\partial t^2}, \tag{2.38}$$

where primary wave, represented by the first term and secondary wave are superimposed, so that the resulting phase velocity in a medium is reduced. Using the relative permittivity in linear approximation the polarization becomes: $\boldsymbol{P} = \varepsilon_0(\varepsilon_r - 1)\boldsymbol{E}$ and thus

$$\Delta \boldsymbol{E}(\boldsymbol{r},t) = \frac{\varepsilon_r}{c^2} \frac{\partial^2 \boldsymbol{E}(\boldsymbol{r},t)}{\partial t^2}, \tag{2.39}$$

yielding the changed phase velocity $v_{Ph'} = \frac{c}{\sqrt{\varepsilon_r}} = \frac{c}{n}$. Here the refractive index

$$n = \sqrt{\varepsilon_r} \tag{2.40}$$

is introduced, which describes how strongly the speed of light is slowed inside a medium due to the occurring polarization. If a linear medium is considered which additionally exhibits a non-negligible conductivity σ, the current becomes $\boldsymbol{j} = \sigma \boldsymbol{E}$ and the solution of

the wave equation leads to an additional term:

$$\Delta \boldsymbol{E}\,(\boldsymbol{r},t) = \frac{1}{v_{Ph}} \frac{\partial^2 \boldsymbol{E}\,(\boldsymbol{r},t)}{\partial t^2} + \mu_r \mu_0 \sigma \frac{\partial \boldsymbol{E}\,(\boldsymbol{r},t)}{\partial t} \tag{2.41}$$

This wave equation can be solved by assuming a plane, monochromatic, electromagnetic wave represented by:

$$\boldsymbol{E}\,(\boldsymbol{r},t) = \boldsymbol{E_0} e^{\mathrm{i}\left(\tilde{\boldsymbol{k}}\cdot\boldsymbol{r}-\omega t+\varphi\right)}, \tag{2.42}$$

with the Amplitude $\boldsymbol{E_0}$, the complex wave vector $\tilde{\boldsymbol{k}} = \boldsymbol{k_1} + \mathrm{i}\boldsymbol{k_2}$ that points in the propagation direction of the wave, the position vector $\boldsymbol{r}$ of the wave, the wave's angular frequency $\omega = 2\pi/\lambda$ and φ that accounts for the phase of the wave. By inserting Eqn. (2.42) into Eqn. (2.41) one receives a relation between $\tilde{\boldsymbol{k}}$ and ω, defining the complex refractive index $\tilde{n}$:

$$\tilde{\boldsymbol{k}}^2 = \frac{\omega^2}{c^2}\left(\varepsilon_r + \mathrm{i}\frac{\sigma}{\omega\varepsilon_0}\right) = \frac{\omega^2}{c^2}\tilde{n}^2 \tag{2.43a}$$

The so-called dispersion relation accounts for the frequency dependency of the permittivity. With this relation also the refractive index can be separated in real part n and imaginary part κ, where κ is called the extinction coefficient which accounts for the energy dissipation or absorption of the electromagnetic wave in the medium. One obtains for the refractive index:

$$\tilde{n}(\omega) = n(\omega) + \mathrm{i}\kappa(\omega) \tag{2.44}$$

This expression can be related to the relative permittivity in condition (2.40), which results in the complex dielectric function:

$$\tilde{\varepsilon}(\omega) = \varepsilon_1(\omega) + i\varepsilon_2(\omega) = \varepsilon_r + \mathrm{i}\frac{\sigma}{\omega\varepsilon_0} \tag{2.45a}$$

$$\varepsilon_1 = n^2 - \kappa^2 \tag{2.45b}$$

$$\varepsilon_2 = 2n\kappa \tag{2.45c}$$

This dielectric function $\tilde{\varepsilon}(\omega)$ will be important later on for the description of the molecular absorption during growth by differential reflectance spectroscopy ($\rightarrow$ Sec. 3.2.5) and is more suited than the complex refractive index, as it directly arises as a result from the oscillator model (which will be described in Sec. 2.4.3).
Furthermore the extinction coefficient can be expressed in a more accessible quantity, the attenuation coefficient, as a material property measurable in transmission experiments:

$$\alpha = \frac{4\pi\kappa}{\lambda} \tag{2.46}$$

2.4.2 Kramers-Kronig Dispersion Relationship

As shown in Eqn. (2.44) and (2.45a) real and imaginary part of the refractive index are connected by a dispersion relationship. It is possible to relate them also through an integral transformation. This means that if a quantity is known over the whole spectral range the other one can be determined. Generally this can mathematically be described by a linear response function to a stimulus, which are susceptibility and dielectric function in response to the electric field as the stimulus. The polarization of a medium according to this theory is then the product of the susceptibility and the electric field at all places and times:[86]

$$\frac{1}{\varepsilon_0}\mathbf{P}(\mathbf{r},t) = \int_{-\infty}^{+\infty}\int_{-\infty}^{+\infty} \chi(\mathbf{r},\mathbf{r}',t,t')\mathbf{E}(\mathbf{r}',t')\mathrm{d}t'\mathrm{d}\mathbf{r}'^3 \tag{2.47}$$

This can be further simplified by assuming that the medium is homogeneous in time and that there is no spatial dispersion, so that the time dependence can be replaced by $t - t'$, while the space dependence vanishes. Considering additionally the causality of the system, meaning that the response has to come after the stimulus 2.47 becomes:

$$\frac{1}{\varepsilon_0}\mathbf{P}(\mathbf{r},t) = \int_{-\infty}^{t} \chi(t-t')\mathbf{E}(t')\mathrm{d}t' \tag{2.48}$$

By applying a Fourier transform and using Cauchy's theorem this can be related to the dielectric function according to $\frac{1}{\varepsilon_0}\boldsymbol{P} = (\varepsilon - 1)\boldsymbol{E}$:[86]

$$\varepsilon_1(\omega) = 1 + \frac{2}{\pi}\mathcal{PV}\int_0^{\infty} \frac{\varepsilon_2(\omega')\omega'}{\omega'^2 - \omega^2}\mathrm{d}\omega' \tag{2.49}$$

$$\varepsilon_2(\omega) = -\frac{2\omega}{\pi}\mathcal{PV}\int_0^{\infty} \frac{\varepsilon_1(\omega') - 1}{\omega'^2 - \omega^2}\mathrm{d}\omega', \tag{2.50}$$

where $\mathcal{PV}$ denotes the Cauchy principal value of the integral. This relation between $\varepsilon_1(\omega)$ and $\varepsilon_2(\omega)$ is called the Kramers-Kronig relation. The obvious limitation of this method is that the spectral range of an experiment can only be finite, meaning that the resulting calculated spectra strongly depend on the covered spectral range and the properties of the examined material. One condition for good results is that the absorption has to be sufficiently small at the boundaries of the measured spectrum and that the material shows well-defined absorption bands.[87]

2.4.3 Optical Oscillator Model

The dielectric function describes the response of matter to a propagating electromagnetic field. In a microscopical, classical picture the interaction between light and matter can be imagined, analogously to two masses connected by a spring-like force, as a periodical displacement of the electrons (or rather the electron cloud) of an atom or molecule due

to a coupling to the electromagnetic field leading to a dipole moment. Due to the small mass, the considerably bigger nucleus can be considered as stationary. Therefore the system can be treated like a damped harmonic oscillator. Firstly introduced by Hendrik Antoon Lorentz, this is known as the Lorentz oscillator model. The model is similar to a one-dimensional harmonic oscillator with the restoring force $\boldsymbol{F} = -q\boldsymbol{E}$, damping represented by γ, the electron mass m_e and the resonance frequency ω_0. The equation of motion for a monochromatic, linearly polarized wave of frequency ω interacting with bound charge carriers is as follows:

$$m_e\ddot{\boldsymbol{r}} + 2\gamma m_e\dot{\boldsymbol{r}} + m_e\omega_0^2\boldsymbol{r} = -q\boldsymbol{E} \tag{2.51}$$

In the case of linear optics this can be directly related to the polarization of the medium over the electrical susceptibility χ as a linear response function according to $\boldsymbol{P} = \varepsilon_0\chi\boldsymbol{E}$(where the susceptibility is defined as $\chi(\omega) = 1 + \tilde{\varepsilon}(\omega)$), whereas a field-induced displacement leads to a polarization $\boldsymbol{P} = -qn\boldsymbol{r}$, proportional to the density n of the charge carriers. With this and the ansatz $\boldsymbol{P} = e^{-\mathrm{i}\omega t}$ this leads to the solution for the susceptibility:

$$\chi(\omega) = \frac{\beta\omega_0^2}{\left(\omega_0^2 - \omega^2\right) - 2\mathrm{i}\beta\omega\gamma}, \tag{2.52}$$

where the coupling constant $\beta = q^2n/m_e\varepsilon_0$ is defined. The dielectric function of a molecule can be represented by an ensemble of oscillators which add up to an overall susceptibility $\chi(\omega) = \sum_i \chi_i$. Considering only the part of the line spectrum around certain resonances of an oscillator unit, all other oscillators that the medium consists of can be treated as a background contribution ε_∞ which yields for the permittivity:

$$\tilde{\varepsilon}(\omega) = \varepsilon_\infty + \sum_i \frac{\beta_i\omega_{0,i}^2}{\left(\omega_{0,i}^2 - \omega^2\right) - 2\mathrm{i}\beta_i\omega\gamma_i} \tag{2.53}$$

This equation can be separated in real- and imaginary part which results in:

$$\varepsilon_1(\omega) = \varepsilon_\infty + \sum_i \frac{\beta_i\omega_{0,i}^2\left(\omega_{0,i}^2 - \omega^2\right)}{\left(\omega_{0,i}^2 - \omega^2\right)^2 + 4\beta_i\omega^2\gamma_i^2}, \quad \varepsilon_2(\omega) = \sum_i \frac{2\beta_i\omega_{0,i}^2\omega\gamma_i}{\left(\omega_{0,i}^2 - \omega^2\right)^2 + 4\beta_i\omega^2\gamma_i^2} \tag{2.54}$$

The principle shape for real and imaginary part of the dielectric function are displayed for exemplary values in Fig. 2.14. The characteristic features of the functions can be observed in this example. The imaginary part describes the absorption and is represented by a symmetric Lorentzian line shape with the maximum at the position close to the resonance frequency ω_0,[11] a height of $\beta\omega_0/2\gamma$ whereby the FWHM is given by 2γ. Maximum and minimum of ε_1 lie at the points of half height of ε_2 and the function converges for $\lim_{\omega\to\pm\infty}\varepsilon_1(\omega) = \varepsilon_\infty$.

11 the actual maximum is slightly lower than ω_0, but for $\gamma/\omega_0 \ll 1$ it holds $\omega_{max} \approx \omega_0$[88]

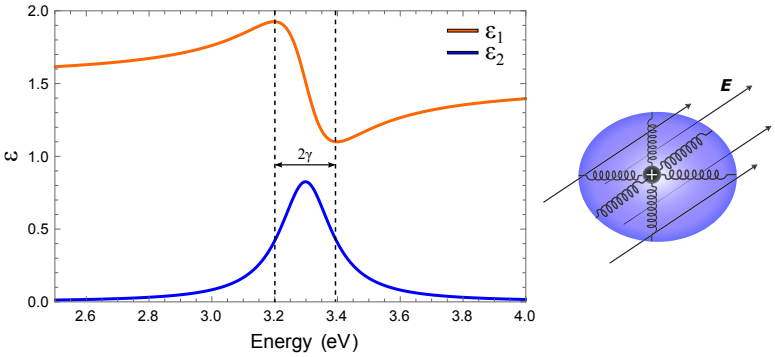

Figure 2.14: Real and imaginary part of the dielectric function ε for $E_0 = 3.3\ eV$, $\beta = 0.05$, $\gamma = 0.1$ and $\varepsilon_\infty = 1.5$ with the model of a displaced electron cloud by an electric field

The microscopic reasons for the spectral line broadening are related to different relaxation mechanisms of the damped harmonic oscillator. On the one hand the so-called natural broadening is related to the fact that every excited state with a finite lifetime shows a certain broadening, which emerges from the uncertainty relation between energy and lifetime of the state, meaning the smaller the lifetime the broader the emission. This is induced by spontaneous emission of the state and results in a decay time of $\tau_N = (2\gamma)^{-1}$ corresponding to the FWHM of the Lorentzian profile.[89] A second mechanism is due to collisions or mutual interactions of the single molecule with the lattice by radiationless decay, namely phonon processes leading to a dephasing of the particles and further broadening of the spectral line with the cumulative FWHM for both processes of:[89,90]

$$\gamma_{Hom} = \frac{1}{\tau_N} + \frac{2}{\tau_{col}} \tag{2.55}$$

The Lorentzian profile, however, only describes an homogeneous broadening of the spectroscopic line, that is in the case of a perfect crystal where all the oscillators 'feel' the same environment and show the same line profile. In the case of molecules in an disordered solid state, the Lorentz oscillator model, is therefore not the most appropriate one to describe the interaction between light and matter. The reason is that defects and disorder create location-dependent strain fields so that the electronic transitions are perturbed and slightly shifted against each other, leading to emitters with slightly different eigenfrequencies. This results in an inhomogeneous broadened line profile. This is composed of a superposition of Lorentzian profiles for every oscillator ensemble which is normally distributed according to a Gaussian shape. To account for both, homogeneous as well as inhomogeneous broadening of the line profile and to describe the resulting dielectric function accordingly, a convolution of a Lorentzian and a Gaussian profile can be conducted. This is known as the Voigt profile. Here, a pseudo-Voigt approximation developed by De Sousa Meneses et al. is presented.[91]

$$V(\omega,\gamma_G,\gamma_L) = (G(\gamma_G) * L(\gamma_L))(\omega) = \int_{-\infty}^{\infty} G(t,\gamma_G)L(\omega - t,\gamma_L)\ \mathrm{d}t, \tag{2.56}$$

with respective FWHM γ_G and γ_L for Gaussian and Lorentzian profile.

However, the Voigt function does not satisfy the causality principle due to its even parity. To ensure this a causal version of the Lorentzian profile as well as the Gaussian distribution is used:

$$L(\omega) = \left[1 + 4\left(\frac{\omega - \omega_0}{\gamma_L}\right)^2\right] - \left[1 + 4\left(\frac{\omega + \omega_0}{\gamma_L}\right)^2\right]^{-1} \tag{2.57}$$

$$G(\omega) = \frac{\sqrt{2\ln 2}}{\gamma_G\sqrt{\pi}} \exp\left(-4\ln 2\left(\frac{\omega}{\gamma_G}\right)\right). \tag{2.58}$$

To solve the integral and determine real and imaginary part of the Voigt profile that obey the Kramers-Kronig transform (→ Sec. 2.4.2) the dielectric function for a causal and renormalized Voigt profile is given as:[91]

$$\tilde{\varepsilon}(\omega) = \varepsilon_\infty + A\frac{V_{KKG}(\omega) + \mathrm{i}V(\omega)}{V(\omega_0)} \tag{2.59}$$

$$= \varepsilon_\infty + C_V^{'}(\omega) + C_V^{''}(\omega), \tag{2.60}$$

with the maximum amplitude A of the imaginary part, the Kramers-Kronig transform V^{KKG} of V and the Kramers-Kronig conform parts:

$$C_V^{'}(\omega) = \beta\frac{\mathrm{Re}\left(w(x - x_0 + \mathrm{i}y) - w(x + x_0 + \mathrm{i}y)\right)}{\mathrm{Re}\left(w(\mathrm{i}y)\right)} \tag{2.61}$$

$$C_V^{''}(\omega) = -\beta\frac{\mathrm{Im}\left(w(x - x_0 + \mathrm{i}y) - w(x + x_0 + \mathrm{i}y)\right)}{\mathrm{Re}\left(w(\mathrm{i}y)\right)}, \tag{2.62}$$

where

$$x = \frac{2\sqrt{\ln 2}}{\gamma_G}\omega, \quad x_0 = \frac{2\sqrt{\ln 2}}{\gamma_G}\omega_0, \quad y = \frac{\gamma_L}{\gamma_G}\sqrt{\ln 2} \tag{2.63}$$

and the so-called complex Faddeeva function is used:

$$w(z) = \frac{i}{\pi}\int_{-\infty}^{\infty}\frac{\exp(-t^2)}{z - t}\,\mathrm{d}t = \exp(-z^2)\mathrm{erfc}(-\mathrm{i}z). \tag{2.64}$$

To achieve a higher computational speed this result is further analytically approximated using generalized Lorentzians leading to an expression for V containing 16 constants (cf. Ref. [91]).

$$V(x,y) \cong \sum_{i=1}^{4}\left(\frac{C_iY_i + D_i(x - X_i)}{Y_i^2 + (x - X_i)^2} - \frac{C_iY_i - D_i(x + X_i)}{Y_i^2 + (x + X_i)^2}\right), \tag{2.65}$$

with $X_i = x_0 + B_i$ and $Y_i = y - A_i$ and the respective Kramers-Kronig transform

$$V^{KKG}(x,y) \cong \sum_{i=1}^{4} \left(\frac{C_i \left(\frac{X_i^2 Y_i^2}{x} - X_i \right) + D_i Y_i}{Y_i^2 + (x - X_i)^2} - \frac{C_i \left(\frac{X_i^2 Y_i^2}{x} - X_i \right) + X_i}{Y_i^2 + (x + X_i)^2} \right), \tag{2.66}$$

In total every resonance is described by the 4 parameters ω_0, A, γ_L, γ_g. Also it has to be noted that the coupling constant β and the Amplitude A cannot be directly compared between Lorentz and Voigt profile. Further models that especially account for the inhomogeneous line broadening of the chromophore by disorder and include a Gaussian profile are the so-called Brendel and Kim oscillator which mainly differ in the computational effort and accuracy.[92,93]

2.4.4 Mixing Models for the Dielectric Function

In the preceding discussion an homogeneously closed layer was assumed. Generally it can not be expected that the molecular growth proceeds in a layer-by-layer fashion. So the question is how the optical properties change when a corrugated surface is present and how they can be described within the existing theory. The theory behind this is the Effective Medium Theory (EMT), where the rough layer is characterized by an effectively homogeneous medium. For the description of such a system, first an isotropic, dipolar, microscopic inclusion is assumed. When this inclusion is inside an electrostatic field $\mathbf{E}$, the particle will be polarized, while the inner microscopic electric field $\mathbf{E}_{micr}$ reduces according to:[89]

$$\mathbf{E}_{micr} = \frac{\varepsilon_h + (\varepsilon - \varepsilon_h)L}{\varepsilon_h} \mathbf{E}, \tag{2.67}$$

with the dielectric function ε of the inclusion and ε_h of the host material as well as the shape factor s, accounting for the shape of the particle:

$$s = \begin{cases} 0 & \text{Disc} \\ 1/3 & \text{Sphere} \\ 1 & \text{Needle} \end{cases} \tag{2.68}$$

To account for N inclusions with the volume fraction f_j that the jth inclusion occupies, a more general formula exists, known as the general mixing model for j different kinds of inclusions:

$$\frac{\varepsilon_{\mathit{eff}} - \varepsilon_h}{\varepsilon_h + (\varepsilon_{\mathit{eff}} - \varepsilon_h)s} = \sum_j f_j \frac{(\varepsilon_j - \varepsilon_h)}{\varepsilon_h + (\varepsilon_j - \varepsilon_h)s} E \tag{2.69}$$

where $\varepsilon_{\mathit{eff}}$ is an effective dielectric function, describing an averaged dielectric function over a certain volume. The equation can be further specialized when one host material can be identified by assuming that the $j = l$ constituent is the host material, with $\varepsilon_h = \varepsilon_l$, so that the sum in 2.69 only runs over $j \neq l$. This approach differs in which species is chosen as host material, since this can lead to either an island like or a holey structure. It is known as the Maxwell Garnett approach. Whereas for a molecular mixture it is assumed that the effective dielectric function is equal to the host material, so that the left side of 2.69

becomes zero, which is is known as the Bruggemann approach. In this case the effective dielectric function for a mixture of two materials (one being vacuum) results in:[94]

$$\begin{aligned} \varepsilon_{eff} &= -\frac{1}{2(s-1)}\left[\sqrt{(A+B)^2-4(s-1)s\varepsilon}+A+B\right] \\ A &= \varepsilon(1-s)-s \\ B &= f(1-\varepsilon). \end{aligned} \tag{2.70}$$

There exist further EMTs depending on the distribution of the mixing materials, described with more detailed models, see for example Refs. [89, 95].

2.4.5 Light at Interfaces

To understand the behavior of light it is crucial not only to know how the light propagates in vacuum and media but also to understand what happens at the interface between two media. The description can be derived from the Maxwell equations when certain boundary conditions are considered. The resulting reflection and transmission at an interface is covered by the Fresnel equations which are directly related to the dielectric optical constants of the material enabling to derive them from experiments where reflection or transmission are measured. Here a system consisting of two isotropic media 0 and 1 with a vanishing charge density is considered. Exemplary a planar wave with the E-field perpendicular to the plane of incidence propagating through medium 0 is assumed (s-polarization). The wave with the incident wave vector $\boldsymbol{k}_i$ hits the interface between medium 0 and 1 forming the angles $\theta_i, \theta_r, \theta_t$ with the interfaces as seen in Fig. 2.15a.

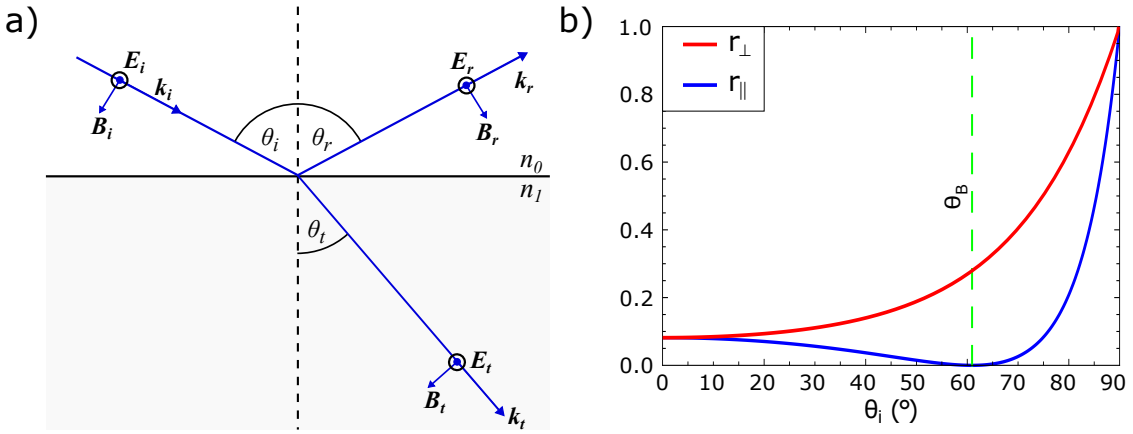

Figure 2.15: Incident s-polarized electromagnetic wave at the interface between the two isotropic media 0 and 1 with electrical field vectors and wave vector that splits up in reflected and transmitted part at the interface (adapted from Ref. [96])

There the incident electrical field $\boldsymbol{E}_i$ with wave vector $\boldsymbol{k}_i$ splits up on the surface in a reflected $\boldsymbol{E}_r$ and a transmitted part $\boldsymbol{E}_t$ (in the case of an anisotropic medium the Poynting vector $\mathbf{S} = \mathbf{E} \times \mathbf{H}$ gives the direction of the energy flux density and the wave vector are not generally parallel anymore). The components of the electromagnetic wave obey special boundary conditions at the interface derived from the Maxwell equations. They yield that

the tangential component of **E** and **H** as well as the normal component of **D** and **B** are continuous across the interface (See for example Ref. [86]). The boundary condition for the tangential component of **E** requires that the sum of incident and reflected amplitude are equal to the transmitted part according to:

$$E_i + E_r = E_t \tag{2.71}$$

Similarly the boundary condition for **H** results in:

$$-\frac{B_i}{\mu_i}\cos\theta_i + \frac{B_r}{\mu_r}\cos\theta_i = -\frac{B_t}{\mu_t}\cos\theta_i \tag{2.72}$$

With the relation $E = v_{PH} \cdot B = \frac{c}{n} \cdot B$ between E and B the so-called Fresnel equations, describing the reflection and transmission of the incoming light at the interface can be derived as ratio of reflected/transmitted and incident electric field amplitudes according to Ref. [96]:

$$r_\perp \equiv \left(\frac{E_r}{E_i}\right)_\perp = \frac{\frac{\tilde{n}_0}{\mu_i}\cdot\cos\theta_i - \frac{\tilde{n}_1}{\mu_t}\cdot\cos\theta_t}{\frac{\tilde{n}_0}{\mu_i}\cdot\cos\theta_i + \frac{\tilde{n}_1}{\mu_t}\cdot\cos\theta_t} \tag{2.73}$$

$$t_\perp \equiv \left(\frac{E_t}{E_i}\right)_\perp = \frac{2\frac{\tilde{n}_0}{\mu_i}\cdot\cos\theta_i}{\frac{\tilde{n}_0}{\mu_i}\cdot\cos\theta_i + \frac{\tilde{n}_1}{\mu_t}\cdot\cos\theta_t} \tag{2.74}$$

Those Fresnel coefficients of reflection and transmission are related to the measurable observables reflectance and transmittance T and R by the square of the absolute value.
In a similar way the Fresnel coefficients for the case of p-polarized light, where the E-field is parallel to the plane of incidence can be deduced:

$$r_\parallel \equiv \left(\frac{E_r}{E_i}\right)_\parallel = \frac{\frac{\tilde{n}_1}{\mu_t}\cdot\cos\theta_i - \frac{\tilde{n}_0}{\mu_i}\cdot\cos\theta_t}{\frac{\tilde{n}_0}{\mu_i}\cdot\cos\theta_i + \frac{\tilde{n}_1}{\mu_t}\cdot\cos\theta_t} \tag{2.75}$$

$$t_\parallel \equiv \left(\frac{E_t}{E_i}\right)_\parallel = \frac{2\frac{\tilde{n}_0}{\mu_i}\cdot\cos\theta_i}{\frac{\tilde{n}_0}{\mu_i}\cdot\cos\theta_t + \frac{\tilde{n}_1}{\mu_t}\cdot\cos\theta_i} \tag{2.76}$$

The behavior of the reflectance R is shown exemplarily in Fig. 2.15b for perpendicular and parallel polarized light for dielectric media 0 and 1 ($\mu_i = \mu_t = 1$). Here a peculiarity can be observed: If $n_i < n_t$, then for the angle:

$$\theta_B = \arctan\left(\frac{n_t}{n_i}\right) \tag{2.77}$$

the reflection of the parallel polarized light completely vanishes. This is known as Brewster's angle. On the other side if $n_i > n_t$, then there is a critical angle:

$$\theta_T = \arcsin\left(\frac{n_t}{n_i}\right) \tag{2.78}$$

where the light is completely reflected, known as angle of total reflection. Nevertheless it has to be considered that those special angles possess a frequency dependence owing to the refractive index.
A two layer system can be well-described with the Fresnel equations, but for more than two layers the determination of reflection and transmission gets increasingly difficult as multiple reflections on every interface contribute to the final outcome as schematically shown in Fig. 2.16 for a three layer system. The incident electromagnetic wave in medium 0 propagates in the direction of medium 1, a plane, parallel-sided, homogeneous layer on a half-infinite substrate, medium 2. For multilayers, like a three layer system multiple, reflections and transmissions occur on every interface of the incident electromagnetic wave and lead to interferences. To obtain the Fresnel coefficient r_{123} of the whole system every fraction has to be summed up that is back reflected into medium 0. This results in $r_1 + t_1 t_1' r_2 e^{-2i\beta} - t_1 t_1' r_1 r_2^2 e^{-4i\beta} + ...$
By carrying out a series expansion and using the relation $t_1 t_1' = 1 - r_1^2$ this can be condensed into

$$r_{123} = \frac{r_1 + r_2 e^{-2i\beta}}{1 + r_1 r_2 e^{-2i\beta}} \tag{2.79}$$

for the total reflection coefficient of the three layer system and both polarizations, with the change in phase

$$\beta = \frac{2\pi}{\lambda} \tilde{n}_1 d \cos\theta_1 \tag{2.80}$$

across layer 1, which depends on the refractive index $\tilde{n}_1$, the thickness d, the angle θ_1 of film 1 and the wavelength λ of the electromagnetic wave. Eqn. (2.79) is a general formula, valid for both polarizations by using the respective Fresnel coefficients, for all incident angles and also for absorbing media with complex refractive index. Similarly the case of transmission can be deduced:

$$t_{123} = \frac{t_1 t_2 e^{-i\beta}}{1 + r_1 r_2 e^{-2i\beta}} \tag{2.81}$$

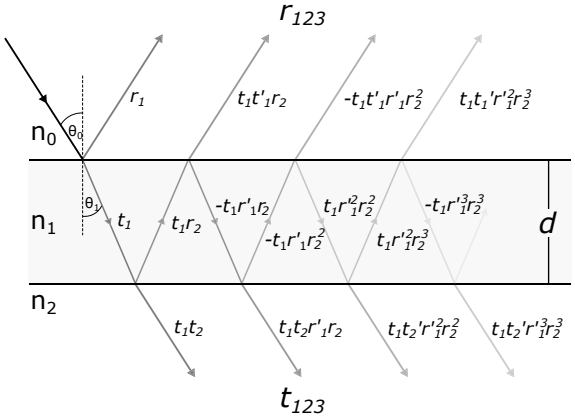

Figure 2.16: Electromagnetic wave propagating through a three layer system indicating the multiple reflection and transmission at each interface showing the corresponding amplitudes (Adapted from Ref. [97]).

2.4.6 Transfer-Matrix Method

When investigating systems with more than three layers the determination of the reflection coefficient becomes rapidly cumbersome. An alternative approach is to describe each layer by a matrix M_k where the N layers of the system are multiplied and add up to the total system matrix of the system

$$M = M_1 M_2 \dots M_k \dots M_{N-1} M_N. \tag{2.82}$$

Thus, the propagation of an electromagnetic wave in the k^{th} layer of the multilayer system is considered. The xy-plane of the coordinate system is formed by the layers plane, the z direction is chosen to be the surface normal. Then by following the continuity the resulting equations for the tangential components of parallel (p) and perpendicular (s) polarized electric and magnetic field are:

$$E_{kx} = (\quad E^p_{ki} e^{-\mathrm{i}\zeta_k z} + E^p_{kr} e^{+\mathrm{i}\zeta_k z}) \cos\theta_k \tag{2.83a}$$
$$H_{ky} = (\quad E^p_{ki} e^{-\mathrm{i}\zeta_k z} - E^p_{kr} e^{+\mathrm{i}\zeta_k z})\, n_k \tag{2.83b}$$
$$E_{ky} = (\quad E^s_{ki} e^{-\mathrm{i}\zeta_k z} + E^s_{kr} e^{+\mathrm{i}\zeta_k z}) \tag{2.83c}$$
$$H_{kx} = (-E^s_{ki} e^{-\mathrm{i}\zeta_k z} + E^s_{kr} e^{+\mathrm{i}\zeta_k z})\, n_k \cos\theta_k, \tag{2.83d}$$

where

$$\zeta_k = \frac{2\pi \tilde{n}_k \cos\theta_k}{\lambda}. \tag{2.84}$$

Following the discussion in Ref. [97] the Eqns. (2.83) are then solved by defining them at the interface between k^{th} and $k-1^{th}$ layer with $z = 0$ and at the interface between k^{th} and $k+1^{th}$ layer with $z = d_k$. For the respective polarizations the relations between k^{th} and $k-1^{th}$ layer can be deduced by eliminating the E_{ki} and E_{kr}. The results are then summarized in a characteristic matrix M_k.

$$\begin{pmatrix} E_{k-1} \\ H_{k-1} \end{pmatrix} = \begin{pmatrix} \cos(\zeta_k d) & \mathrm{i}\frac{\sin(\zeta_k d)}{\eta_k} \\ \mathrm{i}\eta_k \sin(\zeta_k d) & \cos(\zeta_k d) \end{pmatrix} \begin{pmatrix} E_k \\ H_k \end{pmatrix} = M_k \begin{pmatrix} E_k \\ H_k \end{pmatrix}, \tag{2.85}$$

where η is defined for both polarizations as $\eta_\perp = -\tilde{n}_k \cos\theta_k$ and $\eta_\parallel = \tilde{n}_k / \cos\theta_k$. The characteristic matrix of the entire system is then the product of all matrices as shown in Eq. 2.82, while elements of the characteristic matrix are $m_{ij} = \{M\}_{ij}$. To determine the overall reflection of the multilayer system the Fresnel coefficients 2.73 and 2.75 can furthermore expressed in terms of those matrix elements.[98]

$$r = \frac{(m_{11} + m_{12} q_N) q_0 - (m_{21} + m_{22} q_N)}{(m_{11} + m_{12} q_t) q_0 + (m_{21} + m_{22} q_N)}, \tag{2.86}$$

where $q^s_k = n^2_k \cos\theta_k$ and $q^p_k = \frac{1}{n^2_k} \cos\theta_k$ are defined for the respective polarizations.

"It's still magic even if you know how it's done."
— Terry Pratchett

CHAPTER 3

Analytical Methods and Experimental Setups

To elucidate growth processes and be able to control them with sub-ML precision, well defined experimental conditions under a highly pure environment are a prerequisite. This is made possible by growth in a MBE system operated in UHV, whereby growth of layers with the highest possible purity can be achieved. Furthermore, growth in this controlled environment enables the flexible variation of various parameters, such as growth temperature, beam flux and the ability to interrupt the atomic/molecular beam by shutters to precisely prepare atomically abrupt interfaces with desired compositions and properties. In this chapter an overview of the tandem MBE apparatus used for the preparation of thin hybrid inorganic/organic systems and characterization tools that are used in this work is given. These include *in situ* techniques that are installed inside the UHV system, such as methods based on electron diffraction like Reflection High Energy Electron Diffraction (RHEED) and Low Energy Electron Diffraction (LEED). While RHEED is directly installed inside the MBE chamber to monitor growth processes and characterize the crystallinity of the sample, LEED investigations are done post-growth, yet without breaking the vacuum. Furthermore, scanning probe microscopes, namely a Scanning Tunneling Microscope (STM) and Atomic Force Microscope (AFM) with the possibility to simultaneously measure the topography and Kelvin signal for local mapping of the surface potential are installed to investigate morphological and electronic properties of the surface. Finally, inside the organic growth chamber a Differential Reflectance Spectroscopy (DRS) setup was established within this work to monitor processes optically during growth. Furthermore, *ex situ* characterization tools include Transmission Electron Microscopy (TEM), UV-Vis spectroscopy, Ellipsometry and X-ray diffraction.

3.1 Tandem Molecular Beam Deposition System

The samples presented in this work were all grown in a tandem MBE apparatus consisting of two chambers for the growth of inorganic group II-oxide materials and the deposition of conjugated organic molecules as schematically shown in Fig. 3.1. For loading samples a load-lock module equipped with a turbomolecular pump is used to reach a pressure in the low 10^{-7} mbar range. Thereafter, they are introduced in the first buffer chamber. The buffer/analysis modules connect the growth chambers via individually pumped compartments separated by gate valves. By using ion pumps (Varian StarCell), a base pressure of

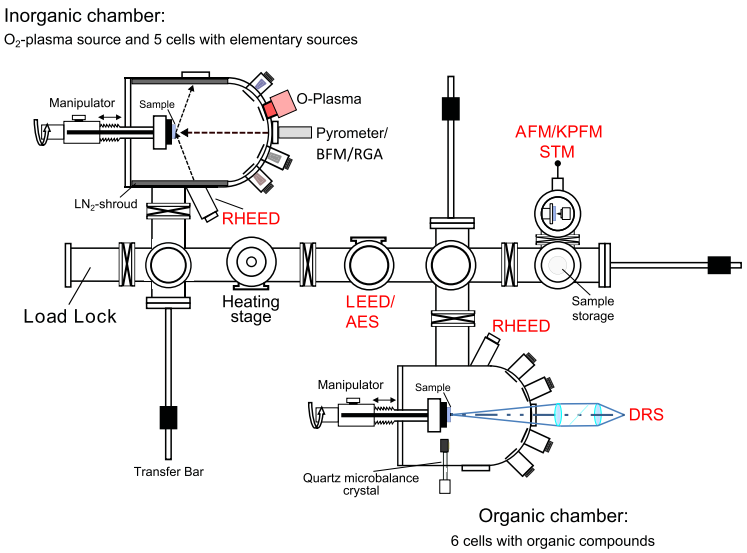

Figure 3.1: Schematic top view of the tandem MBE system used in this work with a growth chamber for inorganic on the left and an organic growth chamber on the right. The different characterization tools are highlighted in red.

$10^{-9} - 10^{-10}$ mbar inside the UHV line is reached. Transportation through the system is done by transfer rods as well as a sample trolley. The inorganic chamber is a DCA-450 MBE apparatus equipped with eight ports for effusion cells containing highly pure materials (5 to 6N) in crucibles made of pyrolitic boron nitride, while O_2 is supplied by an ADDON RF plasma source with the gas supply controlled by a mass flow controller. For pumping, the chamber is equipped with a cryopump and an ion pump. Additionally the chamber is shrouded by LN-cooled cryopanels that serve as a sink for impurities. Thereby the residual gas background pressure can reach values in the low 10^{-10} mbar regime. The chamber for organic growth is a smaller DCA-350 MBE with six ports for different molecular sources. The molecules exist in form of a powder and are filled in crucibles that are heated up to the molecule's respective evaporation point. By temperature adjustment the molecular flux can be controlled. The effusion cells include special low-temperature cells with high temperature stability to avoid thermal damaging of the molecules. In addition to the inorganic and organic growth chambers several preparation and analysis tools are located inside the UHV system to characterize the samples during and after growth *in situ*. A combination of a thermocouple behind the sample holder and a pyrometer (IMPAC) for the range of 250-2000 °C allows a reliable control of the substrate temperature inside the chamber during growth. To determine the flux from effusion cells a beam flux monitor (BFM) measures the beam equivalent pressure of the individual cells with a hot-filament ionization gauge. Additionally a residual gas analyzer (SPECTRA) measures residual gases to control contamination, while it also serves as leak detector. During growth the main analytical tool for inorganic growth is a 35 keV differentially pumped RHEED (STAIB instruments). Its principal will be further explained below. For further post-growth structural analysis of the surface an Omicron multichannel plate-LEED and UHV AFM/STM

(operated by a MATRIX control system) are available. Organic growth proceeds similar to growth in the inorganic chamber, with the difference that the flux of the molecular beam is measured by a quartz crystal microbalance (tectra) and the main tool for analysis during growth is DRS.

3.1.1 Sample preparation

The samples in this work are mainly ZnO substrates with either ZnO(0001), ZnO(000$\bar{1}$) or ZnO(10$\bar{1}$0) surface as well as sapphire (Al_2O_3) crystals supplied by CrysTec GmbH. Additionally, cleaved KBr substrates (Korth Kristalle GmbH) are used. The standard sample sizes are 10x10x0.5 mm^3 and 8x8x0.5 mm^3. The samples are either attached by clamps whereas Ti/Al_2O_3 covered Si substrate are used to be able to determine the substrates temperature by the pyrometer through the transparent ZnO or they are mounted with In directly on a Mo block. Samples which are roughened for DRS experiments are additionally cleaned in an ultrasonic bath before insertion into the UHV system. Here they are treated consecutively 5 min with n-Butyl-acetate, acetone and ethanol and rinsed with deionized water. Newly loaded samples are then placed on a heating stage located in the first buffer chamber, where a degassing step of 20 min at 750 °C is executed. Afterwards the substrates are generally exposed to O-plasma at elevated temperatures for several minutes in the inorganic growth chamber. The samples are overgrown typically with a 100 nm thick film using the standard and low-temperature epitaxial growth protocols for ZnO MBE growth, covered in greater detail in Refs. [12, 99–102]. The crystalline quality of the sample is verified by RHEED during growth (see Sec. 3.2.1).

3.2 *in situ* Characterization

3.2.1 Electron Diffraction LEED and RHEED

Electron diffraction methods are nowadays a vital part of *in situ* crystal growth characterization. The foundations for the development of electron diffraction methods was the postulation by de Broglie that mass-carrying particles exhibit a wave like character with a distinct wavelength[103]

$$\lambda = \frac{h}{\sqrt{2mE}}, \tag{3.1}$$

depending on their respective mass and energy.[12] Therefore, diffraction phenomena can also be observed for particles with mass. With this crystalline properties of materials can be determined by analyzing the diffraction patterns induced by scattered particles. The spatial distribution of the diffracted beam makes it possible to identify crystal structure and potential reconstructions of the surface. Additionally, it is possible to gain information about surface roughness, terrace size or surface steps by analyzing the intensity profile and determine the growth rate by analyzing growth oscillations. In the case of LEED, typically electrons with energies in the range of 10-500 eV are used with corresponding wavelengths of $\sim$ 0.5-4 Å. Due to a short mean free path of just a few Å for low-energy electrons in

12 Relativistic correction is not considered, since it only amounts to less than 1 % for LEED and about 3 % for RHEED

matter, only the first atomic layers are probed, making the technique strongly surface sensitive.[104] The diffraction pattern arises as a result of constructive interference with the lattice. The Laue condition relates the incident $\mathbf{k}_0$ and the scattered $\mathbf{k}$ wave vector with the reciprocal lattice vector $\mathbf{G}_{hkl} = h\mathbf{a_1}^* + k\mathbf{a_2}^* + l\mathbf{a_3}^*$ by

$$\mathbf{k} - \mathbf{k_0} = \mathbf{G}_{hkl}. \tag{3.2}$$

For the here considered case of elastic scattering $|\mathbf{k_0}| = |\mathbf{k}|$ holds. Then Eqn. 3.2 can be graphically depicted by the Ewald's sphere as shown in Fig. 3.2a.

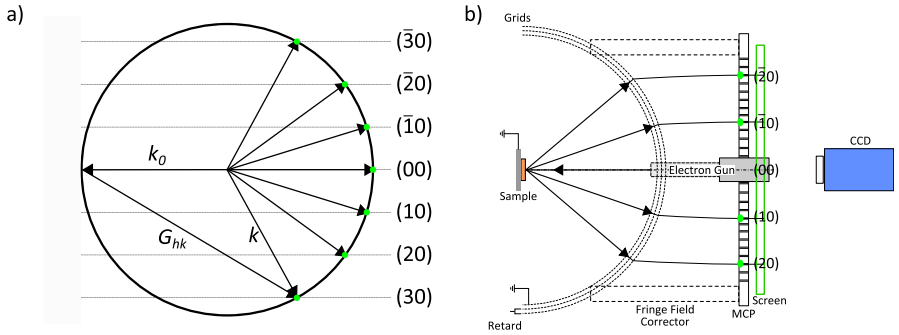

Figure 3.2: a) Ewald sphere construction for a 2D surface lattice b) schematic LEED setup for imaging the diffraction pattern of the surface.

The Ewald's sphere is constructed by drawing the incident wave vector $\mathbf{k}_0$ in the reciprocal lattice of a crystal such that it terminates at a reciprocal lattice point. Then a circle with the radius $k = 2\pi/\lambda$ is drawn at the center of the origin of $\mathbf{k}_0$. Reciprocal lattice points that lie on the surface of the sphere fulfill the Laue condition and correspond to kinetically scattered electrons. For LEED, where information normal to the surface is missing, $\mathbf{a_3}^*$ is virtually zero and the reciprocal lattice points become rods. The intersections of the rods with the Ewald sphere then yield the elastically scattered electrons with wave vector $\mathbf{k}$. The intersections are labeled as (hk) according to the Laue coefficients. The experimental setup consists of an electron gun made from a thoriated tungsten filament with a Wehnelt cylinder emitting a monochromatic collimated beam directed perpendicular to the sample. A hemispherical system of three grids with the sample at the center of curvature of the grids filters inelastically scattered electrons. The first of those grids is grounded to shield the retard potential of the outer grids which is close to the potential of the cathode with a slight offset in order to reject electrons with energies lower than the incident beam energy. In the case of a Microchannel Plate (MCP)-LEED the electrons are then directed at a fluorescent screen through a fringe field corrector in order to be able to project the spherical diffraction pattern onto a plane phosphor screen. Before reaching the screen, however, they get to the MCP, which is a holey wafer with honeycomb structure that serves as amplifier. Here, every hole is a channel electron multiplier creating secondary electrons for impinging electrons. The generated diffraction pattern that represents a cutout of the reciprocal lattice of the sample on the screen is then recorded by a charge-coupled device (CCD) camera. A schematic figure of the setup can be seen in Fig. 3.2b.

In contrast to LEED, generally used after growth, RHEED characterizes samples in real-time during growth, making it one of the most important techniques for MBE. Main differences to the LEED technique are the use of high energy electrons with energies of 5-20 keV and a different geometry with a small angle of incidence/detection of 1-3°. The special reflection geometry of RHEED with grazing incidence enables surface sensitivity even for the high energy electrons that have a mean free path of a few 100 Å in matter, while at the same time inelastic scattering processes are strongly suppressed.[105] The same diffraction laws for LEED also apply to RHEED resulting in constructively interfering electrons for certain angles depending on the crystal structure of the samples surface. Thus, the Ewald's sphere construction can be used in the same way as for LEED. However, due to the high energy of the electrons the corresponding Ewald sphere possesses a large radius with k_0 of about 700 nm^{-1}, which is several ten times larger than a common reciprocal lattice unit. Therefore, the sphere is basically a plane cut through the first layers of the sample. Since only the surface is probed the periodicity perpendicular to the plane of the surface is likewise lost, but due to geometry the reciprocal rods now intersect along the Ewald sphere which results in a streaky pattern.[13] The rods are indexed in the same way as for LEED, with the intersection of the (00) rod corresponding to the specular reflection S. The projected reflections on the fluorescent screen which are formed by the intersection of the rods with the Ewald sphere lie on the so-called Laue circles. Their radius L_n corresponds to the n-th order. A schematic picture for the formation of the RHEED pattern is shown in Fig. 3.3 with a real RHEED pattern of ZnO on the right.

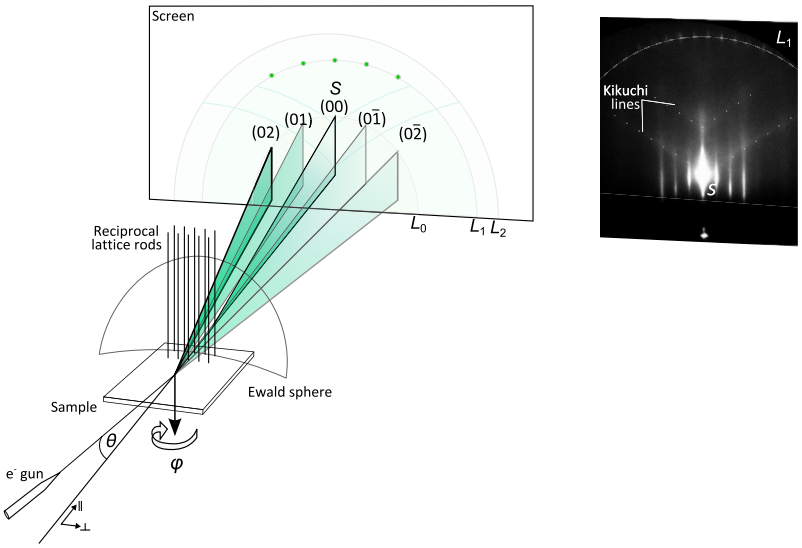

Figure 3.3: Schematic RHEED setup as described in the text with an exemplary ZnO RHEED pattern taken along the $\langle 11\bar{2}0 \rangle$ azimuth on the right.

13 For ideal diffraction the intersection would still result in single points but due to the variations in energy and angular divergence, Ewald sphere and reciprocal rods have a finite thickness and the real diffraction pattern for the zeroth order become streaks.

Due to the geometry, the reciprocal lattice rod separations $g_{\parallel}$ and $g_{\perp}$ parallel and perpendicular to the beam direction can be determined by:

$$ng_{\parallel} = k_0 \left[cos\theta - \frac{1}{\sqrt{(L_n/L)^2 + 1}} \right], \tag{3.3}$$

with the angle of incidence θ and the length L from screen to sample, and

$$ng_{\perp} = \frac{k_0}{\sqrt{(L_n/nl)^2 + 1}} \tag{3.4}$$

where l is the lateral distance between two streaks. MBE systems allow to rotate the samples around the azimuthal angle φ perpendicular to the surface in order to change the angle at which the electrons intersect the crystal lattice, whereby different crystal directions can be probed. To fully understand the RHEED pattern not only kinematic but also dynamic scattering has to be taken into account. Incoherently scattered electrons lose a defined energy in processes that involve phonons and plasmons and eventually get reflected with an isotropic distribution. Those electrons can then be treated in the scope of the kinematic scattering theory, where in this case a 'sphere of reflections' with the radius k_0', centered at the origin of the reciprocal lattice is used to find the vectors $\mathbf{k}'$ that fulfill diffraction conditions.[105,106] Those conditions lead to the formation of characteristic lines in the RHEED pattern, so-called Kikuchi lines. Apart from determining crystallographic properties of the surface, RHEED patterns also contain information of the crystalline quality of the sample's surface. Whereas streaky patterns indicate a smooth surface, the emergence of spotted patterns points to a three-dimensional island growth. Furthermore, angled streaks on the main lines indicate a faceted surface, while an amorphous surface generates rings on the RHEED screen. For surfaces that show a layer-by-layer growth, distinct intensity oscillations of the RHEED pattern during growth can be observed. This periodic intensity variations correspond to surface roughening by individual monolayers as seen in Fig. 3.4.

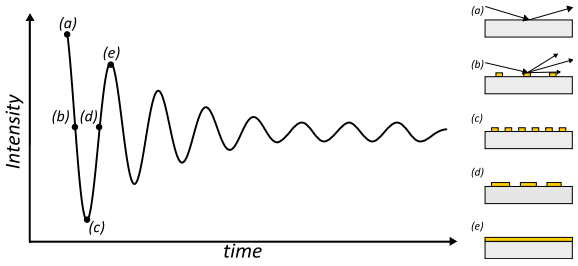

Figure 3.4: Schematic depiction of RHEED oscillations with different stages during monolayer growth on the right (a-e).

Due to the roughening of the surface during growth of a monolayer, incoherent scattering processes increase and the RHEED intensity of the elastically scattered electrons drops. The minimal intensity is reached for the maximal roughness, while it increases with a

widening of the existing islands and obtains a maximum for the closed layer. Since the oscillation period corresponds to the growth of one monolayer, it can be used to determine the growth rate and to precisely control the growth of multi quantum well structures. Generally damping of the oscillations is observed until a steady state is reached. This is interpreted as an increase of the long-range roughness due to a competition between nucleation and diffusion processes. Surface smoothness can be recovered after growth when the sample is kept under equilibrium conditions, *i.e.*, by annealing it.

3.2.2 Scanning Probe Microscopes (SPM)

SPMs are a family of imaging tools that create real space maps of a specimen's surface by scanning a probe over an area in a raster grid consisting of a defined number of points and lines by a controlled and precise movement with piezoelectric actuators in the x and y direction. A specific interaction of the probe with the sample generates the measuring signal in the z direction which is controlled by a feedback system. Due to a strong sensitivity of the signal to changes in the tip-sample distance, the surface can be depicted with a vertical resolution of ≤ 0.1 Å and a lateral resolution of ≤ 1 Å, which makes it possible to resolve molecules or even atomic structures.[107]

3.2.3 Scanning Tunneling Microscope (STM)

The STM technique makes use of the quantum tunneling effect between two conducting materials that are separated by an insulating gap forming a potential barrier. The principle of measuring a distance dependent tunneling current was firstly successfully deployed by Binnig and Rohrer in their groundbreaking research leading to the development of the first scanning probe microscope, the STM, and awarded of the Nobel for their work five years later.[108–110] This technique makes it possible to image investigated surfaces up to an atomic resolution. For probing the sample an ideally mono-atomically sharp conducting tip is used (usually consisting of Pt-Ir, W, or Au). The tips used here (PtIr) are electrochemically etched in a $CaCl_2/H_2O$/acetone solution. At sufficiently close tip-sample distances (in the range of 1-10 Å) and with sufficiently large bias voltage applied, the electrons of the sample have a certain probability of presence in the tip according to the Local Density of States (LDOS) and can be detected by a change in the resulting tunneling current.[111] In the simplified model of a one-dimensional potential barrier $U(z)$, the tunneling current I_t between the tip and the sample can be described by using the one-dimensional Schrödinger equation for n electrons with energy E[112]

$$E\psi_n(z) = -\frac{\hbar^2}{2m_e}\frac{\partial^2}{\partial z^2}\psi_n(z) + U(z)\psi_n(z). \tag{3.5}$$

For $E < U(z)$, a classically forbidden region, Eqn. 3.5 can be solved with the Ansatz $\psi_n(z) = \psi_n(0)e^{-kz}$, giving

$$k = \frac{\sqrt{2m_e(U(z) - E)}}{\hbar}, \tag{3.6}$$

resulting in an exponential decay in the $+z$ direction. For a tip and a sample separated by a vacuum gap the barrier is defined by the work function Φ of the respective materials. By

applying a bias voltage $U = eV$ between tip and sample the Fermi level between the two is shifted so that a net quantum tunneling can occur through the barrier if a sample (or tip) state ψ_n lies between $E_F - eV$. A schematic picture of this situation is given in Fig. 3.5. The probability for an electron to tunnel through a barrier of width d is proportional to the tunneling current, given by

$$I_t \propto \sum_{E_F - eV}^{E_F} |\psi_n(0)|^2 \, e^{-2kd}, \tag{3.7}$$

which is also directly proportional to the number of states on the sample surface in the energy interval eV. A more sophisticated approach to describe tunneling processes and especially the tunneling rate is given by Bardeen's approach that uses time-dependent perturbation theory of two overlapping surface wave functions.[113] Since the tunneling current depends on empty states in the sample, the tunneling signal can be directly related to the LDOS ρ_s in the sample. For a common work function of 4 eV a detectable current can be expected for a sample-tip distance under 10 Å. Furthermore, Eqn. 3.7 shows that by changing the distance to the sample by only 1 Å the tunneling current is already changed by nearly an order of magnitude. This explains the strong sensitivity in the vertical direction.[112]

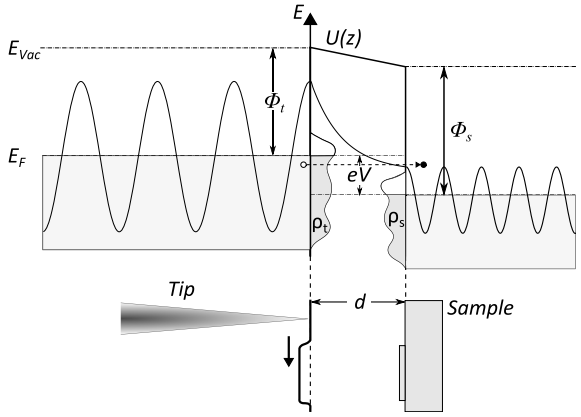

Figure 3.5: Tunneling through a one-dimensional potential barrier between tip and sample with an applied bias voltage of $U = eV$ showing the respective potentials, electron wave function for tip, vacuum gap and sample, as well as the LDOS ρ_t and ρ_s of tip and sample. Furthermore, the movement of the tip over the sample is indicated below.

The STM is basically operated in two main modes. Either the height is kept constant, directly depicting the electronic properties of the surface by measuring the tunneling current and therefore the LDOS. In the other case the tunneling current is kept at a predefined set point by using a feedback loop including piezoelectric transducers, adjusting the height of the tip for every measuring point in the constant current mode. Here the feedback is used to follow the morphology of the surface and generating a topographical image for a constant charge density. However, it has to be considered that in both cases the resulting image is a convolution of the real topography and the LDOS.

3.2.4 Atomic Force Microscope (AFM)

AFM was invented shortly after the STM by Binnig, Quate and Gerber.[114] Similar to the STM the AFM is a measurement technique which enables resolving a structure's morphology in the nanometer scale by using piezoelectric transducers to precisely scan with a probe over a surface. However, in contrast to STM the tips to probe the surface are attached to the end of a cantilever and generally, instead of using the tunneling current as a probing signal, the deflection of the cantilever due to interatomic forces with the samples surface is measured. This allows to investigate also samples that are non-conductive. The scanning is done by a sharp tip with a tip radius of generally about 10 nm at the apex,[115] while the deflection can directly be translated into a topographical image by detecting the reflection of a laser beam from the backside of the cantilever on a 4-quadrant photodetector as shown in Fig. 3.6.

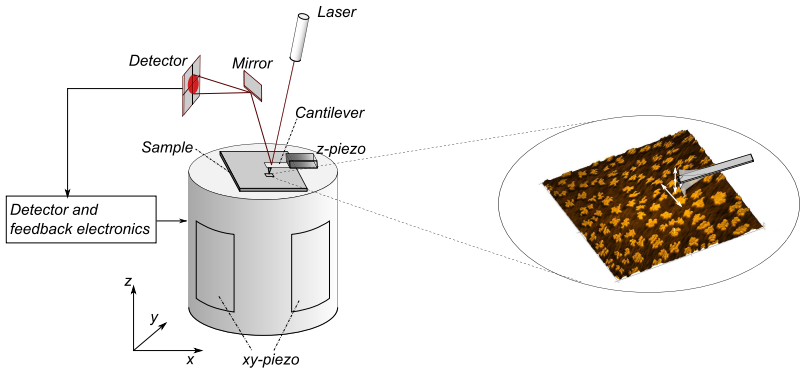

Figure 3.6: Schematic AFM setup, showing the different piezo elements for moving sample and tip. Additionally the detection system is depicted, consisting of a laser, a 4-quadrant photo detector as well as detector and feedback electronics. On the right an exemplary AFM image indicates how the cantilever scans over the surface.

With an AFM it is therefore possible to routinely achieve vertical and lateral resolutions of less than 0.1 nm and 10 nm, respectively. With more sophisticated approaches, like tip functionalization or using qPlus sensors, that are based on a quartz tuning fork, even atomic resolution can be reached.[116] Forces involved in the deflection of the cantilever include long-range van der Waals attraction as well as electrostatic, magnetic and chemical binding forces. Short range forces are governed by the Pauli repulsion and Coulomb interaction. The distant dependent interaction can be approximately described by an empirical Lennard-Jones potential

$$V(r) = 4\varepsilon \left[\left(\frac{\sigma}{r}\right)^{12} - \left(\frac{\sigma}{r}\right)^{6} \right], \tag{3.8}$$

with the depth ε of the potential well and the distance σ where the potential is zero. The basic curve progression is shown in Fig. 3.7a. Different modes for operating an AFM are possible, depending on which regime of the curve the tip measures over the sample. Those are divided into static modes that measure the deflection of the cantilever and dynamic modes that measure changes in the cantilever's oscillation. The most straightforward way is

the static contact mode, where the tip-sample distance is a few Å and the tip measures over the surface in the repulsive regime and is bent according to the topography of the sample (→ Fig.3.7b). This mode itself can be either conducted in constant-height or constant-force mode with a feedback circuit to keep the effective force constant. A disadvantage of the contact mode is that by measuring in the repulsive regime damages of sample or tip can occur, making it unsuited for soft organic matter that is easily affected by the tip.

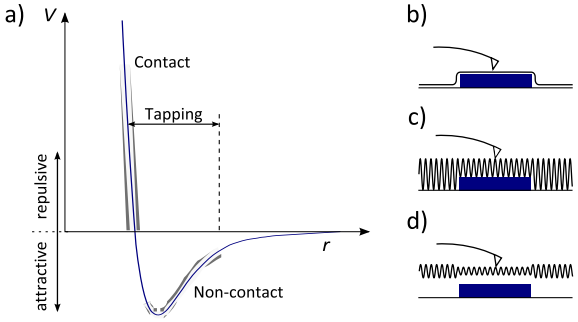

Figure 3.7: a) Force-distance curve between tip and sample in an AFM, described by the Lennard-Jones potential. Additionally the regimes for the different AFM operation modes are marked. Those are b) contact mode c) tapping mode and d) non-contact mode.

To avoid degradation, the cantilever is excited by the z-piezo element with its resonance frequency in dynamic modes, where the tip-sample interaction leads to a change in oscillation. Dynamic modes include tapping and non-contact. The scan in non-contact mode proceeds completely in the attractive regime (Fig.3.7d). Contrary to that in tapping mode the amplitude of the oscillation makes the tip vibrate between the contact and non-contact regime (Fig.3.7c). To maintain the tip-sample interaction in the dynamic modes either amplitude or frequency are used in a feedback loop. Non-contact mode has the advantage that the wear of the tip is greatly reduced, however its application in ambient conditions is limited due to a fluid contamination layer that is almost always present on the surface, so that capillary forces affect the measurement. In UHV conditions where this layer does not exist non-contact scans are the prevailing method. For ambient conditions, however, tapping mode is often used as the tip passes through the contamination layer, whereas contact with the tip is reduced and lateral forces can be neglected due to vertical movement of the tip to the surface.

Kelvin Probe Force Microscopy (KPFM)

Besides mapping the morphology of a sample, different interactions with the surface enable to depict additional properties with an AFM. Kelvin Probe Force Microscopy (KPFM), employed in this work was first developed by Nonnenmacher et al.[117] and is a technique that makes it possible to image the electronic properties of the surface. This is namely the local Contact Potential Difference (CPD) between tip and sample, which exists due to the difference in the respective work functions. Thereby it is possible to create a map of the work function which gives information about the composition and electronic state of the local structures on the surface. A detailed overview of this technique is given in Ref. [118], whereas the fundamentals of it are discussed below. To measure the Kelvin signal the

system of tip and sample is seen as a capacitor, where the electric force is given as:

$$F_{el} = -\frac{1}{2}\frac{\partial C}{\partial z}V^2, \tag{3.9}$$

with the capacitance C and the total voltage V. This voltage is given by the CPD $V_{CPD} = \frac{\Delta\phi}{e}$. To determine the CPD a DC bias is applied to sample or tip which compensates the CPD between them. At the same time an AC-bias is applied that serves as a control parameter, enabling the measurement of the electric force.
Which then becomes:

$$F_{el} = -\frac{1}{2}\frac{\partial C}{\partial z}\left[V_{DC} - V_{CPD} + V_{AC}\sin(\omega t)\right]^2, \tag{3.10}$$

consisting of the DC voltage V_{DC}, the CPD and the AC-voltage $V_{AC}\sin(\omega t)$ with the frequency ω. The electric force can be separated into three components $F_{el} = F_{DC}+F_{\omega}+F_{2\omega}$:

$$F_{DC} = -\frac{\partial C}{\partial z}\left[\frac{1}{2}(V_{DC} - V_{CPD})^2 + \frac{1}{4}V_{AC}^2\right], \tag{3.11a}$$

$$F_{\omega} = -\frac{\partial C}{\partial z}\left(V_{DC} - V_{CPD}\right)V_{AC}\sin(\omega t), \tag{3.11b}$$

$$F_{2\omega} = \frac{1}{4}\frac{\partial C}{\partial z}V_{AC}^2\cos(2\omega t), \tag{3.11c}$$

which can be used for mapping of the topography, the work function and for capacitance microscopy, respectively. From Eqn. 3.11b it becomes apparent that the CPD can be measured by adjusting the DC voltage and minimizing the electric force, with V_{DC} corresponding to the contact potential. The Kelvin measurements can also be conducted in two modes that both have their advantages and disadvantages. Those are namely Amplitude Modulation (AM) and Frequency Modulation (FM) mode, which have to be understood in respect to the applied AC bias and not the resonance frequency of the cantilever as is the case for topography measurements. Since the applied AC bias differs from the resonance frequency in both cases, it is possible to still measure the topography of the sample at the same time. In AM mode the modulation of the electrostatic force with the AC frequency is measured using a lock-in amplifier. During the scan the DC voltage is adjusted so that the signal is minimized. To achieve a high sensitivity to the electrostatic force and make it possible to use low AC voltages of around 100 mV the AC frequency is tuned to the second resonance mode f_1 of the cantilever. This depends on the geometry of the cantilever and is found at ≈ 6.31 times the first resonance mode f_0 for the cantilevers used here. Use of low AC voltages is desirable, so that the electrostatic background in Eqn. 3.11a and band bending at the surface of semiconductors is reduced. In FM mode on the other hand the oscillation of the frequency shift Δf_0 is used as detection signal, which is approximately proportional to the force gradient:

$$\Delta f_0 \propto \frac{\partial F_{\omega}}{\partial z} = \frac{\partial^2 C}{\partial z^2}\left[V_{DC} - V_{CPD}\right]V_{AC}\sin(\omega t), \tag{3.12}$$

To avoid crosstalk to the topography signal, while still remaining within the bandwidth of the frequency demodulator, a typical frequency for the AC voltage is in the rage of 1-3 kHz. Due to the different detection inputs the two modes also differ in their sensitivity for spatial and energy resolution. AM mode uses the long-range electrostatic force as detection, resulting in reduced spatial resolution of typically 25 nm since the tip averages over larger areas of the sample.[119] In contrast the FM mode shows a higher spatial resolution due to the short-range force gradient, making sub-nanometer resolution possible. For AM mode the energy resolution is higher due to the measurement at the second resonance mode. At the same time the band bending for semiconductors is lower as smaller voltages are used.

The AFM measurements in this work were either performed under ambient conditions with a JPK NanoWizard 3 NanoScience AFM in tapping mode or *in situ* with an UHV AFM/STM Omicron operated in non-contact mode using PtIr-coated cantilevers (PPP-EFM, Nanosensors) for Kelvin probe measurements. The work function in the used configuration is given by $\phi_{\mathrm{Tip}} - \phi_{\mathrm{Sample}} = eV_{CPD}$. To obtain the absolute work function the tip was calibrated by scanning the surface of a freshly cleaved HOPG sample with known work function of 4.48 eV.[120] All acquired SPM images in this work were analyzed using the software Gwyddion.[121]

3.2.5 Differential Reflectance Spectroscopy (DRS)

The differential reflectance spectroscopy is the second method besides RHEED in this work, that makes it possible to monitor growth processes *in situ* as well as in real time. By this reorganization of the films in ambient conditions can be excluded. The design and integration of such a setup for the organic MBE chamber as well as the development of suitable evaluation methods were part of this work. DRS is a versatile and sensitive tool to spectroscopically observe the growth of ultra-thin molecular films.[122,123] Those films can be analyzed down to fractions of a monolayer due to the high absorption coefficient of the molecules. This enables the determination of the evolution of the molecule's complex refractive index $\tilde{n}$. Thus, information about the aggregation of the molecules can be studied by optical means. This includes to derive monomer-dimer-oligomer transitions for a layer-by-layer growth, conclusions about the evolution of the crystal structure and the study of interactions between molecules and the substrate, *e.g.*, chemisorption and charge transfer. For DRS the sample is probed with light of photon energy E, which gets reflected. The DRS signal is then given as the normalized change in the sample's reflectance by deposition of a thin surface layer of thickness d. The pristine reflectivity of a half-infinite substrate, $R(E,0)$, is used as reference to detect the change in reflectance $R(E,d)$ with deposited molecules as shown in Fig. 3.8. The DRS signal is accordingly:[124]

$$\mathrm{DRS} \equiv \frac{\Delta R}{R_0}(E,d) = \frac{R(E,d) - R(E,0)}{R(E,0)}, \tag{3.13}$$

The film deposition can hence be observed by the thickness dependent DRS spectra in real-time *in situ*. For the simple three layer system consisting of the ambient medium $\tilde{\varepsilon}_1$, the molecular layer $\tilde{\varepsilon}_2$ and the half-infinite substrate $\tilde{\varepsilon}_3$ the reflection coefficient r_{123} was

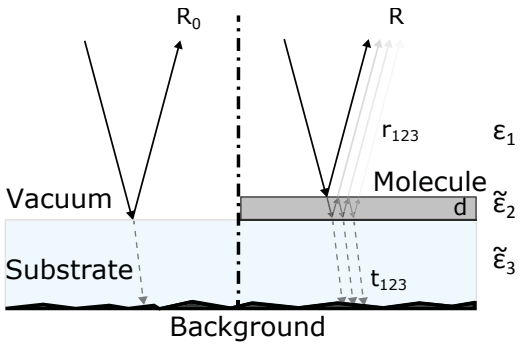

Figure 3.8: Compared reflectance of the bare substrate R_0 with reflectance of the three layer system R. The change in the reflectance due to the organic layer is given by $\frac{\Delta R}{R_0}$.

given in Eqn. 2.79 on the basis of the Fresnel equations as (→ Eqn. 2.79):

$$r_{123} = \frac{r_1 + r_2 e^{-2i\beta}}{1 + r_1 r_2 e^{-2i\beta}}. \tag{3.14}$$

The reflection coefficient accounting for the substrate r_{13} can be equally determined from Eqn. 3.14 for a layer thickness of $d = 0$, *i.e.*, $\beta = 0$:

$$r_{13} = \frac{r_1 + r_2}{1 + r_1 r_2}. \tag{3.15}$$

According to Eqn. 3.13 the DRS signal is hence given by:

$$\mathrm{DRS} = \frac{|r_{123}|^2 - |r_{13}|^2}{|r_{13}|^2}. \tag{3.16}$$

Following the discussion of McIntyre and Aspnes approximations can be made to simplify the expression above.[124] In the regime of thin films, where the thickness of the molecular layer is far below the wavelength of the light ($d \ll \lambda$) the exponential term can be linearized by neglecting terms higher than first order in β. For normal incidence in vacuum ($\varepsilon_1 = 1$) this results in:

$$\mathrm{DRS} = -\frac{8\pi d}{\lambda} \mathrm{Im}\left(\frac{1 - \tilde{\varepsilon}_2}{1 - \tilde{\varepsilon}_3}\right), \tag{3.17}$$

with the complex permittivity $\tilde{\varepsilon}_2$ and $\tilde{\varepsilon}_3$ of molecular layer and substrate. Due to the finite thickness of the substrates of 0.5 mm the system is not strictly consisting of three layers and generally the reflection of the backside has to be considered. Thus, for the performed experiments the backside of the substrates was roughened so that their reflection can be neglected. For more complicated systems the DRS signal, however, is determined by the transfer matrix method for more layers as described in Sec. 2.4.6. To extract the complex dielectric function of the molecules from the spectra, the model functions described in Sec. 2.4.3 are used opposed to a numerical method based on the Kramers-Kronig relation, which requires the absorption index to approach zero at the two interval limits.[87]

The schematic setup for acquisition of the differential reflectance spectra is shown in Fig. 3.9. The light from a xenon arc lamp is coupled into one end of an extreme solarization resistant bifurcated optical fiber ($d = 450$ µm, NA= 0.22). The lamp used for illumination needs to meet certain requirements. Those are coverage of a large spectral range in the UV-Visible, stability of the intensity over a long time period, a 'flat' spectrum without sharp features and adequate luminance. The lamps that fulfill those requirements best are halogen and xenon arc lamps, whereas in this work the xenon lamp (75 W, Müller Elektronik-Optik) was selected due to the stronger intensity in the UV range. A lens system is then used to collimate and focus the light beam through a SiO_2 window on the sample at normal incidence. For alignment purposes the lenses are mounted into a cage system that allows a 4 axis movement of the cage (x, z, ϕ, θ). Additionally a beam splitter (BS) is positioned at an angle of 45° in the beam path, reflecting a fraction of the light ($\approx 4\%$) from the lamp perpendicular to the main beam where it is coupled in another optical fiber into an attached spectrometer (Ocean Optics, USB2000 with detector range of 1.46-6.2 eV and 600 l/mm^{-1} blazed at 300 nm) with a resolution of $\Delta\lambda = 0.63$ nm. By this two-beam spectrometer it is possible to measure the lamp spectrum at all times during the growth used to conduct a drift correction as shown below. The main beam, however, is reflected from the sample and passes through the same optical path where it is coupled into the other arm of the bifurcated fiber connected to the detecting spectrometer (Ocean Optics, HR4000, detector range of 1.13-6.2 eV, $\Delta\lambda = 0.25$ nm) to monitor the DRS signal.

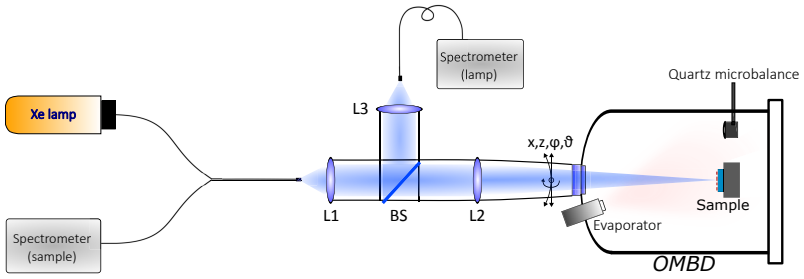

Figure 3.9: Schematic DRS setup with sketched beam path showing the bifurcated optic fiber that combines illumination from the xenon lamp and detection in the spectrometer. A fraction of the light from the lamp is reflected into a second spectrometer by a BS to record the lamp spectrum during measurement for drift correction. The lens system consisting of three lenses L1 (f =75 mm), L2 (f =500 mm) and L3 (f =75 mm) is mounted in a cage system allowing alignment of the beam on the sample in the UHV chamber and on the second spectrometer.

The CCD measures signals that are afflicted by different kinds of noise. Namely photon, dark and read noise. Photon noise stems from a statistical variation of the photon flux, dark noise is temperature dependent and originates from thermally generated electrons in the CCD, while read noise occurs in the process of digitalization. The uncertainty from the different noise contributions thus is:

$$u = \sqrt{PQ_e t_I + Dt_I + N_r^2}, \tag{3.18}$$

with photon flux P, quantum efficiency Q_e, integration time t_I, dark current D and

read noise N_r. As seen in Eq. 3.18 the components for photon and dark noise increase with increasing integration time, so that an integration time as low as possible should be targeted. To further minimize the noise, several spectra are averaged over n consecutive measurements, whereby the uncertainty is reduced by a factor of $1/\sqrt{n}$ for n measurements. Typically integration times of $t_I = 50$ or 100 ms were used with 600 or 300 averaged spectra, resulting in a total measurement time of $t = 30$ s for a single spectrum and an improved signal to noise ratio of 15-30. However, as a consequence a single spectrum represents the evolution of the film in those 30 s. The growth rate is accordingly chosen to be sufficiently low with ≤ 0.1 nm/min, allowing still a considerable sub-ML precision. To be able to measure DR spectra over a long time range, a stable light source is required, since little changes in the incident spectra can result in a great noise in the DR spectra. Also, because the measured reflection is a product of the intensity of the light source $I(\lambda, t)$ and the reflectance of the sample $R(d(t))$, the effect of an intensity change is indistinguishable from the change in the samples' reflection spectra. A drift in the lamp's intensity can be induced by temperature changes, furthermore mechanical instabilities can lead to drift in the spectra. To compensate the occurring lamp drift either an interpolation of the measured linear drift before and after deposition can be performed.[94] Or the lamp spectra is recorded for every DR spectrum of the sample and the measured DR spectrum is corrected by the change in the lamp spectrum. Both methods were used in this work, the drift correction by the latter is shown exemplarily in Fig. 3.10. All spectra shown here are smoothened by the Whittaker-Henderson noise filter.[125]

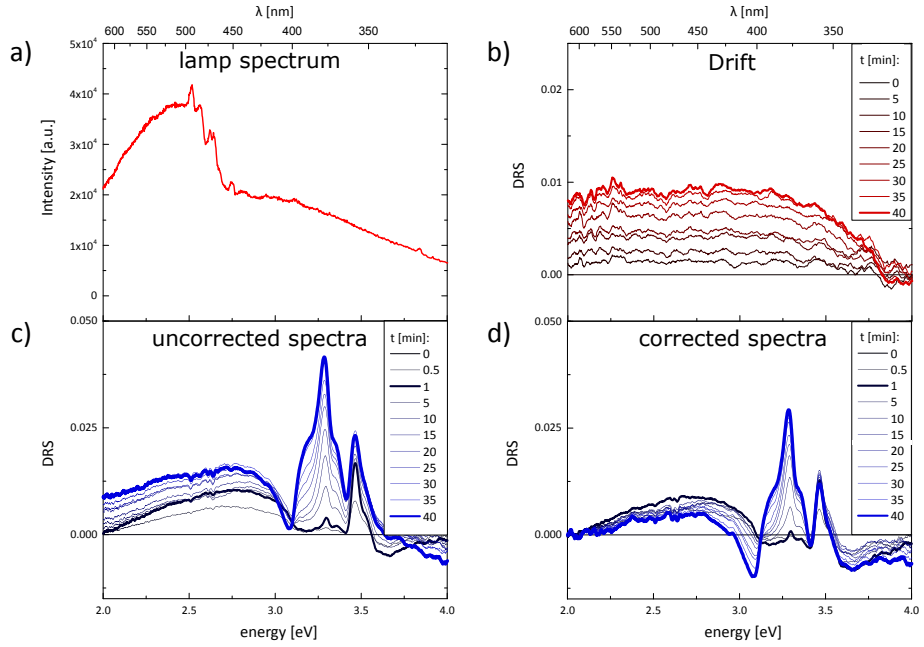

Figure 3.10: a) Measured xenon lamp spectrum using the USB 2000 spectrometer. b) Drift of the spectrum during a deposition c) uncorrected spectra d) same spectra corrected by the corresponding change in the lamp spectra.

The initial measured lamp spectrum is shown in Fig. 3.10a, while the drift during the deposition of the molecules, in this case F6-TCNNQ, is shown in Fig. 3.10b. Uncorrected and corrected DR spectra are compared in Fig. 3.10c and d. Finally, to determine the complex refractive index of the thin molecular layer the measured DR spectra have to be evaluated by a suitable model. The requisite for this was given in Sec. 2.4.3 by the description of the response of matter to an electromagnetic field with the optical oscillator model. By a fit procedure using n oscillators it is possible to reproduce the DRS spectra and extract real and imaginary part of the complex dielectric function.

3.3 *ex situ* Characterization

3.3.1 UV-Vis Spectroscopy

For comparison of the DR spectra with single molecule spectra, transmission measurements of molecules in solution were carried out. In the solvent, aggregation is suppressed and features of the single molecule can be identified, however, inhomogeneous broadening and shift of the spectrum are still present. A characteristic quantity is the transmittance that is defined as the ratio of transmitted and incident intensity $T = I/I_0$. After Beer–Lambert's law the transmittance is influenced by basically three quantities in an isotropic medium: The concentration c of the material interacting with light by absorption, the optical path length l and the probability that the light will be absorbed given by the (decadic) extinction coefficient ε.[14] Their product of the three is called absorbance A.

$$-lg(T) = lc\varepsilon = A, \tag{3.19}$$

Transmission spectra in this work were acquired with a Shimadzu UV-2101PC spectrophotometer in the range of 1.4-6.5 eV using a combination of deuterium and halogen lamps with a possible resolution of 0.1 nm.

3.3.2 Transmission Electron Microscopy (TEM)

TEM is the third presented technique that probes a sample by using electrons. In contrast to LEED and RHEED, the electrons pass through the sample in TEM. This can only be achieved by using very thin specimens (around 100 nm) and a sufficiently high electron energy of the beam in the range of 100 keV. It is possible to operate the TEM in diffraction, as well as real space imaging mode. Hereby diffraction patterns are used to analyze the crystal structure, while real space images with resolutions of up to 0.5 Å make it possible to resolve single atoms.[126] Developed in 1931 by Max Knoll and Ernst Ruska, it is therefore one of the most powerful techniques today for characterizing materials down to the atomic level.[15] A schematic setup of a TEM is given in Fig. 3.11. Due to the high energy of ca. 100 keV, the electrons in the beam reach half of the speed of light, making a relativistic

14 The so-called Napierian extinction coefficient is calculated in base e. Napierian and decadic extinction coefficients are connected by $\varepsilon^* \cong 2.303\varepsilon$

15 Ruska was awarded with the Nobel prize in the same year as Binnig and Rohrer "for his fundamental work in electron optics, and for the design of the first electron microscope"

correction of Eqn. 3.1 for the wavelength necessary:

$$\lambda = \frac{h}{\sqrt{2m_e eU(1+\frac{eU}{2m_e c^2})}}, \tag{3.20}$$

where U is the acceleration voltage of the electron gun. The electron beam is created here in a vacuum column by a field emission gun (FEG) which uses a strong electric field to induce electron emission. The beam is manipulated by using electromagnetic lenses which can be varied in strength to focus and shift the beam and make a change of the magnification possible. First, according to the mode of operation (diffraction or real space imaging), the beam is focused or collimated by the condenser lens system onto the specimen. A condenser aperture acts as adjustment for the beam's spread and to minimize lens aberrations. After the beam passes the specimen, the objective lens system focuses the beam (Schematic beam paths are shown for both modes in Fig. 3.11b and c). Hereafter it passes 1) the back focal plane, where a diffraction pattern of the sample is generated and 2) the first intermediate image plane. At both points an aperture is placed in the plane. (1) The objective aperture in the back focal plane, that controls the collection angle with its size and filters certain angles by using suitable apertures. Hence, either the direct, unscattered beam can be selected, resulting in an image that shows regions where the electron beam interacts with the sample as dark spots. This is called the bright field imaging mode, since the dark specimen appears on a bright background. By selecting diffracted beams, however, regions that interacted with the sample appear brighter, while the background is dark. This is accordingly the so-called dark field imaging mode. (2) Subsequently the selected area aperture which lies in the intermediate image plane and restricts the area of the sample contributing to the diffraction pattern. The following lens system now allows to toggle between diffraction pattern and real space imaging by changing the strength of the intermediate lenses (see Fig. 3.11b and c). Finally the projector lenses magnify the image onto a fluorescent screen allowing a total magnification of up to 10^7. An in-column energy filter (filter lens) between the intermediate and the projector lenses additionally makes it possible to identify chemical elements by their characteristic loss of energy and obtain elemental maps by filtering certain energies.
In order to yield more detailed information about the specimens' crystallites the Scanning Nanobeam Diffraction (SNBD) as further analyzing method is used for TEM investigations. This technique allows mapping of local crystalline orientations, extracted from electron diffraction spot patterns. The SNBD technique is described briefly as follows: The nano-sized, but parallel electron beam is scanned across the cross-section of the sample and diffraction patterns are recorded for every position.[127,128] Crystallographic orientation maps are derived by using a pattern matching procedure comparing the electron diffraction pattern recorded for the individual positions with the set of diffraction patterns calculated for the full range of crystallographic orientations of ZnO. The scans are recorded with a probe size of 1 nm and step width of 3 nm. Analysis and the output of crystallite orientation maps are realized by the Automated Crystallographic Orientation Mapping (ACOM) software package implemented in the ASTAR system.[128]

The greatest challenge at achieving high resolution in TEM is that the image of the true object is modified by the imperfections of the optical system. Because of this, atoms of the same kind can appear in a different contrast in the final image. To be able to especially resolve atomic structures of the sample, High Resolution Transmission Electron Microscopy (HRTEM) is applied. Here, the unscattered beam is interfered with the diffracted beam by using a large aperture, resulting in an image that has to be further processed to achieve high resolution images. Necessary for this is to know how sample and microscope affect the electron wave in the process of image formation. As the incoming electron wave passes the specimen, the interaction with it creates an exit wave with a modified phase. This interaction is represented by the specimen's transmission function $f(x,y)$:

$$f(x,y) = A(x,y)\exp(-\mathrm{i}\phi_t(x,y)), \tag{3.21}$$

with the Amplitude $A(x,y)$, and the thickness dependent phase $\phi_t(x,y)$. The phase change through the specimen solely depends on the projected potential of the specimen $V_t(x,y)$ and an interaction constant σ according to $\phi_t(x,y) = \sigma V_t(x,y)$. To now obtain the phase contrast, an approximation for a thin specimen is applied, where the specimen does not change the amplitude of the incident wave, while the phase is only slightly changed. In this approximation a Taylor series expansion of the exponential function in Eqn. 3.21, which neglects higher-order terms, results in

$$f(x,y) \cong 1 - \mathrm{i}\sigma V_t(x,y), \tag{3.22}$$

which is denoted as the Weak Phase-Object Approximation (WPOA). The exit wave passing the optical system is further modified by lenses and apertures, whereby lens aberrations change the phase and apertures cut high spatial frequencies.

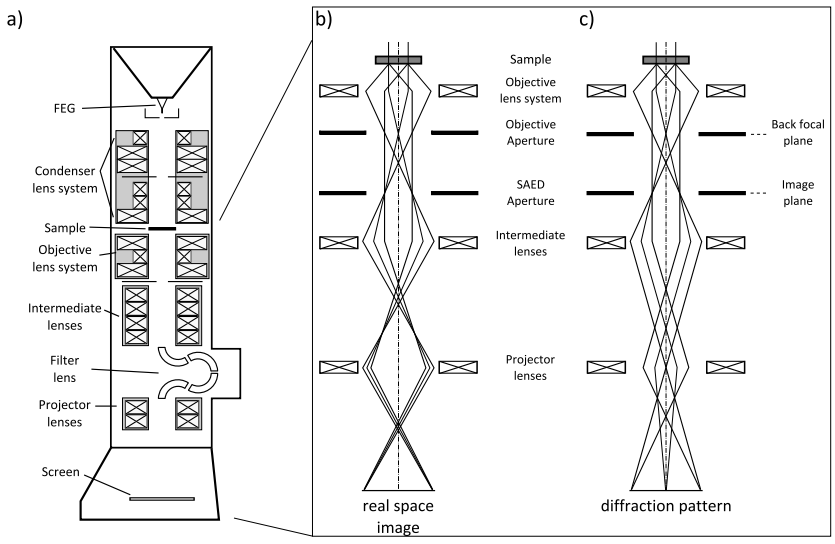

Figure 3.11: a) Schematic setup of a TEM equipped with a FEG showing the different lens systems and the beam path for generating a real space image b) and a diffraction pattern c).

Therefore, the emerging image is represented by a convolution of the specimen function with a point-spread function $h(x,y)$. This describes how every point in the sample contributes to the final image $g(x,y)$:

$$g(x,y) = f(x,y) \otimes h(x,y), \tag{3.23}$$

and thereby defines the effect of the optical system. The convolution of those functions in real space can be represented as a multiplication in the reciprocal space

$$G(\mathbf{k}) = F(\mathbf{k})H(\mathbf{k}), \tag{3.24}$$

with the reciprocal lattice vector $\mathbf{k}$, representing the spatial frequency for a particular direction and the respective Fourier transforms $G(\mathbf{k})$, $F(\mathbf{k})$, $H(\mathbf{k})$ of the functions $g(x,y)$, $f(x,y)$, $h(x,y)$. $H(\mathbf{k})$ is also denoted as Contrast Transfer Function (CTF) and is composed of three contributions itself:[129]

$$H(\mathbf{k}) = A(\mathbf{k})E(\mathbf{k})B(\mathbf{k}). \tag{3.25}$$

Those are the aperture function $A(\mathbf{k})$, a step function, which cuts all spatial frequencies above a value dependent on the radius of the aperture. Secondly the instrument dependent envelope function $E(\mathbf{k})$, which accounts for the product of temporal and spatial coherency envelope functions E_t and E_s. They are mainly caused by chromatic aberration of the lens, movements of the sample, energy spread and energy instabilities (temporal) and beam divergence (spatial). A detailed discussion of the temporal and spatial coherency envelope is given in Ref. [130]. The final contribution is from the aberration function $B(\mathbf{k})$. Following the discussion of Williams and Carter only the imaginary part from a phase-object contributes to the final image intensity of the spherical aberration function $B(\mathbf{k})$ in the WPOA, yielding:[129]

$$B(\mathbf{k}) = \sin(\chi) = sin(\pi \Delta f \lambda k^2 + \frac{\pi}{2} C_s \lambda^3 k^4). \tag{3.26}$$

Hence, the aberration function depends on the defocus value Δf which can be adjusted by the microscope and the spherical aberration C_s, as well as electron wavelength λ and the spatial frequency $\mathbf{k}$. The CTF now tells how the real object is distorted by the optical system. Thus, it allows to estimate the modification to the image and calculate an undistorted image. If the contrast transfer function $H(\mathbf{k})$ is negative a positive phase contrast results in the final image, where atoms appear darker than the background, while for positive $H(\mathbf{k})$, they appear brighter than the background. This also means that when $H(\mathbf{k})$ crosses the $\mathbf{k}$-axis no contrast is transferred, and information is lost. Thus, a $\mathbf{k}$ value results in a higher spatial resolution, equivalent to the point resolution. To achieve an optimum defocus with a broad band at low frequencies and a nearly constant phase close to -1, Scherzer found a relation between the spherical aberration and the wavelength that balances the k^4 and parabolic k^2 term in χ:[131]

$$\Delta f_{Sch} = -1.2(\lambda C_s)^{1/2}. \tag{3.27}$$

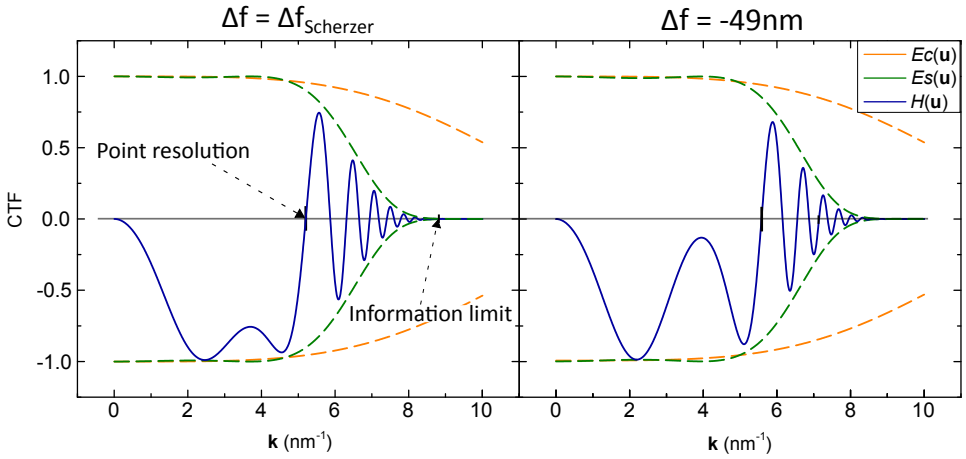

Figure 3.12: CTF ($H(\mathbf{k})$) and envelope functions (E_c and E_s) for the Scherzer defocus $\Delta f = -42.5$ nm and a greater defocus of $\Delta f = -49$ nm ($E_0 = 200$ kV, $C_s = 0.5$ mm).

The effect on the CTF by using different defocus values is shown in Fig. 3.12. For fixed energy and spherical aberration $H(\mathbf{k})$ is shown at the Scherzer defocus of -42.5 nm (left) and a greater arbitrary defocus of -49 nm (right). The point resolution, where the first zero-crossing happens is actually larger for the Scherzer defocus (0.19 nm compared to 0.18 nm at -70 nm) but the CTF has strong amplitude variations for lower spatial frequencies, resulting in not directly interpretable images. However, by knowing the CTF, images can theoretically be simulated up to the information limit, where due to the envelope the function becomes zero. Even so the Scherzer focus is optimal for the characterization of atomic structures with strong phase contrast, the here considered HIOS, which consist both of strong phase crystalline atomic objects and molecular weak phase objects, a new strategy has to be applied as will be shown in Sec. 4.4.

TEM analysis in this work is performed on a TEM/STEM JEOL 2200FS with in-column energy filter operated at an acceleration voltage of 200 kV and equipped with a field emission gun. SNBD is performed using the ASTAR system of NanoMegas attached to the TEM instrument. Successful sample preparation in HIOS materials is achieved by ultramicrotomy.[132] This is done with a Leica EM UltraCut7 room temperature ultramicrotome which allows cutting lamellae of a thickness down to 50 nm. The hybrid structures which are destroyed by conventional preparation techniques can thereby be preserved. For preparation, sample pieces are glued face-to-face and the the cutting direction is chosen normal to the HIOS interface as described in detail in [132].

"See first, think later, then test. But always see first.
Otherwise you will only see what you were expecting."
— Douglas Adams

CHAPTER 4

Results and Discussion

4.1 Investigated organic materials

The vast number of available molecules with various different properties makes it possible to tailor hybrid structures for their respective applications. This is exploited in this work to control the growth of the respective molecules down to sub-monolayer coverages. For instance, the controlled assembly of the molecular structures is improved by exploiting electrostatic molecular-substrate coupling. At the same time, organic material is selected that features efficient electronic and photonic coupling with the ZnO substrate. Here, exemplarily the molecular-substrate interaction of rod-like molecules is studied for the prototypical *para*-oligophenylenes. Due to the extended π-electron system along their Long Molecular Axis (LMA) they are excellently suited for different optoelectronic applications such as OLEDs or OTFTs.[15] Moreover, the rod-like shape leads to a strongly anisotropic optical transition dipole moment and mobility, which defines the optoelectronic properties. Therefore, oligophenylenes offer the possibility to tune properties by manipulating the orientation of the molecules on the surface. At the same time the anisotropic shape significantly affects the growth mode when compared to inorganic semiconductors consisting of zero-dimensional atoms. In particular, structure and growth of inorganic/organic heterostructures will be investigated using the example of the well-studied molecule *para*-sexiphenyl (6P; $C_{36}H_{26}$) and its fluorinated derivatives.[133] First, we study the 6P/ZnO interface in dependence on growth temperature. Then, novel heterostructures of 6P embedded in two ZnO interfaces are created and investigated.[134,135] Another approach is to directly analyze the optical and electronic coupling with the underlying substrate *in situ* during growth using the purpose-built DRS setup. The quality of this method is shown first for perylene based PTCDI on a transparent substrate, by elucidating morphological properties from the spectra.[136] Furthermore, a customized *para*-quaterphenyl, the Ladder-type Quaterphenyl (L4P) which fits the ZnO absorption and exhibits sharp resonances is used to prove that the beneficial properties are still intact at the interface. Finally, dopants are used to investigate charge transfer processes at the HIOS interface. In particular those are the naphtalene based NTCDA and strong molecular acceptor F6TCNNQ. In the following specific features of the respective materials are given.

Table 4.1: Unit cell parameters of 6P polymorphs. Taken from Ref. [13]

Polymorph	a (Å)	b (Å)	c (Å)	β (°)
α-phase	26.282	10.999	15.995	99.79
β-phase	8.091	5.568	26.241	98.17
γ-phase	7.98	5.54	27.64	99.8

4.1.1 *Para*-oligophenylenes

para-Sexiphenyl (6P) (also denoted as hexaphenyl) is a well-studied rod-like model system on a vast number of substrates.[13,15,20,137–140] It is investigated for its potential use in OTFTs, OLEDs, waveguides and random lasers.[141–144] Its high-energy gap of 3.1 eV enables blue light emission and its strong electro-, photoluminescence and thermal stability make it suitable for optoelectronic applications.[145–147] The crystal structure of 6P is shown in Fig. 4.1. It consists of six phenyl units linked in the para position, which generally allows twisting around the longitudinal axis. However, in the solid state the rings are largely arranged in a molecular plane and in the crystal the molecules are packed in a herringbone fashion held together by van der Waals forces.[148] This configuration balances the quadrupole moment of the molecules most effectively.[15] The crystal grows in a monoclinic fashion with two inequivalent molecules in the unit cell, where three polymorphs are reported, namely α-, β- and γ-phase.[13] While the β-phase is known as the equilibrium bulk crystal structure at room temperature, α- and γ- describe the low and high temperature phases, respectively.[148–150] The corresponding lattice parameters are shown in table 4.1. Additionally, the unit cell with two molecules in the common β-phase is displayed in Fig. 4.1a. The layer and herringbone structure are shown in Fig. 4.1b, c respectively. For the aforementioned applications it is important to gain a precise control over the molecular orientation and growth mode, since exciton and charge transfer crucially depend on the contact plane of the crystal. While OLEDs require a π-system parallel to the electrodes, hence flat-lying molecules, OTFTs need upright standing molecules for optimal performance.[15] Both, theory and experiment, show that sexiphenyl is ideally suited for this task, since the growth mode can be controlled by the choice of the underlying ZnO surface termination. The choice of ZnO surface, together with the molecules' anisotropic shape, allows to manipulate the energy-level alignment between inorganic/organic semiconductor by influencing the orientation of the organic crystallites.[15,70,151] As the surface energy is minimal for the 6P(001) face, this is the prevailing contact plane for systems where

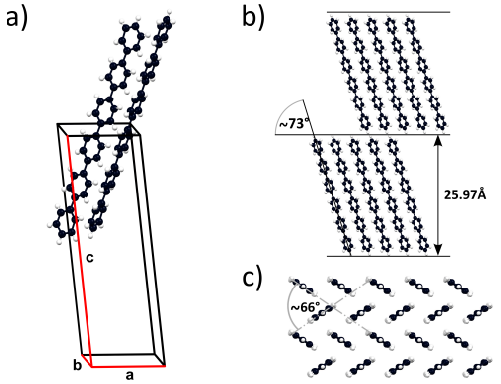

Fig. 4.1: a) Crystal structure of *para*-sexiphenyl within the β-phase. b) Schematic layers of 6P with a ML thickness of 25.97 Å. c) Herringbone alignment of 6P projected along the long molecular axis.

intermolecular interaction dominate,[152] resulting in island like structures of nearly upright standing molecules with a ML thickness of 25.97 Å (Fig. 4.1b). On the other hand, for dominating molecule-substrate interaction, an alignment of flat-lying molecules in a needle like arrangement can be achieved. Here, the long axis of the molecule forms the contact plane, corresponding approximately to the 6P($20\bar{3}$) crystal plane.[13] For ZnO the flat-lying molecules align themselves parallel to zinc and oxygen rows.[70,151] Beside the usual growth control parameters, like using different substrate surfaces or varying the substrate/cell temperature a new additional way is presented here, which involves fluorination of the molecule as will be shown in Sec. 4.3.1. The investigated chemically modified 6P molecules were created in the group of Prof. S. Hecht of the chemistry department of the Humboldt-Universität zu Berlin. Here a symmetrical, terminally fluorinated derivative 6P-F_4 and the asymmetrical derivative 6P-F_2 were synthesized, shown in Fig. 4.2. *In situ* experiments show that film structure and morphology of these derivatives are substantially altered due to the modified intermolecular electrostatic interactions.

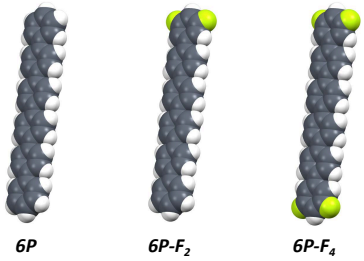

Figure 4.2: Spacefill models of *para*-sexiphenyl ($C_{36}H_{26}$) and the fluorinated derivatives 6P-F_2 ($C_{36}H_{24}F_2$) and 6P-F_4 ($C_{36}H_{22}F_4$).

Another property of 6P that will be exploited in this work is the molecules' high thermal stability that makes it possible to manufacture ZnO hybrid stacks containing 6P molecules embedded in ZnO.[153] To achieve this structure, ZnO is grown on top of 6P crystallites, while leaving the organic crystal unimpaired by the growth process, as will be proven with Transmission Electron Microscope (TEM) measurements in Sec. 4.4.

Furthermore, the optical properties of *para*-oligophenylenes will be exploited in Differential Reflectance Spectroscopy (DRS) experiments in Sec. 4.5.2, where the growth of molecules will be monitored *in situ* to model the dielectric properties of the molecules. Generally, 6P exhibits an energy gap of 3.1 eV, which matches the energy gap of ZnO and promotes electronic coupling and hybridization.[154] Nonetheless as can be seen in Fig. 4.3a the absorption spectrum of 6P is rather broad, owing to its internal degree of freedom along the longitudinal axis. This makes it unsuited for coupling or energy transfer to other structures, as well aggravating the interpretation of potential optical measurements.[155–157] The molecules' flexibility can be limited by introducing a backbone structure that results in bridged *para*-oligophenylenes. These so-called ladder-type *para*-oligophenylenes exhibit a red shift in their optical spectra compared to their parent species, which increases with the degree of bridging. The red-shift arises through the forced coplanarity, which suppresses rotational and torsional degrees of freedom and therefore strengthens the effective

Table 4.2: Unit cell parameters for PTCDI and NTCDA. Taken from Refs. [160, 161]

	a (Å)	b (Å)	c (Å)	β (°)	Space group
PTCDI	4.865	14.660	10.844	91.33	$P2_1/n$
NTCDA	7.880	5.322	12.601	107.257	$P2_1/c$

π-conjugation, while at the same time increasing the extinction coefficient significantly.[155] While the ladder-type 6P (L6P) has sharp resonances with recognizable vibronic progression, its transitions do not fit those of ZnO very well. The shorter and therefore more blue shifted L4P, however, shows exciton transition almost in resonance with those of ZnO, as can be seen in Fig. 4.3b. This with a radiative yield close to unity makes L4P an appealing choice for hybrid light emitters or strong coupling applications in lasers.[155–157]

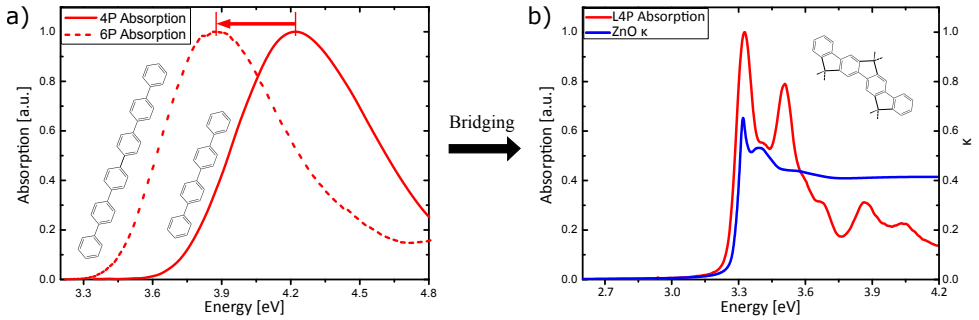

Figure 4.3: a) Absorption spectra comparing the red shift going from 4P to 6P b) absorption of the bridged L4P molecule in comparison with the absorption coefficient of ZnO.

4.1.2 Perylenes and Naphtalenes

The class of the best-investigated organic molecular model systems include besides the phenylenes, planar polyzyclic aromatic compounds based on naphthalene ($C_{10}H_8$) and perylene ($C_{20}H_{12}$) cores. Perylenes are widely applied as organic pigments and dyes with intensive color. They form highly ordered films on a variety of substrates and are used as n-type semiconductors in organic devices, such as transistors, OLEDs or organic solar cells and were even employed as first inorganic–organic semiconductor diode altogether in the form of PTCDA.[30,145,158] In this work the perylene based 3,4,9,10-Perylenetetracarboxylic diimide (PTCDI) will be investigated. It consists of a planar perylene core unit with two terminal imide moieties which distinguish it from PTCDA. Along its long axis HOMO and LUMO have a node plane, so that the transition dipole moment along the axis is especially high.[159] The molecular structure of PTCDI is shown in Fig. 4.4a. The system of the bulk crystal is monoclinic with the unit cell containing two molecules forming a herringbone structure.[160] Eventually Fig. 4.4c shows the absorption spectrum of PTCDI solved in toluene. Due to the rigidity of the molecule the transitions are sharp and S_{00} transition as well as vibronic progression (≈170 meV) are well recognizable. Due to the distinct spectral features PTCDI is used as model system for DRS measurements on a weakly interacting, transparent substrate (→ Sec. 4.5.1).

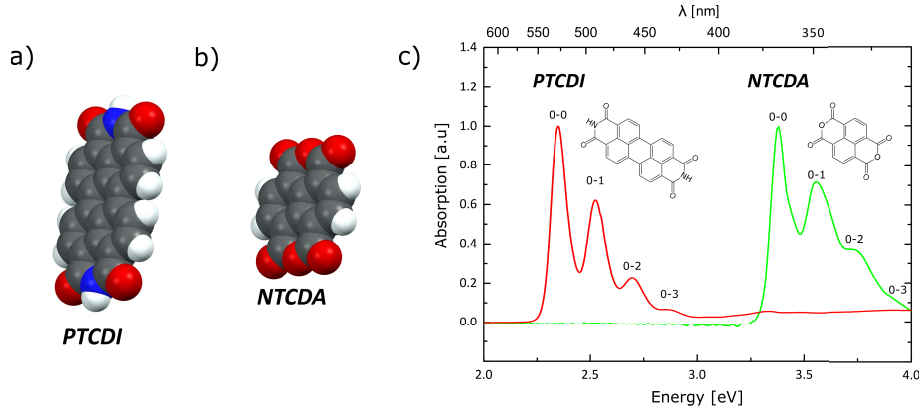

Figure 4.4: a) Spacefill model of PTCDI and b) NTCDA with c) Absorption spectrum of PTCDI in toluene (red) and NTCDA in methanol (green).

Additionally a similar but smaller molecule, the 1,4,5,8-Naphthalenetetracarboxylic dianhydride (NTCDA) is used to investigate charge redistribution at the interface with ZnO. It consists of a planar naphthalene aromatic core with two terminal carboxylic anhydride groups. Its molecular structure is shown in Fig. 4.4b. NTCDA is an efficient blue-emitter with a high electron affinity and a high charge carrier mobility. Hence, it is used as n-type organic semiconductor as well as electron transport material.[162,163] Additionally it has attracted attention for exhibiting strong exciton-photon coupling in organic but also hybrid organic-inorganic microcavities in connection with ZnO using the short-ranged Förster-type energy transfer.[164,165] This was utilized in the development of organic lasers.[166] For metal surfaces a charge transfer between the surface and the molecule was found.[167] In this work, especially the effect of charge transfer with ZnO during growth will be investigated employing the DRS technique.

4.1.3 F_6TCNNQ

For the same purpose 1,3,4,5,7,8-hexafluorotetracyano-naphthoquinodimethane (F_6TCNNQ) is used in Sec. 4.5.3. The molecule was shown to be a strong electron acceptor with charge accumulating at the cyano groups.[168,169] This qualifies it as potential p-dopant in OLEDs or organic field-effect transistors.[170,171] It has a sublimation temperature of 220-260 °C and hence a lower volatility compared to the smaller F_4TCNQ, which exhibits a slightly higher doping strength but easily contaminates the evaporation chamber.[168] As shown by UPS/XPS measurements F_6TCNNQ can be used to tune the work function of an underlying inorganic semiconductor like ZnO, GaN or graphene due to a change in the surface dipole and band bending induced by charge transfer.[172,173] In this work F_6TCNNQ will be used to confirm this interaction with the substrate by optical spectroscopy.

All chemical structures and formulas of the molecules used in this work are shown in Table 4.3

Table 4.3: List of organic molecules used in this work.

Acronym	Full Name	Sum Formula	Molecular Weight [g/mol]	Skeletal Formula
p-6P	*para*-sexiphenyl	$C_{36}H_{26}$	458.6	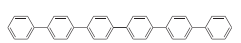
p-6P-F_2	3,5-difluoro-*para*-sexiphenyl	$C_{36}H_{24}F_2$	494.6	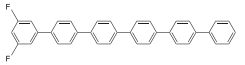
p-6P-F_4	3,3',5,5'-tetrafluoro-*para*-sexiphenyl	$C_{36}H_{22}F_4$	530.7	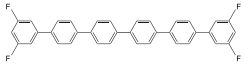
L4P	Ladder-type quaterphenyl	$C_{33}H_{30}$	426.6	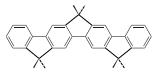
PTCDI	3,4,9,10-perylenetetracarboxylic diimide	$C_{24}H_{10}N_2O_4$	422.4	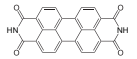
NTCDA	1,4,5,8-naphthalenetetracarboxylic dianhydride	$C_{14}H_4O_6$	268.2	
F6-TCNNQ	2,2′-(perfluoronaphthalene-2,6-diylidene)dimalononitrile	$C_{16}H_6N_4$	254.3	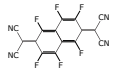

4.2 Inorganic growth: ZnO

The internal interface between the organic molecule and an inorganic substrate is critical to achieve a controlled growth of the molecules. Here, surface reconstructions, defects, and morphology are all affecting the molecules assembly. Therefore, a crucial prerequisite is a well-defined surface of the inorganic material. In this work this is accomplished by preparing and epitaxially overgrowing single crystalline ZnO substrates as described in Sec. 3.1. To ensure the required quality of the ZnO surfaces they are investigated by *in situ* techniques before the organic growth takes place. Those include RHEED (during growth), LEED and AFM. The results of typical epitaxial overgrowth is presented in the following.

4.2.1 ZnO faces

Different ZnO faces are investigated in this work to take advantage of their respective specific properties (cf. Sec. 2.2.4). In particular the polar (c-plane) surface ZnO(000$\bar{1}$) and ZnO(0001) and non-polar (m-plane) ZnO(10$\bar{1}$0) surfaces will be employed. Fig. 4.5 shows RHEED and LEED patterns of those surfaces. The RHEED patterns compare the differences of as received substrates and epitaxially overgrown samples. The patterns after growth also display different azimuths. All *as received* patterns show streaky 1x1 patterns from a single crystal (see Fig. 4.5a). However, they are rather broad, suggesting undefined and disordered surfaces. The 1x1 reconstruction is mainly found for the ZnO faces. It is associated with a hydroxyl-termination of the surface in literature, while clean oxygen-terminated ZnO surfaces show a 1x3 reconstruction, which is not stable due to its high reactivity.[61] Apart from this, also a $\sqrt{3}x\sqrt{3}$R30° reconstruction is reported, attributed to a different preparation and rest-gas composition.[174] By homoepitaxially overgrowing the substrates with ZnO and a subsequently annealing step the 1x1 reconstruction is retained, however, sharp and streaky RHEED patterns develop, which indicate very smooth surfaces (see Fig. 4.5b). This is especially the case for the O-polar ZnO(000$\bar{1}$) surface. The reflexes of the $\langle 11\bar{2}0 \rangle$ azimuth for this surface even feature Kikuchi lines and are therefore of high structural quality. For standard layer-by-layer growth also lasting and distinct intensity oscillations of the RHEED patterns are observed as exemplarily shown in the inset of Fig. 4.5b. On the other hand the Zn-polar growth is harder to control and hence the patterns are generally broader. The same is observed by comparing the LEED patterns of the polar ZnO faces in Fig. 4.5c. At 80 eV the diffraction spots for both surfaces constitute an equilateral hexagon, indicating a 1x1 structure. However, striking is the difference in shape of the single diffraction spots. The O-polar surface shows very sharp and small spots, while the pattern of Zn-polar surface is again rather broad. Another peculiarity can be seen for the non-polar ZnO(10$\bar{1}$0) surface. Here, the $\langle 1\bar{2}10 \rangle$ azimuth shows a very sharp 1x1 pattern, while the perpendicular $\langle 0001 \rangle$ azimuth exhibits a pattern with distinct split streaks respectively spots in the case of the LEED pattern which emerge during the epitaxial overgrowth. The reason for this particular splitting is the surface structure of the ZnO(10$\bar{1}$0) surface. Due to the presence of regular arranged step arrays along the [1$\bar{2}$10] direction, the diffraction pattern splits up in this direction too according to the respective terrace width.[175]

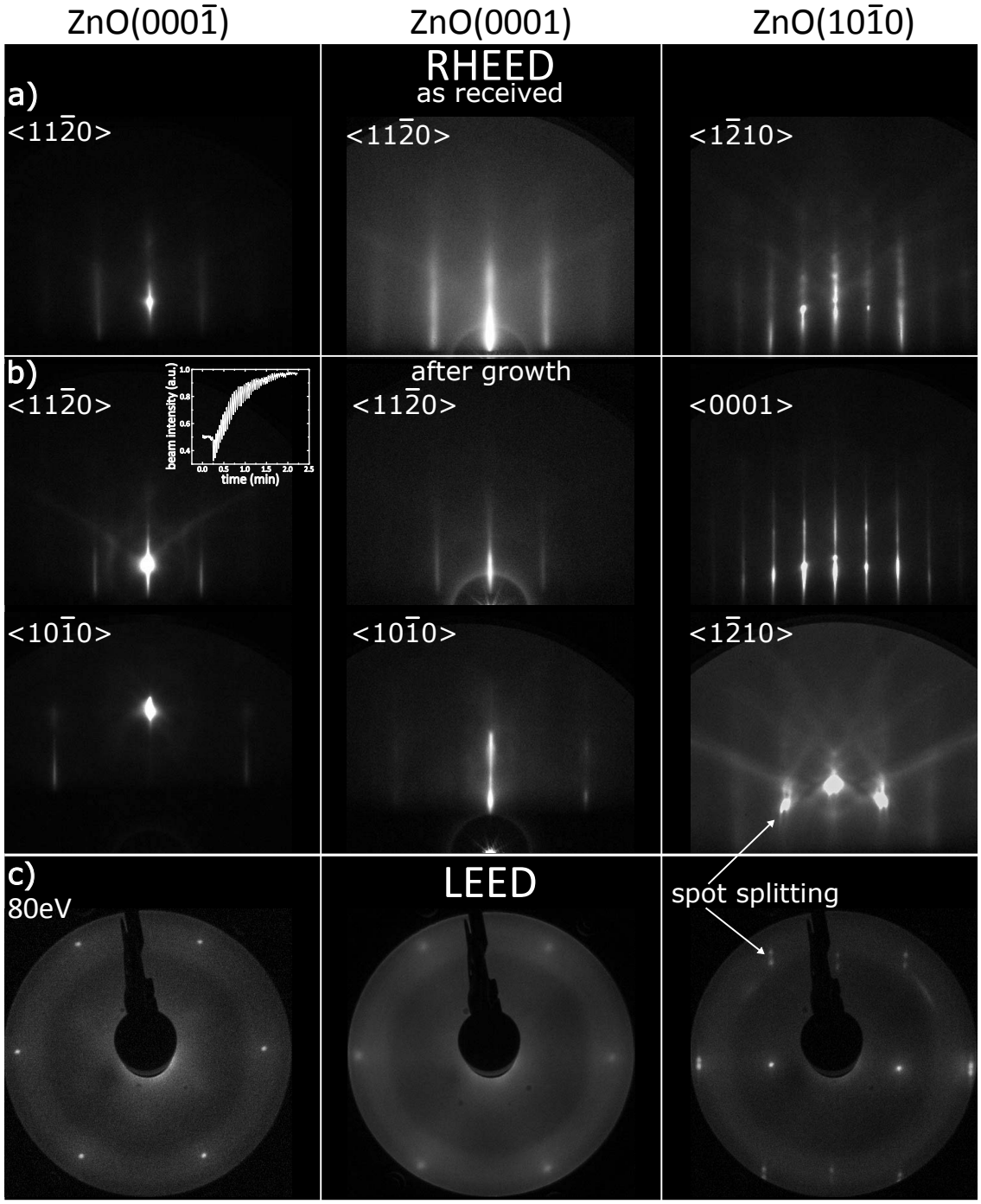

Figure 4.5: RHEED patterns of the polar ZnO c-plane surfaces for the [11$\bar{2}$0], [10$\bar{1}$0] azimuths and the [1$\bar{2}$10], [0001] azimuths for the non-polar ZnO m-plane surface for typical samples. LEED images of the same surfaces, taken at 80 eV.

4.2.2 Surface morphology

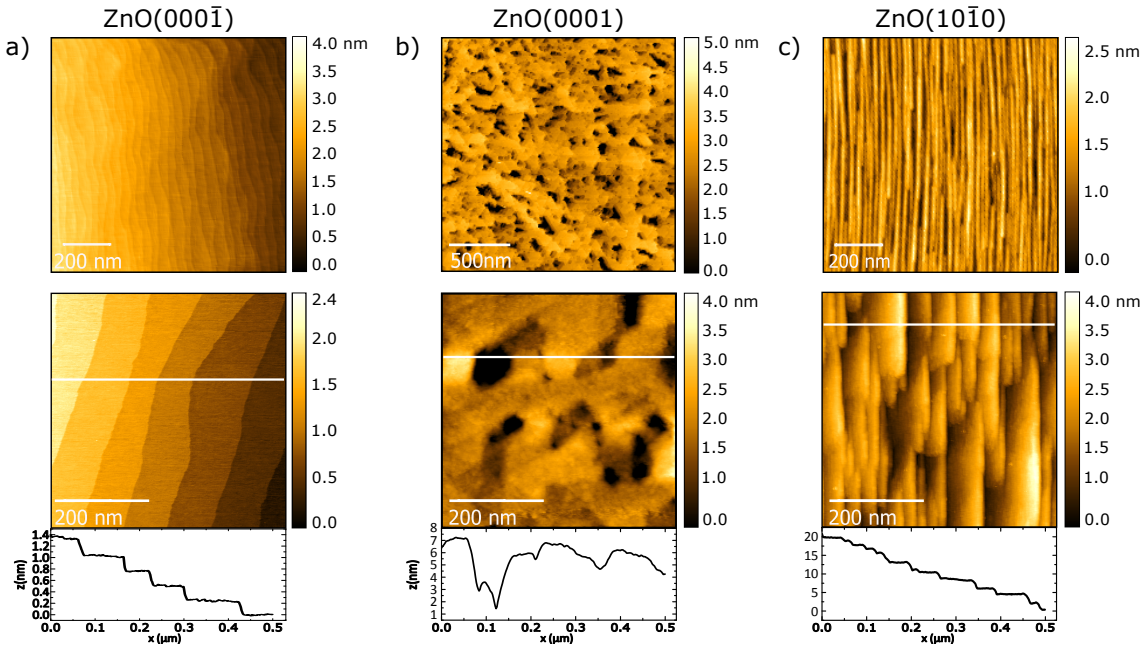

Figure 4.6: UHV-STM scans of the a) ZnO(000$\bar{1}$), b) ZnO(0001) and c) ZnO(10$\bar{1}$0) surfaces in comparison. The top shows a larger area, while the bottom shows a 0.5 x 0.5 nm^2 snapshot with a corresponding line profile underneath.

The findings of the diffraction patterns are also directly reflected in the real space STM images seen in Fig. 4.6. Typical morphologies for the ZnO(000$\bar{1}$), ZnO(0001) and ZnO(10$\bar{1}$0) surfaces are compared. Fig. 4.6a shows the atomically smooth and well-defined O-polar surface, where slightly wavy extended monoatomic terraces are present (see line profile). They exhibit heights of 0.25 nm, matching the lattice constant of ZnO, while the terrace have widths of 100 nm. In contrast to this ordered terraces the Zn-polar surface (cf. Fig. 4.6b) is considerably rougher and holey. Monoatomic steps are also identifiable, but the structure is dominated by hexagonal islands and holes, partly several nm deep. Therefore, the O-polar is surface is preferred to the Zn-polar surface in this work. On the other hand the non-polar ZnO(10$\bar{1}$0) can easily be controlled at ZnO growth. The surface consists of straight thin terraces, which are extended up to a micron in the c-direction, while they only exhibit widths of up to 50 nm. As opposed to the monoatomic steps for the case of O-polar ZnO, the steps show varying heights from the monoatomic step height to some nm. However, the steps are quite regular and monotonous in height.

4.3 Controlling the Organic Growth: Morphological Investigations

Crucial for the interplay of individual components in a hybrid inorganic/organic structure is the nature of the interface. Combining two dissimilar material groups in a way that the advantages of both worlds are merged into one heterostructure requires to gain an understanding of the growth processes and thus a control down to the molecular level. Mastering this, enables device design of defined structures for optoelectronic applications as transistors, light-emitting or photovoltaic devices. Their functionality critically depends on the molecular orientation and morphology which modify direction of the transition dipole moment, electrical injection and charge transport. Different strategies of controlling the growth mode of the organic layer will be discussed in this chapter. A straightforward way is to use the interaction between substrate and molecule to control growth in a desired way by using suitable surface terminations. A further method to manipulate diffusion mechanisms is to vary the substrate temperature and thus modify the diffusion coefficient itself. A more elaborate way to control the growth mode is to slightly modify the molecule without affecting its optical properties, which will also be presented here.

4.3.1 Growth of *para*-sexiphenyl

In this section various ways of controlling the growth of *para*-sexiphenyl (6P) are demonstrated. The basic properties of this molecule were introduced in Sec. 4.1.1. Generally 6P grows in two configurations, namely in islands composed of upright standing or needles built of flat-lying molecules. In this work it will be shown by means of *in situ* AFM growth studies how variation of the substrate temperature affects the growth of native 6P. Ultimately, the remarkable feature of organic molecules to allow functionalization is analyzed. This is done by studying the impact of partial fluorination on the growth-mode of the molecule. Here two derivatives of 6P, the symmetrically fluorinated species 6P-F_4 ($C_{36}H_{26}F_4$) and the asymmetrically fluorinated p-6P-F_2 ($C_{36}H_{24}F_2$) on the ZnO($10\bar{1}0$) surface will be investigated by *in situ* AFM and simultaneous KPFM measurements.

4.3.1.1 The Role of the Surface

The role of the ZnO surface on organic molecular growth was already investigated in earlier studies. Those will shortly be discussed here to motivate the next steps of this work. For aggregation of organic molecules the surface planes of an underlying inorganic semiconductor presents a way to engineer molecular morphology. Blumstengel et al. found structures of 6P molecules of uniform height in the sub-ML regime on the Zn-terminated ZnO(0001) surface, corresponding to nearly upright standing molecules.[151] Those island-like structures did not feature a preferential in-plane orientation irrespective of the investigated temperature. The islands formation of standing molecules was rationalized by a predominance of intermolecular over substrate-molecular interaction, leading to the formation of 6P crystallites in their equilibrium crystal structure. The isotropic orientation of the molecular islands was further explained by a missing epitaxial relation with the hexagonal symmetry of the substrate. The growth at higher temperatures was reflected in increased mean island size and distance between the islands, which was explained by diffusion-mediated growth processes. Aggregation on the non-polar ZnO($10\bar{1}0$) surface yielded a completely different growth mode. Instead of islands, needle-shaped crystallites with lengths of several µm and heights of about 10 nm emerged, strongly oriented along the ZnO[0001] direction. XRD investigations revealed that those were composed of lying molecules with 6P($20\bar{3}$) as contact plane in agreement with photoluminescence polarization measurements. For the O-terminated ZnO($000\bar{1}$) surface Blumstengel et al. eventually found a coexistence of island and needle growth independent on the investigated growth temperature.[151] The needle-like configuration on the non-polar surface was reasoned by a study of Della Sala et al. using a combination of classical calculations and density-functional theory.[70] As shown in Sec. 2.2 the ZnO($10\bar{1}0$) surface exhibits alternating rows of equal numbers of Zn and O ions perpendicular to the c-axis. This produces an electric dipolar surface field with strengths of several V/nm. A 6P molecule physisorbed on this charge pattern is therefore polarized, whereby the molecule minimizes its total energy by maximizing the molecular dipole moment leading to a molecular alignment with the long molecular axis along the rows and on top of the positively charged Zn rows. This is sketched in Fig. 4.7. The strength of this effect is determined by the multipole moments of the molecule, resulting in a strong angular-dependent molecule-substrate interaction energy for 6P, while for example no significant dependency is existent for pentacene.[176] Those findings were confirmed by a study of Palczynski and Dzubiella with molecular dynamics simulations as well as Monte Carlo simulations by Kleppmann and Klapp.[177,178] They also claimed a strongly anisotropic diffusion of 6P on the ZnO($10\bar{1}0$) surface, with many orders of magnitude slower diffusion coefficient for ZnO[0001] than for perpendicular directions. This anisotropic behavior can be reinforced or reduced as perpendicular diffusion coefficients show a strong temperature dependency, which follows an Arrhenius-like relationship with different slopes for the respective direction. Furthermore, lying and standing configurations can be simulated.

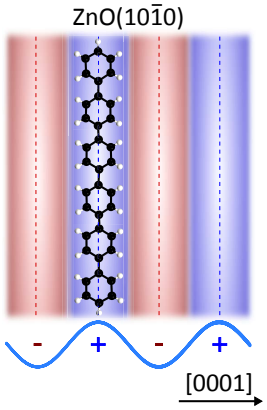

Fig. 4.7: Top view of 6P on the ZnO($10\bar{1}0$) electric surface field.

4.3.1.2 The Role of Temperature

In Sec. 2.1.1 the general dependence of growth processes on the temperature was discussed. In the special case of 6P several studies showed that it is possible on certain substrates such as TiO_2, KCl or Al to obtain control over the orientation of molecules on the substrate through variation of the growth temperature.[179–181] Here, the role of temperature on the growth of 6P (provided by TCI Deutschland GmbH) on ZnO($10\bar{1}0$) is analyzed. To assure a well-defined pristine surface, ZnO($10\bar{1}0$) substrates (by CrysTec GmbH) were overgrown with a 100 nm epilayer by radical source molecular beam epitaxy using the procedure described in Sec. 3.1. For the molecular layer typically growth rates of approximately 0.1 nm/min were used. The resulting films were then investigated with *in situ* AFM (Omicron UHV-AFM/STM) to determine the structural change of the growth mode with temperature. In Fig. 4.8 sub-ML films on ZnO($10\bar{1}0$) for room temperature and nominally $T_S = 100$ °C as well as $T_S = 150$ °C substrate temperature are compared in 3D images of the morphology. Their nominal thickness is ∼1 nm as measured by quartz microbalance. For deposition at room temperature (Fig. 4.8a) polygonal islands with uniform height of 2.6 ± 0.3 nm are found that correspond to nearly upright standing molecules, as in the crystal structure of 6P (→ Fig. 4.1). Those nearly upright standing molecules suggest that the intermolecular interaction is dominant over molecule-substrate interaction.[151] Furthermore, the morphology of the single islands resemble the equilibrium crystal structure of 6P which exhibits an octagonal shape.[152] The nearly upright standing molecular orientation is characteristic and often seen for rod-like molecules on weakly interacting substrates and corresponds to crystallites with 6P(001) as the contact plane representing the face of minimal surface energy.[13,152] At the same time the arrangement of the islands implies that they are composed of single crystallites that possess a preferential in-plane orientation with 6P[010] alongside the c-axis of the ZnO crystal. This suggests a substrate induced alignment of the molecular islands.

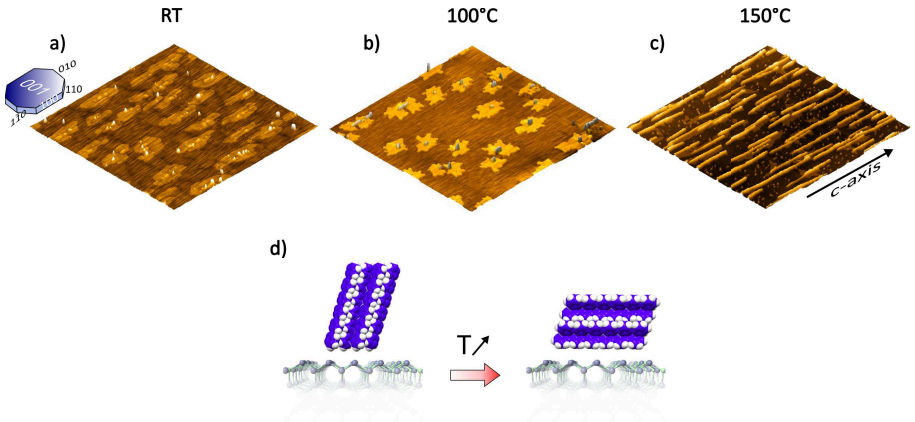

Figure 4.8: AFM scans (4 x 4 µm^2) of 1 nm 6P layer grown on ZnO($10\bar{1}0$) at a) Room Temperature (RT) and b) 100 °C c) 150 °C substrate temperature. On the very left side the equilibrium crystal structure of *para*-6P is shown.[152] d) Schematic drawing of standing and lying growth of 6P on ZnO($10\bar{1}0$) at low and high temperature.

At a higher temperature of 100 °C a transition is observed, where the islands lose their characteristic equilibrium shape and become more dendritic, while at the same time needle-like crystallites start to form on top of islands of standing molecules (Fig. 4.8b). Those exhibit an approximate uniform height of 8 nm and show partly an alignment along the c-axis of the ZnO surface. For even higher temperatures of 150 °C the needle growth becomes predominant over the island growth, with needles of several µm length that are all distinctly aligned along ZnO[0001] (Fig. 4.8c). However, the islands of standing molecules are seemingly still the starting point for the nucleation of needles, since the needles are seen mainly on top of islands. Additionally, on the bare substrate, in the open spaces between islands and needles, randomly distributed smaller clusters of various heights can be found.

Needle-like growth is generally observed on strongly interacting substrate surfaces, like on metal, alkali halides or crystalline mica.[13,182,183] This occurs due to the nature of the rod-like molecules to initially adsorb in a flat-lying manner parallel to the substrate and diffuse like this until they meet other molecules. Then the molecule-substrate or molecule-molecule interaction decides over the alignment of the molecules.[183] For a strongly interacting substrate, the flat-lying configuration of the molecules also persists in the higher layers, leading to a needle-like aggregation, due to the anisotropy in diffusion and incorporation probability of the rod-like molecules. The formation of needles is described in the case of 6P on mica(001) as a result of strain induced rearrangement of crystallites at a critical density.[184,185] Depending on the strength of the interaction different substrate-induced polymorphs with different contact planes are observed.[13] For the ZnO($10\bar{1}0$) surface X-ray diffraction revealed that the 6P($20\bar{3}$) is the contact plane for the needle-like aggregates. Here the molecules are arranged in a herringbone structure with the long axis in contact with the surface. Furthermore, the alignment of the single molecules parallel to the dimer rows of the ZnO is confirmed by polarization dependent photoluminescence spectra.[151] It was shown that the nature of the ZnO($10\bar{1}0$) surface and the diffusion of the single molecule play a key role to understand the adsorption of rod-like molecules and their special alignment. As stated above the 6P molecule adsorbs flat-lying. Consisting of Zn^{2+}-O^{2-} dimer rows the ZnO($10\bar{1}0$) surface exhibits a significant dipolar surface field with a charge pattern that then induces a dipole moment in the π-system of the molecule and generates a preferential alignment with the long axis parallel to the oxygen/zinc rows and an anisotropy in the diffusion paths of a single 6P molecule.[70,177] A very similar behavior is found for the nucleation of 6P on crystalline mica, where K^+ and Al^{3+} ions form surface dipoles whereby the 6P molecules orient themselves in the dipolar field and form aligned needles.[183,186,187] Crystallites which are located in the space between the needles can be explained by similar findings in literature for growth of 6P on mica and TiO_2, where the formation of those crystallites was ascribed to Ostwald ripening of an initially formed wetting layer.[188,189] The most surprising result is the island growth mode at low temperatures and needle like growth at high temperatures, which is not observed in this form on other substrates. There are other studies, which also find control mechanisms for the orientation of 6P. For one, a reason for orientational change is a surface modification as for example for carbon covered mica or air-passivated TiO_2(110).[187,189] Others select the orientation also by temperature, however, in contrast to our findings they report consistently growth of

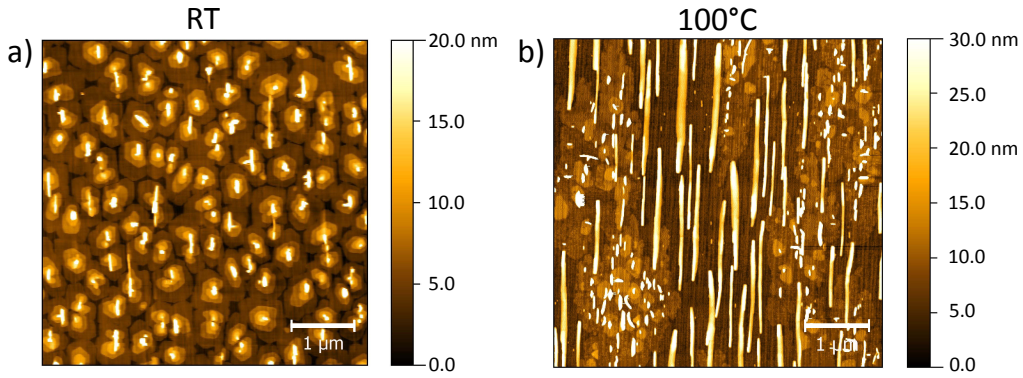

Figure 4.9: AFM scans (5 x 5 µm^2) of a nominally 5 nm 6P layer grown on ZnO(10$\bar{1}$0) at a) RT and b) 100 °C substrate temperature.

lying molecules at lower temperatures and a reorientation to the standing configuration at elevated temperatures.[179–181,190,191] Upright standing molecules with the (001) as contact plane signify a strong intermolecular interaction and in fact it is shown to be the generally energetically favored plane as Nabok et al. have shown by *ab initio* calculations. However, for strong substrate-molecule interaction lying molecules are to be expected.[152] In our case one would also expect that the formation of needles is favored, since the molecules adsorb flat-lying on the ZnO(10$\bar{1}$0) surface and need to overcome an energy barrier to reorient for nucleation in the island configuration. This is also confirmed by molecular dynamics simulations of 6P on the 6P(001) surface by Potocar et al.: Standing aggregates up to a cluster size of 4 molecules are completely unstable, while lying molecules are energetically favored up to a cluster size of 14 molecules, where clusters of standing molecules become more favorable.[21] A strong substrate-molecule interaction as for ZnO would favor lying clusters even more, due to a larger adsorption energy, what makes the present results more difficult to interpret. A possible explanation for the orientation on the ZnO(10$\bar{1}$0) surface could be the formation of an initial Wetting Layer (WL) of lying 6P molecules at room temperature with molecules aggregating on top, where the molecule-molecule interaction dominates and the standing configuration is kinetically favored. Polarization dependent reflectance difference spectroscopy verified such a formation of a WL beneath islands of standing molecules for 6P on TiO_2(110) and also UPS measurements confirmed a formation of a WL on different ZnO surfaces.[192,193] For higher temperatures this WL then appears to change in such a way that the substrate-molecule interaction becomes dominant over the intermolecular.

The further evolution of the film is examined at a higher coverage. The characteristic polygonal shape of the 6P crystallites is still observed at room temperature (cf. Fig. 4.9a). Between the polygonal islands the layers do not close up completely, leading to islands that build up as tapered 'wedding cake' like structures with higher coverage, which are separated by crevices. The process of this piling up is referred to as Zeno effect.[194] The terraces are formed by single monolayers of nearly upright standing 6P molecules. Similar structures were observed before for 6P grown on ion-bombarded mica surfaces and assigned to a

pronounced Ehrlich-Schwoebel barrier, hampering interlayer mass transport and leading to a rough, mound-like profile that can be well-described by a Poisson distribution as done by Hlawacek et al.[20] Furthermore, it can be seen that at a certain thickness also needles start to form on top of the islands. Remarkably those needle structure are preferably oriented mainly along ZnO[0001] even on top of the 3^{rd} monolayer of standing molecules. Needle structures emerging at a certain thickness were also described by Hlawacek et al. for 6P growth on mica. However, they observed branched needle structures without any preferential orientation. Thus, the substrate induced anisotropic alignment of the molecules is influencing growth far above the 1^{st} ML. The needle growth is again more pronounced at elevated temperatures (Fig. 4.9b). Here needle-like structures along the ZnO[0001] direction exhibit lengths of several µm and heights of approximately 30 nm on the substrate, while shorter and higher needles form on top of additional widespread elongated islands o standing molecules. Similar structures for 6P are also reported on the reconstructed TiO_2(110)-(1x1) surface.[192,195] In this case also needles are oriented perpendicular to the oxygen rows of the surface, while the molecules are flat-lying aligned parallel to the oxygen rows. An important difference, however, is that the needles emerge at room temperature, whereas extended islands arise at higher temperatures that opposite to ZnO are elongated along and not perpendicular to the oxygen rows.

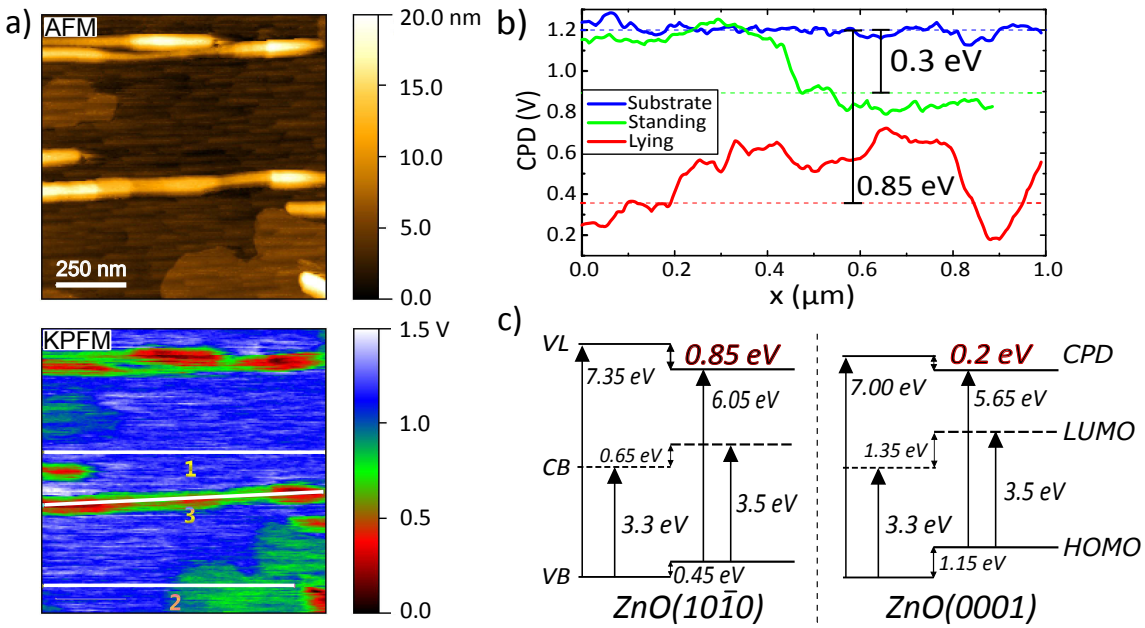

Figure 4.10: FM-KPFM (1 x 1 µm^2) of 6P on ZnO with b) line profile. c) Energy level alignment of ZnO(0001)/6P and ZnO(10$\bar{1}$0)/6P derived from UPS and optical absorption data (Adapted from Ref. [151]).

Apart from the morphological aspect and roughening mechanisms that arise as a result of the different growth modes, the distinct alignment of the molecules also plays a crucial role for the electronic structure of the HIOS.[180] The change of the molecular domain

orientation is accompanied by a shift of the energy levels at the semiconductor interface. This can be attributed to a modification of the surface dipole for molecules standing or lying on the surface, resulting in a charge redistribution and Pauli-repulsion at the heterointerface.[151] The molecular orientation is a powerful control mechanism to engineer band offsets between organic and inorganic hybrid. This difference was experimentally determined before by Ultraviolet Photoemission Spectrocscopy (UPS) experiments with 6P samples grown on different ZnO surfaces that featured primarily one orientation of the molecules.[151] UPS is an effective technique to extract the electronic structure from an adsorbate. A disadvantage of the method is that it gives an area averaged value. A powerful method for the direct determination of the local work function with a high resolution is the Kelvin probe force microscopy technique which was applied here to probe a ZnO$(10\bar{1}0)$/6P sample exhibiting both crystal orientations, standing-up molecules in monolayer islands as well as lying-down molecules situated in the aligned needles. The measurement was done in the Omicron UHV-AFM in FM mode in a single-pass, meaning a simultaneous scan of morphology and Kelvin probe. Fig. 4.10a shows the simultaneously measured AFM (top) and KPFM (bottom) scans, illustrating morphology and work function of the surface. A noticeable contact potential difference (CPD) between substrate and differently oriented molecules in the KPFM measurement can be observed. The values of the CPD for representative structures are given by a line profile in Fig. 4.10b for substrate (1), standing (2) and lying (3) molecules. For 6P islands of standing molecules a uniform CPD to the substrate of $eV_{CPD} = -0.3$ eV can be derived, while the needles show an average value of $eV_{CPD} = -0.75\ eV$. Variations of about ± 0.2 eV are seen inside the needle structure. The reason for this strong variation is the limited spatial resolution of the KPFM. The needles are comparably thin with dimensions of under 100 nm, resulting in averaging effect of the tip over substrate and molecular structure. However, in the center of the structure, where the averaging effect is the weakest, the biggest value for the CPD can be identified. In comparison the values for the work function difference between substrate and organic molecule determined by UPS amounted to $eV_{CPD,ZnO(0001)} = -0.2$ eV and $eV_{CPD,ZnO(10\bar{1}0)} = -0.85$ eV. Considering the uncertainty for the Kelvin probe method and different surface preparations, values determined by UPS can be confirmed with this complementary method, while it further makes a local probing of the electronic structure possible. Remarkably, the reduction of the work function presented by Blumstengel et al. occurred on different ZnO surfaces with different initial work functions of the pristine ZnO. Nonetheless, the work function change for the respective molecular aggregates, standing or lying, appears to be independent of the surface termination, while the stronger interaction with the lying molecules is reflected in the stronger work function change. At the same time the flat-lying molecules form a negatively charged plane with their π-electron system, so that also ionization potential and electron affinities are orientation dependent. The fundamental reason for the generally observed reduction of the work function is explained by a 'push-back' effect of the surface dipole due to Pauli-repulsion with the molecule.[151,196] This applies only to physisorbed non-polar molecules without any charge transfer. This shows that the change of the orientation also makes it possible to tune the energy levels in a hybrid structure and defines beside the optical dipole moment the efficiency of a device.

Conclusion

The choice of surface termination as well as temperature variation proved to be important parameters to control the growth mode of hybrid inorganic/organic structures shown here using the example of 6P on ZnO. Molecular orientation plays a crucial role for application in devices. For one as the orientation affects the charge injection and transport, for another since the energy level alignment is changed, while additionally needle-like arrangement enables laser operation.[15,144,151,181] It was shown that the surface orientation as well as the growth temperature are crucial parameters to determine the strength of the substrate-molecule interaction. Thereby the molecular orientation can be controlled in the case of 6P. For the polar ZnO(0001) surface interaction with the molecule showed to be especially weak and intermolecular interaction dominant, hence 6P islands of standing molecules were observed.[151] The non-polar ZnO($10\bar{1}0$) surface, however, exhibits dimer rows that produce an electrostatic surface field which induces an alignment in the 6P molecules. By this aligned needles can be created along ZnO[0001], consisting of lying molecules with 6P($20\bar{3}$) as contact plane.[70] Growth of the molecule on the ZnO($10\bar{1}0$) surface, on the other hand, turned out to be strongly temperature dependent with needles forming only at higher temperatures, while growth at room temperature featured islands in the shape of the equilibrium crystal structure with 6P(001) as contact plane with the lowest free surface energy. This result is in contrast to investigations of 6P on other surfaces, where needles were observed at room temperature while islands formed at higher temperatures. This finding might, however, be explained by a wetting layer only existent at room temperature hampering the influence of the substrate. Whether a wetting monolayer is present is a question of ongoing discussion and could not be conclusively answered in this work. Methods to answer this would be TD spectra, UPS or polarization dependent reflectance difference spectroscopy. For higher coverages on the ZnO($10\bar{1}0$) surface terraced polygonal mounds were observed at room temperature, which originated due to a pronounced ESB at the edges of the islands, while at a certain thickness aligned needles also formed on top of the islands. The importance of the molecules' orientation for the energy level alignment could be confirmed by Kelvin probe force measurements, where it was shown that the work function strongly depends on the orientation of the molecule and that this complementary method is consistent with results from UPS experiments on different ZnO faces.

4.3.1.3 Chemical tuning: Partial Fluorination

In the preceding sections the growth of *para*-sexiphenyl was discussed on different ZnO surfaces and for different temperature regimes, featuring the possibility to control the molecular alignment. Despite successfully demonstrating those control mechanisms, in both cases a rapid roughening of the emerging layers was observed, unfavorable for high charge carrier mobilities and with this, potential device application. In the next section a new way to gain control over growth processes will be introduced to transform the rough three-dimensional growth into a layer-by-layer growth mode. This was made possible by the work of Y. Garmshausen, who found a synthesizing route to specifically chemically modify the 6P molecule.[133,197] Here, partially fluorinated sexiphenyl molecules were used to investigate the underlying mechanisms of growth and illustrate the impact of those small atomic changes that influence molecule-molecule and molecule-substrate interaction. An important prerequisite for the study was to alter the growth mode of the sexiphenyl derivative without changing its inherent optical properties. That the partial fluorination of the molecule indeed does not change its optical properties and possesses nearly identical optical fluorescence and absorption spectra as 6P can be seen in Fig. 4.11. The reason for this is that the π-electron system is not changed by the fluorination. The complete synthesis of the symmetrically fluorinated 6P can be found in the supplementary information of Ref. [133]. Those altered molecules were investigated in terms of their growth evolution by an *in situ* AFM study from sub- to a few ML. In particular the symmetrically, terminally fluorinated 6P-F_4 ($C_{36}H_{22}F_4$) and the asymmetrically, terminally fluorinated 6P-F_2 ($C_{36}H_{24}F_2$) with a permanent dipole moment were used and compared to the initial 6P growth.[133] For 6P-F_2 temperature dependent measurements were conducted to determine the influence of this additional control parameter. Furthermore, 6P-F_2 and 6P-F_4 growth studies applying Kelvin measurements were done to compare the influence of the permanent dipole moment and the asymmetrical fluorination on the growth processes. We focused here on the growth of the non-polar ZnO($10\bar{1}0$) surface to take advantage of its previously discussed electrostatic coupling to the molecule, exhibiting now modified multipolar moments. A complementary method to further look into the film growth dynamics by real-time *in situ* X-ray Reflectivity (XRR) investigations, as well as post-growth XRD scans were performed by A. Zykov, P. Beyer, L. Pithan, C. Weber, F. Carlà and S. Kowarik. The complete results of the here presented study for 6P-F_4 were published in Ref. [133].

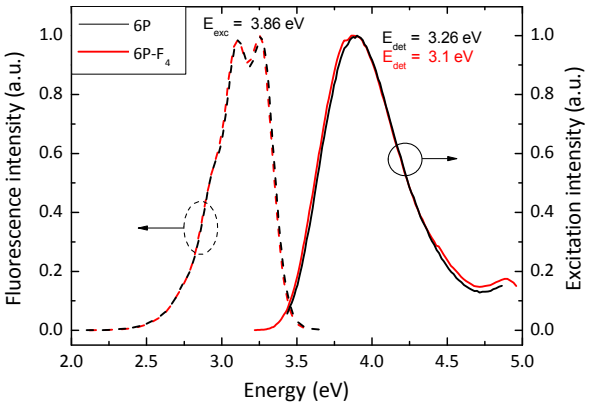

Fig. 4.11: Optical spectra comparing excitation (solid line) and fluorescence (dashed line) spectra of 6P and 6P-F_4 in $CHCl_3$ at RT, normalized to 1 at the peak maxima.

6P-F_4

Fig. 4.12 compares the nominally 5 nm thick layer of 6P which was investigated before (Fig. 4.12a) with a nominally 6 nm thick layer 6P-F_4 (Fig. 4.12b) grown on epitaxially overgrown ZnO($10\bar{1}0$) substrates (Crystec GmbH) at RT with constant deposition rates for 6P and 6P-F_4 of $\approx 1 \ldots 1.5$ Åmin^{-1} as monitored by quartz microbalance. As previously discussed, 6P exhibits characteristic shaped terraced mounds of uniform height as shown by the cross profile in the inset with aligned needles on top. The 3D mound-like structures of the 6P and their emergence was explained before by a significant ESB. On the other side the fluorinated 6P-F_4 grows in extended 2D islands with irregular shape (Fig. 4.12b). Strikingly is the significantly smoother surface even for a slightly thicker film of 6P-F_4. While the 6P surface is strongly roughened with 3 MLs of islands and additional needle growth for the 6P-F_4 film the third layer has barely started to nucleate yet. This is reflected by the magnitude of the Root Mean Square (RMS) roughness, being 3.2 nm for the 6P layer including needle-shaped crystallites (1.7 nm without) and 0.8 nm for the 6P-F_4 layer. Surprisingly, post-growth Θ-2Θ XRD scans of a 18 nm 6P film (not shown) yield a coexistence of two polymorphs as seen by a splitting of higher order Bragg reflections. The determined lattice spacings of $d_{6P,\beta} = 2.59$ nm (implying a tilt angle of 17°) and $d_{6P,\gamma} = 2.72$ nm are assigned to β- and γ-polymorphs of 6P ($\rightarrow$ Sec. 4.1.1).[148,150] The XRR spectrum shows approximately equal intensity of the respective polymorph indicating a simultaneous growth of both phases, while in previous studies only pure phases for different growth temperatures were found as for example for 6P on glass.[150] For the 6P-F_4 layer the XRR measurements yield an average lattice spacing of 2.42 ± 0.03 nm, suggesting a larger tilt of 27° (when assuming the same van-der-Waals length as for 6P) and hence a different crystal structure of the growing fluorinated molecules. However, real-time X-ray reflectivity measurements of the initial growth steps clearly yield a decreasing in the out-of-plane lattice spacing from 1^{st} to 3^{rd} ML of 2.64, 2.46 to 2.42 nm.

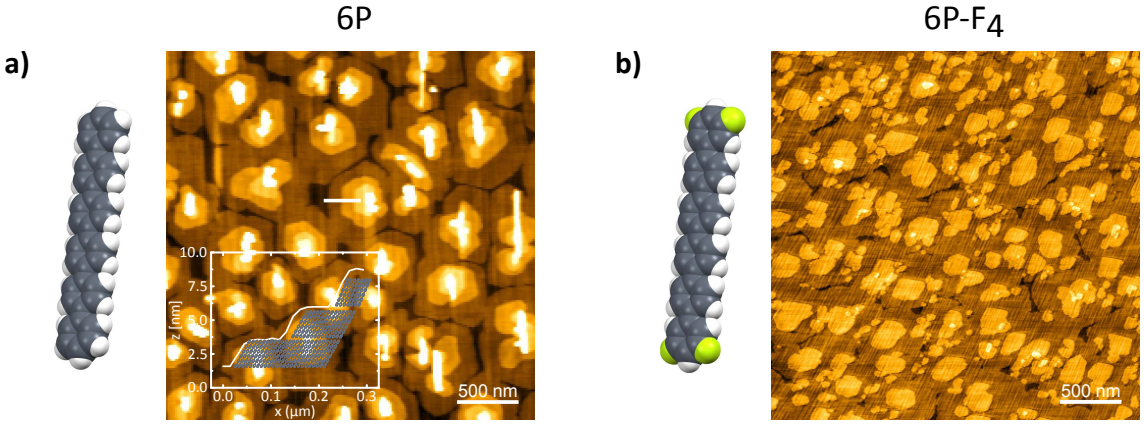

Figure 4.12: AFM scans (3 x 3 µm^2) with corresponding height profile for a) 6P recorded along the white line of a nominally 5 nm thick 6P layer measured *ex situ* and b) a nominally 6 nm thick 6P-F_4 layer measured *in situ*. Both films were grown at RT on ZnO($10\bar{1}0$).

The structural evolution of the thin film morphology of 6P-F_4 is traced in the following by introducing growth interruptions and taking *in situ* AFM snapshots of increasing layer thickness. Those single shots make it possible to directly follow the deposition of molecules and monitor the different growth phases. Moreover, this allows to determine the stable size of a nucleus, being the crucial parameter to describe nucleation processes. When re-evaporation is excluded this can be done by analyzing the data in the aggregation regime using island nucleation distribution and capture zone scaling as described in Sec. 2.1.1. The AFM scans of increasing 6P-F_4 coverage are shown in Fig. 4.13. Strikingly at a nominal thickness of 0.2 nm (as measured by the quartz microbalance) no island formation of 6P-F_4 can be yet observed. The AFM scan only reveals a corrugated surface with extended terraces parallel to ZnO[0001] as it is characteristic for the epitaxial ZnO($10\bar{1}0$) surface. However, the amount of deposited molecules corresponds to roughly one ML of flat lying molecules assuming a sticking coefficient of one. Island growth is first observed at a deposition of 0.4 nm. The first emerging islands are of compact circular shape, slightly elongated along ZnO[0001] with an aspect ratio of approximately 1.5 hinting at diffusion anisotropy. The emerging islands in the sub-ML regime, however, show a height of 1.6 ± 0.2 nm (cf. inset Fig. 4.13), *i.e.*, considerable smaller values than the average lattice parameter deduced from the Θ-2Θ XRD scans of a thick 6P-F_4 film. An additional AFM scan is carried out to identify the origin of the mismatch of determined values for the directly measured island height from AFM of merely 1.6 nm and the lattice spacing of 2.4 nm measured by XRR. Hence, a scan in contact mode is carried out for the 6P-F_4 layer with a nominal thickness of 1.0 nm. The applied force on the surface is chosen sufficiently high enough to push away a soft molecular layer by the tip. A subsequent non-contact AFM scan over a scratched area of 2x2 µm^2 reveals the formation of a trench of about 1.0±0.3 nm in depth (cf. Fig. 4.14). The line scan indicates a molecular layer that is piled up at the edges of the trench, pushed there by the tip (Fig. 4.14a). Consequently, this suggest the formation of a WL in the space between the islands that follows exactly the surface morphology of the ZnO surface. A wetting layer for sexiphenyl is not unusual as it was verified before on other surfaces such as TiO_2, Cu and mica.[187,188,190,192,198,199]

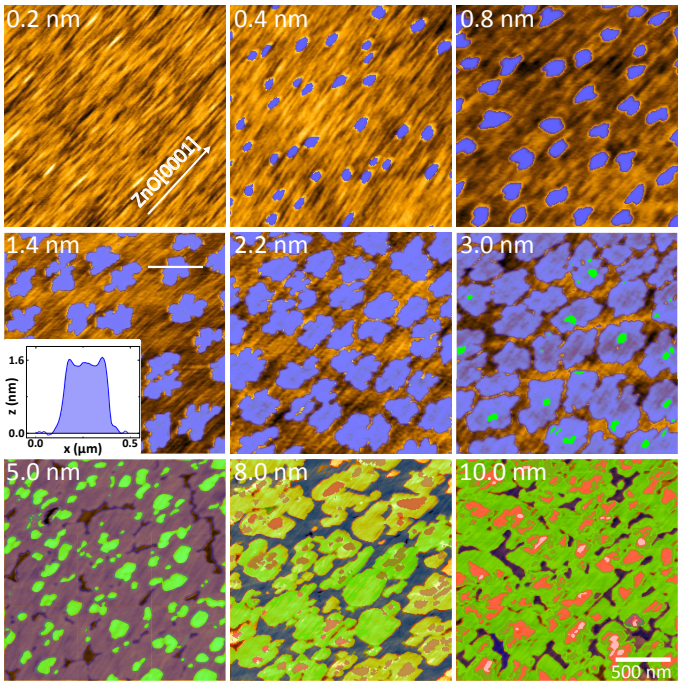

Fig. 4.13: UHV-AFM snapshots (2 x 2 µm^2) of 6P-F_4 on ZnO($10\bar{1}0$) of increasing coverage. The 1^{st}, 2^{nd}, 3^{rd} and 4^{th} ML are highlighted in blue, green, red and white respectively. The inset (nominal thickness of 1.4 nm) shows the height profile measured along the white line.

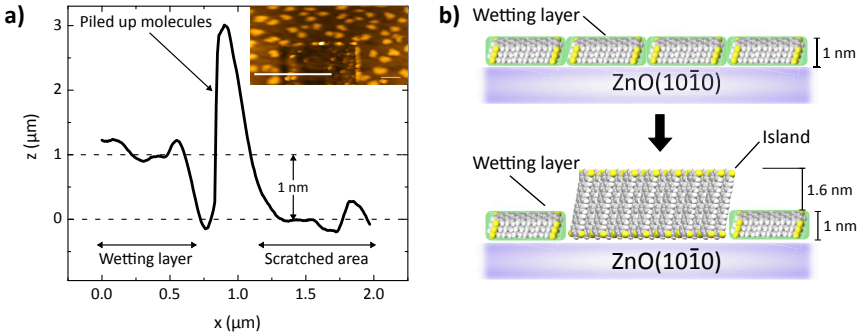

Figure 4.14: a) Non-contact AFM scan of 1.0 nm 6P-F_4 layer containing a previously scratched area in contact mode and corresponding cross-section profile over the scratched area (white line) showing a trench at the scratched area and piled up molecules at the edge. b) Schematic depiction of the 6P-F_4 morphology in the initial stages of growth. Please note that the actual arrangement of the molecules in the wetting layer is not known.

The arrangement of 6P-F_4 in this wetting layer is not known, however, the thickness implies that the layer is either composed of tilted molecules or that it contains more than one layer of flat lying molecules as for instance in the case of Rubicene on SiO_2 or 6P on mica.[198,200] A schematic depiction of this scenario is given in Fig. 4.14b. Furthermore, at higher coverages of the 6P-F_4 film it can be seen that the initially round islands take on a more dendritic shape. However, for a given coverage they exhibit uniform shape and size. At 1.8 nm first coalescing islands can be observed. A significant nucleation of the second layer sets in at a coverage of the first layer of almost 90 %. Beyond the 1^{st} ML a noticeable change in the morphology of the molecular islands can be recognized. The islands become more shapeless and are of various sizes. Nonetheless, also 3^{rd} and 4^{th} layer only start to grow when the underlying layer has almost completely formed. This is confirmed by a comparative study to determine the coverage evaluation by using real-time XRR measurements on one side and AFM snapshots at several thicknesses on the other, as shown in Fig. 4.15. Additional coverage curves determined from XRR measurements over several MLs are shown for comparison for 6P-F_4 as well as 6P films. The q_z dependent X-ray reflectivity data contain rich information about the growth mode. The spectra are acquired over a broad q_z-range and growth oscillations at fixed q_z-values of $1/2, 2/3$ and $3/4$ q_{Bragg} with corresponding oscillation periods of 2, 3 and 4 ML are fitted to estimate the layer coverage of each ML. This is done by using a rate-equation model of growth developed by Trofimov et al.[201] The exact procedure of the quantitative analysis is described elsewhere.[133,202] Considering the different methods for determining the coverage, the data points deduced from AFM in Fig. 4.15b are nearly perfectly coinciding with the lines given by the model of Trofimov et al. The coverage in Fig. 4.15a and Fig. 4.15b is given as a function of molecular exposure =(exposure time)·(molecular flux) and its evaluation gives a detailed picture of the different growth modes of 6P and 6P-F_4. While for both molecules the first layer is more than 75 % complete before the second layer reaches a coverage of 5 %, the growth mode starts to differ significantly from the second ML onwards. For 6P a 3D island growth mode sets in, as the third and even fourth layer start to grow simultaneously with the second layer as evidenced by the shallow coverage curves.

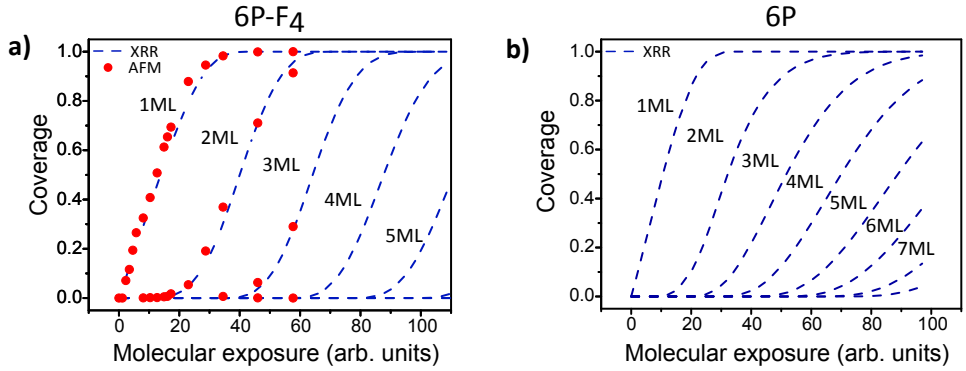

Figure 4.15: Coverage evolution for the different MLs extracted from XRR and AFM data comparing layers of a) 6P-F_4 and b) 6P. While the curves from the XRR are fitted using the Trofimov model, the AFM data is directly determined from AFM snapshots at different thicknesses. The measurements for 6P-F_4 show an excellent agreement between the AFM data and the Trofimov model.

This is accompanied by a steep increase of the RMS roughness for 6P while it stays nearly constant from the 2^{nd} ML onwards below 1 nm for 6P-F_4. For the fluorinated molecule the coverage curves show a steep slope up to at least the 7^{th} ML (where the deposition was terminated), i.e. growth proceeds in a layer-by-layer mode. The growth mode for 6P-F_4 is further described by determining the evolution of the island density as shown in Fig. 4.16a with corresponding contour images extracted from the AFM scans for the first 2 MLs at two coverages Θ in Fig. 4.16b. Analyzing the nucleation shows an instant rise of the island density after the deposition of 0.2 nm to approximately 8 µm^{-2} at a nominal thickness of 0.4 nm and a subsequent rapid decrease of the island density with a saturation to approximately 6 µm^{-2} in the range from a nominal thickness of 1.0 nm to 2.6 nm (Fig. 4.16a). The initial peak and subsequent decrease in the island density is also accompanied by the morphological change of the islands from compact elongated, to more dendritic shape as can be seen in the contour image in the top of Fig. 4.16b. The following phase of constant island density generally defines the aggregation regime. However, first coalescing islands are also already observed at 1.8 nm, yet a decrease in the island density of the first ML cannot be observed until a nominal thickness of 3 nm, so that either islands are still forming up to this point or reorganize, *i.e.*, detachment and diffusion processes take place. Thereafter, the islands grow in size, associated with coalescing islands that close the layer and a rapid decrease of the density of the 1^{st} ML. Simultaneously the island density of the second ML steeply increases to values of about 20 µm^{-2}, roughly 4 times the island density of the first layer. This high value is reflected in the contour images for the 2^{nd} ML, where images of the same coverage are compared (Bottom Fig. 4.16b). In the 2^{nd} ML a vast number of small particles can be seen, opposed to the islands of uniform shape and size in the 1^{st} ML. For the higher coverage it also comes apparent that not only a preferential orientation is induced by the diffusion anisotropy on the substrate, but also the shape of the islands is mediated by the substrate, since those features drastically change from the 2^{nd} ML onwards. While in the 1^{st} ML the islands are of uniform shape and increasing dendritic shape, the 2^{nd} ML islands are of various size and rather compact and

the aligning character is mostly lost. Strikingly, despite the much broader size distribution of the islands, the growth still proceeds in a layer-by-layer fashion after the 1^{st} ML, even when for the 3^{rd} ML an even higher island density of 25 µm^{-2} is observed. The higher island density and morphology change are hence a sign that the fluorinated molecules diffuse substantially different on substrate and molecular layer, which can be according to Eq. 2.2 attributed to a altered diffusion barrier E_D as well as a changed attempt frequency ν_0 on the fundamentally different bottom layer resulting in a lower diffusion coefficient.[198] Additionally, a lowering of the Ehrlich-Schwoebel barrier, which could be induced by the terminal fluorine atoms, facilitates downward mass transport from one layer to another.

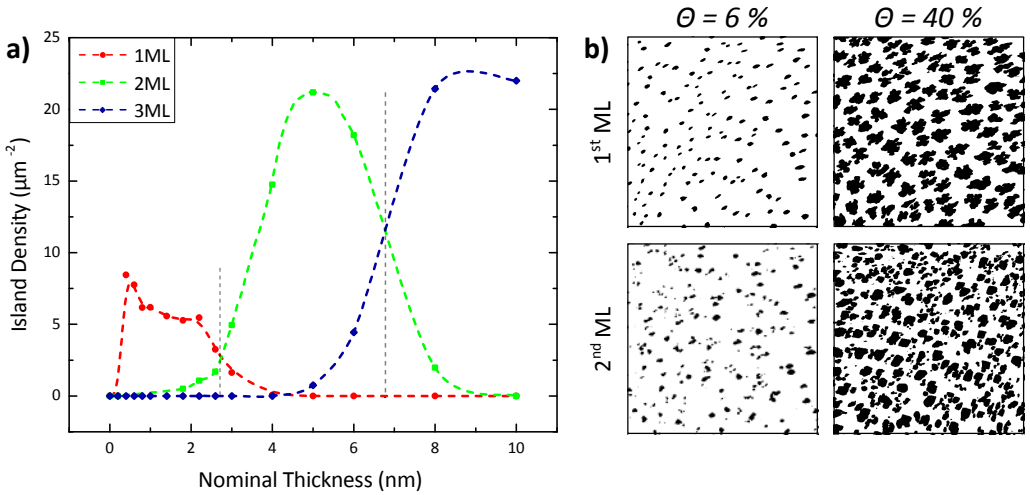

Figure 4.16: a) Island density evolution for the different MLs determined from AFM snapshots for the growth of 6P-F_4 with the dashed lines as guide to the eye and b) corresponding contour images (4x4 µm^2) derived from the AFM scans for 1^{st} and 2^{nd} ML at two equal coverages $\Theta = 6$ % and 40 %.

Finally, to better understand the processes in the sub-ML regime a closer look is taken at the distribution of the island size and capture zones in the aggregation regime of nearly constant island density. For this the critical nucleus size i^* to form stable islands is determined. As described in Sec. 2.1.1 this parameter is elementary for the morphology of the growing film. For small i^*, islands form more easily, while a large critical island size leads to fewer stable islands and a rougher film.[183] Therefore, in the study of thin-film growth the critical nucleus size is a key parameter. Due to the dynamic scaling assumption it is possible to determine the critical nucleus size by the island size distribution (ISD) in the aggregation phase, making it an easily accessible parameter from AFM pictures.[23] Apart from the ISD, an approach of Pimpinelli and Einstein was established more recently, the capture zone distribution. Here, areas around an island are used that define regions where the molecules are incorporated with a high probability into the island.[25,203] The border of the capture zones are approximated by Voronoi polygons and the generalized Wigner distribution is used as an analytical tool to calculate i^* as introduced in detail in Sec. 2.1.1. Hereby, it is possible to describe any aggregation-limiting process, which is not possible for the ISD.[203] Additionally the capture zones distribution (CZD) only depends on the center

of mass and not as much on the island's shape, which can be distorted by errors in the AFM measurement.[17,204] Also, the slightly asymmetric function of the CZD fits the experimental data generally better than the symmetrical ISD. Nonetheless, there are restrictions to the CZD in the case of especially ramified islands as shown by Lorbek et al., because the Voronoi polygons overestimate too small islands and underestimate too big islands.[204] Lorbek et al. observed this especially in the case for growth at higher temperatures, where dendritic islands form, while the determination of growth at room temperature showed a good agreement of ISD and CZD. However, in the presented experiment the fractality is not as distinctive. In Fig. 4.17 normalized histograms for island size and capture zone distributions are compared, determined from AFM scans in the aggregation regime between 0.4 and 1.4 nm nominal thickness. The evaluation of the histograms was performed by using an optimal bin size as proposed by Scott:[205]

$$h = 3.49 \cdot \sigma n^{-1/3}, \tag{4.1}$$

where σ is the standard deviation and n accounts for the number of data points. The abscissa of each histogram is rescaled: For the ISD the island size s is normalized by the mean island size S, for the CZD the fluctuating variable $s \equiv A/\langle A \rangle$ contains the area A of the capture zone and the mean area $\langle A \rangle$. In Fig. 4.17a the ISDs for different film thicknesses are compared with the scaling functions of Amar and Family introduced in Sec. 2.1.1 for critical island sizes ranging from $i^* = 1 - 4$. For the ISD the experimental data is reproduced best by the curve for $i^* = 2$. However, it becomes apparent that the data points exhibit a large scattering and especially at the flanks the curve does not fit the data well. In Fig. 4.17b the alternative method of CZDs is used with the Generalized Wigner Surmise (GWS) described by Pimpinelli and Einstein using values of $\beta = 2 - 5$. A fit to the data using the least squares method with the Levenberg-Marquardt algorithm yields a value of $\beta = 2.7$. The GWS fits the experimental data fundamentally better than the scaling function in the case of the ISD. The reason is that it is difficult to accurately enough describe the island contour with AFM measurements, whereas the capture zones are easily identified. Additionally, the islands are not exceedingly ramified, so that the distribution can still be well performed by capture zones. As shown in Sec. 2.1.1 β depends on the prevalent aggregation limiting mechanism. The classical growth scenario is isotropic diffusion limited aggregation (DLA), where $\beta_{DLA} = i^* + 2$ holds. This would indicate that in the present case $i^* = 1$ and approximately two molecules already form a stable nucleus. This small value is in agreement with reported results obtained for plain 6P molecules on different surfaces, ranging from $i^* = 1 - 3$.[21,188,204] Yet, the nucleation of rod-like molecules is the origin of extensive on-going discussion. The reason is that the conditions for DLA are not necessarily fulfilled for those molecules. The underlying growth mechanisms crucially depend on the surface treatment as well as on growth rate and temperature.[22] DLA assumes a capture probability of unity, however, rod-like molecules exhibit an energetically favorable binding orientation which is parallel to each other. Additionally single molecules diffuse generally preferentially flat-lying and parallel to their long axis, and especially in the case of the ZnO$(10\bar{1}0)$ surface perpendicular to ZnO[0001].[21,177] Since the islands consist of standing molecules, the incorporation of the approaching flat lying molecules

is hindered by an effective activation barrier, which can only be overcome at sufficiently high temperatures. Therefore many publications on rod-like molecules, *e.g.* for 6P and Pentacene (5A), suggest that the model of diffusion limited aggregation is not adequate to fully describe the growth kinetics for those molecules.[17,21,22,198] The case of anisotropic monomer diffusion is instead described by the attachment-limited aggregation (ALA) as discussed in Sec. 2.1.1. This growth mechanism can only be reproduced in the case of CZD which correlates the exponent β_{ALA} with the critical island size as $\beta_{ALA} = (i^* + 3)/2$. For the 6P-$F_4$ growth this results in a critical island size of approximately $i^* = 3$. A remaining question is how the nuclei aggregate on the surface, lying or standing, and if a transition takes place. This is estimated by the binding energy of the aggregate, defined as the energy required to break the cluster into n monomers. This parameter is dependent on the cluster size and its orientation. Assuming that the binding energy of 6P-F_4 is in the range of 6P, values from Potocar et al. derived with molecular dynamics simulation on a 6P(001) surface can be used as rough estimation to answer the question of orientation.[21] The analysis of Potocar et al. revealed that small clusters with standing molecules of n < 4 are unstable, larger standing clusters of up to $n = 14$ are metastable, while the lying configuration is favored for up to 14 molecules. Their simulation was performed for the 6P(001) surface that exhibits only a weak molecule-substrate interaction. Transferred to the case of 6P-F_4 on ZnO($10\bar{1}0$) this means that with a stronger molecule-substrate interaction the lying molecules are even more favored due to a higher adsorption energy.[21] Therefore, stable island clusters with 4 or more 6P-F_4 molecules are most probably adsorbed in a lying state on ZnO($10\bar{1}0$) before they merge into standing islands at higher island sizes. As mentioned before the growth mechanism depends crucially on the temperature of the substrate as well as the growth rate. By plotting $\ln N$ vs $\ln F$ or T^{-1} the parameters χ or E_{n,i^*} can be directly extracted from the slope according to Eqn. 2.7. For 6P and 5A a bend of the slope at a critical point is described in literature, when going from low to high temperatures/growth rates, marking a crossover from attachment limited to diffusion limited aggregation for the investigated systems.[17,21,22,198] The explanation for this behavior is

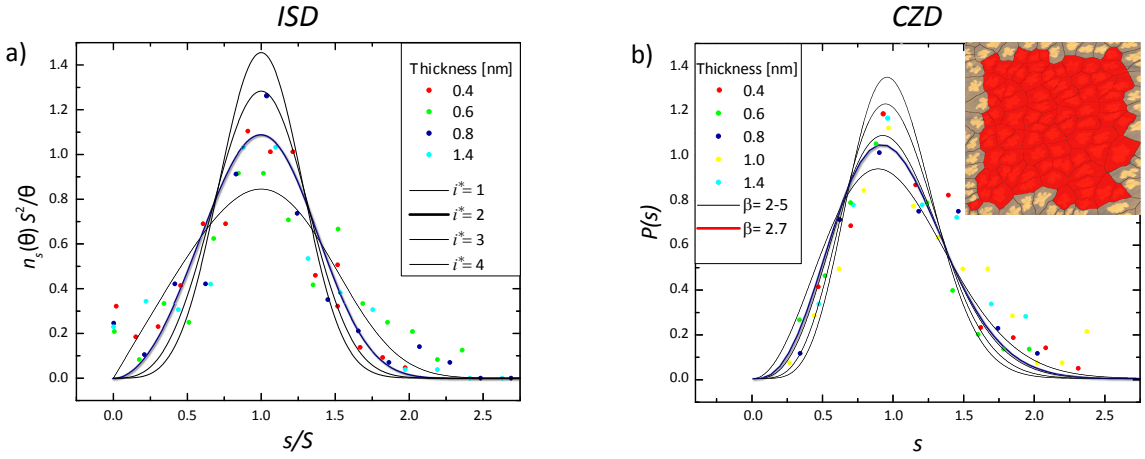

Figure 4.17: Derived ISD and CZD for various coverages of the 6P-F_4 film.

given by a critical temperature/growth rate, that is needed to overcome the attachment barrier for aggregation and transition from lying to standing formation. The crossover is also accompanied by a change of the islands shape from compact to dendritic, an indication for DLA. This change in shape is also observed in our case for 6P-F_4, which becomes more dendritic with temperatures of 100 °C (not shown). For 6P a transition was observed slightly above room temperature,[21,198] which also agrees with our measurements that show rather compact islands in the aggregation phase. Additionally Yang et al. proposed an explanation where at lower substrate temperature (< 60 °C) 6P molecules immediately freeze when they hit the surface (SiO_2) and form a metastable disordered film, which due to high surface free energy relaxes to an energetically more favorable state.[198] An alternative approach to describe aggregation is a model given by Winkler and Tumbek that includes the translational energy of the molecules while being adsorbed, which then remain in a hot precursor state.[206] To decide which processes are relevant for 6P-F_4 combined extensive temperature and growth rate dependent investigations have to be performed which are beyond the scope of this work. Those should be a prospect for further investigations especially with growth rate dependent processes, since this also introduces the possibility to determine the critical island size without knowledge of the actual aggregation scenario by the relation $\chi \cdot \beta = i^*$ as shown by Pimpinelli et al.[17]

All in all the experiments indicate that sub-ML growth of 6P-F_4 cannot be described within the framework of diffusion-limited aggregation with the wetting layer affecting the growth. Combining all so far obtained information, two scenarios are conceivable for the sub-ML growth of 6P-F_4 on ZnO: (1) A wetting layer grows and when it is completed, islands start to nucleate on top. The islands are composed of one layer of molecules which are considerably stronger tilted than in the bulk as the height of the islands is only 1.6 nm. (2) A WL grows and eventually, when a critical amount of molecules is deposited (supersaturation), it starts to transform into islands. The latter, representing the energetically more stable entities, consume the metastable WL in the course of the growth as schematically depicted in Fig. 4.14c. A similar picture has been invoked before for the growth of 6P on SiO_2 and Cu(110)$2 \times 1-$O as well as for Rubicene on SiO_2.[187,200,207] If (2) is valid, the tilt of the molecules in the first ML is similar to that in the bulk as the actual height of the islands is close to the XRD value of the lattice spacing d. Furthermore, scenario (2) is also in agreement with the conclusion that in the sub-ML regime 6P-F_4 cannot be described by a diffusion-limited aggregation process. AFM and post-growth XRD measurements do not provide sufficient information to finally decide the issue. The real-time XRD-measurements, however, also suggest that scenario (2) is appropriate.[133]

Eventually modifications of the 6P molecule by the introduction of two terminal local dipole moments evoke changes in the intermolecular electrostatic interactions. The resulting variations in the growth mode are discussed below. First of all the intermolecular interaction is connected with the crystal cohesive energy and hence different for fluorinated and unfluorinated species. Furthermore, the electrostatic field of the fluorinated 6P can be substantially altered due to the different exposed atoms of the flat-lying molecules. As a consequence, the surface diffusivity for molecules on the islands as well as the Ehrlich-

Schwoebel barrier, both critical parameters in a kinetically controlled growth process, will differ. An increase of the Ehrlich-Schwoebel barrier has been associated with increasing crystal cohesive and surface binding energies.[28] Our result of 6P-F_4 layer-by-layer growth therefore suggests that both cohesive as well as binding energies are reduced by terminal fluorination. However, theoretical input is required to verify the sign and to assess the magnitude of the change.

Modifications of the intermolecular electrostatic interactions are apparent in subtle changes of the bulk structure by a larger molecular tilt angle of 6P-F_4 determined by XRR measurements. This tilt angle has also been correlated to the magnitude of the Ehrlich-Schwoebel barrier.[20,208] For rod-like molecules, a larger molecular tilt has been related to a smaller step edge barrier since less energy is required to bend the molecule around an island boundary during its downward movement. This results in enhanced downward mass transport and thus facilitated layer-by-layer growth.[20] In the thin-film-phase close to the interface, a surface induced structure was resolved for 6P-F_4 by XRR. In the first three 6P-F_4 MLs, the molecular tilt angle changes gradually from more upright standing to slightly tilted. Therefore, one would expect the more upright standing surface induced phase to increase the Ehrlich-Schwoebel barrier and hinder layer-by-layer growth. However, this may be counterbalanced by better molecular diffusivity due to a lower surface energy. Its minimization is the driving force behind such a surface induced structure, so that for more upright standing molecules the surface energy is presumably lower than for tilted molecules found in the bulk phase of the film. A lower surface energy on top of the first monolayers leads to enhanced diffusivity of ad-molecules and therefore contributes to better layer-by-layer growth. This is verified by the AFM results revealing a morphological modification and substantial island density change between 1^{st} and 2^{nd} ML. Similar to the present case, a surface induced phase with more upright standing molecules has been correlated with layer-by-layer growth in the similar molecular system diindenoperylene.[209,210]

While the ML growth of 6P-F_4 proceeds via a WL, for 6P no indication for the presence of a WL was found. Nucleation of the second layer starts for both molecules when the ZnO surface is almost completely covered by islands and a roughening of the 6P film sets in only in the course of the growth of the second layer. The conclusion of this is that the WL has only a minor effect on the growth mode. Another difference is the coexistence of the β- and γ-phase in 6P films, while 6P-F_4 grows in a single phase. Grain boundaries occurring between different phases can act as nucleation sites for succeeding layers and thus cause roughening.

Conclusion

Combined *in situ* AFM and in situ real-time X-ray studies were applied to study the effect of chemical modification on the growth process and in particular the influence on molecule-substrate and intermolecular interaction were investigated. It was shown that terminal fluorination of 6P, does not change the molecules optical properties, but substantially influences the thin film growth mode on ZnO($10\bar{1}0$) for deposition at room temperature. While 6P grows in two different phases that build up in polygonal mound-like 3D structures with a rather rough surface morphology, 6P-F_4 exhibits an almost perfect 2D layer-by-layer growth with phase purity. This is schematically depicted in Fig. 4.18.

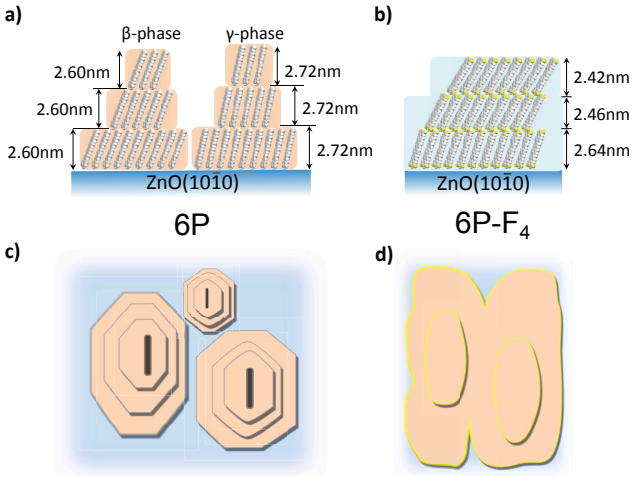

Fig. 4.18: Schematic side and top view drawing of a), c) the rough 6P growth with two different polymorphs and b), d) smooth 6P-F_4 growth with surface induced structure.

Additionally, 6P-F_4 shows a strongly surface induced structure with initially uniform shape and size but slight elongation of the islands in the 1^{st} ML, while shape and size are various in the 2^{nd} ML. Finally the nucleation process was described by island size as well as capture zone distribution. While ISD cannot adequately describe the aggregation of the fluorinated molecules, CZD can describe the nucleation process by attachment limited aggregation and a critical island size of $i^* = 3$.

6P-F_2

After a strong impact on the growth processes by symmetrical, terminal fluorination of 6P has been demonstrated in the preceding section, another fluorinated derivative of 6P will be analyzed in the following in its interplay with ZnO. This is the asymmetrical derivative 6P-F_2 on the non-polar ZnO($10\bar{1}0$) surface. By the fluorine modification of the sexiphenyl at just one end a significant permanent dipole moment is induced. This study aims to gain a deeper understanding of the effect of asymmetrically molecular modification in comparison to the pure 6P as well as the symmetrically fluorinated 6P-F_4. The growth behavior is characterized coverage dependent from sub-ML up to the 3^{rd} ML, as well as temperature dependent by *in situ* AFM, including Kelvin probe measurements. It can be shown that the growth morphology of 6P-F_2 differs greatly from 6P as well as from the observed 6P-F_4 structures and that 6P-F_2 features a characteristic island shape and preferential alignment, as well as a fundamentally different island density in the respective growth stages.Yet, as its related fourfold fluorinated 6P derivative, the asymmetrically substituted 6P-F_2 grows in a substantially smoother fashion on ZnO than the pure 6P. Furthermore, a striking difference between the first and the second molecular layer can be detected, indicating a strong interaction with the ZnO in the first ML, particularly apparent from Kelvin probe measurements.

The investigated films were grown in a tandem MBE system. ZnO wafers (CrysTec GmbH) were overgrown with a 100 nm thick ZnO epilayer by radical source molecular beam epitaxy at a base pressure of $1.0 \cdot 10^{-10}$ mbar using the standard procedure as described in Sec. 3.1. The substrate was kept at RT during the molecular deposition with constant values for the growth rates of 6P-F_2 between $\approx 1 \ldots 2.5$ Å min^{-1} for all measurements as monitored by quartz microbalance. The asymmetrically fluorinated derivative 6P-F_2 ($C_{36}H_{24}F_2$) was synthesized by Y. Garmshausen (Humboldt University of Berlin), as discussed in the introduction to this chapter. The deposition process was interrupted at different stages to analyze the growth of 6P-F_2 at successively higher coverages by UHV-AFM measurements, including Kelvin probe investigations. Fig. 4.19 compares such a layer of 6P-F_2 with the previously investigated 6P-F_4 of similar coverage. Noticeable in Fig. 4.19a is that the surface morphology of the fluorinated 6P-F_2 is considerably smoother (RMS $\approx$ 1.3 nm) than the unsubstituted 6P species ($\approx$ 3.2 nm, compare Fig. 4.12a) in the present regime. The same was already observed before in the case of the fourfold fluorinated 6P suggesting a fundamental effect of fluorination to tune the growth mode into a smoother fashion. In the depicted situation of Fig. 4.19a the first ML is already completely closed and islands of uniform height are observed, indicating nearly upright standing molecules. The 2^{nd} ML in Fig. 4.19a covers ca. 45 % of the surface, while also a small fraction (3 %) is covered with islands of 3^{rd} and higher MLs. Striking is a strongly anisotropic shape of the islands with an approximate aspect ratio of 2, which is in contrast to 6P-F_4 thin films, where the islands form compact and isotropic structures. This becomes especially apparent in direct comparison with 6P-F_4 films grown at the same conditions (cf. Fig. 4.19b). Furthermore, the 6P-F_2 islands appear to exhibit a preferential orientation, which is analyzed in an orientation map for the long axis of the island in Fig. 4.19c, with

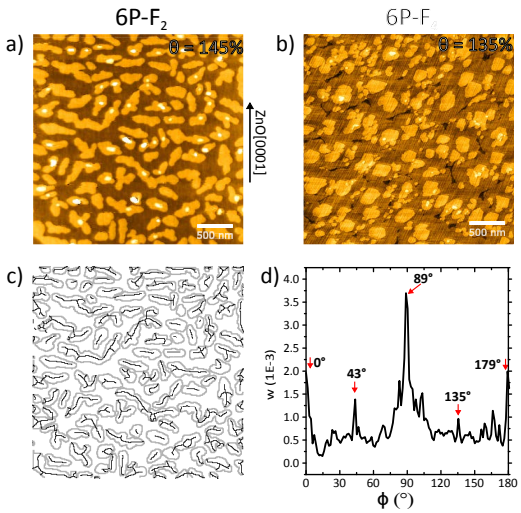

Figure 4.19: UHV-AFM scans (2.5x2.5 µm^2) of a) 6P-F_2 and b) 6P-F_4 films on ZnO(10$\bar{1}$0), with an c) orientation map for the 6P-F_2 film, exhibiting the island orientation through lines with the corresponding d) angular distribution.

an angular distribution graph in Fig. 4.19d.[16] The distribution reveals a preference for the islands to align their long axis predominantly parallel and perpendicular to the c-axis of the ZnO substrate. The slight deviation from perfect values is attributed to a misalignment of the scan direction. Beside the main peaks some minor peaks at around 45° and 135° are present. This preferential alignment even in the 2^{nd} ML could be ascribed to an anisotropic diffusion induced by the electrostatic surface field of the substrate as it is observed also for 6P.[70] However, the asymmetrically fluorinated molecule behaves fundamentally different than pure 6P and 6P-F_4 as it exhibits an anisotropic alignment in the islands of standing molecules.

To understand the underlying growth processes of the asymmetrically fluorinated 6P-F_2 now a closer look at the film during growth is taken by tracing the sub-ML film evolution of 6P-F_2. A series of *in situ* AFM topographies as a function of coverage Θ is presented in Fig. 4.20. The initial growth interruption with a low coverage of $\Theta = 9$ % (nominal thickness of 0.5 nm) exhibits small isotropically distributed islands, which neither show a distinct preferential growth direction nor any kind of ordering. However, they are not completely shapeless and already feature some elongation. Striking is the comparable high nucleation density of approximately 30 islands/μm^2, which indicates a low diffusion coefficient D.[21,22,183] The nucleation phase, defined by an increasing nucleation density further progresses approximately until around $\Theta = 25$ % substrate coverage, as pictured in the second AFM snapshot in the set of Fig. 4.20. This image reveals a peculiar, irregular branched shape inherent in the islands. Here, the respective branches of the islands appear already aligned at this point. For layer-by-layer growth the next phase is the aggregation. It is defined by a constant nucleation density, where the islands generally

16 Here, also the branches of the islands are considered as distinct orientation, which would be otherwise neglected in a conventional directional distribution evaluation procedure.

keep their characteristic shape and arriving molecules are exclusively incorporated through the capture zones of existing islands. Thus, the islands just grow laterally until they finally coalesce as seen in the last two panels in Fig. 4.20. This coalescent regime, where the islands merge, is eventually accompanied by a decrease and drop to zero of the island density for the respective ML. The shape and growth mode of the first molecular layer on the foreign substrate can reveal fundamental details about intermolecular versus molecule-substrate interaction and energetics at the phase boundaries. First, the uniform island height of nearly a molecular length and complete closing of the first ML indicates that also the asymmetrical fluorination induces a strong change of basic parameters, which result in an improvement of the growth mode on a macroscopic scale. This suggests that molecules arriving on top of already pre-existing islands are nearly instantaneously incorporated at the island edge by inter-layer processes. This can be due to an improved diffusivity of the molecules on the islands. At constant substrate temperature the diffusion is mainly described by the attempt frequency ν_0 of the molecules and the energy barrier for diffusion E_D, according to Eq. 2.2. Also a lowering of the Ehrlich-Schwoebel barrier E_{ES} at the islands edges could result in an enhanced step-down diffusion. Additionally, the very high island density already at the initial nucleation step seen in Fig. 4.20 is a factor for an improved smoothening and can be the reason for a layer-by-layer growth. This is because for the smaller islands molecules on top get to the edge more often and therefore reach the underlying layer with a higher probability, while at the same time the probability for multiple molecules to form nuclei on the islands and contribute to a roughening is significantly decreased. Furthermore, the emerging islands appear to exhibit a dendritic character, but are not completely dominated by random diffusion processes which would otherwise lead to a complete fractal growth as is the case in diffusion limited aggregation. Beyond that it is not clear what the underlying reason for the high island density compared to the pure 6P is, however, its high value suggests a lower diffusivity (cf. Eqn. 2.7) on the substrate surface. A reason could be the permanent dipole moment, resulting from asymmetrical fluorination, which alters the molecule-substrate interaction. The high island density could be attributed in an altered value and especially small number of molecules needed to form a stable island, namely the critical nucleus size i^*.

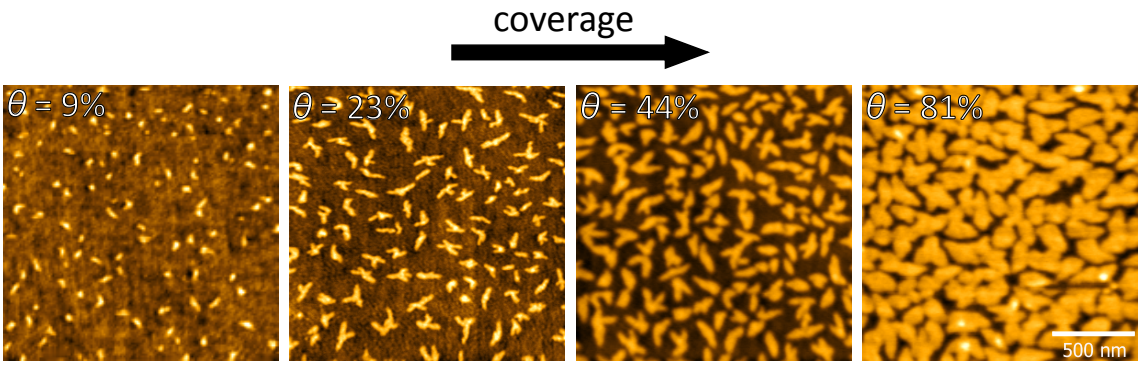

Figure 4.20: UHV-AFM snapshots (2x2 µm^2) of the 1st ML of 6P-F_2 of increasing coverage.

As for 6P-F_4 before to get a deeper insight into nucleation at the aggregation regime the critical island size is determined. We will follow the approach of Pimpinelli and Einstein using the Wigner surmise to evaluate i^* from capture zones, as it turned out to be the more fitting method than the island size distribution and furthermore principally capable to describe any aggregation-limiting process. In Fig. 4.21 the histograms of increasing coverage are plotted with $\beta = 2-3$ of the distribution function of the GWS. Additionally, a fit to the data using the least squares method with the Levenberg-Marquardt algorithm is given, resulting in a value of $\beta = 1.6$. From the high island density on one side and the apparent anisotropy of the islands seen in the AFM scans it can be concluded that the growth mode is attachment limited, so that for determining the critical island density $\beta = (i^* + 3)/2$ is used. This, however, yields a value of ≈ 0, meaning that already one molecule forms a stable nucleus. This is unusual, but it reflects the finding of the especially high island density in the first ML, being five times as high as for 6P-F_4 and is similar to the value of $i^* = 1$, Zykov estimated for the 2^{nd} ML of 6P-F_2 on SiO_2.[202] Assuming a similar energetic landscape as for 6P the binding energy clearly favors lying molecules for a small cluster size as shown by Potocar et al.[21]

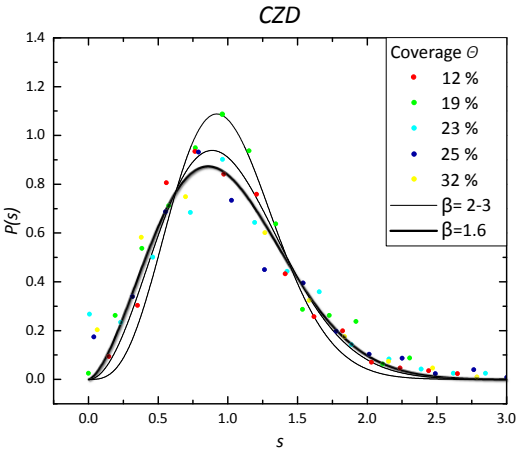

Fig. 4.21: Derived CZD of 6P-F_2 for various coverages.

According to Eq. 2.7 the island density can moreover be described as a function of the deposition rate by a power law. Hereby, it is possible to unambiguously determine the critical island density independent of the growth mode by the product of $\beta \cdot \chi = i^*$ as shown by Pimpinelli et al. in Ref. [17]. While β can be determined as in the preceding section by the scaling assumption, the exponent χ is obtained from the slope of plotting $\ln N$ vs. $\ln F$. The exponential term in Eq. 2.7 additionally shows a dependence of the substrate temperature for the island density that exhibits an Arrhenius behavior by plotting $\ln N$ vs. $1/T$, which then basically makes it possible to determine the nucleation energies E_{n,i^*} in Eq. 2.7 and the attempt frequency ν_0.[21,22,198,202] Therefore, by varying temperature or growth rate more detailed information about the underlying growth processes can in principal be obtained. For rod-like molecules growth/temperature dependent experiments for instance, revealed a transition of different growth modes, from attachment limited at low temperatures/growth rates to diffusion limited aggregation at higher temperatures.[17,21,22,198,206] This critical temperature at the crossover is needed to overcome the attachment barrier, which also was accompanied by a morphological change of the islands from compact to dendritic. Figs. 4.22a-d show selected AFM scans of 6P-F_2 on ZnO($10\bar{1}0$) as a function of the substrate temperature for a temperature range from

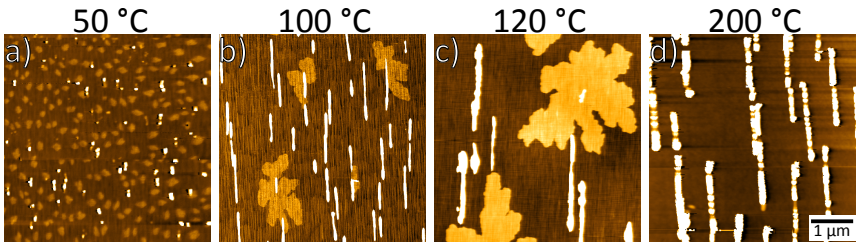

Figure 4.22: AFM scans (5x5 µm^2) for 6P-F_2 on ZnO(10$\bar{1}$0) of increasing temperature from a) 50 °C, b) 100 °C, c) 120 °C to d) 200 °C.

50 °C−200 °C for a similar nominal thickness.[17] The growth at room temperature was discussed before and revealed small branched islands of standing molecules with a high island density. At 50 °C a second growth mode emerges. Alongside small compact islands, still exhibiting a high island density, needles of around 15 nm height appear that are slightly aligned along the c-axis of the ZnO(10$\bar{1}$0) surface (Fig. 4.22a). Those further develop with increasing temperature by growing larger and in greater number, while the islands become fewer but bigger and more dendritic at 100 °C (Fig. 4.22b). This tendency continues for a temperature of 120 °C, where the islands become even bigger, exhibiting a greater fractality (Fig. 4.22c). Eventually at 200 °C the same scenario as for high temperature growth of unsubstituted 6P is observed, when only aligned needles are found. This evolution with increasing temperatures shows two different things: For one, the evolution of the islands is reversed for increasing temperatures compared to the classic atomistic DLA model, where fractal islands initially form at low temperatures. By the higher energy barrier of step edge diffusion than adatom diffusion, the deposited adatoms diffuse until they hit and stick onto an aggregate. Fractals then transition into dendritic and finally compact structures for increasing temperatures where the adatoms relax into an energetically more favorable configuration.[14] The reversed trend which is observed here for molecules, however, is well-known also for other rod-like molecules like 6P and 5A. They exhibit an attachment limited growth mode at low temperatures, evoked by the kinetics during critical nuclei formation.[21,206] Two mechanisms are discussed in literature for being responsible for this behavior. Yang et al. described the growth of 6P on the SiO_2 surface by immediately freezing molecules in a metastable disordered film.[198] By reorganization of this film ordered compact islands are formed. For higher temperatures molecules would then start to diffuse along the island edges and on the surface, while surface diffusion would be favored due to the lower energy barrier, so that fractality increases with temperature accompanied by a decrease in island density and increase in island size. In contrast Potocar et al. claim a high attempt frequency for 6P and hence no freezing and proposed that the anisotropic, rod-like molecules form compact island due to steric constraints of the molecules which diffuse along a preferential direction parallel to their long axis and only bind when parallel to each other.[21] In this scenario a supersaturated monomer gas phase is assumed wherein

17 The nominal thickness is approximately 1 ML for 50, 100 and 120 °C and approximately 2 ML for 200 °C

stable clusters of first lying and then standing molecules would form, which then facilitate incorporation of further molecules, leading to growth of compact islands. Aside from the formation of islands, however, our case shows secondly the formation of needle like structures on the ZnO($10\bar{1}0$) surface. This is induced by the electrostatic peculiarity of the ZnO($10\bar{1}0$) surface, which promotes anisotropic diffusion along the [$1\bar{2}10$] direction. With rising temperature the diffusion, which follows an Arrhenius-like law, also increases so that the formation of needles along [0001] become energetically more favorable. As a result, the common model to evaluate fundamental growth parameters out of temperature dependent experiments is not applicable in this case. Obviously the growth is in a way influenced by the strongly interacting substrate that the ordinary applied model fails here as 6P derivatives generally transitions to needle like growth at higher temperatures.

In the following the structural evolution of 6P-F_2 on the ZnO($10\bar{1}0$) surface is investigated also beyond the 1^{st} ML by *in situ* AFM snapshots during growth interruptions of increasing layer thickness. By this the evolution of the MLs is traced and the interaction with the substrate can be evaluated. The coverage dependent series of selected AFM scans is displayed in Fig. 4.23, evaluated together with surface coverage and island density evolution for the respective ML. The AFM scans (Fig. 4.23a) show very detailed the evolution from closing of the 1^{st} ML, progressing coverage of the 2^{nd} ML and an emerging 3^{rd} ML of small islands up to a coverage of 170 %. The corresponding coverage and island density evolution is given in Fig. 4.23b and c. In the coverage plot it can be reproduced how the first layer closes almost completely before growth of the 2^{nd} layer begins. The islands in the first layer exhibit, similar to 6P-F_4, heights of about 1.6 nm (cf. Fig. 4.23a), indicating again a WL. Further examinations of the AFM scans indicate that first nucleation of the 2^{nd} ML sets in at 80 % coverage, although a significant amount is only noticeable over 90 %. In this aspect the derivative 6P-F_2 behaves very similar to the smoothly growing fluorinated 6P-F_4. Fig. 4.23c, however, shows that in strong contrast to the symmetrically fluorinated 6P-F_4 the island density exhibits an instantly very high value in the 1^{st} ML. The peaking value is around 35 µm^{-2} compared to the low island density of 6 µm^{-2} for 6P-F_4. As discussed before the island density in the 1^{st} ML is most likely associated with the substrate interaction. Apart from that, the change of the permanent dipole moment of 6P-F_2 can also strongly influence the intermolecular interaction and by this induce a distinct change of the growth mode. A modification of the interaction between molecules and substrate by the asymmetric fluorination affects the diffusion on the surface in any case, evoking a higher diffusion barrier, which in turn is also the reason for the exceptional small critical island size. Nevertheless, this high island density does not exclude the single layer growth and may even promote it due to a smaller diffusion area on top of existing islands, which results in an increased interlayer transport rate. After the peaking value is reached, coalescence begins at a coverage of around $\Theta = 40$ %, which is accompanied by a drop in the island density. The coverage evolution of the 2^{nd} ML proceeds with a similar steep slope than the 1^{st}, implying again a steady closing of this layer. The island density of the 2^{nd} ML on the other side (Fig. 4.23c) exhibits an initial bump, where the first small islands form, with a value of 3 µm^{-2}. The subsequent aggregation reaches a value of 17 islands/µm^2.

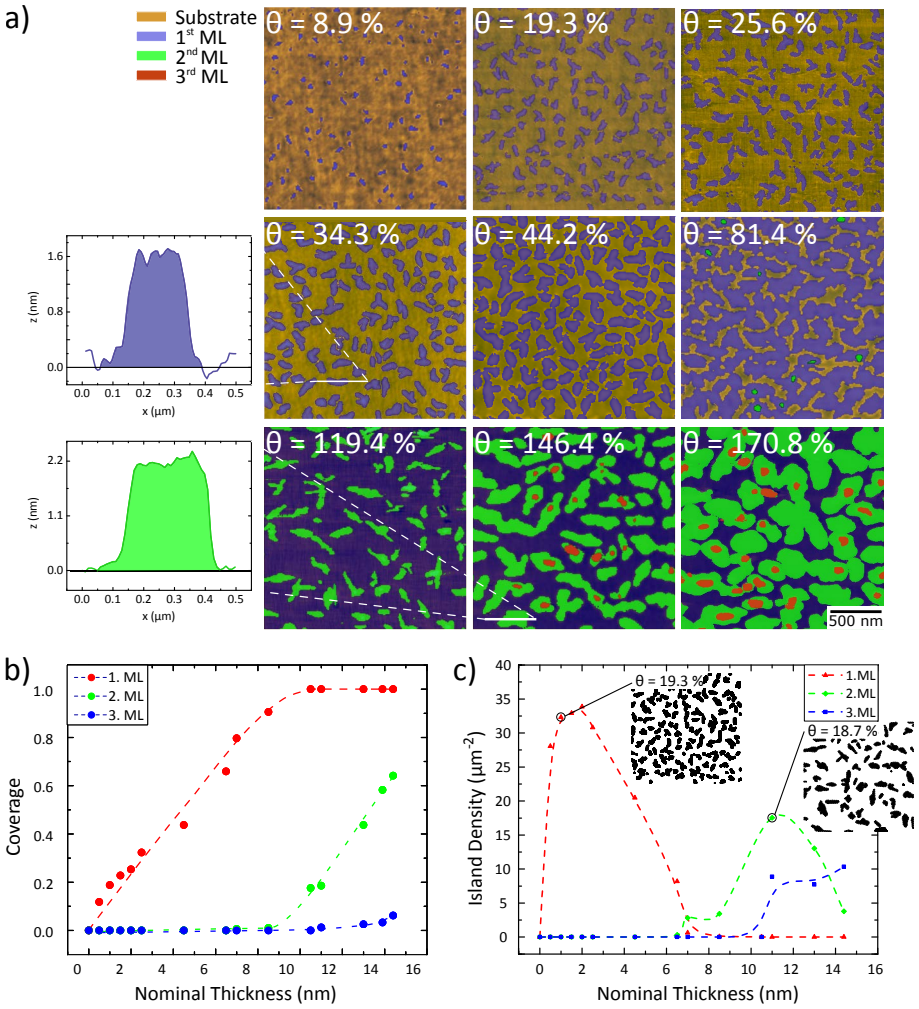

Figure 4.23: a) UHV-AFM snapshots (2 x 2 µm^2) of 6P-F_2 on ZnO(10$\bar{1}$0) with increasing coverage. Line profiles of selected scans are shown. The substrate, 1^{st}, 2^{nd} and 3^{rd} ML are highlighted in brown, blue, green, red. Nominal Thickness dependent plot of the respective MLs show b) coverage and c) island density. Contour images for equal ML coverage are derived from AFM scans.

In contrast to the 1^{st} layers island density the absolute value of the 2^{nd} ML is similar to 6P-F_4, indicating a fundamental difference of the molecules in interaction with the substrate. The 3^{rd} ML provides a slightly different picture. Nucleation sets in at a rather early phase and first islands can already be observed when the 2^{nd} ML still nucleates (Fig. 4.23b). For the final layer thickness the coverage still stays under 5 %, however, a quite high island density is present already for those low coverages and indicates a constituting roughening of the surface and a disruption of the ideal layer-by-layer growth with increasing thickness (Fig. 4.23c), which is also reflected by a steady increase of the RMS to $\approx$ 1.3 nm (versus 0.9 nm for 6P-F_4). The lower island density in the 2^{nd} ML reflects the diffusion on the weakly interacting molecule surface now strongly enhanced compared to diffusion on the

interacting ZnO surface. Thus, by a lower diffusion length the formation of bigger and overall less islands is facilitated. A similar finding of a lower island density in the 2^{nd} ML due to an improved diffusivity was made by Zykov with the system 6P-F_2 on silicon oxide and by Frank et al. for diindenoperylene on silicon oxide, where the activation energy was found to be 100 meV lower for the 2^{nd} layer.[202,210] Moreover, the model of hot precursor aggregation was discussed by Zykov for 6P-F_2, explaining the different island densities for substrate and molecular surface with a change in the dissipation coefficient from hard and soft material.[202,206] This coefficient is related to the amount of post-adsorption kinetic energy present in the molecule, the so-called hot precursor state before it equilibrates to the surface temperature.[206] If such a hot precursor state is existent in molecular growth is still topic of on-going discussion. A method to account for its existence is temperature dependent investigations of the island density, deviating from the usual straight line in an Arrhenius plot, which is expected for a pure DLA growth from Eq. 2.8. Unfortunately since the interaction with the ZnO($10\bar{1}0$) surface leads to the formation of needles at higher temperatures, the possibility to answer this question is hampered in this case, but should be a object of further investigation. To do this, growth on ZnO(0001) should be performed temperature dependent, since the aligning force of the substrate surface should not be present there.

At last 6P-F_2 and 6P-F_4 are compared regarding the evolution of the electronic surface during organic film growth on the ZnO surface. Energy level alignment across the interface between organic and inorganic semiconductor is crucial in respect of designing efficient hybrid devices. This can be achieved by introducing a molecular dipole perpendicular to the surface, inducing a substantial work function shift by an electric dipole layer.[211,212] This has been shown using aligned self-assembled monolayers, which tune the work function of ZnO in the range of some eVs.[212–215] The shift of the work function due to the dipole moment μ of the molecules is given by Helmholtz equation:[215]

$$\Delta\Phi = -\frac{e\mu \sin\alpha N}{\varepsilon_0 A}, \tag{4.2}$$

with the molecular tilt angle α, the number of dipoles per area N/A and a reduction factor k_{red}, accounting for a depolarization by an interaction between the dipole moments of densely packed molecules. Assuming a similar structure for 6P-F_2 as for 6P a tilting angle of $\alpha = 70\%$ and $N/A = 4\ nm^{-2}$ with a dipole moment of $\mu = 2.86$ yields a work function change of about 4 eV for no depolarization ($k_{red} = 1$). This value, however, lies far above all so far reported values. Thus, the real effect on the work function in the case of the fluorinated 6P species will be measured, also illuminating the orientation of the asymmetrically fluorinated 6P. Here, the terminal fluorine atoms of the molecule can be aligned altogether in one direction, arranged alternating or be completely random. This is done by simultaneously measuring the local work function alongside non-contact AFM by Kelvin probe force microscopy. Hereby, the contact potential difference (CPD) between substrate and the respective layers can be determined. The results are shown in Fig. 4.24.

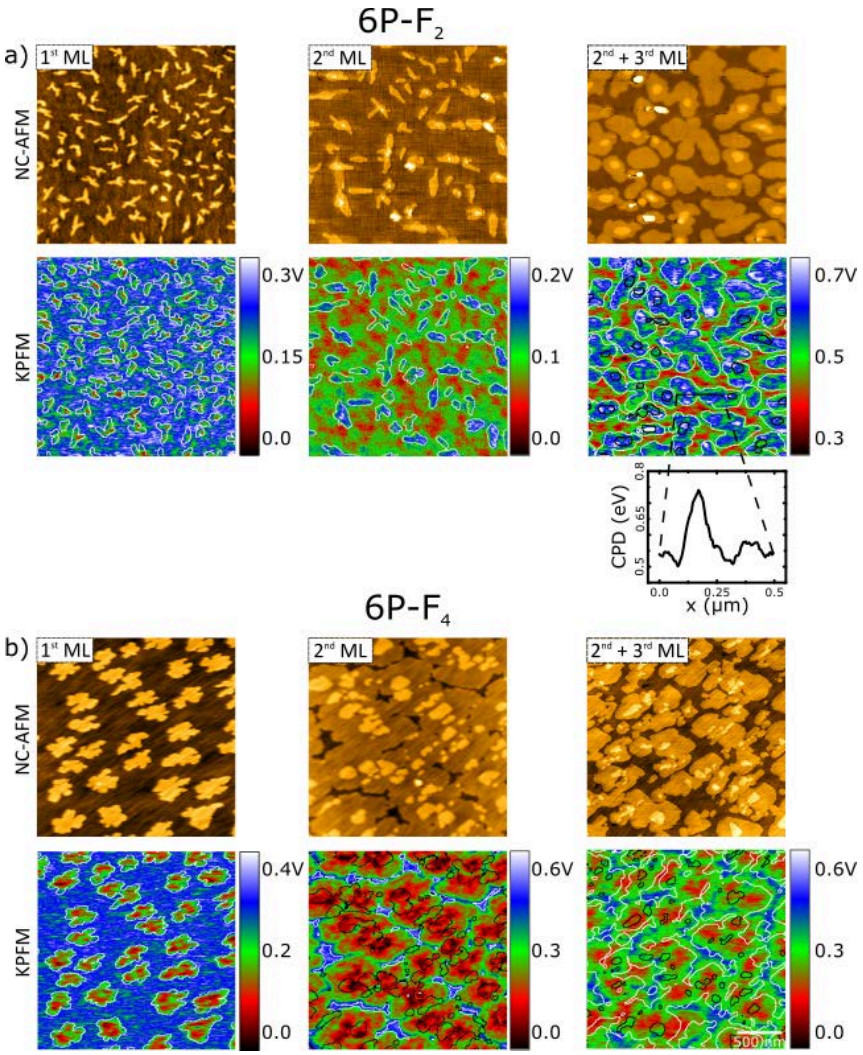

Figure 4.24: Topographic UHV-AFM (top) and KPFM (bottom) snapshots (2 x 2 µm^2) of a) 6P-F_2 and b) 6P-F_4 on ZnO($10\bar{1}0$) of increasing coverage.

Initially a Kelvin measurement of the pure ZnO substrate was done and compared with seemingly uncovered space between molecular islands (not shown), yielding a $\mathrm{CPD}_{ZnO-Mol} = -400$ meV, indicating a wetting layer of molecules. The topographic image (top) of 1^{st}, 2^{nd} and beginning 3^{rd} ML of the respective molecular film is given with the simultaneously obtained KPFM images (bottom). In the KPFM images the topographic edges of the molecular islands are overlayed for better recognition. The KPFM image of the 1^{st} ML of the 6P-F_2 film in Fig. 4.24a exhibits a clearly visible CPD between the substrate surface and the molecular aggregates, which can well be correlated with the topographic image. The molecules introduce a downward shift of approximately $\Delta\phi = -150$ meV in the first layer. The second pair of SPM images in the middle exhibits the 2^{nd} ML of the 6P-F_2 film on top of the 1^{st} layer. Remarkably, also the molecular islands of the 2^{nd} layer can be distinctly recognized in the KPFM image and show a potential difference of $\Delta\phi = +80$ meV.

However, the transition between islands of the 2^{nd} and 3^{rd} layer is hardly distinguishable anymore in the Kelvin signal as seen in Fig. 4.24a on the right. Still, by investigating the molecular structure within an island of those layers it appears that strong variations exist, as can be seen in the line profile below the KPFM image. It shows that in an island of the 2^{nd} ML the CPD fluctuates between 0.5 and 0.7 eV. Furthermore, domains of equal work function inside an island are visible. Yet, they seem not to be correlated to the 3^{rd} layer islands which are seen in the topography image above. On the other side the symmetrically fluorinated 6P-F_4 shows a CPD of around $\Delta\phi = -300$ meV at the topographical locations of the islands in the 1^{st} layer, which are also well distinguished in the Kelvin signal (Fig. 4.24). The KPFM image in the middle shows islands of the 2^{nd} on top of the 1^{st} 6P-F_4 layer, which in contrast to 6P-F_2 molecule are indistinguishable from the underlying layer. Then, however, with the overlying 3^{rd} layer the Kelvin signal shows no real correlation to the morphological image anymore.

Ruling out charge transfer or chemisorption the above observations can be explained with two possible mechanisms:[196,216] The organic layer either changes the work function of the surface by pushing back the electron cloud of the inorganic semiconductor. Alternatively for polar molecules the inorganic/organic interface is affected more directly by the charges of the molecule, which create a large interfacial dipole and induce a shift in the work function. The former is what is likely happening in the 1^{st} layer of the symmetrically 6P-F_4, which does not exhibit a permanent dipole moment, but still induces a significant change in the work function. However, also the local dipole moment at the end group of the molecule could induce this change. In any case, the vacuum level is reduced with adsorption of the 1^{st} layer organic layer, while the following layers do not further change their value. What can be seen in the mid-image of Fig. 4.24b is that grain boundaries at the locations where the islands grow together are resolved also in the Kelvin probe scans. This is also the reason why strong potential differences can still be seen in the right image of Fig. 4.24b, stemming from the grain boundaries of the closed first layer. In the case of asymmetrically fluorinated and thus polar molecule 6P-F_2 the second mechanism is the prevalent one. However, the magnitude of the change is much lower than expected. Reason for this can be the initial formation of the wetting layer of molecules which reduce the Vacuum level by 400 meV, but also acting as a buffer layer, so that the 1^{st} layer of standing molecules only introduce a small shift of another 150 meV, which may also be smaller than for 6P-F_4 due to orientational fluctuations. Conceivable is also that the 150 mV are in reference to the WL, resulting in an overall change of 550 mV. Still the islands in the 1^{st} layer exhibit an overall uniform value for the CPD, suggesting a preferential alignment of all molecules with the fluorine atoms pointing downwards indicated by the downward VL shift.[217] A preferential alignment also seems to be present in the 2^{nd} layer with the molecules now aligned the other way round, albeit with a weaker effect and as the line profile suggests, flipped domains exist inside the islands, while in the 3^{rd} ML the aligning character seems to be lost. A possibility to further identify the actual ordering of the 6P-F_2 molecules would be by using HRTEM and distinguish between different intensity patterns of the lattice planes as theoretically shown by Kirmse et al. with image contrast simulations.[218]

Conclusion

The effect of chemical tuning on growth mechanisms using a molecule with local and permanent dipole moment was analyzed in this study by *in situ* AFM investigations. For this, the model system of the rod-like 6P molecule was taken and modified by fluorination, resulting in the derivatives 6P-F_2 and 6P-F_4. Those were compared in respect to their growth mode on the non-polar ZnO($10\bar{1}0$) surface and their influence on the electronic interface, which was studied by Kelvin measurements. A series of *in situ* AFM scans of 6P-F_2 with increasing coverage, revealed an essentially different growth than for the unsubstituted 6P species as well as the fluorinated 6P-F_4, reflecting the asymmetry of 6P-F_2. In the 1^{st} layer branched and partially aligned islands with an island height of 1.6±0.2 could be observed. The island density turned out to be five times as high as for 6P-F_4, being indicative for a small diffusion coefficient. The determination of the critical island size additionally showed that one molecule was found sufficient to form a stable nucleus, explaining the high island density

In the subsequent layers the island density strongly decreases and took similar values as for 6P-F_4, indicating a higher diffusivity on top of the islands. However, already above the 2^{nd} layer the formation of needles set in, resulting in a noticeable roughening. Still the growth was shown to be in general much smoother than in the case of the unsubstituted 6P, but not as smooth as for the symmetrically fluorinated 6P-F_4. Also, temperature dependent investigations showed a gradual formation of broader but fewer islands and emergence of needles with higher temperature. The only other study with 6P-F_2 to date is the mentioned investigation on silicon oxide by Zykov.[202] In direct comparison with the molecule 6P Zykov found a similar smoothening in the 6P-F_2 films by an order of two as a result of increased interlayer transport. However, in contrast to the observations here the molecules grew similar to 6P on the silicon oxide substrate and independently of temperature and growth rate in islands of roundish shape. Furthermore, despite the finding of a seven orders of magnitude higher attempt frequency, the overall diffusivity added up to be lower due to a smaller diffusion barrier than 6P. This was in any case qualitatively observed here too.

Eventually, Kelvin probe scans of both fluorinated molecules for different coverages were compared. The two molecules showed a distinct difference in this investigation as well. Where the symmetrically fluorinated 6P-F_4 only featured a single decrease of the vacuum level in the 1^{st} layer by 300 mV associated with the push-back effect, the electronic structure is modified differently for the asymmetrically fluorinated 6P-F_2 film. Here the permanent dipole moment of the molecule leads to the formation of an interface dipole layer and a general preferential orientation with the fluorine atoms pointing downwards in the 1^{st} layer, resulting in a decrease of the vacuum level by 150mV. Additionally an initial lowering of the vacuum level by 400 mV indicated a WL. Counter-intuitively in the 2^{nd} layer the molecules exhibit a preferential orientation now with the fluorine atoms pointing upwards with an average increase of the vacuum level by 80 mV, whereas also domains of different CPDs inside the islands can be seen. The results of this are schematically summarized in Fig. 4.25.

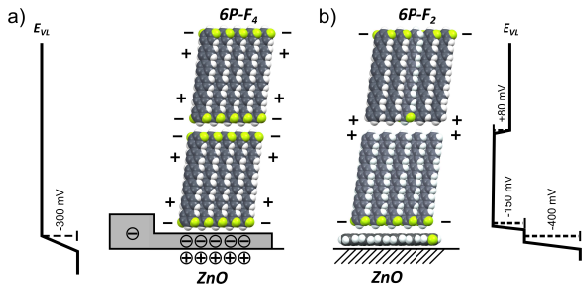

Figure 4.25: Schematic depiction of a molecular dipole layer for a) 6P-F_4 showing the push-back effect and b) for 6P-F_2 interface dipole layer.

4.4 Growth of ZnO/6P/ZnO Hybrid Stacks

A prerequisite for highly efficient inorganic/organic based optoelectronic devices is not only to control the growth of molecules on inorganic semiconductors, but also to be able to grow inorganic overlayers on top of the organic without impairment. With this hybrid light-emitting diodes become feasible where charge carries are injected from the inorganic to the color-tunable organic emitters.[10,147,219,220] For photovoltaic applications, on the other hand, organic/inorganic semiconductor heterointerfaces serve for exciton dissociation and charge separation. In Sec. 4.3.1 the control of orientation and morphology of 6P by different ZnO surface terminations and growth temperatures was discussed. Here, the growth of hybrid stacks consisting of embedded submonolayers of 6P nanocrystals in ZnO is studied for differently terminated substrate surfaces and analyzed in depth by cross-sectional High Resolution Transmission Electron Microscopy. Studies of organic thin films by cross-sectional HRTEM are scarce in literature as a consequence of the challenging specimen preparation of the fragile organic material.[221–225] Images with molecular resolution were only achieved for diindenoperylene before, however, simultaneous imaging of structural details of the inorganic material were not possible due to the thickness of the sample.[222] Here, this could be routinely achieved by using ultramicrotomy, where lamellae of a thickness down to 25 nm can be prepared. Hence, this study provides an unprecedented view on the embedded molecular layer and the inorganic surrounding. The HRTEM images give in-depth information on details of the crystalline structure, lattice defects, material interdiffusion, and homogeneity of the interface but could also resolve the structure of the ZnO overlayer.

Accordingly this section is divided in a part focusing on the resolution of the crystalline structure of organic 6P nanocrystallites in a ZnO hybrid stack by cross-sectional high-resolution TEM, while a second part discusses the texture and morphology of the ZnO Top Layer (TL).

The results on the structural analysis of the grown ZnO/6P/ZnO hybrid structures have been published in Refs. [135] and [134]. The study was performed in close cooperation with H. Kirmse, F. Polzer, E. Öhlschlegel, who did TEM imaging, image contrast simulations and ultramicrotomy preparation (for details of this see Ref. [132]) as well as A. Zykov and S. Kowarik who did X-ray diffractometry.

4.4.1 Structure of 6P Nanocrystallites

ZnO, which served as substrate for 6P growth in the preceding investigations is used here again in the making of hybrid stacks, consisting of a ZnO bottom and top layer with embedded 6P nanocrystallites. This layout is chosen due to the exceptional property of ZnO to grow epitaxially practically at room temperature, where other inorganic semiconductors are typically grown at substrate temperatures of several hundred degrees centigrades.[12] Thus, only just the low temperature growth of ZnO makes it possible to overgrow organic material without impairing the crystal structure of the organic. Also, though ZnO epitaxy requires highly reactive atomic oxygen to proceed, it was shown before that optical properties of organic molecules (using a spirobifluorene derivative) remain unchanged upon overgrowth.[226] Beside the integrity of the organic inclusion the interfaces of such a hybrid stack are vital, too. To visualize the embedded 6P nanocrystallites cross-sectional high-resolution TEM combined with image contrast simulations is performed, while X-ray diffraction measurements are done to determine the crystalline structure. For preparation ultramicrotomy is the method of choice to preserve the organic structure, which would be otherwise amorphized by the standard Focussed Ion Beam (FIB) milling preparation.[132] Additionally, to be able to identify respectively atomic and molecular structure of the hybrid interface and the organic inclusion, different focus conditions have to be applied, as will be discussed below. The results of this study have been published in Ref. [135] before.

The surface used for studying the organic crystallites and the interfaces of the hybrid is the non-polar ZnO($10\bar{1}0$), as the morphology of the 6P layer can be determined by the growth conditions as shown before. To provide a pristine surface for 6P deposition the ZnO wafers (CrysTec GmbH) are overgrown with a ZnO layer (100 nm) using the standard growth protocol (→ Sec. 3.1). A 6P layer with a nominal thickness of 10 nm is grown with a deposition rate of 0.1 nm/min and at a substrate temperature of 100 °C on the Bottom Layer (BL). At this substrate temperature the 6P molecules arrange in needle like crystallites, oriented with the long axis along ZnO[0001]. Finally, an embedding ZnO Top Layer (TL) of 30 nm is grown at a substrate temperature of 100 °C using the low temperature growth protocol.[100] The corresponding sample layout is schematically depicted in Fig. 4.26a. In Fig. 4.26b an AFM scan shows the morphology of the overgrown molecular layer. The expected aligned needle-shaped 6P aggregates are still visible when overgrown with ZnO. The average height of the needles accounts to 15 nm as seen in the

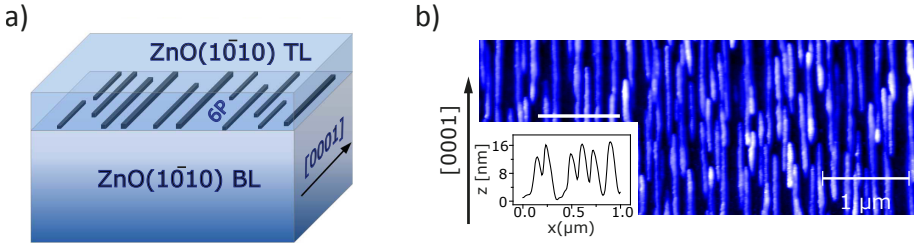

Figure 4.26: a) Sample design of a hybrid stack on a ZnO($10\bar{1}0$) template consisting of a ZnO BL, 6P molecules arranged in needle like crystallites and a ZnO TL b) Surface morphology of the hybrid stack acquired by AFM with a height profile as inset taken along the white line.

line profile in Fig. 4.26b. For determining the crystalline structure of the hybrid stack XRR and rocking curve scans are performed (cf. Fig. 4.27a). In XRR, the intensity of the specular reflected X-ray beam is measured as a function of the scattering vector q_z, giving information about the out-of-plane crystal structure. To analyze the mosaicity, *i.e*, the general angular disorder of the 6P crystallites, rocking scans are performed for two orthogonal azimuthal directions. Opposed to XRR measurements, the detector is fixed at a specific Bragg angle for rocking scans while the specimen is tilted.

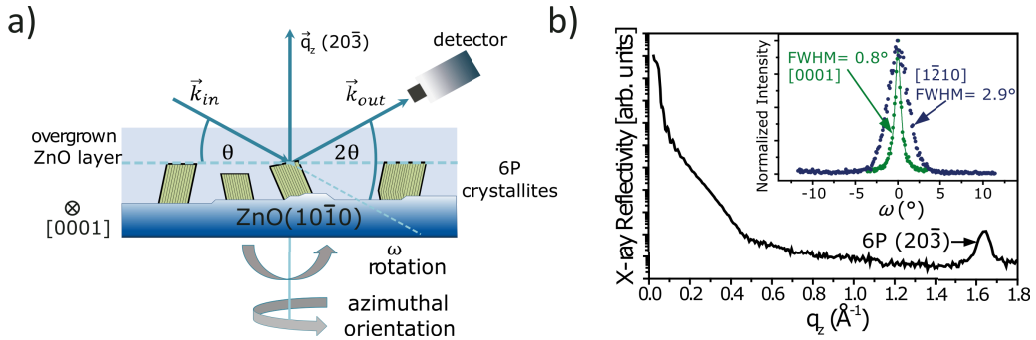

Figure 4.27: Crystalline structure of a ZnO/6P/ZnO hybrid stack. a) Measuring geometry of X-ray rocking scans and schematic depiction of the sample geometry. b) X-ray reflectivity and rocking scans (inset) of the 6P(20$\bar{3}$) Bragg reflection along ZnO[0001] (green) and ZnO[1$\bar{2}$10] (blue).

The results of XRR and rocking curve scans are shown in Fig. 4.27b. A Bragg reflection at $q_z = 1.64$ Å^{-1} is detected which corresponds to the 6P(20$\bar{3}$) lattice plane. This shows that ZnO overgrowth is not influencing the integrity and high structural perfection of the embedded nanocrystallites. However, the two polymorphs of 6P cannot be detected here as the distance between (20$\bar{3}$) lattice planes in the β- and γ-phase is very similar. Still, the XRR data gives additional information in the initial oscillations in the low q_z range of Fig. 4.27b, known as Kiessig fringes, which can be used to determine the thickness of thin films. The acquired thickness corresponds to the nominal ZnO TL, indicating a conformal overgrowth. The (20$\bar{3}$) Bragg reflection is furthermore used to study the mosaicity in rocking scans as depicted in Fig. 4.26a and inset of Fig. 4.26b. It shows that the mosaicity along ZnO[0001] is considerably smaller than along the perpendicular [1$\bar{2}$10] direction. This can be explained by the corrugation of the ZnO$(10\bar{1}0)$ characterized by elongated terraces along the ZnO[0001] direction separated by several monolayer deep trenches (cf. Fig. 4.6c). This leads to 6P nanoaggregates which adopt the structure of the ZnO bottom layer and are therefore exhibiting a tilt in the [1$\bar{2}$10] direction as schematically depicted in Fig. 4.26a. Hence, a larger width of the rocking curve is found in this direction as compared to the perpendicular direction. To further resolve the crystalline order of the 6P inclusions and the ZnO/6P interfaces cross-sectional HRTEM is performed. For the experiments, the thickness of the 6P layer is reduced to nominally 2.5 nm, while the ZnO top layer thickness is increased to 100 nm to provide better stability of the HRTEM specimen. Challenging for imaging hybrid stacks by HRTEM is that they are composed of a weak phase object, the organic material, accompanied by a strong phase object, the inorganic material.

Hence, structural imaging of both components in one HRTEM image is difficult. By using the previously introduced (→ Sec. 3.3.2) contrast transfer function (CTF) imaging of the respective material, however, becomes possible. Fig. 4.28 shows the CTF for four different defocus values calculated for the TEM JEOL JEM2200FS operated at 200 kV according to the weak phase-object approximation presented in Sec. 3.3.2. For the Scherzer defocus of $df = -43$ nm, the maximum range of spatial frequencies is transferred with identical sign (cf. Fig. 4.28a). At this defocus, the theoretical point-to-point resolution of $d_{\text{r-r}} = 0.19$ nm is the lower limit of homogeneous contrast transfer.

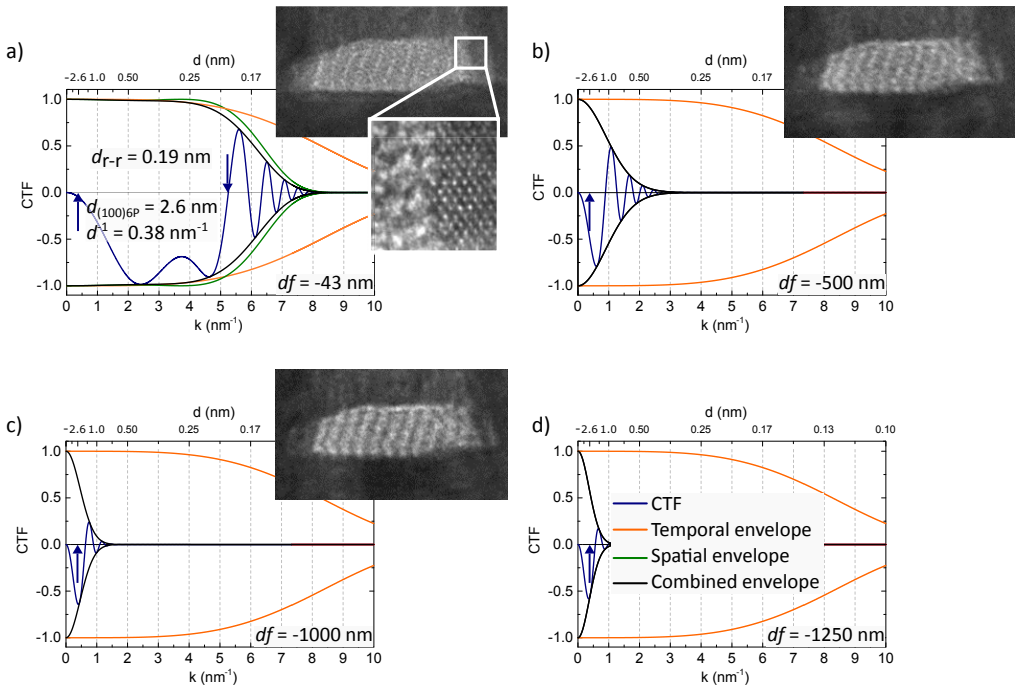

Figure 4.28: Contrast transfer function (CTF) for HRTEM imaging of 6P utilizing a JEOL JEM 2200 FS at different defocus values, showing additionally temporal, spatial and combined envelope functions and experimental images as inset.

Under this condition, the crystal structure of the inorganic component ZnO with lattice parameters of a = 0.325 nm and c = 0.52 nm can be resolved, see inset Fig. 4.28a (bottom). On the other hand, contrast transfer for the 6P(100) lattice planes having a distance of 2.6 nm is almost negligible (cf. in Fig. 4.28a). The HRTEM image of the HIOS structure shows only weak bright lines corresponding to the 6P(001) lattice planes, see inset Fig. 4.28a (top). Weak phase objects, however, can be visualized by applying a large defocus enhancing the contrast transfer of low spatial frequency features. The contrast transfer is strongly enhanced by setting the defocus to $df = -1000$ nm. The lattice planes of 6P are now clearly seen in the corresponding HRTEM image (cf. inset Fig. 4.28c). Tuning the defocus to a higher value, further damps the contrast transfer again, as seen in Fig. 4.28d. Hence, an optimum defocus for transfer of spatial frequencies corresponding to the 6P lattice constant of $df_{opt} = -1000$ nm was identified for HRTEM imaging of 6P and consequently applied on the hybrid specimen.

This knowledge is used in the following to display HRTEM images revealing 6P nanocrystallites in Fig. 4.29. The lamellae are cut normal to ZnO[0001], i.e., the cross section perpendicular to the long axis of needle-shaped 6P nanocrystallites is imaged. The large defocus value needed to visualize weak phase objects like organic crystals is accompanied by a loss of spatial resolution. Therefore, the atomic structure of the surrounding ZnO cannot be resolved in the images. Nonetheless, the 6P inclusions are well-resolved and represented by a light gray contrast. Lattice fringes are also well visible by contrast differences inside the nanoaggregates. The inclusion features a weak shadow underneath as diffracted and non-diffracted electron beams are slightly laterally shifted.

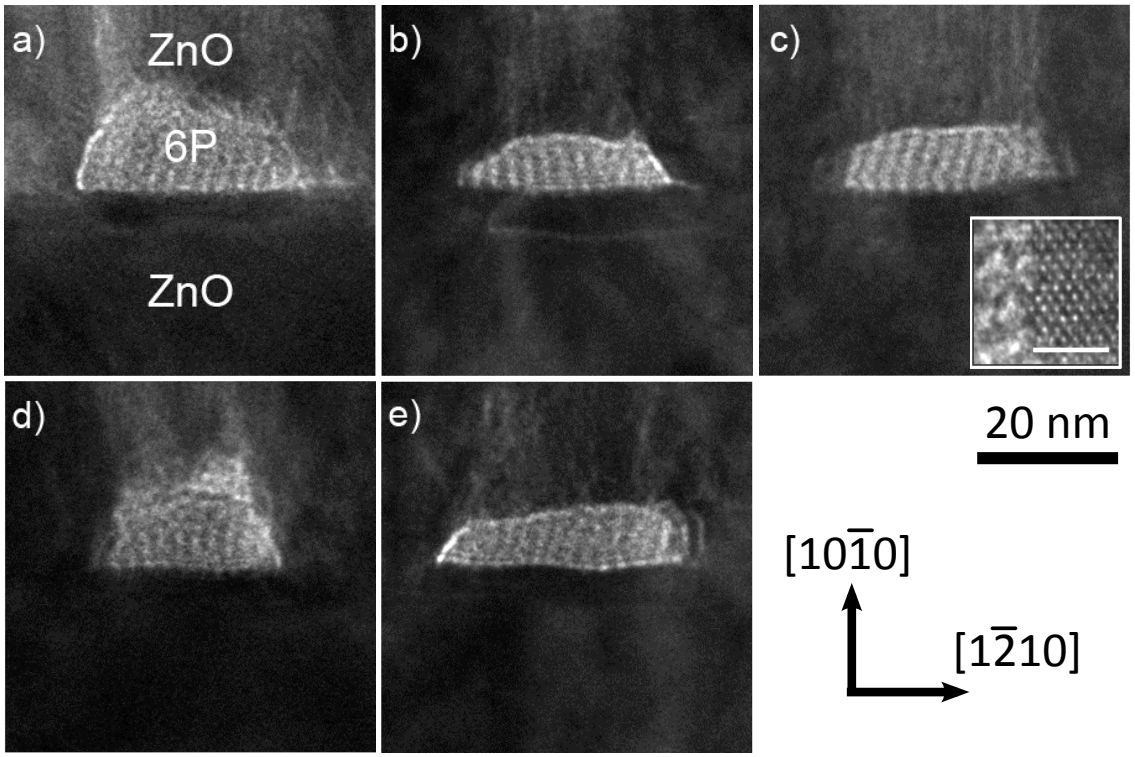

Figure 4.29: a-e) Representative selection of cross-sectional HRTEM images of 6P nanoaggregates embedded in a ZnO$(10\bar{1}0)$ hybrid stack. The deposited amount of 6P corresponds to a nominal layer thickness of 2.5 nm. The dark lattice fringes of the 6P nanoaggregates correspond to the (100) lattice planes. The images are recorded at an defocus of $df = -1000$ nm except for the inset of (c), which is obtained at a Scherzer defocus of $df = -43$ nm to image the ZnO columns as well. The scale bar in the inset corresponds to a length of 2 nm.

Atomic resolution can be achieved by setting the focus to the Scherzer defocus of $df = -43$ nm (cf. inset of Fig. 4.29c), showing a lateral 6P/ZnO interface. The hexagonal ZnO structure is clearly visible. Thus, combined analysis of both 6P and ZnO is possible by just changing the defocus value. A detailed HRTEM investigation of the crystalline structure of the ZnO top layer will be given in the next subsection. What is most remarkable, is that the interface between the molecular nanocrystallites and the ZnO top layer is defined

on a molecular level. Lattice planes of 6P are discernible and extend to the lateral and top interfaces of the overgrown ZnO layer without visible distortion. What appears to be blurry feature of ZnO on 6P in Fig. 4.29a and d can be explained by height corrugation of the 6P nanocrystallites. At those positions, ZnO top layer and 6P partially overlap. Furthermore, there are no traces of interdiffusion of ZnO into the organic layer are found. This is in strong contrast to previous studies where organic materials were overgrown by vapor deposition with metals (Au)[222] or by atomic layer deposition with ZnO.[227,228] In both cases, interdiffusion of the inorganic component into the organic film was observed on a length scale of tens to a hundred nm. What further catches the eye is that the 6P lattice planes are inclined with respect to the surface of ZnO either to the left or to the right by an angle of approximately 70° as seen in Fig. 4.29a and b. This is corroborated by XRR measurements since the vertical growth direction of 6P was designated to be along $[20\bar{3}]$, with the 6P long molecular axis thus exactly parallel to the ZnO surface. The alignment of the needle-shaped 6P nanocrystals along the ZnO[0001] implies that 6P molecules are oriented parallel to ZnO$[1\bar{2}10]$. Hence, the observed lattice fringes should correspond to 6P(100) planes, which results in an angle between the (100) and $(20\bar{3})$ plane of 71.9°, as observed in Fig. 4.29a and Fig. 4.29b. Obviously, there is no preference for molecules to grow shifted either to the right or to the left. This leads to characteristic stacking faults upon coalescence of 6P nuclei as distinctly visible in Fig. 4.29c. On the upper terrace (right side of the step edge on the ZnO surface), 6P molecules aggregate with the (001) lattice planes inclined to the right, whereas on the lower terrace (left side of the step edge), 6P grows with the (001) lattice planes inclined to the left. At a vertical distance of approximately 3 nm from the interface to the ZnO bottom layer, the lattice planes pass a kink and assume an inclination to the right. The aggregate on the lower terrace thus adapts the crystallographic orientation of that on the upper terrace. The vertical distance of the kink from the ZnO substrate surface corresponds to the step height of the ZnO surface. Additionally, but with much lower occurrence, 6P nanocrystallites with vertical (001) lattice planes are found, indicating the presence of the 6P γ-phase (cf. Fig. 4.29d). The molecules are oriented here in the same manner in respect to the ZnO surface as in the β-phase nanocrystals. However, in the γ-phase, the molecules stack exactly on top of each other, resulting in an angle between the (100) and $(20\bar{3})$ plane of 90° as shown in Sec. 4.3.1.3. At strongly corrugated regions of the ZnO surface, the growth of 6P is disturbed, and the inclination of the (001) lattice planes deviates from that expected for the bulk crystal phases. An example is depicted in Fig. 4.29e. Such growth imperfections seem to be the cause for the observed larger mosaicity along the ZnO$[1\bar{2}10]$ direction found in the X-ray rocking scans. To verify this interpretation, image contrast simulations of the HRTEM data in Fig. 4.29a and c are performed, which are displayed in Fig. 4.30 and Fig. 4.31. The structural models for the simulation are created using the CrystalMaker software. The interface models are then caged in supercells and transferred to the JEMS software package.[229] The size of the supercell is 10.5 nm x 10.3 nm x 4.0 nm for the 6P/ZnO$(10\bar{1}0)$ interface. The large size of the supercells hampers the recognition of contrast details at the atomic scale but closely corresponds to the selected magnification of HRTEM imaging of 100 kx. Utilizing JEMS the HRTEM image contrast of the supercell is calculated for a series of specimen thicknesses and defocus values corresponding to

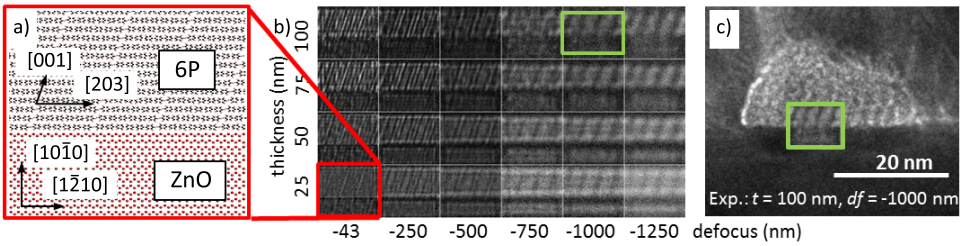

Figure 4.30: HRTEM image contrast simulation of the 6P/ZnO(10$\bar{1}$0) interface. The viewing direction is along ZnO[0001]. a) Structural model of the 6P/ZnO(10$\bar{1}$0) interface and b) corresponding calculated HRTEM images for a series of thicknesses and defocus values. c) Superposition of a contrast-adapted calculated pattern obtained for a defocus value of $df = -1000$ nm and a lamella thickness of $t = 100$ nm (framed in green) with the measured HRTEM image of Fig. 4.29a.

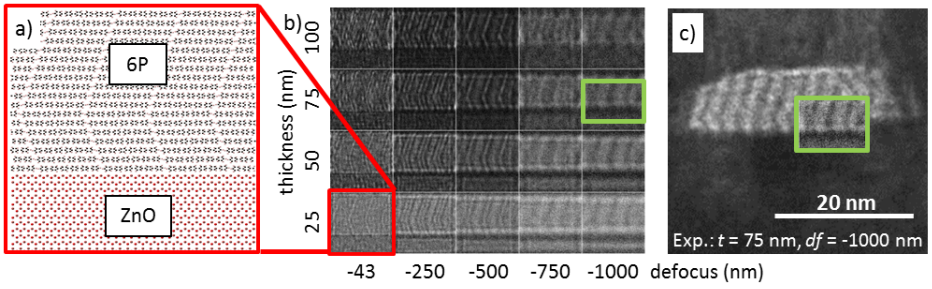

Figure 4.31: HRTEM image contrast simulation of a 6P/ZnO(10$\bar{1}$0) interface containing a typical 6P stacking fault. The viewing direction is along ZnO[0001]. a) Structural model used as basis for the simulations. A twinning plane is introduced in the 6P layer. b) Calculated thickness/defocus map. c) Superposition of a contrast-adapted calculated pattern obtained for a defocus of $df = -1000$ nm and a lamella thickness of $t = 75$ nm (framed in green) with the experimental HRTEM image of Fig. 4.29c.

the achievable thicknesses of ultramicrotomy-fabricated TEM lamellae. As there is no indication for a wetting layer of 6P on ZnO the bulk crystal structures of both ZnO and β-phase 6P are chosen as the basis. In- and out-of-plane orientations of 6P with respect to the underlying ZnO are ZnO[0001] $\perp$ 6P[20$\bar{3}$] and ZnO$\left(10\bar{1}0\right)$ $\parallel$ 6P$(20\bar{3})$, respectively, following the discussion above. The interface gap is set to 0.3 nm according to Ref. [70]. As the exact adsorption site of 6P on the ZnO surface is not known from experiments, and HRTEM image contrast is not influenced by this, displacement of the 6P crystal in the lateral direction is chosen arbitrarily. The utilized structural model is depicted in Fig. 4.30a. The calculated thickness/defocus map is shown in Fig. 4.30b. The defocus calculated HRTEM images feature values ranging from the Scherzer defocus and extends to $df = -1250$ nm, with a step width of 250 nm. Again it can be seen that at larger defocus the phase contrast in the organic layer is enhanced up to -1250 nm, where it declines again. Comparing the experimental image with the calculated thickness/defocus map, the best match is found for a thickness of $t = 100$ nm and $df = -1000$ nm in agreement with

experimental conditions. By superposing calculated pattern with the experimental image it appears that the dark contrast corresponds to the molecules while the bright fringes are the gap between them (see Fig. 4.30c). Furthermore, the contrast at the interface, including the Fresnel diffraction, and the lattice fringe alignment are well-reproduced at the correct defocus value, confirming the presented structural model. Another simulation is done for a 6P nanoaggregate including a stacking fault (Fig. 4.29c). Here, a rotated 6P layer is introduced at a distance of 3 nm from the 6P/ZnO interface as shown in Fig. 4.31a. The resulting kink can be seen in all simulated images of the defocus map (cf. Figure Fig. 4.31b), but best agreement with the experimental image is obtained for a thickness of $t = 75$ nm and $df = -1000$ nm (cf. Fig. 4.31c). This is again in agreement with experimental conditions, which verifies the structural model.

Conclusion

It was shown that HRTEM images of combined weak and strong phase objects as in the case of hybrid inorganic/organic samples can reveal the crystalline structure by using ultramicrotomy for preparation and appropriate focus conditions. At Scherzer defocus the structure of the inorganic component can be resolved, while at large defocus also the lattice planes of the organic inclusion even in very thin specimens can be visualized. Using 6P again as model system in a hybrid stack, crystalline perfections could be revealed by combination of HRTEM analysis and X-ray diffraction. By this is could be shown that all interfaces are defined on an atomic/molecular level when embedded in an inorganic environment of ZnO. Further detailed analysis of HRTEM images and XRD scans revealed the impact of the ZnO$(10\bar{1}0)$ surface topography on the crystallinity of 6P. It was shown that surface corrugations cause some degree of mosaicity of 6P nanocrystallites along the ZnO$[12\bar{1}0]$ direction and lead to a characteristic stacking fault described by a kink in the 6P(001) lattice planes. Further improvement of the 6P crystalline perfection can be achieved by varying the growth protocol of the ZnO bottom layer. For example, by changing the growth temperature, the width and height of terraces can be adjusted and thus growth imperfections in 6P avoided. The quintessence of this study is that embedded organic/inorganic structures can be grown without compromising the organic molecules. This opens new opportunities for the design of novel inorganic/organic hybrid structures and a considerable functionality expansion can be foreseen. New device concepts become feasible, for example, light-emitting diodes where organic nanocrystallites are embedded in an inorganic p-n junction or devices relying on inorganic/organic multilayer stacks.

4.4.2 Texture and Morphology of ZnO Top Layer

After focusing on the organic inclusion in a hybrid stack consisting of ZnO/6P/ZnO in Sec. 4.4.1 the morphology and crystallographic structure of the ZnO top layer will be analyzed in greater detail in this subsection. Here, also the growth on the ZnO(0001) surface is investigated, where 6P aggregates in islands consisting of nearly upright standing molecules with 6P(001) as contact plane occur. In the same way the growth of the TL on the ZnO($10\bar{1}0$) surface is studied, where the molecules align preferentially flat-flying at a substrate temperature of 100 °C with 6P($20\bar{3}$) as contact plane. Thereby needle-like crystallites are formed as described in Sec. 4.3.1. With those polar and non-polar hybrid stacks *ex situ* AFM, cross-sectional HRTEM and Photoluminescence (PL) measurements are performed to reveal morphology, crystallographic structure and texture of the TL, as well as to further demonstrate the integrity of the enclosed organic layer. The crystallinity and the structural perfection of the ZnO layer atop 6P are analyzed by high-resolution TEM imaging with a point resolution of 0.19 nm. For visualization of the local orientation, Fourier transforms of selected areas of the HRTEM images are calculated utilizing the Digital Micrograph software package of GATAN. To obtain the local crystallographic orientation of ZnO, Scanning Nanobeam Diffraction (SNBD) is performed on samples prepared by standard ion milling. To likewise achieve molecular resolution for the ZnO(0001) surface a specimen is again prepared using the method of ultramicrotomy making a specimen with a thickness of 50 nm possible. For PL measurements a frequency doubled Ti:sapphire laser in fs-mode as excitation source is used. The PL signal is recorded using a CCD camera after passing a spectrograph. The results of this study have been published in Ref. [134] before.

BL and TL are grown employing the standard and low-temperature epitaxial regime, respectively. In the low-temperature regime, the substrate is kept at 100 °C. The growth rate during deposition of the organic layer is kept constant at 0.1 nm/min. The substrate temperature during organic growth is 25 °C and 100 °C, depending on the desired orientation. The 6P growth mode is adjusted by the substrate temperature and the deposition time. To control the growth direction of ZnO as well as the 6P film morphology, hybrid stacks for structural characterization are fabricated on either (0001) or ($10\bar{1}0$) oriented ZnO templates (CrysTec GmbH). The design of the structures is schematically depicted in Fig. 4.32.

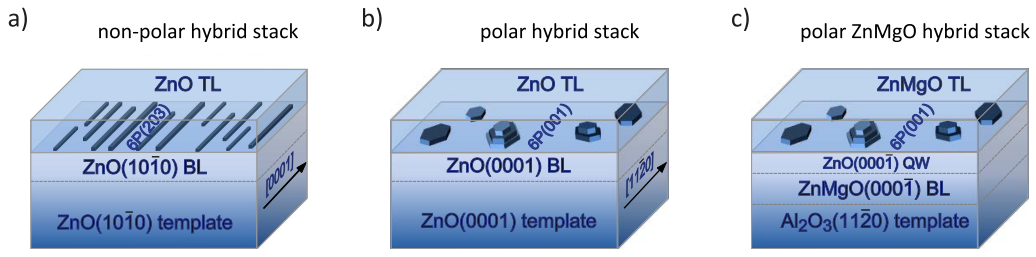

Figure 4.32: Schematic depiction of the different used hybrid stacks grown for structural and optical investigations. a) Non-polar hybrid stack with needle shaped ($20\bar{3}$) oriented crystallites. b) Polar ZnO(0001) hybrid stack where 6P forms island-like crystallites with (001) orientation. c) Polar Al_2O_3/ZnMgO/ZnO/6P/ZnMgO sample used for PL experiments.

The non-polar and polar hybrid stacks which are used for structure analysis of the ZnO TL are shown in Fig. 4.32a and Fig. 4.32b. The design of the polar hybrid stack is changed For PL experiments, conducted to confirm the structural integrity of the nanoaggregate. For this the stack is grown on *a*-plane sapphire to avoid deep-level emission from the ZnO template (Fig. 4.32c). In this case ZnO BL and TL are alloyed with Mg to widen the band gap, hence making ZnO transparent at the energy where the 6P molecules are excited. Thickness and temperature of BL, TL and 6P film of the hybrid stacks are adjusted as required for the respective sample.
As the crystallographic structure of the 6P inclusion on the ZnO(0001) was not investigated in the previous study, at first cross section HRTEM image is acquired shown in Fig. 4.33a for the polar ZnO(0001)/6P/ZnO hybrid stack.

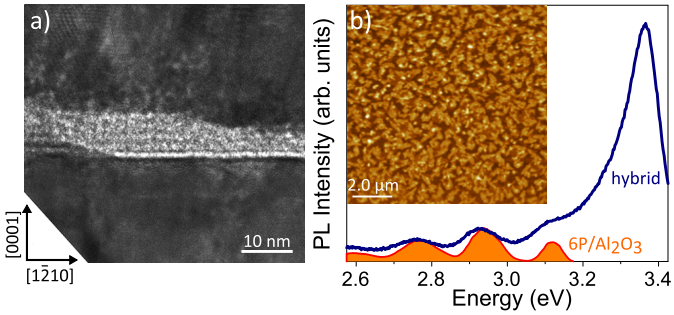

Figure 4.33: a) HRTEM cross-section image of a polar ZnO/6P/ZnO hybrid stack grown on a ZnO(0001) template. The imaging direction is ZnO[10$\bar{1}$0]. The prominent bright horizontal line at the lower 6P/ZnO interface is an artifact due to Fresnel diffraction. b) Room-temperature PL spectrum of the Al_2O_3/ZnMgO/ZnO/6P/ZnMgO hybrid stack. The reference spectrum is taken of a 6P film deposited on sapphire. The excitation energy is 3.5 eV. The inset shows an AFM scan of the surface topography of the hybrid stack. The height scale is 20 nm. Despite the thin ZnMgO TL, the morphology of the embedded 6P layer is still visible.

The substrate temperature during 6P and ZnO overgrowth is kept at $T_S = 100$ °C. Nominal thickness of the 6P layer ($d_{6P} = 10.5$ nm) is chosen in order to completely cover the ZnO BL by 6P. The ZnO TL has a thickness of $d_{TL} = 100$ nm. The image is recorded with a defocus of -1000 nm to assure a large phase contrast to visualize 6P lattice planes. The embedded 6P layer can be clearly distinguished by the higher brightness. Furthermore, 6P(001) lattice planes of the crystallite can be identified as well, confirming the integrity of the film. The actual thickness of the 6P layer varies. In the center of the image, one can count four layers of standing 6P molecules. The 'wedding cake'-like morphology of 6P on ZnO(0001) is reflected in the decreasing layers at the edges. As already shown for growth on the ZnO(10$\bar{1}$0) surface in the previous subsection all interfaces of 6P on ZnO but also of ZnO on 6P are atomically sharp and abrupt on a monolayer length scale. Again the ZnO TL nucleating on top of the 6P layer follows its surface topography. As well as there are no indications for penetration of ZnO or formation of Zn clusters in the organic layer found by diffraction contrast TEM imaging nor by energy-filtered TEM (data not shown). To fully exclude that the 6P film is impaired by overgrowth with ZnO, PL measurements of a 6P reference sample are performed as shown in Fig. 4.33b. For the polar ZnMgO hybrid stack

used the thicknesses of the ZnO and ZnMgO TL are $d_{QW} = 3.5$ nm and $d_{TL} \approx 20$ nm. The Mg content in the ZnMgO BL and TL is 8 %. The nominal thickness of 6P is $d_{6P} = 1.7$ nm. The substrate is kept at $T_S = 25$ °C during 6P growth. The nominal thickness of 6P is chosen to be in the sub-ML range, but due to the limited surface diffusion over step edges, further layers have already started to nucleate on the first ML as seen in the AFM scan in the inset of Fig. 4.33b. Comparing the PL of the hybrid sample with a reference of 6P on Al_2O_3 shows that apart from a slight red-shift the PL spectra of 6P in the reference and the hybrid stack match. The peak seen at 3.36 eV corresponds to the emission of the ZnO QW. The low intensity of the 6P emission compared to the QW emission might be related to the energy level alignment at the interface between molecular orbitals and valence/conduction bands of ZnO. According to photoemission experiments energy level alignment is of type-II, hence facilitating exciton dissociation and charge separation.[151] All in all for the polar hybrid stack too interfaces are well-defined and abrupt when overgrown by ZnO. Furthermore, the structure of the organic inclusions are unimpaired as optical measurements demonstrates. Consequently morphology and crystallographic structure of the ZnO TL are further examined in the following.

First the surface topography is analyzed by AFM scans shown in Fig. 4.34a and b, comparing non-polar and polar ZnO/6P/ZnO hybrid stacks. In this case the ZnO BL is not fully covered by 6P to still recognize the topography of the molecular layer. Specifically the structural parameters are a thickness of $d_{6P} = 1$ nm, $d_{TL} = 70$ nm for the non-polar stack and $d_{6P} = 0.4$ nm, $d_{TL} = 15$ nm for the polar hybrid stack. In both cases 6P is deposited at $T_S = 100$ °C.

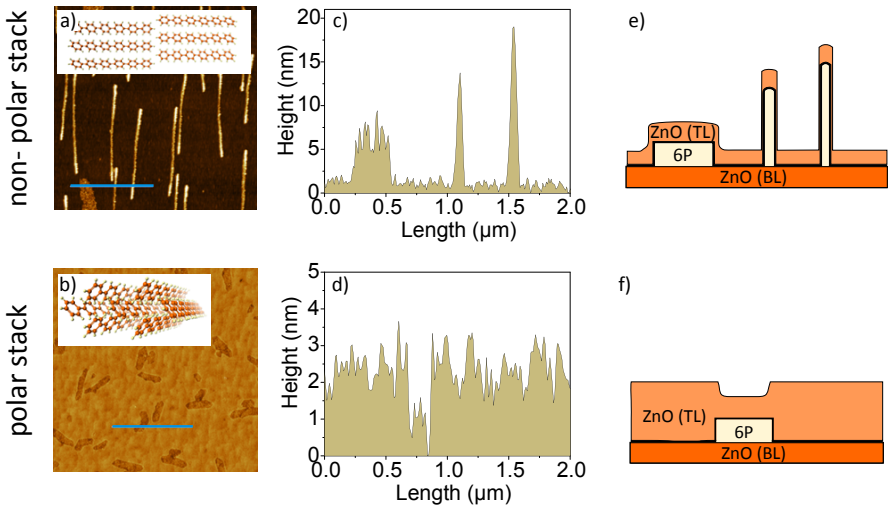

Figure 4.34: AFM scans of the surface topography of a) non-polar and b) polar ZnO/6P/ZnO hybrid stack grown on ZnO(10$\bar{1}$0) and ZnO(0001) templates, respectively. Top views on the 6P(20$\bar{3}$) and 6P(001) contact planes of the buried needle- and island-shaped crystallites are visualized in the insets of a) and b), respectively. c) and d) show height profiles taken along the blue lines. e) and f) shows a schematic depiction of the structure in c) and d).

In both AFM scans of those structures the organic 6P crystallites are still clearly visible. Apparently the ZnO TL follows exactly the topography of the 6P film. However, a distinct

difference between the two surface orientations is found. For the non-polar hybrid stack, the expected needle-shaped 6P crystallites are found, which appear as protrusions. A few island-shaped 6P crystallites with (001) orientation are found as well. Those can be used beneficially to evaluate the differences in the nucleation and growth rate of the ZnO TL atop and aside 6P islands. The needle-shaped crystallites do not allow such an analysis as their height is not defined. Fig. 4.34c shows the height profile measured over island and needle-shaped crystallites. Since the island-shaped crystallite is composed of one monolayer of (nearly) upright standing molecules the islands height corresponds to the thickness of ca. 2.6 nm for the β-phase 6P. The height profile in Fig. 4.34c indicates a larger value. This implies that nucleation and/or growth of ZnO proceed faster atop than in the space between the 6P islands. Considering the TL thickness, the growth rate atop would be ca. 4 % faster. In contrast, on the polar hybrid stack depressions of ≈ 1.5 nm depth are visible (cf. Fig. 4.34d) at the position of the 6P island-like crystallites . In this case the nucleation and/or growth of the ZnO TL atop 6P must be slower by ca. 27 %. The results of the AFM investigations are furthermore summarized in a schematic drawing in Fig. 4.34e and f. A different growth velocity indicates different orientations for the ZnO crystallites atop 6P. Furthermore, the striking anisotropy in the shape of the 6P islands in Fig. 4.34b, hints at partial lateral overgrowth with ZnO of the same orientation as the surrounding ZnO. This will be seen more clearly below. RHEED patterns (not shown) recorded after completion of the ZnO TL corresponds for the hybrid stacks to that of single crystalline ZnO($10\bar{1}0$) and ZnO(0001), respectively. However, weak additional polycrystalline features are also present. Naturally, the orientation of the ZnO TL in the space between the organic crystallites should correspond to that of the substrate. Hence, those polycrystalline features seem to originate from ZnO atop the 6P crystallites. To analyze the structure of the TL a combination of cross-sectional HRTEM and SNBD is performed. The overview HRTEM image in Fig. 4.35a depicts the region around a needle-shaped 6P inclusion in a non-polar ZnO/6P/ZnO hybrid stack taken along the [0001] direction. The ZnO BL (region 1) appears perfect and shows no dislocations. This is also confirmed by the respective Fourier Transform (FT) in Fig. 4.35b. It exhibits 6 spatial frequency maxima corresponding to $\{1\bar{1}00\}$ lattice planes. The ZnO TL aside the 6P inclusion is represented by regions 2 and 4. The orientational relationship of ZnO TL in regions 2 and 4 with the underlying ZnO BL (region 1) becomes clear by the FT depicted in Fig. 4.35b. The identical arrangement of the spatial frequency maxima of the $\{1\bar{1}00\}$ lattice planes confirms that regions 2 and 4 of the TL have the same orientation like the ZnO BL, which is in agreement with the RHEED observations. The magnified view of the atomic structure of region 2 in Fig. 4.35c further supports that $\{1\bar{1}00\}$ lattice planes are aligned parallel to those of the BL. The lattice planes extend even to the region above 6P. Noticeable brightness fluctuations on a length scale of about 10 nm are seen in both, BL and TL, indicating that they are an artifact of the TEM specimen preparation. Thickness modulation as well as structural defects caused by a final ion milling step still used here result in local variations of the image contrast. Altogether the data do not give evidence that growth interruption and organic molecule deposition induce further crystal imperfections in the ZnO TL aside 6P. However, the region above the 6P inclusion gives a different picture. The circular pattern of the FT of region 3 indicates polycrystallinity (cf. Fig. 4.35b). This is also corroborated

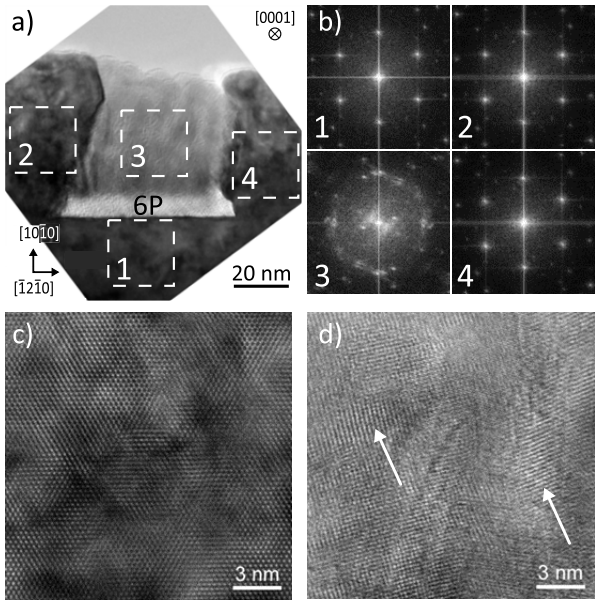

Figure 4.35: Structure analysis by HRTEM imaging of the non-polar ZnO/6P/ZnO hybrid stack: a) Cross-section HRTEM of the region around a needle-shaped 6P inclusion. Regions for further analysis are framed. b) FT of the areas marked in a) visualizing the crystalline quality and the orientation of the different regions. HRTEM images of the ZnO TL: c) aside (region 2) and d) in the center atop (region 3) a 6P crystallite. The white arrows in d) point towards two ZnO nanocrystallites with different orientations.

by a magnified view of region 3 (→ Fig. 4.35d) depicting the ZnO TL in the center atop a 6P inclusion shows the formation of nanocrystallites of about 5–10 nm in diameter with different orientations. Accumulation of diffraction spots in the FT of region 3 in selected directions still hint at the formation of a preferred orientation of the nanocrystals, which will be elaborated in more detail below by SNBD with the ability to locally resolve the crystal orientation. Further examination of the HRTEM image in Fig. 4.35a reveals that the lateral interface between the single crystalline and the nanocrystalline region of the ZnO TL can be clearly identified from the brightness contrast. This stems from different thicknesses of the TEM specimen in the respective regions introduced by the ion milling process. Partly, the lateral interface is formed by $\{10\bar{1}0\}$ facets which are prismatic planes. The left interface extends laterally up to 15 nm into the region atop 6P. Merging of laterally growing facets over 6P needles was not observed for the 70 nm-thick ZnO TL. Thus, either the 6P inclusions must be smaller or the ZnO TL thicker for this to occur. Finally, also the ZnO-on-6P interface atop a needle-shaped crystallite is very smooth.

SNBD is performed to analyze the texture of the nanocrystalline ZnO atop 6P in more depth and to check if the ZnO surface or the organic crystal termination has an influence on nucleation and growth of the TL. Fig. 4.36 compares typical SNBD maps for polar (a and b) and non-polar (c and d) ZnO/6P/ZnO hybrid stacks around an organic inclusion. To eventually achieve lateral overgrowth the mean island size is reduced for the polar stack

by lowering the substrate temperature during 6P growth to $T_S = 25$ °C and shortening the deposition time resulting in a nominal thickness of $d_{6P} = 0.2$ nm. The thickness of BL and TL is $d = 70$ nm.

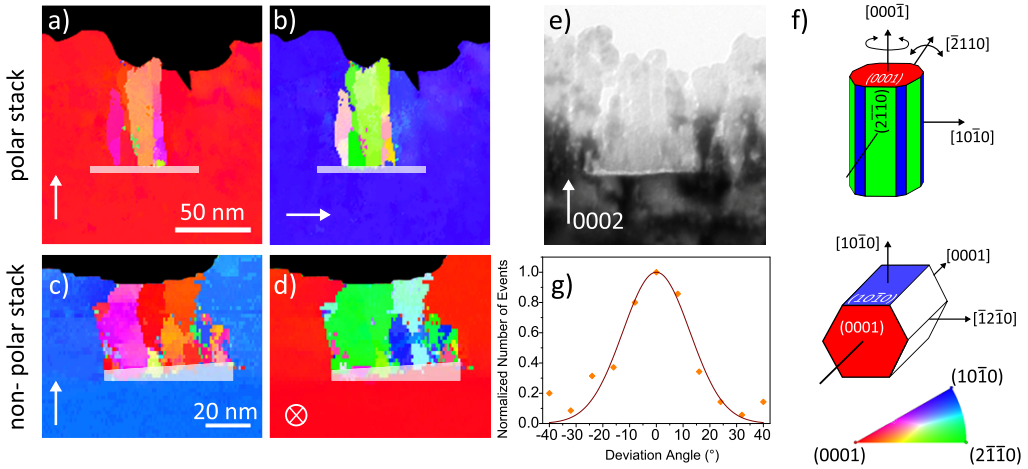

Figure 4.36: Crystal orientation mapping of polar (a, b) and non-polar (c, d) ZnO/6P/ZnO hybrid stacks around an organic inclusion. The surface normals of the imaged lattice planes are marked by the white arrows. a), b) Polar hybrid stack: the imaging direction corresponds to ZnO[$\bar{1}$2$\bar{1}$0]. c), d) Non-polar hybrid stack: the imaging direction corresponds to ZnO[0001]. e) Polar hybrid stack: for comparison, the bright field TEM image of the sample region depicted in a), b) is shown. f) Color coding of low-index lattice planes of wurtzite ZnO with (0001) orientation (top), (10$\bar{1}$0) orientation (middle) and color zone selector of the maps for wurtzite ZnO crystallites (bottom). g) Distribution of the deviation angle derived from the orientation of ZnO grains in the center atop a larger island analyzing ca. 40 grains. The presented data points are collected atop a 6P island in the non-polar hybrid stack. The solid line corresponds to a Gaussian distribution with a standard deviation of 12°.

The position and size of the 6P inclusions are derived from the bright field TEM image of the same sample region. For comparison, this is shown for the polar hybrid stack in Fig. 4.36e. the orientation maps derived from SNBD in Fig. 4.36a-d visualize the lattice planes normal to the white arrows. The local orientation is color encoded in correspondence to the color zone selector depicted in Fig. 4.36f. The color code of selected low-index planes of wurtzite ZnO is shown as well. In both hybrid stacks, the ZnO TL in regions aside 6P inclusions appears in the same color as the homoepitaxial ZnO BL as structure and orientation of the template are retained in agreement with RHEED and HRTEM. Independent of the termination of the ZnO BL and the 6P crystal shape and orientation, ZnO nucleated atop 6P shows a distinct columnar structure, whereby the reddish color in Fig. 4.36a and c indicates that the c-axis of the crystallites is preferentially oriented parallel to the substrate surface normal. The occurrence of pink and orange colored grains indicates, however, significant deviations from normal orientation (Fig. 4.36a and c). The distribution of the deviation angle (Fig. 4.36g) is deduced analyzing the orientation of grains in the center atop a larger 6P(001) island. It follows rather well a Gaussian distribution with a standard deviation of 12°. This result is independent of the polarity of the ZnO BL and is obtained for 6P(001) islands occurring naturally on ZnO(0001) and occasionally on ZnO(10$\bar{1}$0) (cf.

Fig. 4.34b). On the other hand, the grains around the substrate surface normal have random in-plane rotational orientations as indicated by the variation from blue to green in Fig. 4.36b and d. A preferred c-axis orientation of ZnO atop the organic crystallites can be either caused by preferential nucleation or preferential growth in a certain direction. As there is no epitaxial relation between ZnO and 6P, preferential growth is more likely. This can occur even when the nuclei have a random orientation but exhibit a prevalent growth direction normal to the substrate. This is the case if surface diffusion between planes within a grain is possible, so that the plane with higher surface energy becomes the preferred orientation.[230,231] The highest surface energy applies to the (0001) plane, meaning that the direction of fastest growth is along [0001].[232] As higher substrate temperatures enhance diffusion, the deviations from the c-axis alignment should become smaller. This may explain, why the deviation angle is larger under the present conditions than that observed for instance in ZnO growth on amorphous substrates at elevated temperatures (400 °C) by pulsed laser deposition.[233] Another possible explanation for preferential c-axis alignment was given by Claeyssens et al., who proposed a graphitic-like phase with minimum surface energy that forms predominantly in the first ML of the ZnO growth and then transits to the thermodynamically more favorable (0001) morphology for higher coverages without a energy barrier.[234] This leads to c-axis alignment also on amorphous substrates.[233] However, observed prevalent ZnO grains with small lateral extension (5–10 nm) support the first explanation. Thereby, limited diffusion of adatoms on 6P leads to domination of [0001] oriented grains already after growth of some nm of ZnO. While the organic crystal termination does not have a visible impact on the structure of the ZnO TL, the choice of the ZnO surface induces differences.

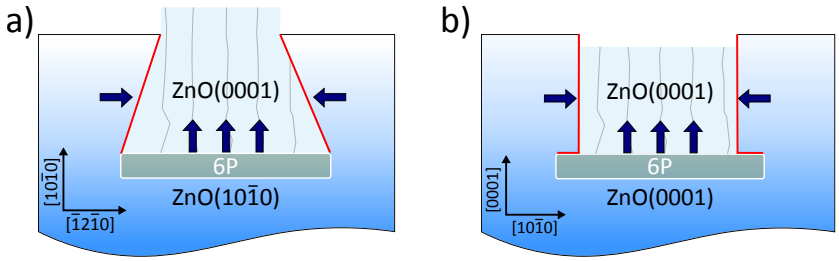

Figure 4.37: Schematic depiction of the evolution of the ZnO TL in a) non-polar and b) polar ZnO/6P/ZnO hybrid stack. Horizontal and vertical arrows depict the competition between lateral overgrowth and nucleation/ growth atop 6P.

As already pointed out above, in the non-polar hybrid stack, formation of $\{10\bar{1}0\}$ facets with the same orientation as the ZnO BL is observed. In Fig. 4.35a one observes a gradually lateral overgrowth of the organic nanocrystallites, which is depicted schematically in Fig. 4.37a. The ZnO(10$\bar{1}$0) plane has the lowest surface energy, so that by energetic considerations, its formation is favored.[234,235] However, the development of such facets is only possible if ZnO atop 6P has not started to grow yet. Hence, nucleation atop 6P must be delayed. Once, nucleation and growth have set in, the c-axis oriented grains quickly dominate the film as already discussed. As these grains grow with a faster rate than the surrounding homoepitaxial ZnO, the organic inclusions are visible as mounds in the AFM scan of Fig. 4.34a despite delayed nucleation.

Delayed nucleation also explains why the 6P islands appear as depressions in the AFM scan of the polar hybrid stack in Fig. 4.34b. As the growth direction atop as well as aside 6P is along [0001], the growth rate should not differ. Fig. 4.36a and b imply furthermore that epitaxial lateral overgrowth occurs also in the polar hybrid stack. According to Fig. 4.36a and b, the ZnO TL possesses the same orientation as the surrounding homoepitaxial ZnO at the edges atop the 6P island. In contrast to the non-polar hybrid stack, this orientation is already assumed at the 6P interface as now the low-energy $\{10\bar{1}0\}$ facets are parallel to the surface normal (cf. schematic depiction in Fig. 4.37b). Lateral overgrowth proceeds consequently parallel to the interface. The orientational relationship is lost in the central region of the 6P island as nucleation atop 6P and lateral overgrowth are competing processes. This finding is most strikingly visualized by a cross-section HRTEM image of a polar hybrid stack taken along the ZnO$[\bar{1}2\bar{1}0]$ direction (see Fig. 4.38), whereby the imaged sample slice apparently stems from a region close to the edge of the 6P island, where the organic layer is only one ML thick.

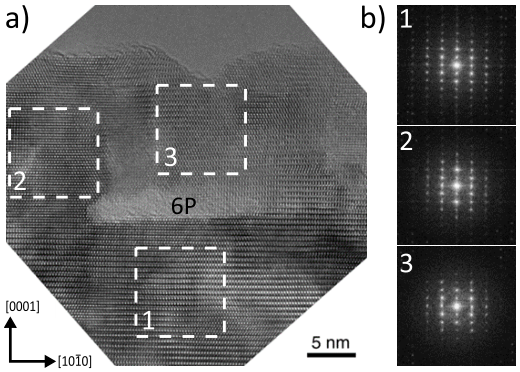

Figure 4.38: a) HRTEM image of the polar ZnO/6P/ZnO hybrid stack in the region around a 6P island. b) FT of the marked areas in a) indicating the crystalline quality and the orientation of different regions of the TL with respect to the BL.

The HRTEM image (Fig. 4.38a) and identical FT patterns of the BL in region 1 and the TL in region 2 (Fig. 4.38b) confirm that the ZnO TL asides the organic inclusion retains the symmetry and orientation of the ZnO BL in agreement with the above discussion. But now, even atop 6P, continuous lattice planes of {0001} oriented ZnO are visible, which is confirmed by the FT of region 3 showing the same arrangement of the frequency maxima as that of the ZnO BL. Apparently, the ZnO TL here has the same orientation as the surrounding material also atop 6P, although the ZnO lattice above 6P is not free of defects. Inspecting the region above the left edge of the 6P island, reveals a vertical shift is seen of the (0001) lattice planes by half of a monolayer compared to that of the homoepitaxial ZnO. This misalignment results in a local tilt of the (0001) lattice planes. When imaging thicker TEM specimen of the same hybrid stack (not shown) Moiré patterns become visible in the region above 6P islands signifying the presence of differently oriented ZnO crystallites when moving away from the edge of the island as already observed by SNBD.

Conclusion

In conclusion, the above study demonstrated that ZnO can be grown on an organic molecular crystal with an abrupt interface. Interdiffusion resulting in the formation of ZnO or Zn clusters within the organic layer was not observed. The ZnO TL nucleated atop the crystalline organic inclusion showed a distinct columnar structure with preferred c-axis orientation while aside the inclusion, the ZnO TL was single crystalline retaining the orientation of the ZnO BL. This finding is independent of the organic crystal surface termination. Both, in polar and non-polar hybrid stacks, partial lateral overgrowth of the organic inclusion with ZnO of the same orientation as the BL occurs. The ZnO growth direction determines how lateral overgrowth evolves: in non-polar stacks, energetically favored ZnO$\{10\bar{1}0\}$ facets forming an angle of 60° with the interface overgrow gradually laterally the organic inclusion, while in the polar hybrid stack, lateral overgrowth of ZnO$\{10\bar{1}0\}$ facets proceeds parallel to the interface. Therefore, ZnO atop 6P assumes already at the interface the orientation of the surrounding material. These observations define a way for further improvement of the crystalline quality of the ZnO TL required to achieve a high charge carrier mobility as well as PL yield as grain boundaries have a detrimental effect on both properties. By changing the aspect ratio and size of the organic crystallites also by change of temperature one could attempt to achieve coalescence of facets and subsequent single crystalline ZnO overgrowth of the organic inclusion.

4.5 Observing the Organic Growth: *in situ* Optical Properties

Objective of this chapter is to provide an insight into the structure of the deposited molecules and the interplay with the substrate directly observed in real-time during growth. This is done optically by differential reflectance spectroscopy (DRS), which allows for *in situ* analysis of the change in optical properties when the molecules are brought on the surface. By this, conclusions about the molecules' structure and interaction with the substrate in the different phases of the growth process can be drawn. Detailed studies to investigate thin organic films during growth via DRS have been done before.[122,123] Those works addressed the modification of DRS in the course of structural changes of the molecules, revealing layer-by-layer growth and monomer-dimer-oligomer transitions with a strong focus on growth of PTCDA on different substrates.[87,236–240] Furthermore, hybridized metal-organic systems[241,242] and charge transfer were investigated.[240,243] By using polarization dependent measurements even statements about the alignment on the substrate and existence of a wetting layer in the case of 6P could be made.[179,199,244] However, except for one recent study,[243] which investigated ZnO away from the absorbing region, all those studies were limited to insulators or metallic substrates.[243] Here, organic systems on transparent and semiconducting substrates will be compared regarding different interactions. The first investigated system is PTCDI on KBr, showing exemplarily the structural development during growth in the case of an inert and non-absorbing substrate. In the next step an only weakly interacting, but in the molecule's spectral range absorbing substrate is used. Thereby, the model to extract the molecule's dielectric properties is presented. For this, growth of L4P on ZnO is exemplarily shown. In the final step electronic coupling of the adsorbate is investigated, namely for NTCDA and F_6TCNNQ on ZnO. Those molecules show charge transfer accompanied by band bending of ZnO, which can be investigated by characteristic changes in the DR spectra.

The DRS study of PTCDI on KBr has been done in cooperation with J. Megow, T. Körzdörfer, T. Renger and V. May, who introduced the model to analyze the crystalline structure of the molecular deposit from DR spectra as published in [136]. A paper about the interactions of the different molecules (L4P, NTCDA, F_6TCNNQ) on ZnO is in preparation. Here, the experiments have been done together with T. Meisel, while the calculations for a Wannier-Mott exciton in an electric field were done by M. Gawek.

4.5.1 From Molecule to Crystal: PTCDI on KBr

First the simplest case is investigated: The growth of a molecule on a transparent, weakly interacting substrate. As a model system the molecule PTCDI (→ Sec. 4.1.2) deposited on the alkali halide KBr(100) is used. In that case the imaginary part of the refractive index of the molecule can easily be extracted out of *in situ* DRS measurements by Eqn. 3.17

$$\mathrm{Im}(\tilde{\varepsilon}) = -\mathrm{DRS} \cdot \frac{\lambda}{8\pi d}(1 - \varepsilon_{KBr}),$$

with the known optical properties for KBr.[245] Those are used with the empirical Sellmeier equation $n^2 = A + \sum_i B_i\lambda^2/\ (\lambda^2 - C_i)$ valid for transparent substrates.[246]

The DRS measurements allow to identify the transition of the single molecule spectrum to the crystal spectrum and by that to observe the gas-to-crystal shift. Beside optical investigations, the morphology of the sample is analyzed by UHV-AFM measurements. The model presented here for explaining the localized, site-dependent interactions resulting in the experimental spectra is given by Megow et al., as published in Ref. [136]. Alongside the intensively studied perylene PTCDA, also studied by DRS,[236] the similar molecule PTCDI is rather unexplored. However, the molecular structure on several substrates is investigated in literature by means of XRD, AFM and STM.[247–251] Depending on the substrate interaction strong differences are found in structure and morphology, showing either closed layers of completely flat lying molecules or a thin film phase, which deviates from the single crystalline phase.

Single crystalline KBr(100) (Korth Kristalle, Germany) samples were cleaved just before loading, producing atomically flat terraces which are several 100 nm broad. PTCDI was deposited at RT with about 1 Å/min. Fig. 4.39 displays the corresponding DR spectra as a function of thickness between sub-ML coverage to nominally 5.0 ML film thickness as well as the extracted Im(ε). During the deposition the spectra are subject to a striking change. At a low coverage in the sub-ML range the DR spectra in Fig. 4.39a exhibit four distinct equidistant maxima at 2.36, 2.54, 2.71 and 2.88 eV with an energy difference of ∼170 meV. At this stage the molecules are widely spread on the substrate surface and do not feel intermolecular interaction. Hence, the sub-ML spectra agree very well with the monomeric spectrum of PTCDI in solution, featuring the $S_0 - S_1$ transition and the corresponding vibronic progression. This shape, however, undergoes a quick evolution above 0.3 ML substrate coverage. Striking is an emerging low energy shoulder at 2.21 eV, while the monomer peaks are still visible at the same time. In addition, the two main peaks of the monomer fuse more and more together in the following spectra and finally

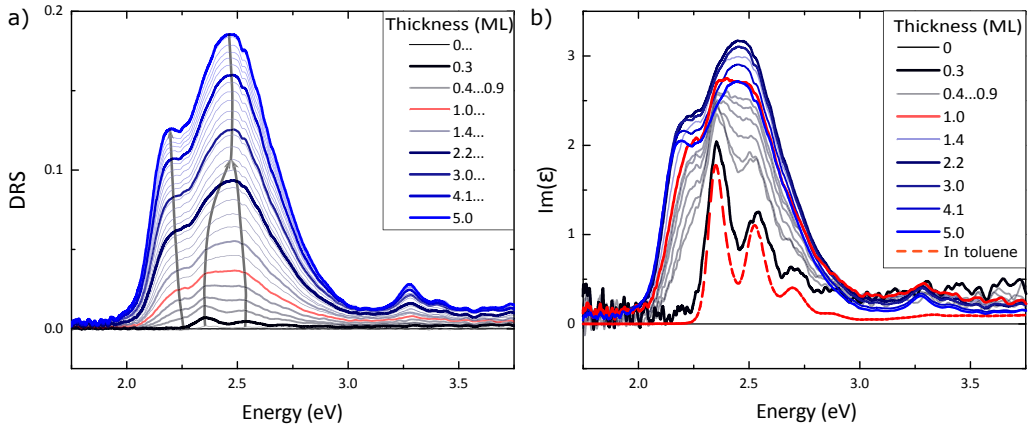

Figure 4.39: a) Drift-corrected DR spectra of PTCDI on KBr(100) with an integration time of 50 ms and 600 averaged measurements for a single spectrum. The arrows show the general development of the characteristic features. b) Calculated spectra of the imaginary part of ε. The dashed line shows an absorption spectrum of PTCDI in toluene.

form a broad band at 1 ML coverage, whereas the low energy peak further shifts to the red (indicated by the arrows). Moreover, another peak at about 3.25 eV arises at this coverage. With increasing thickness the spectra grow proportionally, while the shape qualitatively stays the same. At the final thickness of 5 ML the low-energy peak is located at 2.2 eV, while the monomer peaks completely merged into a single peak at 2.47 eV. Additionally, a prominent smaller peak is visible at 3.28 eV. For the calculated imaginary part of the refractive index in Fig. 4.39b the single features, especially at low, coverages are even better visible. The spectrum for the film thickness of 0.3 ML shows very clearly the features of the monomer as seen in direct comparison with the absorption spectrum of PTCDI in toluene. The FWHM of ∼110 meV in the DR spectrum also corresponds to the monomeric absorption spectrum in solution. The reason for the broadening in solution are the different dielectric surroundings. This indicates also different adsorption sites on the substrate for the molecule in contrast to a similar investigation for PTCDA on KCl(100), where a commensurate relation to the substrate was found with a FWHM of only 40 meV.[239] Noticeable is also that the intensity increases continuously and no dimerization is observed in the DR spectra. In summary the optical spectra clearly exhibit the sharp features of the monomer absorption spectrum in the initial stage, but are strongly altered to a broad double-peak structure with increasing film thickness.

In the following a morphologic investigation of PTCDI on KBr(100) by UHV-AFM experiments of thin film and bulk is given. The investigated film thicknesses are 0.2 ML and 4.9 ML, which are shown in Fig. 4.40. An overview of the overgrown KBr substrate is given in Fig. 4.40a, featuring a terraced surface with steps corresponding to the lattice constant of KBr of ∼ 6.60 Å. This is seen in the graph below which shows a line scan taken along the white line. Fig. 4.40b shows a detail of the larger AFM scan in Fig. 4.40a.

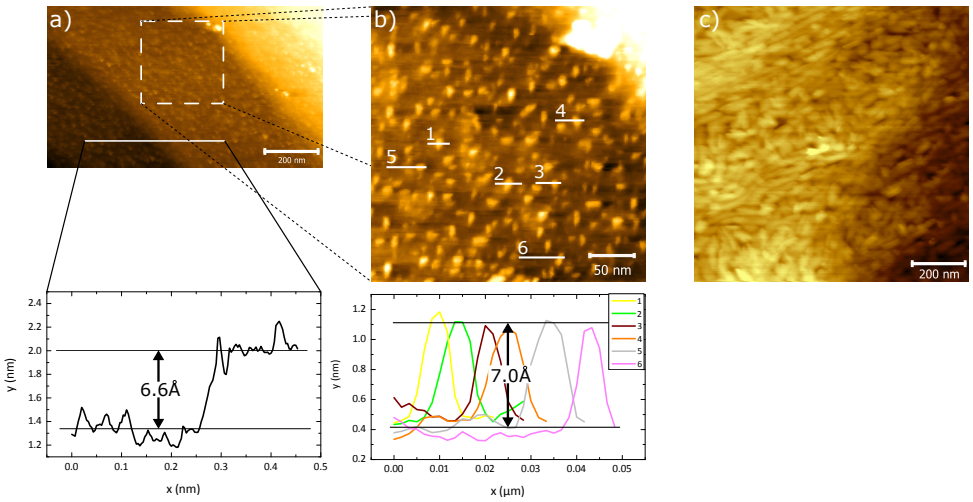

Figure 4.40: Top panel: UHV-AFM scans of PTCDI deposited on KBr(100). The film thicknesses are a), b) 0.2 ML and c) 4.9 ML with height scales 1.5 and 6 nm, respectively. Bottom panel: Line profiles of respectively a) KBr step and b) PTCDI crystallites.

PTCDI aggregates can be distinctly located on the KBr surface, revealing an island like growth with the formation of many small isotropically distributed elongated islands (15 x 8 nm). A large fraction of the molecular aggregates have heights of ca. 7 Å as seen in the line profiles below the AFM scan. This is similar to the distance between the [020] lattice planes (0.724 nm) of the bulk PTCDI crystal. This indicates that the molecules predominantly do not lie flat on the surface but are tilted like in the bulk crystal with the [020] plane as contact plane. However, also aggregates with deviating heights and lower islands can be found, implying that also other orientations are present, as for example flat lying molecules. At a higher coverage, the thin film morphology is characterized by formation of small, slightly elongated crystallites with no preferred single in plane orientation (Fig. 4.40c). In comparison the grown thin film structures look fundamentally different than the nominally same KBr/PTCDI structures by Topple et al.[250] There, needle shaped islands with dimensions of 150 nm × 30 nm × 1.5 nm are prevalent. Those are far more elongated than the islands measured here, while the height corresponds to 2 MLs of the bulk crystalline structure. Furthermore, in contrast to our findings their nucleation density is much lower and step edges were recognized as preferred nucleation sites. This differences can be ascribed to a different preparation of the surface (Topple et al. cleaved the KBr *in situ* and performed a degassing step), resulting in the adsorption of contaminants. Those act as nucleation sites leading to a higher nucleation density and thus smaller islands. As shown in Sec. 2.3.4 changes at the transition from the monomer to the aggregate spectrum are associated with a gas-to-crystal shift.

To learn more about the evolution of the optical spectra and the structure of the PTCDI aggregates, calculations for the gas-to-crystal shift, when molecules are moved from the gas phase into a crystalline morphology were performed by Megow et al. in Ref. [136]. Those calculations assume a site-dependent energy shift, strongly varying with the environment of the molecule. To model the transition of the absorption spectrum, when going from single molecules to aggregates, many contributions affecting the gas-to-crystal shift have to be considered. Those are (i) Coulomb coupling of static charge distributions between molecule m and k, (ii) inductive polarization shifts due to the interaction of a static charge density with induced multipoles, (iii) Frenkel exciton states coupled to charge transfer states (FE/CT), (iv) excitonic shifts due to the coupling of an excited molecule with surrounding molecules and finally (v) dispersion shifts by London forces caused by the formation of instantaneous dipoles or non-zero multipole moments. In Ref. [136] it is shown that the dispersive shift (v) is the dominant effect, responsible for the change during growth of the optical spectra shown in Fig. 4.39. The shift basically arises from non-resonant Coulomb coupling and resonant excitonic coupling. The non-resonant part is calculated by summing the interaction of the molecule m in the first excited state with all surrounding molecules k. Hence, the shift depends on the position of the molecule relative to all other molecules, being $\Delta\mathcal{E}_m = \Delta E_{me} - \Delta E_{mg}$, with the individual level shift ΔE_{me} and ΔE_{mg} of the first excited state e and ground state g. As described in more detail in Ref. [252]

the level shifts can be derived by second order perturbation theory:

$$\Delta E_{ma}(k) = -\sum_{f,f'} \frac{|J_{mk}(ag,ff')|^2}{E_{mfa} + E_{kf'g}}, \tag{4.3}$$

with $a = e, g$. The transition energies are given by $E_{mfa} = E_{mf} - E_{ma}$, $E_{kf'g} = E_{kf'} - E_{kg}$ where f, f' correspond to the higher excited states, while $J_{mk(ag,f'f)}$ is the non-resonant Coulomb coupling between the electronic transition density of molecule m and k. As further described in Ref. [136] Eqn. 4.3 is simplified by using the extended dipole approximation where negative and positive charges $\pm q$ are placed at the boundary of the π-electron system, classified into states with transition dipole parallel and perpendicular to the long molecular axis as seen in Fig. 4.41a. With the extended dipole approximation the non-resonant Coulomb coupling can be factorized according to $J_{mk}(ag,ff') = q(a,f)q(g,f')V_{mk}$, into the effective charges $q(a,f)$, $q(g,f')$ and the distance dependence V_{mk}, which averages over the two different transition dipole directions. Hence, the site-dependent transition energy shift of molecule m can be written as:

$$\Delta\mathcal{E}_m = -QW_m, \tag{4.4}$$

with the molecule dependent Q-factor

$$Q = \sum_{f,f'} q^2(g,f') \left(\frac{q^2(e,f)}{E_{mfe} + E_{kf'g}} - \frac{q^2(g,f)}{E_{mfg} + E_{kf'g}} \right), \tag{4.5}$$

which accounts for all non-resonant electronic transitions and the geometry factor W_m

$$W_m = \sum_k V_{mk}^2, \tag{4.6}$$

which is dependent on the structure of the nanocrystalline film. Here, basically only experimentally accessible quantities are included for deriving the gas-to-crystal shift.

The Q-factor can in general be determined by absorption measurements of an amorphous molecular film, where the experimentally measured spectral shift can be used to identify site-dependent energy shifts dependent on the structure of the film correlating with the disorder average $\langle W_m \rangle_m$ over all molecules. To simulate the effect of different environments the absorption spectra of a PTCDI derivative in various nonpolar solvents is determined. By this the energy shift in the absorption spectra can be described by Bayliss' equation as a function of the refractive index n of the solvent[253]

$$\Delta\mathcal{E}_m = -\mathcal{F}(n^2 - 1)/(2n^2 + 1) = -\mathcal{F}f(n). \tag{4.7}$$

This expression is derived from the interaction of a point dipole in the center of a spherical solute cavity with a surrounding homogeneous dielectric continuum.[252,253] By plotting the respective $S_{00} \rightarrow S_{10}$ transition energies of the absorption spectra in different solvents

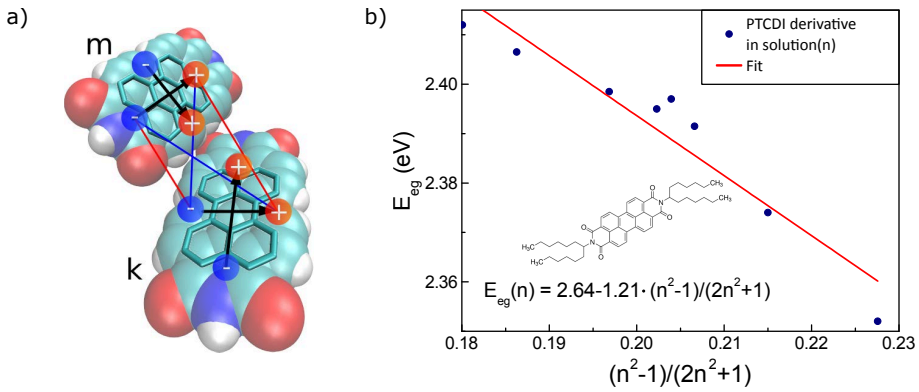

Figure 4.41: a) Space-filling model of two PTCDI molecules m and k. The graphic depicts the interaction in the extended dipole approximation with the positive and negative partial charges of the extended dipole model. b) Transition energies of $S_{00} \rightarrow S_{10}$ for the PTCDI derivative N,N'-bis(1-hexylheptyl)perylene-3,4:9,10-bis(dicarboximide) in different nonpolar solvents with respective refractive indices n.

against $f(n)$, the transition energy shift can be derived. Then, intersection with the y-axis and slope give gas phase excitation energy E_{gp} and the molecule dependent factor $\mathcal{F}$ respectively. Since PTCDI is not well soluble the alkyl substituted PTCDI derivate N,N'-bis(1-hexylheptyl)perylene-3,4:9,10-bis(dicarboximide) is used for the experiment. This is justified since the UV-vis spectrum coincides with that of PTCDI, as the substituents do not affect the π-electron system. Fitting the data for the various absorption spectra yields $E_{gp} = 2.64$ eV and $\mathcal{F} = 1.21$ eV (cf. Fig. 4.41b). Using those values and the refractive index for a thin polycrystalline PTCDI film $n_{PTCDI} = 1.96$[251] in Eqn. 4.7 results in a substantial level shift of $\Delta\mathcal{E}_m = -400$ meV. Calculations to obtain the absorption spectra were performed utilizing Molecular Dynamics (MD) simulations to determine the crystalline geometry as further explained in Ref. [136] and Supporting Information therein. The theoretical optical spectra were generated by Megow, Körzdörfer, Renger and May, hence the exact procedure to do so is not discussed in detail here. However, the significance of the different contributions is described in the following. The shift caused by Coulomb coupling (i) is found to be small (< 5 meV) and hence inductive polarization shifts (ii) are neglected. FE/CT coupling (iii) is neglected due to its small effect as well, as is justified in Refs. [136, 159, 254, 255]. Excited states and transition partial charges were calculated by Density Functional Theory (DFT) and time dependent DFT, used to determine the resonant excitonic coupling (iv) with respective screening factors, resulting in a shift of 20 meV.[256] The single monomer spectrum of PTCDI is modeled with a single vibrational progression per molecule and the single particle approximation is used to derive an electron-vibrational Hamilton matrix where a single vibronically excited molecule couples to surrounding molecules in the vibrational ground state. The absorption line shape results as the sum over all exciton levels α with transition energies E_α, weighted by the respective oscillator strengths and broadened by a Gaussian profile with FWHM of 0.15 eV. Assuming a perfect crystalline layer from a cube with 4.5 nm edge length, it is not possible to reconstruct the experimental spectra as depicted in Fig. 4.42a for 1, 3 and 5 MLs of PTCDI.

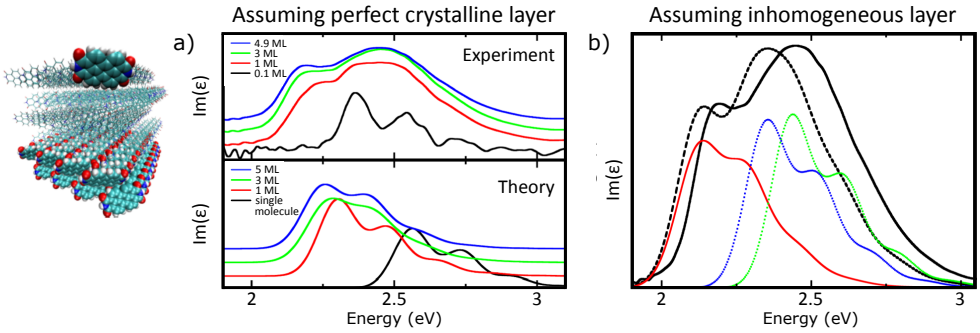

Figure 4.42: a) Measured Im(ε) spectra of different thicknesses of a PTCDI film (upper panel) and computed absorption line shapes assuming perfect two-dimensional films (lower panel). Spectra are shown with an offset for better visibility. The black line of the measured spectrum represents 0.1 ML coverage, while the calculated black line shows the absorption spectrum for a single PTCDI molecule on the surface, according to the geometry on the left. b) A partly inhomogeneous film is assumed. Solid black line: experimental spectrum for a 4.9 ML film of PTCDI on KBr. Dashed black line: calculated spectrum of a nanocrystalline film of nominally 5 ML thickness (see text). Red line: calculated spectrum of a crystalline film composed of 5 ML arranged as on the left. Dotted lines: calculated spectra for two types of thin films consisting of regular arranged small crystallites each containing 12 molecules.

The dispersive energy shifts have been computed assuming periodic boundary conditions in the directions parallel to the KBr surface. Using Eqn. 4.7 the Q-factor can be calculated, with the numerically calculated W_m and the experimentally obtained $\mathcal{F}f(n)$. This results in $Q = 3.2$ eVÅ^2 for the 5 ML perfectly crystalline film. Comparing experiment and calculated spectra in Fig. 4.42a shows that the experimental spectrum of a 0.1 ML is strongly red-shifted compared to the monomer spectrum. This is due to the fact that for the calculated curve upstanding molecules were assumed, while in the case of the experiment molecules are expected to lay flat on the surface in the first ML and thus receive an additional red-shift. The experimentally observed red-shift with increasing coverage is also seen in the calculated spectra, however, the broad peak at around 2.5 eV cannot be reproduced. The calculated spectra still feature a vibronic progression at 5 ML coverage. This suggests that using a perfect crystalline layer for the calculation is too naive. Since it appears that the measured thin film spectra consists of a red-shifted absorption peak and a broad band in the spectral range of the solution spectrum a second phase of crystallites is assumed. This is a disordered phase of small crystallites (12 molecules), which contribute to the broad feature at 2.5 eV, while perfectly grown crystallites constitute the peak at 2.1 eV (red line in in Fig. 4.42b). This assumption is also corroborated by the AFM scans, exhibiting crystallites of various sizes. For the disordered phase two configurations are considered, consisting of 12 π-stacked molecules (green line in in Fig. 4.42b) and a cluster without π-stacking (blue line in in Fig. 4.42b). The ratio between ordered and disordered phase is assumed to be nearly 1:1, considering the height of the different features. The Q-parameter was therefore recalculated taking into account the size-distribution of crystallites in the film. Because of the fact that the average over the W_m is smaller in a disordered film, setting $Q\langle W_m\rangle$ equal to the experimentally obtained $\mathcal{F}f(n)$ yields a larger

$Q = 4.26$ eVÅ^2. Hence, also the lineshape for a perfect crystal in Fig. 4.42b is red-shifted with respect to the one in Fig. 4.42a. Best agreement with the experimental spectrum was obtained when assuming that the PTCDI film consists to 53 % of the ordered phase. The red-shift of the calculated curve by about 0.05 eV may be due to errors when deriving the parameters $\mathcal{F}$ and E_{gp}. The only '*free parameter*' used in order to calculate the spectrum in Fig. 4.42 is the structure of the disordered film. (its ratio with respect to the ordered phase is more or less fixed by the integral over the lineshapes). A reduction of the packing density by more than 30 % results in blue-shift of at least 0.2 eV with respect to the spectrum from the ordered crystal. The assumption of disorder in the film leads to a broad and unstructured absorption band as modeled by the simulation.

Conclusion

In summary, DRS experiments of PTCDI on KBr proved to be a method to observe the *in situ* growth of molecules and analyze the structural characteristics by using calculations to model absorption spectra of polycrystalline thin films. For this purpose, first the $\mathrm{Im}(\varepsilon)$ spectra of the molecule were extracted from the DR spectra using an approximation formula. Those were then reconstructed by simulating the gas-to-crystal shift a molecular spectrum experiences when brought in a crystalline configuration. For this, the special morphology of the PTCDI crystallites on the KBr surface is considered. The calculation showed that the distinct double-peak structure in thin film DR spectra of PTCDI on KBr originates from the coexistence of two molecular phases. Large crystals, which can be recognized in AFM scans, give rise to the component on the low-energy side. The second feature is originating from a phase of loosely-packed smaller aggregates resulting in a weaker gas-to-crystal shift as most molecules reside at or close to the surface. By this, dispersion effects were recognized as dominating for shifts in the spectra while site-dependent structural disorder was as well identified to have a strong impact on the spectra.

4.5.2 Molecules on Absorbing Substrates: L4P on ZnO

In the preceding section the growth of molecules was observed via optical spectroscopy on a transparent substrate, allowing a structural analysis. In this section the challenge is to investigate the molecules on an absorbing substrate. The evolution of the optical properties are reflected by DRS, however, in this case the dielectric properties of the deposited chromophore cannot be acquired as easily. It will be shown that it is possible from differential reflectance data to extract the contribution of the molecule by using a three-layer system and the oscillating model introduced in Sec. 2.4.3. This will be investigated with the system of L4P on ZnO (→ Sec. 4.1.1). Owing to the exciton resonance of the S_0-S_1 transition with ZnO and the high radiative yield of L4P makes this an attractive hybrid structure combination to enable resonant energy transfer or hybrid excitons.[156,219] With the sensitivity of the DRS it can be demonstrated that those favorable properties are unaffected even at the heterointerface just where inorganic and organic meet.

As shown before in Sec. 4.1.1 L4P features sharp resonances in the absorption spectrum, which match the absorption of the ZnO crystal spectrum. This property is reflected in Fig. 4.43a, where the absorption spectrum of L4P in chloroform (top) is compared with

the refractive index of ZnO (bottom), showing that both materials exhibit an absorption feature at around 3.3 eV. For the experiment it has to be considered that most crystal systems are anisotropic for incident electromagnetic waves, leading to birefringence for all directions offside the optic axis of the crystal. For the uniaxial ZnO the optic axis is parallel to the c-axis of the crystal, so that by using c-plane crystals no polarization dependence for the refractive index of the substrate has to be considered. Hence, either ZnO(0001) or ZnO(000$\bar{1}$) are possible candidates, whereas ZnO(000$\bar{1}$) is chosen in this study due to its simpler handling and growth properties. The thickness-dependent DR spectra were measured *in situ* during MBE growth. The optical functions of a bare epitaxially overgrown ZnO substrate was determined beforehand by ellipsometry measurements (performed by SENTECH Instruments GmbH).

Fig. 4.43b shows the measured DR spectra exhibiting a nominal film thickness of 0.05 to 8 nm, determined via quartz microbalance grown at RT with a deposition rate of about 1 Å/min. In contrast to the initial sub-ML spectra of PTCDI on KBr, the spectra of L4P on the absorbing medium differ from the monomer spectrum of the molecule. Still, away from the ZnO band gap the features of the monomer spectrum are well recognizable. Noticeable is furthermore a considerable red-shift of the peaks (marked by lines in Fig. 4.43) with increasing coverage, which converges at a maximal red-shift of 50 meV at a thickness of around nominally 3 nm. Hereafter, the qualitative change of the spectra is small. Striking

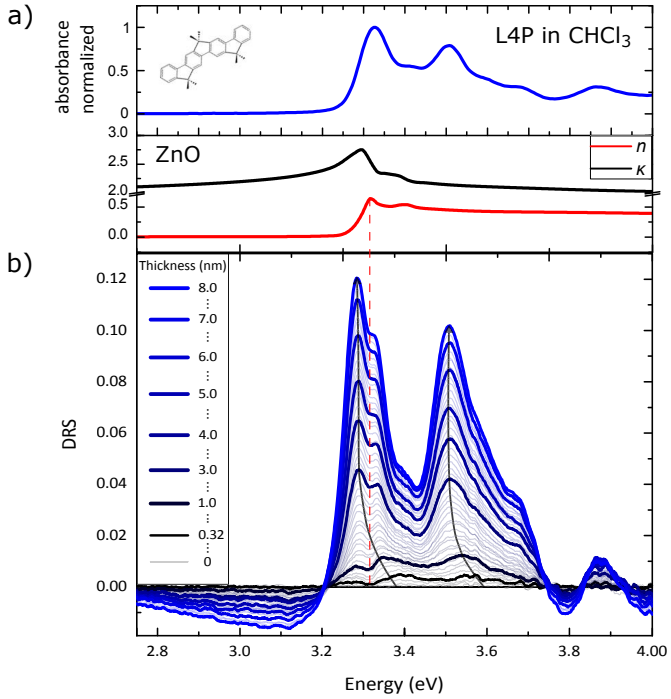

Figure 4.43: a) Absorption spectrum of L4P in Chloroform (top) compared with refractive index n and extinction coefficient κ of ZnO (bottom). b) Drift-corrected DR spectra of L4P on ZnO(000$\bar{1}$) with an integration time of 50 ms and 600 averaged measurements per spectra. The shift during growth and the influence of the ZnO absorption at 3.31 eV are indicated.

is that now the shape of the spectra above this thickness bears a strong resemblance with the absorption spectrum of L4P in solution even for films with a total thickness of 8 nm. The only pronounced deviation from the absorption spectrum is located at the position of the ZnO band gap at 3.31 eV. Here, the ZnO absorption leads to a notch in the DR spectra, creating the impression of two peaks at the main peak of the $S_0 - S_1$ transition. The ratio of the '*two peaks*' changes during deposition due to the gas-to-crystal shift, causing the first L4P absorption peak to float over the ZnO band gap. Another striking feature is the negative decreasing signal below 3.2 eV with increasing thickness. This is an indication for thickness oscillations, originating from thickness interferences, their pronounced emergence can albeit also be a sign for island formation.[94] To quantitatively analyze the data and extract the dielectric function of the molecule the spectra are fitted numerically by the oscillator model. To demonstrate the effect of inhomogeneous broadening Lorentzian and Voigt profiles are compared in their quality of fitting the data, where the analytical approximation of Eq. 2.66 is used for the Voigt profile. The results for selected coverages are presented in Fig. 4.44. The fits for Lorentz and Voigt profiles use three and four parameters respectively for every peak with an additional parameter for the background dielectric function ε_∞. The other parameters are oscillator strength β, oscillator energy E_0 and the FWHMs for Lorentz and Gauß distribution γ_L and γ_G. For the fitting of the L4P spectra 6 oscillators are used to account for the vibronic transitions of the L4P molecule. This can be justified by looking at the absorption spectrum of L4P in Fig. 4.43a, where the three most distinct peaks correspond to the $S_0 - S_1$ transition with the first vibronic progression at an interval of approximately 185 meV and a second one with vibrational energies of 80 meV. The energies of the oscillators are used as initial values for the fit procedure, which then are varied within certain boundaries. In direct comparison of the fits, it is apparent that the Voigt profile (Fig. 4.44b) is more suited than the Lorentz profile (Fig. 4.44a) to describe the molecular response to light. With the simple Lorentz profile it is not possible to adequately fit the features of the different peaks due to the inhomogeneous broadening, which is not considered in the Lorentz approach. With the use

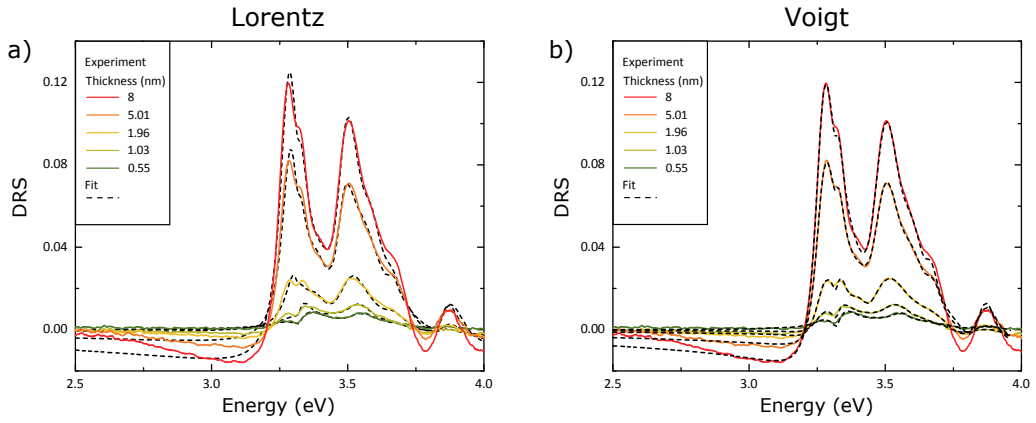

Figure 4.44: Fitted graphs of selected experimental L4P DR spectra of Fig. 4.43 comparing the a) Lorentz and b) Voigt profile.

of the Voigt profile, however, the DR spectra can be fitted excellently. Noticeable is a slight deviation of experimental and fitted data at the position of the band gap of ZnO at 3.31 eV. This is explainable by the strong dependence of the DRS signal on the complex refractive index of the ZnO substrate in the range of the band gap. Small errors in the simulation of the ellipsometric data can then in turn have a strong impact on the end result of the DRS simulation. Furthermore, both simulations show a decrease of the DR spectra with increasing thickness below zero in the low energy range reflecting thickness oscillations. However, also with the Voigt profile it is not possible to perfectly fit the experimental feature in this area. This can also be an indication that the morphology of the organic layer is not a homogeneously closed layer. It was shown before for PTCDI and discussed in detail elsewhere that the morphology of the organic layer can affect the spectra to a great extent.[94,237] This will be discussed in the following:

In general structural deviations from a perfect layer-by-layer growth can give an explanation for a discrepancy between experimental and simulated spectra. That such an assumption of a rough surface with piled up structures is reasonable can be deduced from AFM scans. Such an *ex situ* AFM scan of the ZnO$(000\bar{1})$/L4P surface is seen in the inset of Fig. 4.45b. The surface is clearly not composed of a closed film of flat lying molecules but islands and needles of up to 500 nm are recognizable. However, those measurements have to be treated with care as they were taken in ambient conditions after the growth, where the molecule is known to rearrange, while *in situ* measurements show a smooth layer. In the case of piled island structures, the simple model of layer-by-layer growth cannot be assumed unconditionally anymore. A sign that the growth mode deviates from LBL growth can be that there are no isosbestic points present in the DR spectra.[236] Those are intersection points of consecutive spectra, which indicate the presence of an equilibrium of two species $A \rightleftharpoons B$, namely transitions from monomer to dimer and trimer. Missing of such a feature can indicate a Stranski-Krastanov like growth. To exemplarily

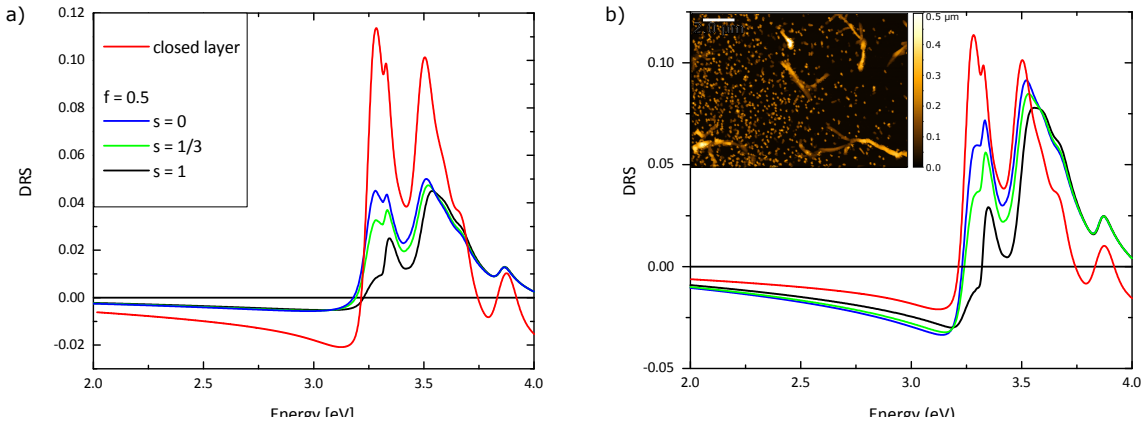

Figure 4.45: a) Simulated spectra for L4P on ZnO$(000\bar{1})$ for a thickness of 8 nm. The figure compares the spectrum of a closed layer with spectra generated with the effective medium approximation for a volume fraction of $f = 0.5$ and values for the shape factor of $s = 0; 1/3; 1$. b) The same spectra with an effective thickness of $d = 16\ nm$. The inset shows an *ex situ* AFM of the surface.

account for such an island formation in the DR spectra a qualitative simulation with an effective medium is assumed (EMA). The molecular islands are modeled as spherical inclusions in a host material, following the Bruggeman approach as described in Sec. 2.4.4. The parameters in this approach are the volume fraction f of the covered surface and the shape factor s, describing the shape of the islands from flat discs ($s = 0$) to needle structures ($s = 1$). Its effect is seen in Fig. 4.45 for a volume fraction of a half-covered surface ($f = 0.5$) in a simulated spectrum of L4P on ZnO. Fig. 4.45a shows simulated spectra for a volume fraction of $f = 0.5$ and values for s between 0 and 1, compared with the simulated spectrum of a closed layer. While the filling factor f basically only shifts the DRS signal in position and intensity, the shape factor also significantly distorts the form of the spectra. Here, the strongest modification occurs for the needle island shape with $s = 1$. Fig. 4.45b shows the same spectra, but by assuming an effective thickness of $d = 16$ nm in the case of a volume fraction of $f = 0.5$, where island structures would pile up twice as high. In the simulated spectra the negative low energy feature nevertheless decreases when assuming piled up structures. Hence, the effective medium approach rather worsens the fit, indicating in fact a rather smooth layer during growth in contrast to what the ambient AFM scans imply. An additional XRD scan did not show any Bragg reflexes either, indicating an amorphous layer without the crystallites seen in ambient AFM. That the preceding simulations of the DR spectra can indeed reconstruct the evolution of the refractive index of the molecule without the assumption of piled islands can be seen in the corresponding evaluated refractive index and extinction coefficient for selected spectra, which are given in Fig. 4.46.

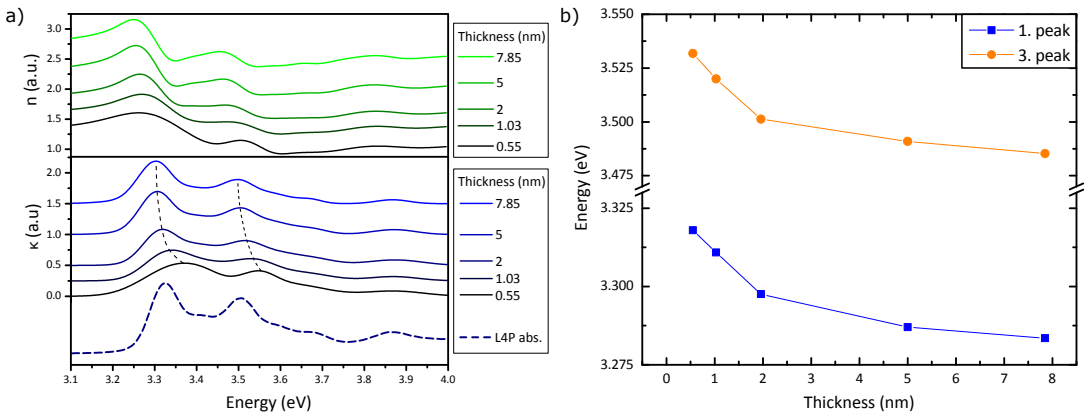

Figure 4.46: a) Simulated refractive index n (top) and extinction coefficient κ (bottom) for L4P on ZnO$(000\bar{1})$ for selected thicknesses. For better visibility the spectra exhibit a vertical offset. The spectra show the evolution of the optical properties for the organic molecule. For comparison the absorption spectrum of L4P in chloroform is shown at the bottom. b) Position of 1^{st} and 3^{rd} peak with increasing coverage.

The initial sub-ML spectra strike the eye by being broad and not as distinct as the following ones as seen in the dielectric function in Fig. 4.46a. This is in contrast to the results of PTCDI on KBr, where especially the sub-ML spectra appear monomeric with distinct features. Here, the evolution proceeds the other way round and the most pronounced spectra

can be derived at higher thicknesses. A reason for this can be an initial greater molecular disorder, where the local environment is different for every molecule in he sub-ML, but additionally also a higher noise at lower coverage can contribute to the broadened spectrum, making an exact determination of the dielectric properties difficult in the beginning. For comparison the simulated extinction coefficient spectra in Fig. 4.46a are shown together with the L4P absorption spectrum in chloroform at the bottom. In this way it is revealed that the absorption spectrum and simulated extinction coefficient for higher thickness nearly perfectly coincide. The simulation therefore confirms the successful application of the fit algorithm to deduce optical properties of a molecular layer on an absorbing substrate, also demonstrating a rather small effect of the shape factor. Furthermore, those results reveal that only a weak electronic interaction with the substrate and no Charge Transfer (CT) is present, hence no modifications of the optoelectronic properties of the molecule directly at the inorganic/organic interface are observed. The general red-shift seen in the DR spectra as a consequence of increasingly interacting molecules when forming aggregates and an additional polarization effect with the surface is also confirmed by the simulated spectra. The quantitative extent of this shift for the most distinct first and third peak is given in Fig. 4.46b. The trend for both peak positions is very similar. The calculated shifts for an end thickness of nominally 8 nm are 40 and 50 meV for 1^{st} and 3^{rd} peak respectively. The most noticeable change is, however, observed for low coverages when also the environment of the molecules changes the most. After deposition of 2 nm the change clearly saturates, since the short-ranged molecule-molecule interaction in islands does not strongly contribute to changes in the spectra anymore.

Conclusion

Altogether this study showed that interaction of the ladder-type quaterphenyl L4P with the ZnO interface can be analyzed down to the sub-ML range by DRS measurements. By extracting the refractive index of the organic molecule from the DR spectra no noticeable modification of the spectral shape and position of neither the molecule nor the underlying ZnO was found. Due to the coinciding absorption spectrum of L4P with ZnO the spectra had to be fitted using the oscillator model. The results of the simulation reveal monomeric features even for thicker films and a remarkable agreement between the fitted extinction coefficient of a grown L4P film on ZnO with its absorption spectrum in solution. Hence, the findings indicate a negligible interaction between neighboring molecules as well as of L4P with the ZnO substrate, *i.e.* significant charge transfer between molecule and ZnO and related band bending or chemisorption can be ruled out. Only a small gas-to-crystal shift of approximately 50 meV in the first MLs is observed, which is attributed to interactions between the molecules. Eventually, it was qualitatively shown that a rough surface can in general considerably change the spectral form of the measured spectra and impose an uncertainty factor in determining the optical parameters of the molecule. However, analyzing the simulated extinction coefficient spectra points to an insignificant effect of a modification in this case.

4.5.3 Molecules interacting with the Substrate: NTCDA and F_6TCNNQ

In the preceding section molecules with little substrate interaction were treated and investigated with DR spectroscopy. Here the consequences on the recorded *in situ* spectra with a non-negligible substrate interaction will be presented. It can be shown that DRS is able to identify charge redistribution at a ZnO interface. Similar experiments by DRS which investigated the interaction with the substrate and show CT and hybridization processes have been performed before, *e.g.* for PTCDA on gold or ZnO.[240,243] However, those experiments could only identify the CT by the emergence of an ion's signature in the spectra. In contrast the experiments conducted here show charge redistribution without this signature but by the change of the substrate's band gap. The molecules investigated here are NTCDA, which is resonant to ZnO and F_6TCNNQ, already known for its charge redistribution at the ZnO interface.[173]

Yet, first of all an experiment will show the progression of the NTCDA DR spectra on a transparent, inert substrate, namely KBr. This allows for extracting the dielectric function of the molecule grown in a thin film. The single crystal KBr(100) (Korth Kristalle, Germany) sample is cleaved just before loading, NTCDA is then deposited at RT on the substrate with a rate of about 1 Å/min. The DRS data of NTCDA on KBr(100) as a function of thickness varying between sub-ML coverage to nominally 2.4 nm film thickness and evaluated imaginary part of the dielectric function are shown in Fig. 4.47. The DR spectra in Fig.4.47a exhibit the expected red-shift for molecular thin-film deposition and a thickness-dependent increase of the signal. Furthermore, the decrease of the DRS signal below zero for values smaller than 3.0 eV is observed. The data is analyzed in more detail using the calculated imaginary part of the dielectric function ε in Fig. 4.47b. Those spectra are calculated using Eqn. 3.17 and the refractive index of KBr.[245] The first spectrum of 0.1 nm already shows monomeric features at energies above 3.25 eV. For comparison the

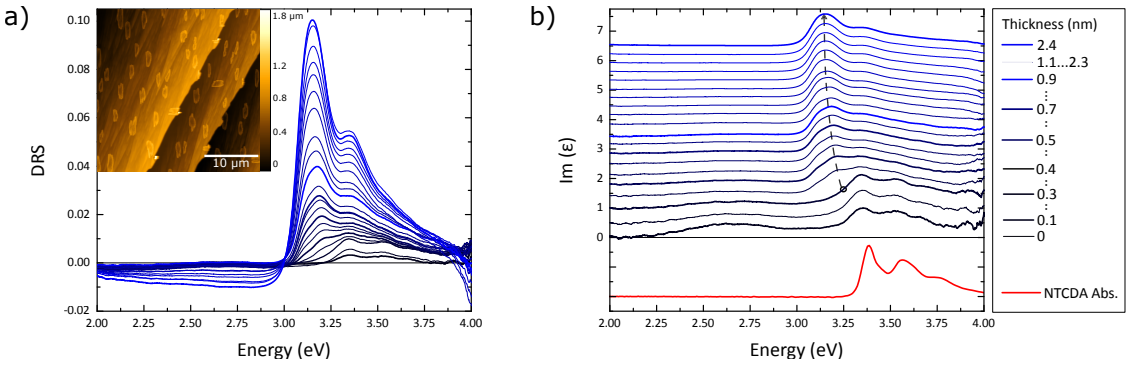

Figure 4.47: a) Drift-corrected DR spectra of NTCDA on KBr(100) recorded with an integration time of 50 ms and 600 averaged measurements for a single spectrum, covering a thickness of up to nominally 2.4 nm. The inset shows an AFM scan of the surface (30 x 30 µm) at the final thickness. b) Calculated spectra of the imaginary part of ε showing also the NTCDA absorption spectrum in methanol for comparison. For better visibility the spectra are depicted with a vertical offset.

absorption spectrum of NTCDA in methanol is shown in Fig. 4.47b, revealing a red-shift of ca. 35 meV for the sub-ML spectra. The following sub-ML spectra reveal a good agreement with the solution spectrum showing three distinct peaks corresponding to the $S_{00} - S_{10}$ transition and the corresponding vibronic progression. However, with completion of the 1^{st} ML (ca. 0.3 nm) an abrupt change in the DR spectra is seen with the emergence of an additional peak at 3.2 eV, which gradually red-shifts. It becomes the dominating peak at around the completion of the 2^{nd} ML, while monomeric features are still visible. Above this point no pronounced change in the spectra is perceivable. This behavior implies the emergence of a second molecular phase when the first ML is completed. Such a transition can be the initial formation of an ordered wetting layer with flat-lying molecules which devolve into a bulk-like phase with the molecular plane perpendicular to the surface as it was shown for NTCDA on graphite and MoS_2.[257] The exact origin for the spectral shape and the underlying crystal structure of NTCDA on KBr will not be treated in further detail here, as the similar system PTCDI on KBr was already extensively investigated in Sec. 4.5.1 and the focus here is the interaction with the ZnO substrate. However, for further evaluation, selected spectra of a sub-ML and thicker film were fitted with three Voigt oscillators to extract the complex refractive index of the molecule for two thicknesses (not shown). Compared to literature the shape of the dielectric function for the higher coverage fits very well with reported values of thick NTCDA films, however the absolute value is only a third of the reported, which can be an issue of backside reflection or different molecular orientation.[164] In the following the extracted dielectric function will be used to investigate the interaction of NTCDA with ZnO. ZnO is used as substrate due to its resonance with the molecule and since it is known as hybrid interface, showing energy and charge transfer for various molecules.[156,243,258] Especially the ZnO$(000\bar{1})$ surface is chosen as it does not exhibit birefringence. A growth experiment was carried out up to a nominal film thickness of 1.4 nm. The drift-corrected spectra of the HIOS are shown together with spectra of NTCDA on KBr as comparison in Fig. 4.48.

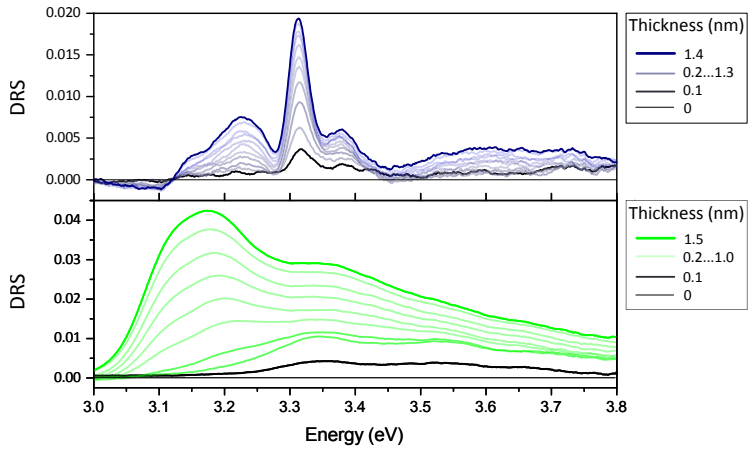

Figure 4.48: a) (top) Drift-corrected DR spectra of NTCDA on ZnO$(000\bar{1})$ recorded with an integration time of 100 ms and 300 averaged measurements for a single spectrum and (bottom) NTCDA on KBr for comparison.

The DR spectra of NTCDA on ZnO exhibit two distinct peaks at 3.31 eV and 3.38 eV, which do not shift during deposition. What first strikes the eye is the sharpness of the peak at 3.31 eV (FWHM $\approx$ 40 meV). Furthermore a low-energy shoulder emerges at 3.22 eV. The peak at 3.31 eV is not present in the NTCDA on KBr spectra and is also much too sharp for a monomeric feature even if a commensurate relation with the substrate would exists. Apart from this the high energy peak at 3.38 eV could originate from the monomer spectrum, being altered by the ZnO absorption, while the emerging low-energy peak could also stem from the same feature which arises on KBr above the 1^{st} ML. To further evaluate the data a simulation of a three-layer system is carried out using the complex dielectric function of the molecule from the previous NTCDA on KBr measurement. Differences for growth of NTCDA on ZnO are generally expected but a qualitative description should be possible using the respective parameters deduced from growth on KBr. Simulations are done for the experimental spectra with a nominal thickness of 0.1 nm and 1.4 nm. The results are shown in Fig. 4.49. Here, it becomes apparent that the simple assumption to use the optical parameters from the previous measurement cannot be applied. The simulated spectra for the assumed three-layer system in Fig. 4.49 cannot reproduce the experimental features. Most striking is the clear deviation at the position of the ZnO band gap. The sharp peak in the experimental spectra at 3.31 eV corresponds to a distinct minimum in the simulation. This is despite the fact that the first molecular oscillator at a nominal coverage of 0.2 nm exhibits its resonance at 3.34 eV close to the dominant peak. However, the oscillator strength does not suffice to exceed the ZnO absorption at 3.31 eV in the simulation. The simulation for the higher coverage shows that the oscillator is too much red-shifted and too broad to create the sharp peak at 3.31 eV. Noticeable is also that the simulated spectra in Fig. 4.49b exhibit considerably larger intensities, indicating that the observed DRS signal originates mainly from a ML of molecules. This indicates a Stranski-Krastanov like growth mode with a molecular wetting layer, an observation corroborated by AFM scans showing scattered crystallites on a predominantly flat surface, which dewets over time (not shown). The obtained results lead to the conclusion that either the determined molecule's dielectric function of NTCDA on ZnO is completely

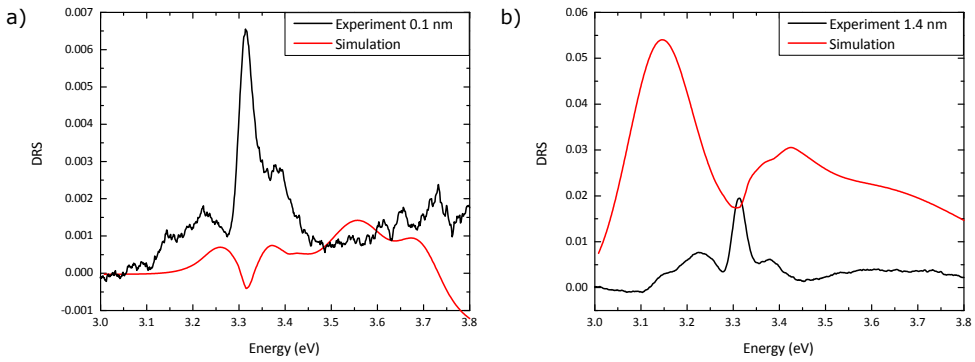

Figure 4.49: Experimental DR spectrum of a) 0.1 nm and b) 1.4 nm layer NTCDA on ZnO(000$\bar{1}$) with simulation using the respective dielectric functions of NTCDA extracted from the experiment on KBr.

different than on KBr or that the dielectric function of ZnO changes with deposition of the molecule. The first possibility would demand a very sharp peak for the molecule's dielectric function at 3.31 eV, which surmounts the ZnO absorption and additionally does not shift during deposition. This, however, is very unlikely. For the second assumption of an altered dielectric function it is helpful to take a look at electro-reflectance spectra, where just like for DRS the normalized change in reflectance is recorded. At electro-reflectance the band structure of a semiconductor is modified by modulating its internal electric field by photo-injection, resulting in third-derivative modulation peaks similar to the ones observed here.[259–261]

That the striking resemblance with such derivative peaks is more than just a structural similarity but indeed based on the same physical origin is shown in the following. The connection between those seemingly different phenomena is an induced surface band bending of the inorganic semiconductor, albeit in this case by CT to the molecule. By this means an electric field at the semiconductor surface is created. The electronic band structure is in the first place bent in the vicinity of the surface due to the interruption of the crystal's periodicity and hence the formation of a space charge region with extension d_{SCR} occurs. Consequently, the band structure is nonlinearly bent up or down at the surface, which is described by the Poisson equation. This results in an approximately linearly decreasing electric field in the space charge region. The band bending can be increased by an interacting adsorbed molecule. The change of the internal electric field is then visible in DR spectra as a derivative-like peak at the band edge. To determine the change in the dielectric function of ZnO, the effect of the electric field on the Coulomb potential of a Wannier-Mott exciton is considered according to a theory by Blossey.[259] The theory assumes only one isotropic and parabolic conduction and valence band, with only Coulomb interaction present between the electron-hole pair. Since A and B exciton are only separated by 6 meV for ZnO and the C exciton is not excited the assumptions are still reasonable. By applying an electric field the Coulomb potential is asymmetrically lowered also causing a widening of the well (see inset in Fig. 4.50). For fields strong enough to lower the barrier height below the electron's potential level the exciton is ionized. For the dielectric function the ratio between the applied field E and the ionization field E_I of the exciton is the significant quantity.[18] The basis for Blossey's approach is the Schrödinger equation for a hydrogenic atom in an electric field, using a reduced mass for the exciton. The imaginary part of the dielectric function is for the unpolarized radiation given in the following way:[259]

$$\varepsilon_2(\omega) = \frac{4}{3}\varepsilon \left| \frac{\mathbf{p}_{cv}}{m\omega a_{ex}} \right|^2 \phi^2(0), \tag{4.8}$$

where ε is the static dielectric constant, $\mathbf{p}_{cv}$ the interband momentum-matrix and a_{ex} the exciton radius of the semiconductor. The dependence of the electric field is included in the dimensionless density-of-states function $\phi^2(0)$ which contains all allowed transitions for the

18 For ZnO the ionization field accounts to $E_I = 2.56 \cdot 10^7$ V/m

eigenstates κ_i:

$$\phi(0)^2 = \left(\frac{E}{E_I}\right)^{1/3} \sum_{i=1}^{\infty} f_{\kappa_i}^2(0) g_{\kappa_i'}^2(0). \tag{4.9}$$

with the solutions f and g of the Schrödinger equation in the effective mass approximation for the dimensionless distance $x > 0$ and $x < 0$ respectively. Additionally to Eqn. 4.8 a Lorentz broadening Γ of the exciton at RT has to be considered which is given by Dow:[262]

$$\varepsilon_2(\omega,\Gamma) \approx \frac{2\Gamma\hbar}{\pi} \int_{\omega_a}^{\omega_b} \frac{\varepsilon_2(\omega')}{\hbar^2(\omega-\omega')^2 + \Gamma^2} d\omega', \tag{4.10}$$

with the considered spectral range $\omega_a < \omega < \omega_b$. In order to obtain also the real part of the dielectric function the Kramers-Kronig relation has to be applied (cf. Sec. 2.4.2).

$$\varepsilon_1(\omega,\Gamma) \approx 1 + \frac{2}{\pi}\mathcal{PV} \int_{\omega_a}^{\omega_b} \frac{\omega'\varepsilon(\omega',0)}{\omega'^2 - \omega^2} d\omega' \tag{4.11}$$

With the known constants for ZnO, the refractive index and extinction coefficient can be calculated for different E/E_I ratios as is done in Fig. 4.50. For ratios below 1 the spectra have excitonic character and comparing the theoretical spectra of low electric field with the experimental ellipsometry spectrum shows a good agreement. Although a striking deviation to the experimental spectra is the missing shoulder about 70 meV higher in energy, attributed to exciton-phonon complexes, which are not considered in the model.[263] With increasing E/E_I ratios a decrease of the excitonic maximum is observed. Moreover, the maximum energy slightly shifts to lower energies.

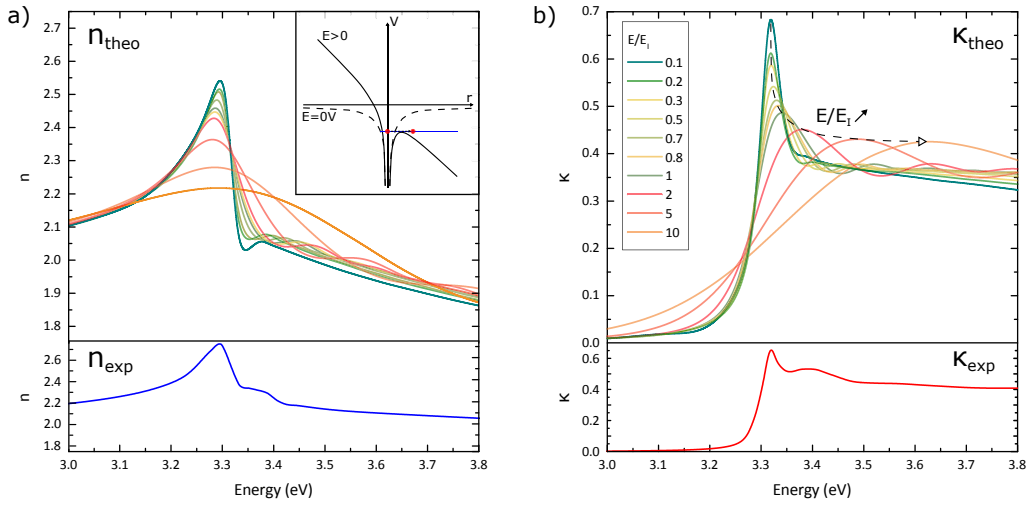

Figure 4.50: a) Calculated (top) and experimental (bottom) refractive index n and b) extinction coefficient κ for ZnO at different E/E_I ratios. The inset in a) shows a sketch of the exciton's potential well with and without externally applied electric field.

This is contributed to the broadening of the potential well of the exciton, leading to a decrease of the electron levels, which is known as second-order Stark effect. If the field ratio gets above 1 the exciton is ionized and the resulting spectra are dominated by the Franz-Keldysh effect. Here, the excitons vanish and the maxima originate only from the Franz-Keldysh oscillations. This is associated with the strong shift of the maximum to higher energies, a broadening of the absorption band and also the lowering of the absorption edge. The field-dependent ZnO spectra of refractive index and extinction coefficient can now be used to evaluate the field-induced changes in the differential reflectance signal. The simulated DRS is generated for the reflectance of $E/E_I = 0.1$ and an additional layer with higher field ratio as shown in Fig. 4.51. The spectra show a minimum at approximately 3.3 eV, which deepens with higher fields but shifts by 12 meV to lower energies when increasing to E/E_I=1. At around 3.35 eV a sharp peak arises, which increases in intensity for higher fields, while the energy first shifts to lower energies and then begins to shift by 4 meV to higher energies. Next to it another minimum at around 3.4 eV shows up, followed by emerging oscillations at higher energies, stemming from the Franz-Keldysh effect. Thus, a qualitative structural resemblance with the features in the NTCDA spectra can be generated by assuming a change in the ZnO absorption. General deviations are expected since the simulation of the DR spectra assumes an abrupt change of the band structure, which in reality linearly decreases at the surface in the depletion region which is shown in the following. To account for this the actual structure and depth of the band-bending has to be known. Moreover, in this model the molecule's absorption is not included. Yet, the simulation suggests that the assumption of a ZnO band gap modification by CT processes with the molecule during the deposition seems plausible. However, the proof that band bending and as a consequence the change of the internal electric field is really the origin of the observed features in the DR spectra for NTCDA on ZnO is still lacking. For further evaluation of this phenomenon a different molecule is investigated, where the induced band-bending is well known.

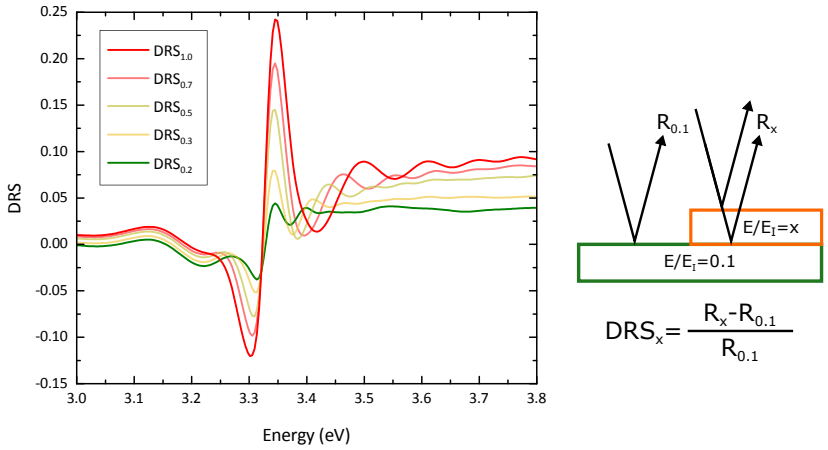

Figure 4.51: Simulated DRS signal in dependence of the electric field, using 50 nm as thickness for the space charge region. The reference spectrum uses the previously calculated n and κ spectra for a electric field ratio of $E/E_I = 0.1$ as shown in the sketch on the right.

For the molecular acceptors F_4TCNQ and F_6TCNNQ on ZnO the induced band-bending has recently been presented with photoemission studies and explained by a minute electron transfer at the interface.[172,173,264] Since the change of the surface band bending must result in a distinct change of the DRS signal during deposition, the DR spectra pose a general tool for analyzing the electronic structure of the surface. In the following F_6TCNNQ (Novaled GmbH) will be used to investigate if the preceding observations can be explained by CT processes. To be able to exactly describe the observed features in the NTCDA DR spectra the electronic structure has to be taken into account. CT for F_6TCNNQ on the ZnO(0001) surface has been associated with a considerable increase in the total work function $\Delta\phi$. The observed work function change can be described in a simple electrostatic model as the sum of two contributions:[264]

$$\Delta\phi = \Delta\phi_{BB} + \Delta\phi_{ID}. \tag{4.12}$$

Namely the formation of a space charge region in the inorganic semiconductor due to surface band bending ($\Delta\phi_{BB}$) and secondly an interface dipole due to charge separation ($\Delta\phi_{ID}$) which charges the molecules. The band bending of a HIOS occurs at the interface due to charge transfer. The CT creates differences in the charge concentration across the hybrid interface, resulting in a counteracting electric field and eventually in bending of the band gap of the inorganic semiconductor. Thereby a space charge region emerges. As shown before the spectra are very sensitive to this band bending, which makes it possible to simulate the DR spectra when extent of the space charge region and electric field at the surface are known. Prior to the DRS study, a Kelvin probe experiment is performed to confirm if a change in the work function can be observed as well in the present sample. For this, the ZnO substrate was scanned *in situ* by parallel non-contact AFM and Kelvin measurements before and after deposition of F_6TCNNQ as shown in Fig. 4.52.
By this, the work function change induced by the molecules can directly be determined. Fig. 4.52a displays the pristine surface of a ZnO(0001) substrate overgrown with approximately 100 nm ZnO. This reveals a holey surface structure with an overall RMS roughness of 0.4 nm. The Kelvin measurement in Fig. 4.52b, however, shows a very uniform surface potential with an average value of -0.26 V. A subsequent scan of a HOPG surface as reference yields a CPD of -0.43 V. Using the known work function of HOPG as well as the equation of Sec. 3.2.4, the work function of the tip results in: $\phi_{\mathrm{Tip}} = \phi_{\mathrm{Sample}} + eV_{CPD} = 4.05\ eV$ and likewise $\phi_{\mathrm{ZnO}} = 4.31\ eV$. Scans after the deposition of the molecule expose the formation of crystallites with heights of up to 100 nm. To avoid contamination of the tip by molecules a smaller area of 0.5x0.5 µm^2 is scanned on the F_6TCNNQ covered sample as shown in Fig. 4.52c. The corresponding Kelvin scan in Fig. 4.52d reveals a profound work function change to an average value of -2.34 eV. With this the new work function is $\phi_{\mathrm{ZnO-F_6TCNNQ}} = 6.39\ eV$ and so the work function change accounts to $\Delta\phi = 2.08\ eV$. Previous UPS measurements accounted the total work function change for F_6TCNNQ deposited on ZnO(0001) to be 2.4 eV. The slight deviation can be assigned to a different surface preparation resulting in different doping concentrations or surface terminations and by this a change of the initial ZnO work function.[173,265] Hence, the results are consis-

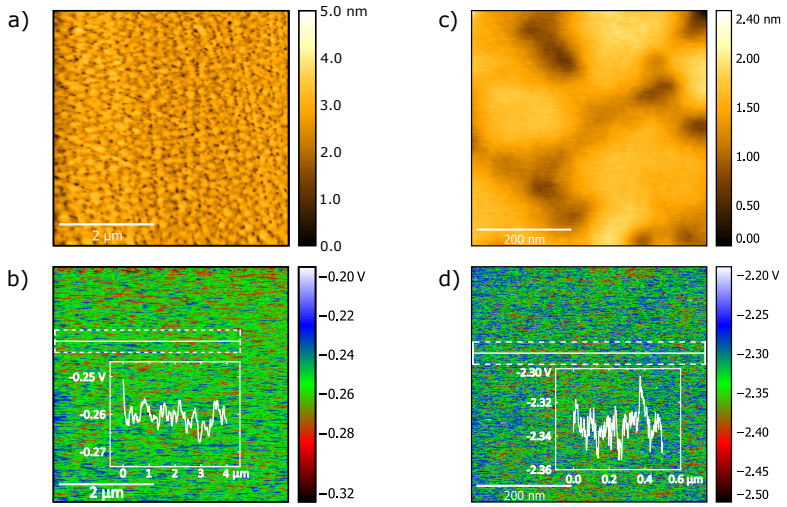

Figure 4.52: a) and c) Non-contact *in situ* AFM of ZnO(0001) before (5 x 5 µm^2) and after (0.5 x 0.5 µm^2) deposition of F_6TCNNQ. b) and d) Corresponding KPFM scans, with line scan profiles as inset.

tent with the UPS measurements, confirming band bending of the surface as observed before.

In the next step a DRS measurement is performed as reference to obtain the spectral shape of F_6TCNNQ on a transparent, non-interacting substrate. For this purpose F_6TCNNQ is deposited at RT on $Al_2O_3(11\bar{2}0)$ with a growth rate of about 0.5 Å/min. The resulting DR spectra are displayed in Fig. 4.53, showing also an absorption spectrum of the neutral molecule in dichloromethane solution for comparison. The spectra feature a broad unstructured peak at 2.7 eV with a general resemblance to the absorption spectrum in solution. However, the feature is much broader (FWHM: 0.5 eV compared to 0.35 eV) and exhibits a slight blue-shift during deposition. The broadening indicates that the molecules are rather randomly distributed on the surface, while the blue shift can arise due to a different packing of the molecules.

Subsequently, the interaction of the acceptor molecule F_6TCNNQ with the surface and potential band bending is investigated by DRS using ZnO(0001) as substrate. For this system the known photoemission data can be used to simulate the spectra.[173] The results of the DR spectra for F_6TCNNQ grown at RT with a growth rate of about 0.5 Å/min on ZnO(0001) are shown in Fig. 4.54. In great structural resemblance to the NTCDA spectra the sub-ML DR spectra of F_6TCNNQ show the emergence of a sharp peak at approximately 3.31 eV with a shoulder at energies around 3.37 eV (see Fig. 4.54a). Apart from the low energy shoulder in the NTCDA spectrum, which was attributed to the molecular absorption, the same features of the NTCDA spectra are recognized also in the spectra of F_6TCNNQ on ZnO. It shows that the energetic maximum shifts during deposition, at first to smaller energies, then after a thickness of 0.1 nm to higher energies, whereby a second shoulder at lower energies arises. The shift saturates at an energy of

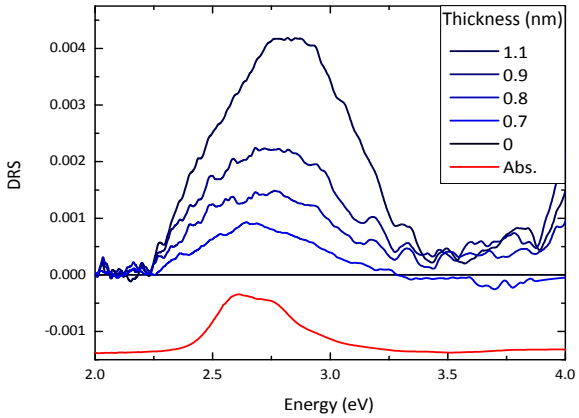

Figure 4.53: DR spectra of F_6TCNNQ on $Al_2O_3(11\bar{2}0)$ (top), compared with the molecular absorption measured in dichloromethane solution (bottom).

3.323 eV and a thickness of nominally 0.29 nm, which can be ascribed to the thickness of a closed monolayer of molecules directly interacting with the surface. The closing of the ML can be considered as the first phase of growth. Striking is the missing feature of molecule absorption at 2.7 eV at this phase. In the following phase, distinct minima emerge on the left and right of the sharp peak at around 3.3 eV and 3.38 eV, while at the high-energy side above 3.4 eV the signal becomes increasingly negative (cf. Fig. 4.54b). Furthermore, the feature of the molecule evolves in this phase as a broad maximum at 2.7 eV, exhibiting the same shape as on sapphire (shown for comparison at the bottom of Fig. 4.54b). In the process of this decrease the qualitative shape of the spectrum does not change. The progression of the spectra is discussed in the following.

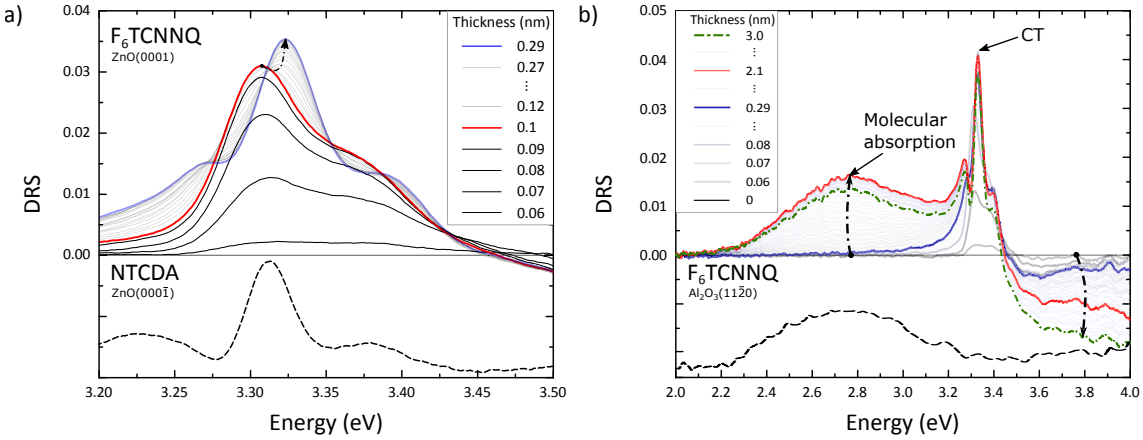

Figure 4.54: a) Drift-corrected DR spectra of the first ML of F_6TCNNQ on ZnO(0001) recorded with an integration time of 100 ms and 300 averaged measurements per spectra (top), features the final spectrum of NTCDA on $ZnO(000\bar{1})$ for comparison (bottom). b) DR spectra from sub-ML to final thickness for broader spectral range (top) and for comparison a 1 nm thick layer of F_6TCNNQ on $Al_2O_3(11\bar{2}0)$ (bottom).

The first phase of growth is characterized by the formation of the first ML and the interaction of this molecular layer with the underlying substrate. As mentioned before, this interaction with the surface is defined by CT, which induces surface band bending. This interaction is limited to the first layer of molecules, which effectively are located on the surface. Therefore the shift of the sharp main peak is also only observed in the 1^{st} ML. As seen before for the simulated DRS spectra, for different electric fields the course of the shift, first to lower then to higher energies, is correlated to an increasing electric field, or in this case to an increasing band bending with the covering of the 1^{st} ML. Hence, the assumption from the NTCDA measurement that the sharp peak in the proximity of the ZnO band gap in the DR spectra is induced by band bending can be validated by the experiment with F_6TCNNQ. The same features are observed in both cases, while band bending has been experimentally verified by photoemission measurements for F_6TCNNQ.[173,264] The shift with increasing coverage, which eventually saturates, can be associated with the closure of the monolayer as already observed in [264]. In the next phase also the molecular absorption is identifiable, although only gradually growing in intensity. The late appearance can be attributed to a different growth mode after the 1^{st} ML is closed. Beside the broad low energy feature associated to the molecules' absorption, there is no indication of an ionized molecular absorption in the spectra as expected for CT. An additional measurement in the infrared below 1.4 eV to detect eventual low energy resonances of the ionized molecules did not show any signs either. However, since a minute CT in the range of only 0.02 electrons per molecule has been described by UPS measurements, it is not expected to observe a signal of the ionized molecule. During the whole deposition a decrease of the signal above 3.5 eV can be seen. This can be understood by the absorption of the ZnO in this region, without an absorbing molecular layer on top. In the third phase of growth this decreasing intensity is not restricted to the high energy region, but the whole spectrum decreases in intensity, now due to thickness oscillations from the organic layer.

To quantify the results, the known band bending for F_6TCNNQ on ZnO(0001) from Schultz et al. is used to simulate the DR spectra.[173] To model the change of the dielectric function induced by an adsorbed molecule a detailed knowledge of the depth-dependent electric field at the surface is mandatory. In the special case of F_6TCNNQ on ZnO(0001) the total surface band bending accounts to $\Delta\phi_{BB} = 1.0$ eV for a fully covered surface.[173] This band bending creates a linear decreasing electric field in the depletion region of the inorganic semiconductor, which modifies the dielectric function at the surface. The electric field in the space charge region can be estimated using the Poisson equation

$$\frac{d^2\Phi}{dz^2} = -\frac{dE}{dz} = -\frac{\rho(z)}{\varepsilon\varepsilon_0}. \tag{4.13}$$

To solve the equation the depletion approximation is used, where it is assumed that the semiconductor is fully depleted in the space charge region.[266] Then the charge density ρ can be described by a step function

$$\rho(z) = eN_D^+\Theta(d_{SCR} - z), \tag{4.14}$$

with the ionized donor density N_D^+ and the width of the space charge region d_{SCR}. Inserting this in Eqn. 4.13 and integrating the equation yields a linearly varying electric field in the space charge region reaching its maximum at the surface:

$$E(z) = \frac{eN_D^+}{\varepsilon\varepsilon_0}(z - d_{SCR}), \tag{4.15}$$

and respectively for the potential

$$\Phi(z) = \Phi_b - \frac{eN_D^+}{2\varepsilon\varepsilon_0}(z - d_{SCR})^2. \tag{4.16}$$

with the bulk potential Φ_b which vanishes at the interface.

Hence, for $\Phi(0) = \Phi_{BB} = 1\ eV$ the width of the space charge region can be estimated from Eqn. 4.16 by assuming a donor density of $N_D \approx 3 \cdot 10^{23}\ m^{-3}$ and $\varepsilon = 8.12$ for ZnO, resulting in $d_{SCR} = 55$ nm. Thus, the maximal electric field at the covered surface can be calculated with Eqn. 4.15 yielding a substantial electric field of $E(0) \approx 3.7 \cdot 10^7$ V/m. Comparing this to the ionization field for ZnO ($E_I = 2.56 \cdot 10^7$ V/m) yields the maximal field ratio at the surface of approximately $E/E_I = 1.4$. For the uncovered ZnO surface also slight downward band bending is present at the surface amounting to 200 meV as established from UPS measurements.[173] This results in a space charge region of $d_{SCR} = 25$ nm and a surface field of $E(0) \approx 1.65 \cdot 10^7\ V/m$ with a ratio of $E/E_I = 0.6$. Based on these values a multilayer system for the reference and covered surface is constructed with decreasing field ratios going from surface to bulk. The linearly decreasing structure is approximated by steps of constant values. Fig. 4.55 shows the simulation together with the structure of the electric field.

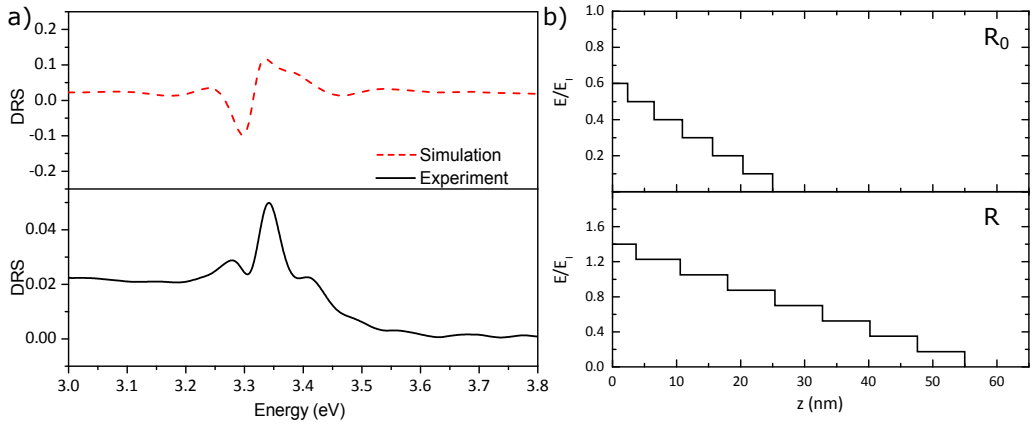

Figure 4.55: a) Comparison of selected experimental and simulated spectra calculated by a multilayer system, using the field distribution b) for uncovered (R_0) and covered (R) ZnO at the surface.

By using the known band structure modifications induced by the F_6TCNNQ molecule at the ZnO surface, the major protruding features of the DR spectrum can be reproduced.

The extrema around 3.3 eV can be attributed to the change of the ZnO adsorption in the presence of an electric field, while eventual features at higher energies are attributed to Franz-Keldysh oscillations. It has to be noted that the intensities are slightly overestimated. This is ascribed to insecurities in the values for material parameters, *e.g.* the exact value of the donor density, the line broadening of the ZnO excitonic resonance and the actual dielectric function at the surface.

Conclusion

DRS proved to be a method to reveal even minuscule charge transfer effects of organic molecules and an inorganic semiconductor. NTCDA and F_6TCNNQ on ZnO were used as model systems to investigate this charge transfer optically at the interface of an inorganic/organic hybrid during growth. The observable in DRS experiments for CT turned out to be a change in the band bending of the inorganic semiconductor, profoundly changing the spectra even for small charge transfer. This was reflected in the DR spectra for both molecules by similar characteristic derivative like peak features in the vicinity of the band gap. With comparable photoemission measurements those could be assigned to a changed band bending of the ZnO. Which in turn is induced by charge transfer at the HIOS interface from ZnO to the molecule, resulting in the formation of a linearly decreasing electric field, extending to around 50 nm into the inorganic semiconductor. An associated change of the total work function could be identified by KPFM scans in accordance to UPS measurements of the same system. Furthermore, only the feature of the neutral molecule was recognized in the spectra, while no ionized molecules were detectable. This is due to the small fraction of molecules that even show CT, which is not enough for a direct detection of the ionized molecules in the spectra, but still causes a substantial modification of the ZnO optical properties at the surface. Eventually, by using the known band bending of pristine and covered ZnO, space charge region and course of the electric field were calculated and the observed features could be well reproduced in a multi-layer simulation. This opens the possibility to quantitatively determine changes in the surface band bending by analyzing DR spectra, which however, requires a deeper theoretical description than the simple Blossey model.

CHAPTER 5

Conclusion

The endeavor of this thesis was to combine novel hybrid inorganic/organic semiconductor structures in a controlled way, which is a necessity for future applications in optoelectronic devices. Using the inorganic ZnO and selected organic molecules, it was illustrated that structure and morphology of the organic film can be actively changed, controlled and monitored in real time. The first part focused on the morphological aspect of growth, investigated by *in situ* AFM scans. As a prime example the well-investigated molecule 6P had been chosen for fundamental growth studies. It was illustrated that the substrate temperature poses an effective tool for controlling morphology and orientation of the molecules on the ZnO($10\bar{1}0$) surface. At room temperature islands composed of nearly upright standing molecules in the shape of the equilibrium crystal structure formed. At intermediate temperatures the island shape turned out to be more dendritic, while at even higher temperatures aligned needle like structures formed along the ZnO[0001] direction. Those are composed of lying molecules with their long axis perpendicular to the needle axis (see Fig. 5.1a).

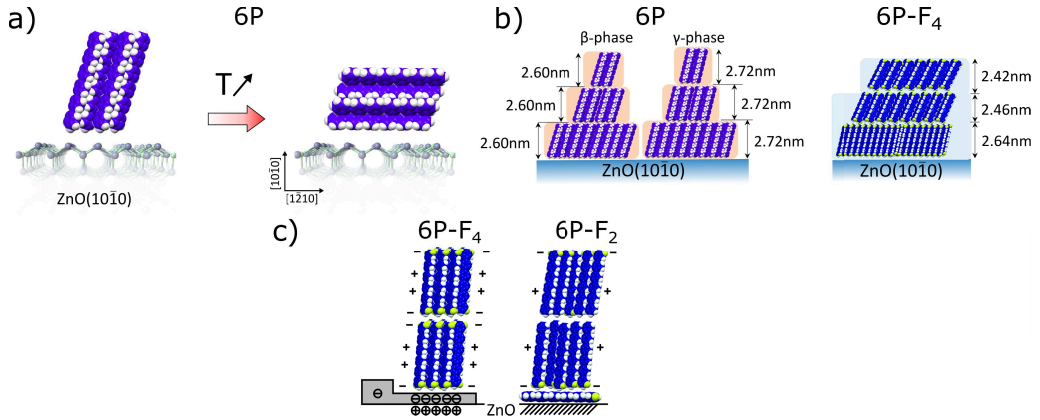

Figure 5.1: Schematic depiction of growth modes for 6P and derivatives on ZnO: a) Temperature dependence for growth at low and high temperature. b) Comparison of the growth modes between 6P and 6P-F_4. c) Interaction of local and permanent dipole moment of 6P-F_4 and 6P-F_2.

Their formation is induced by the electrostatic surface field of ZnO($10\bar{1}0$) resulting in an alignment of the single 6P molecule. The observed temperature dependence is inverse to investigations of 6P on other surfaces, where needles formed at room temperature while islands emerged at higher temperatures. The importance of orientation control of the molecules has been confirmed by KPFM measurements, showing an orientation dependent work function for the molecules. For one, a general work function change is induced by the 'push-back' effect, whereby the electron cloud of the substrate surface is pushed back due to Pauli-repulsion with the molecules. On the other hand an orientation dependency is constituted by a change of the molecules' ionization energy due to the intra-molecular charge distribution. For flat-lying molecules the conjugated backbone with the π-electron system forms a negatively charged plane, while standing molecules exhibit an almost non-polar end group. To achieve further control over the molecular growth and improve the surface structure, 6P has been modified by terminal fluorination. While the optical properties of the fluorinated 6P were unchanged, the thin film growth mode on ZnO($10\bar{1}0$) at room temperature was substantially altered. As schematically depicted in Fig. 5.1b the rough mound-like growth of 6P with two different phases, transitions into a 2D layer-by-layer growth for 6P-F_4, with phase purity and stronger tilt angle of the molecules. Investigation of the asymmetrically fluorinated 6P-F_2 furthermore revealed just another growth mode, different from 6P or 6P-F_4. Growth was shown to be in general much smoother than in the case of the unsubstituted 6P, but not as smooth as for the symmetrically fluorinated 6P-F_4. In the 1^{st} layer branched and partially aligned islands have been observed. The island density turned out to be five times higher than for 6P-F_4, indicative for a small diffusion coefficient. This was further confirmed by the determination of the critical island size, revealing that already one molecule is sufficient to form a stable nucleus. Temperature dependent investigations showed a gradual formation of broader but fewer islands and emergence of needles with higher temperature. Eventually, Kelvin probe scans of both fluorinated molecules for different coverages have been compared to show the effect of the dipole moment in the molecules. The permanent dipole moment in 6P-F_2 leads to the formation of an interface dipole layer and a general preferential orientation with the fluorine atoms pointing downwards in the 1^{st} layer, while in the 2^{nd} layer the molecules exhibit a preferential orientation now with the fluorine atoms pointing upwards (See Fig. 5.1c).

To make new HIOS device concepts feasible, it should also be possible to overgrow organic structures with an inorganic material without compromising the structural integrity of the organic material. This has been investigated by HRTEM, using 6P as organic inclusions in ZnO. The choice of ZnO was motivated by the possibility to grow it with high crystalline quality at substrate temperatures as low as 50 °C. A combined HRTEM and X-ray diffraction analysis of those hybrid stacks revealed a high crystalline perfection with all interfaces defined on an atomic/molecular level without interdiffusion of ZnO in the organic layer as shown in Fig. 5.2 together with image contrast simulations. The study showed that embedded organic/inorganic structures can be grown without impairment of the organic crystalline structure. In another study the top layer (TL) has been examined on a deeper level. Here, the ZnO nucleated atop the crystalline organic inclusion showed a distinct columnar structure with preferred c-axis orientation, while aside the inclusion the

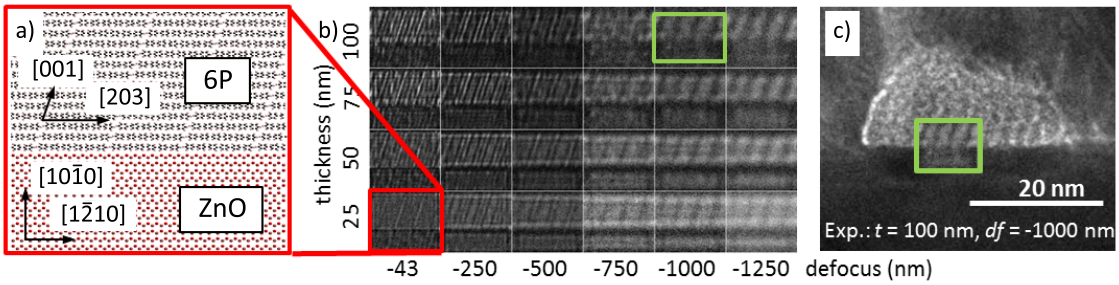

Figure 5.2: HRTEM image contrast simulation of the 6P/ZnO(10$\bar{1}$0) interface. a) Structural model of the 6P/ZnO(10$\bar{1}$0) interface and b) corresponding calculated HRTEM images for a series of thicknesses and defocus values. c) Superposition of a contrast-adapted calculated pattern obtained for a defocus value of $df = -1000$ nm and a lamella thickness of $t = 100$ nm (framed in green) with a measured HRTEM image.

ZnO TL was single crystalline, retaining the orientation of the ZnO bottom layer (BL). This finding is independent of the organic crystal surface termination. In polar as well as non-polar hybrid stacks, partial lateral overgrowth of the organic inclusion with ZnO of the same orientation as the BL occurs. The ZnO growth direction determines how lateral overgrowth evolves: in non-polar stacks, ZnO facets, which form an angle of 60° with the interface, gradually overgrow the organic inclusion laterally. On the other hand for the polar hybrid stack lateral overgrowth of ZnO facets proceeds parallel to the interfaces. Therefore, ZnO atop 6P adopts the orientation of the surrounding material already at the interface. These observations define a way for further improvement of the crystalline quality of the ZnO TL required to achieve a high charge carrier mobility and PL yield as grain boundaries have a detrimental effect on both properties. By changing the aspect ratio and size of the organic crystallites one could attempt to achieve coalescence of facets and subsequent single crystalline ZnO overgrowth of the organic inclusion.

By implementing differential reflectance spectroscopy (DRS) it has been furthermore possible to obtain information on the morphology of the molecular layer and electronic structure during growth with a sensitivity well below a molecular monolayer. DRS experiments with PTCDI on KBr allowed for the analysis of the structural characteristics by using calculations to model absorption spectra of polycrystalline thin films. The calculations showed that the distinct double-peak structure in thin film DR spectra of PTCDI on KBr seen in Fig. 5.3 originates from the coexistence of two molecular phases. Large crystals, which have been found in AFM scans, give rise to the component on the low-energy side. The second feature is originating from a phase of loosely-packed smaller aggregates resulting in a weaker gas-to-crystal shift as most molecules reside at or close to the surface. Thus, dispersion effects have been recognized as the dominant factor for shifts in the spectra, while site-dependent structural disorder has been as well identified to have a strong impact on the spectra. The findings demonstrate the general potential of differential reflectance spectroscopy to describe and understand the evolution in absorption spectra from a monomer to a crystal in real time under UHV conditions.

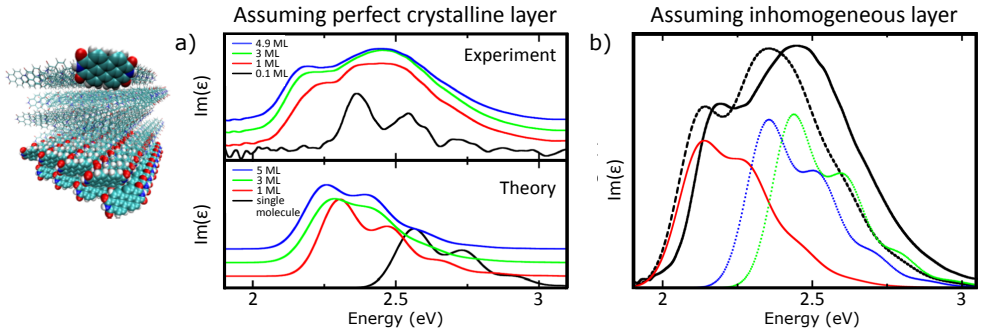

Figure 5.3: Measured Im(ε) of PTCDI on KBr and computed absorption line shapes assuming perfect crystalline layer and partly inhomogeneous molecular films.

Another study investigated the ladder-type quaterphenyl L4P deposited on ZnO down to the sub-ML range by DRS (Fig. 5.4a). It has been demonstrated how the dielectric function can be extracted in the case of an absorbing substrate by an oscillator model using a Voigt profile (Fig. 5.4b). The results of the simulation revealed monomeric features even for thicker films and a remarkable agreement between the fitted extinction coefficient of a grown L4P film on ZnO with its absorption spectrum in solution. Hence, the findings indicate a negligible interaction between neighboring molecules as well as of L4P with the ZnO substrate, *i.e.* no significant charge transfer between molecule and ZnO and related band bending or chemisorption. The molecular spectra exhibited only a small gas-to-crystal shift of approximately 50 meV in the first MLs, which is attributed to interactions between the molecules. Eventually, it has been qualitatively shown that a rough surface can in general considerably change the spectral form of the measured spectra and impose an uncertainty factor in determining the optical parameters of the molecule. However, comparing extracted extinction coefficient and absorption spectra points to a smooth surface during growth.

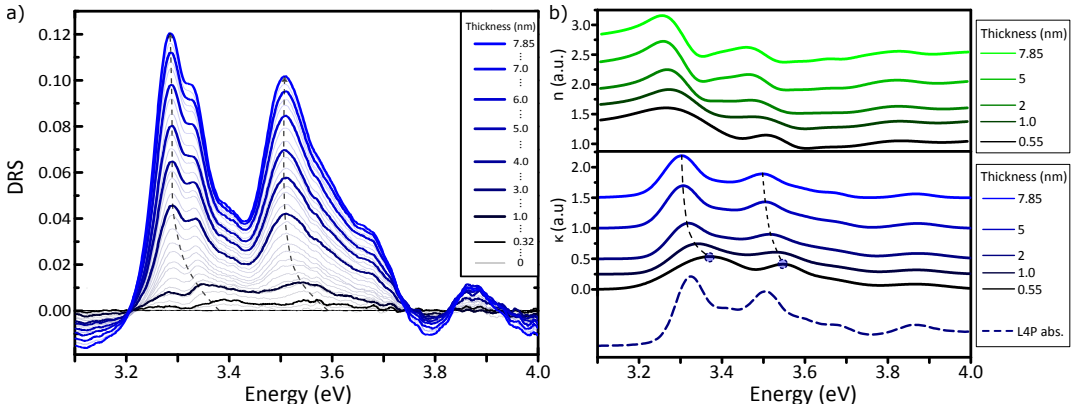

Figure 5.4: Drift-corrected DR spectra of L4P on ZnO($000\bar{1}$) and simulated refractive index n (top) and extinction coefficient κ (bottom) for selected thicknesses.

Ultimately, it was shown that DRS can be used to reveal charge transfer processes at the hybrid interface of organic molecules and an inorganic semiconductor. Here NTCDA and F_6TCNNQ on ZnO were used as model systems. It was shown that by a change in the electric field at the surface of ZnO, *i.e.* band bending, characteristic peak features emerging in DRS could be assigned to charge transfer at the HIOS interface (see Fig. 5.5). This was confirmed by a change of the total work function observed in KPFM scans in accordance to UPS measurements. By using the known band bending of pristine and covered ZnO, space charge region and course of the electric field have been calculated and the observed features were well reproduced in a multi-layer simulation.

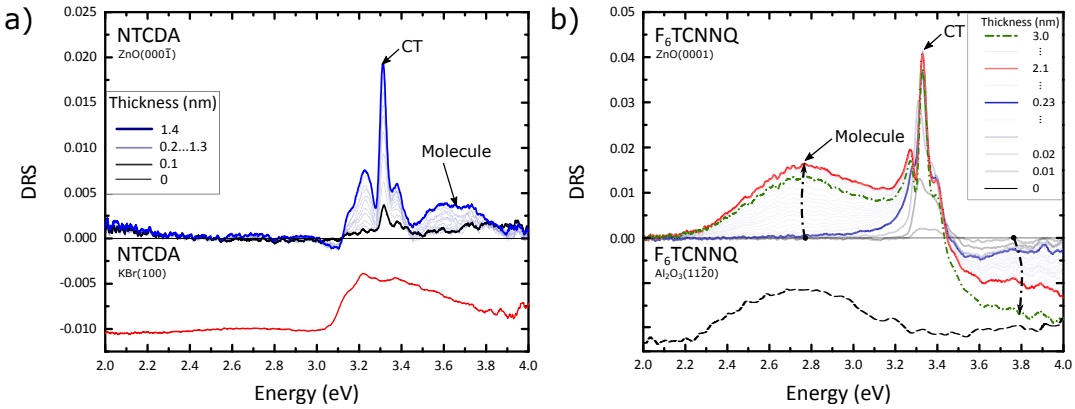

Figure 5.5: Drift-corrected DR spectra of a) NTCDA on ZnO(000$\bar{1}$), showing a spectrum on KBr(100) for comparison and b) F_6TCNNQ on ZnO(0001), showing a spectrum on $Al_2O_3(11\bar{2}0)$ for comparison.

In conclusion, control over the growth mode was achieved by the rather classical approach of temperature variation in combination with the special property of the ZnO surface, while chemical tuning by substituting single atoms of a molecule was introduced as a new method to improve the film smoothness. Here, further modifications of the molecules are conceivable to influence the growth mode: For example end groups with differing dipole moment or functionalized donor/acceptor end-groups in regard to optoelectronic devices. Furthermore, it was possible to reveal well-defined interfaces of the grown structures between the inorganic and organic material by TEM. In future TEM experiments the question of vertical multilayer stacking of inorganic/organic components in the HIOS should also be tackled in respect of possible optoelectronic devices, as it was shown here that the ZnO layer atop 6P is randomly in-plane oriented. Here, different growth conditions, which change the aspect ratio and size of the organic crystallites could induce lateral overgrowth of the surrounding ZnO layer. With the DRS technique a highly sensitive method was established to describe hybrid inorganic/organic structures during growth, which in the future can be used as a standard technique to obtain information about morphology and electronic structure of a growing molecular film during deposition. Possible are also applications for temperature dependent experiments to observe for example polymerization processes of the organic molecules.

Bibliography

1. Koenigsberger, J. and K. Schilling: 'Über Elektrizitätsleitung in festen Elementen und Verbindungen. I. Minima des Widerstandes, Prüfung auf Elektronenleitung, Anwendung der Dissoziationsformeln'. *Annalen der Physik* (Jan. 1910), vol. 337(6): pp. 179–230 (cit. on p. 2).
2. Pope, M., H. P. Kallmann, and P. Magnante: 'Electroluminescence in Organic Crystals'. *The Journal of Chemical Physics* (Apr. 1963), vol. 38(8): pp. 2042–2043 (cit. on p. 2).
3. Tang, C. W. and S. A. VanSlyke: 'Organic electroluminescent diodes'. *Applied Physics Letters* (Sept. 1987), vol. 51(12): pp. 913–915 (cit. on p. 2).
4. Horowitz, G.: 'Organic Field-Effect Transistors'. *Advanced Materials* (Mar. 1998), vol. 10(5): pp. 365–377 (cit. on p. 2).
5. Groves, C.: 'Organic light-emitting diodes: Bright design'. *Nature Materials* (July 2013), vol. 12(7): p. 597 (cit. on p. 2).
6. Editorial: 'Let there be light'. *Nature Materials* (May 2015), vol. 14(5): p. 453 (cit. on p. 2).
7. Green, M. A., Y. Hishikawa, W. Warta, E. D. Dunlop, D. H. Levi, J. Hohl-Ebinger, and A. W. H. Ho-Baillie: 'Solar cell efficiency tables (version 50)'. *Progress in Photovoltaics: Research and Applications* (July 2017), vol. 25(7): pp. 668–676 (cit. on p. 2).
8. Agranovich, V. M., D. M. Basko, G. C.L Rocca, and F. Bassani: 'Excitons and optical nonlinearities in hybrid organic-inorganic nanostructures'. *Journal of Physics: Condensed Matter* (1998), vol. 10: p. 9369 (cit. on p. 2).
9. Basko, D., G. C. La Rocca, F. Bassani, and V. M. Agranovich: 'Förster energy transfer from a semiconductor quantum well to an organic material overlayer'. *The European Physical Journal B - Condensed Matter and Complex Systems* (Apr. 1999), vol. 8(3): pp. 353–362 (cit. on p. 2).
10. Blumstengel, S., S. Sadofev, C. Xu, J. Puls, and F. Henneberger: 'Converting Wannier into Frenkel Excitons in an Inorganic/Organic Hybrid Semiconductor Nanostructure'. *Physical Review Letters* (Dec. 2006), vol. 97(23) (cit. on pp. 2, 102).

11. Itskos, G., G. Heliotis, P. G. Lagoudakis, J. Lupton, N. P. Barradas, E. Alves, S. Pereira, I. M. Watson, M. D. Dawson, J. Feldmann, R. Murray, and D. D. C. Bradley: 'Efficient dipole-dipole coupling of Mott-Wannier and Frenkel excitons in (Ga,In)N quantum well/polyfluorene semiconductor heterostructures'. *Physical Review B* (July 2007), vol. 76(3): p. 035344 (cit. on p. 2).

12. Blumstengel, S., S. Sadofev, H. Kirmse, and F. Henneberger: 'Extreme low-temperature molecular beam epitaxy of ZnO-based quantum structures'. *Applied Physics Letters* (2011), vol. 98(3): p. 031907 (cit. on pp. 3, 20, 45, 103).

13. Simbrunner, C.: 'Epitaxial growth of sexi-thiophene and *para*-hexaphenyl and its implications for the fabrication of self-assembled lasing nano-fibres'. *Semiconductor Science and Technology* (May 2013), vol. 28(5) (cit. on pp. 3, 64, 65, 74, 75).

14. Michely, T. and J. Krug: *Islands, Mounds and Atoms - Patterns and Processes in Crystal Growth Far from Equilibrium*. Vol. 42. Springer Series in Surface Sciences 1. Springer-Verlag Berlin Heidelberg, 2004 (cit. on pp. 6, 8, 11, 12, 95).

15. Hlawacek, G. and C. Teichert: 'Nucleation and growth of thin films of rod-like conjugated molecules'. *Journal of Physics: Condensed Matter* (Apr. 2013), vol. 25(14): p. 143202 (cit. on pp. 7, 63, 64, 79).

16. Venables, J. A., G. D. T. Spiller, and M. Hanbucken: 'Nucleation and growth of thin films'. *Reports on Progress in Physics* (1984), vol. 47(4): p. 399 (cit. on pp. 8, 9).

17. Pimpinelli, A., L. Tumbek, and A. Winkler: 'Scaling and Exponent Equalities in Island Nucleation: Novel Results and Application to Organic Films'. *The Journal of Physical Chemistry Letters* (Mar. 2014), vol. 5(6): pp. 995–998 (cit. on pp. 9, 10, 86–88, 94).

18. Witten, T. A. and L. M. Sander: 'Diffusion-Limited Aggregation, a Kinetic Critical Phenomenon'. *Physical Review Letters* (Nov. 1981), vol. 47(19): pp. 1400–1403 (cit. on p. 9).

19. Kandel, D.: 'Initial Stages of Thin Film Growth in the Presence of Island-Edge Barriers'. *Physical Review Letters* (Jan. 1997), vol. 78(3): pp. 499–502 (cit. on p. 9).

20. Hlawacek, G., P. Puschnig, P. Frank, A. Winkler, C. Ambrosch-Draxl, and C. Teichert: 'Characterization of Step-Edge Barriers in Organic Thin-Film Growth'. *Science* (July 2008), vol. 321(5885): pp. 108–111 (cit. on pp. 9, 11, 64, 77, 89).

21. Potocar, T., S. Lorbek, D. Nabok, Q. Shen, L. Tumbek, G. Hlawacek, P. Puschnig, C. Ambrosch-Draxl, C. Teichert, and A. Winkler: 'Initial stages of a *para*-hexaphenyl film growth on amorphous mica'. *Physical Review B* (Feb. 2011), vol. 83(7) (cit. on pp. 9, 76, 86–88, 92, 94, 95).

22. Tumbek, L. and A. Winkler: 'Attachment limited versus diffusion limited nucleation of organic molecules: Hexaphenyl on sputter-modified mica'. *Surface Science* (Aug. 2012), vol. 606(15-16): pp. L55–L58 (cit. on pp. 9, 86, 87, 92, 94).

23. Amar, J. G. and F. Family: 'Critical cluster size: Island morphology and size distribution in submonolayer epitaxial growth'. *Physical review letters* (1995), vol. 74(11): p. 2066 (cit. on pp. 9, 85).

24. Mulheran, P. A. and J. A. Blackman: 'Capture zones and scaling in homogeneous thin-film growth'. *Physical Review B* (Apr. 1996), vol. 53(15): pp. 10261–10267 (cit. on p. 10).

25. Pimpinelli, A. and T. Einstein: 'Capture-Zone Scaling in Island Nucleation: Universal Fluctuation Behavior'. *Physical Review Letters* (Nov. 2007), vol. 99(22) (cit. on pp. 10, 85).

26. Ehrlich, G. and F. G. Hudda: 'Atomic View of Surface Self-Diffusion: Tungsten on Tungsten'. *The Journal of Chemical Physics* (Feb. 1966), vol. 44(3): pp. 1039–1049 (cit. on p. 11).

27. Schwoebel, R. L. and E. J. Shipsey: 'Step Motion on Crystal Surfaces'. *Journal of Applied Physics* (Sept. 1966), vol. 37(10): pp. 3682–3686 (cit. on p. 11).

28. Goose, Joseph E., Eric L. First, and Paulette Clancy: 'Nature of step-edge barriers for small organic molecules'. *Physical Review B* (May 2010), vol. 81(20) (cit. on pp. 11, 89).

29. Palczynski, Karol, Philipp Herrmann, Georg Heimel, and Joachim Dzubiella: 'Characterization of step-edge barrier crossing of para-sexiphenyl on the ZnO (100) surface'. *Physical Chemistry Chemical Physics* (Sept. 2016), vol. 18(36): pp. 25329–25341 (cit. on p. 11).

30. Forrest, S. R.: 'Ultrathin Organic Films Grown by Organic Molecular Beam Deposition and Related Techniques'. *Chemical Reviews* (Oct. 1997), vol. 97(6): pp. 1793–1896 (cit. on pp. 11, 19, 66).

31. Bauer, E.: 'Phänomenologische Theorie der Kristallabscheidung an Oberflächen. I'. *Zeitschrift für Kristallographie* (1958), vol. 110(1-6): pp. 372–394 (cit. on p. 12).

32. Bauer, E. and Jan H. van der Merwe: 'Structure and growth of crystalline superlattices: From monolayer to superlattice'. *Physical Review B* (Mar. 1986), vol. 33(6): pp. 3657–3671 (cit. on p. 12).

33. Frank, F. C. and J. H. van der Merwe: 'One-Dimensional Dislocations. I. Static Theory'. *Proceedings of the Royal Society of London. Series A, Mathematical and Physical Sciences* (1949), vol. 198(1053): pp. 205–216 (cit. on p. 12).

34. Frank, F. C. and J. H. van der Merwe: 'One-Dimensional Dislocations. II. Misfitting Monolayers and Oriented Overgrowth'. *Proceedings of the Royal Society of London. Series A, Mathematical and Physical Sciences* (1949), vol. 198(1053): pp. 216–225 (cit. on p. 12).

35. Frank, F. C. and J. H. van der Merwe: 'One-Dimensional Dislocations. III. Influence of the Second Harmonic Term in the Potential Representation, on the Properties of the Model'. *Proceedings of the Royal Society of London. Series A, Mathematical and Physical Sciences* (1949), vol. 200(1060): pp. 125–134 (cit. on p. 12).

36. Stranski, I. N. and L. Krastanow: 'Zur Theorie der orientierten Ausscheidung von Ionenkristallen aufeinander'. *Monatshefte für Chemie und verwandte Teile anderer Wissenschaften* (1938), vol. 71(1): pp. 351–364 (cit. on p. 12).

37. Volmer, M. and A. Weber: 'Nucleus formation in supersaturated systems'. *Zeitschrift für physikalische Chemie* (1926), vol. 119 (cit. on p. 12).

38. Özgür, Ü., Y. I. Alivov, C. Liu, A. Teke, M. A. Reshchikov, S. Dogan, V. Avrutin, S.-J. Cho, and H. Morkoç: 'A comprehensive review of ZnO materials and devices'. *Journal of Applied Physics* (Aug. 2005), vol. 98(4): p. 041301 (cit. on pp. 13, 14).

39. Morkoç, H. and Ü. Özgür: *Zinc Oxide: Fundamentals, Materials and Device Technology*. Wiley-VCH, 2009 (cit. on pp. 13–15, 17, 18, 20).

40. Klingshirn, C. F., B.K. Meyer, A. Waag, A. Hoffmann, and J. Geurts: *Zinc Oxide: From Fundamental Properties Towards Novel Applications*. 120. Springer-Verlag Berlin Heidelberg, 2010 (cit. on pp. 13, 14, 16).

41. Reynolds, J. G. and C. L. Reynolds: 'Progress in ZnO Acceptor Doping: What Is the Best Strategy?' *Advances in Condensed Matter* (May 2014), vol. 2014 (cit. on pp. 13, 14).

42. Craddock, P. T.: *2000 Years of Zinc and Brass*. British Museum, 1998 (cit. on p. 13).

43. Suryanarayanan, R. and T. Okada: 'ZnO Nanocrystals and Allied Materials'. Vol. 180. Springer India, Sept. 2014. Chap. Zinc Oxide: From Optoelectronics to Biomaterial - A Short Review: pp. 289–307 (cit. on p. 13).

44. Wöll, C.: 'The chemistry and physics of zinc oxide surfaces'. *Progress in Surface Science* (2007), vol. 82(2-3): pp. 55–120 (cit. on p. 13).

45. Pollard, M. A. and C. Heron: *Archaeological Chemistry*. 2nd ed. Royal Society of Chemistry, 2008 (cit. on p. 13).

46. Fritsch, O.: 'Elektrisches und optisches Verhalten von Halbleitern. X Elektrische Messungen an Zinkoxyd'. *Annalen der Physik* (1935), vol. 414(4): pp. 375–401 (cit. on p. 13).

47. Bunn, C. W.: 'The lattice-dimensions of zinc oxide'. *Proceedings of the Physical Society* (1935), vol. 47(5): p. 835 (cit. on p. 13).

48. Yearian, H. J.: 'Intensity of Diffraction of Electrons by ZnO'. *Physical Review* (Oct. 1935), vol. 48(7): pp. 631–639 (cit. on p. 13).

49. Mollwo, E.: 'Die Wirkung von Wasserstoff auf die Leitfähigkeit und Lumineszenz von Zinkoxydkristallen'. *Zeitschrift für Physik* (June 1954), vol. 138(3-4): pp. 478–488 (cit. on p. 13).
50. Hopfield, J. J.: 'Fine structure in the optical absorption edge of anisotropic crystals'. *Journal of Physics and Chemistry of Solids* (1960), vol. (cit. on p. 13).
51. Thomas, D. G.: 'The exciton spectrum of zinc oxide'. *Journal of Physics and Chemistry of Solids* (1960), vol. (cit. on p. 13).
52. Dietz, R. E., J. J. Hopfield, and D. G. Thomas: 'Excitons and the Absorption Edge of ZnO'. *Journal of Applied Physics* (1961), vol. (cit. on p. 13).
53. Park, Y. S., C. W. Litton, and D. C. Collins T. C.and Reynolds: 'Exciton Spectrum of ZnO'. *Physical Review* (1966), vol. (cit. on p. 13).
54. Drapak, I. T.: 'Visible luminescence of a ZnO-Cu_2O heterojunction'. *Sov. Phys. Semicond.* (1968), vol. 2: pp. 624–625 (cit. on p. 13).
55. Avrutin, V., D. J. Silversmith, and H. Morkoç: 'Doping Asymmetry Problem in ZnO: Current Status and Outlook'. *Proceedings of the IEEE* (July 2010), vol. 98(7): pp. 1269–1280 (cit. on p. 13).
56. Amano, H., N. Sawaki, I. Akasaki, and Y. Toyoda: 'Metalorganic vapor phase epitaxial growth of a high quality GaN film using an AlN buffer layer'. *Applied Physics Letters* (Feb. 1986), vol. 48(5): pp. 353–355 (cit. on p. 14).
57. Bagnall, D. M., Y. F. Chen, Z. Zhu, T. Yao, S. Koyama, M. Y. Shen, and T. Goto: 'Optically pumped lasing of ZnO at room temperature'. *Applied Physics Letters* (Apr. 1997), vol. 70(17): pp. 2230–2232 (cit. on p. 14).
58. Look, D. C. and B. Claflin: 'P-type doping and devices based on ZnO'. *physica status solidi (b)* (Mar. 2004), vol. 241(3): pp. 624–630 (cit. on p. 14).
59. Tsukazaki, A., A. Ohtomo, T. Onuma, M. Ohtani, T. Makino, M. Sumiya, K. Ohtani, S. F. Chichibu, S. Fuke, Y. Segawa, H. Ohno, H. Koinuma, and M. Kawasaki: 'Repeated temperature modulation epitaxy for p-type doping and light-emitting diode based on ZnO'. *Nature Materials* (Jan. 2005), vol. 4(1): pp. 42–46 (cit. on p. 14).
60. Jiang, X., J. Shi, M. Zhang, H. Zhong, P. Huang, Y. Ding, X. Cao, M. Wu, and Liao, Z.: 'Breakthrough of the p -type doping bottleneck in ZnO by inserting an ultrathin ZnX (X = S, Se and Te) layer doped with N X or Ag Zn'. *Journal of Physics D: Applied Physics* (2016), vol. 49(9): p. 095104 (cit. on p. 14).
61. Klingshirn, C.: 'ZnO: From basics towards applications'. *physica status solidi (b)* (Sept. 2007), vol. 244(9): pp. 3027–3073 (cit. on pp. 16, 69).
62. Triboulet, R.: 'Growth of ZnO bulk crystals: A review'. *Progress in Crystal Growth and Characterization of Materials* (Mar. 2014), vol. 60(1): pp. 1–14 (cit. on p. 17).
63. Ntep, J.-M., S. Said Hassani, A. Lusson, A. Tromson-Carli, D. Ballutaud, G. Didier, and R. Triboulet: 'ZnO growth by chemical vapour transport'. *Journal of Crystal Growth* (Nov. 1999), vol. 207(1): pp. 30–34 (cit. on p. 17).

64. Schulz, D., S. Ganschow, D. Klimm, M. Neubert, M. Rossberg, M. Schmidbauer, and R. Fornari: 'Bridgman-grown zinc oxide single crystals'. *Journal of Crystal Growth* (Oct. 2006), vol. 296(1): pp. 27–30 (cit. on p. 17).

65. Takahashi, K. and A. Yoshikawa: *Wide Bandgap Semiconductors: Fundamental Properties and Modern Photonic and Modern Photonic and Electronic Devices*. 1. Springer-Verlag Berlin Heidelberg, 2007 (cit. on p. 17).

66. Reynolds, D. C., C. W. Litton, D. C. Look, J. E. Hoelscher, B. Claflin, T. C. Collins, J. Nause, and B. Nemeth: 'High-quality, melt-grown ZnO single crystals'. *Journal of Applied Physics* (May 2004), vol. 95(9): pp. 4802–4805 (cit. on p. 17).

67. Ohshima, E., H. Ogino, I. Niikura, K. Maeda, M. Sato, M. Ito, and T. Fukuda: 'Growth of the 2-in-size bulk ZnO single crystals by the hydrothermal method'. *Journal of Crystal Growth* (Jan. 2004), vol. 260(1-2): pp. 166–170 (cit. on p. 17).

68. Ohtomo, A. and A. Tsukazaki: 'Pulsed laser deposition of thin films and superlattices based on ZnO'. *Semiconductor Science and Technology* (2005), vol. 20(4): S1 (cit. on p. 18).

69. Wöll, C.: 'The chemistry and physics of zinc oxide surfaces'. *Progress in Surface Science* (2007), vol. 82(2-3): pp. 55–120 (cit. on p. 20).

70. Della Sala, F., S. Blumstengel, and F. Henneberger: 'Electrostatic-Field-Driven Alignment of Organic Oligomers on ZnO Surfaces'. *Physical Review Letters* (Sept. 2011), vol. 107(14) (cit. on pp. 20, 64, 65, 73, 75, 79, 92, 108).

71. Pope, M. and C. E. Swenberg: *Electronic Processes in Organic Crystals and Polymers*. Second Edition. Oxford University Press, 1999 (cit. on pp. 21, 23, 25, 29–31).

72. Schwoerer, M. and H. Wolf: *Organic Molecular Solids*. Wiley-VCH Verlag, 2007 (cit. on pp. 21, 22, 26, 27, 30).

73. Haken, H. and H. C. Wolf: *Molekülphysik und Quantenchemie*. 5th ed. Springer-Verlag Berlin Heidelberg, 2006 (cit. on p. 23).

74. Condon, E.: 'A theory of intensity distribution in band systems'. *Physical Review* (1926), vol. 28(6): p. 1182 (cit. on pp. 23, 24).

75. Condon, E.: 'Nuclear motions associated with electron transitions in diatomic molecules'. *Physical Review* (1928), vol. 32(6): p. 858 (cit. on pp. 23, 24).

76. Franck, J. and E. G. Dymond: 'Elementary processes of photochemical reactions'. *Transactions of the Faraday Society* (1926), vol. 21(February): pp. 536–542 (cit. on p. 24).

77. Sauer, M., J. Hofkens, and J. Enderlein: *Handbook of Fluorescence Spectroscopy and Imaging: From Single Molecules to Ensembles*. Wiley-VCH, 2011 (cit. on pp. 25, 26).

78. Kasha, M.: 'Characterization of electronic transitions in complex molecules'. *Discussions of the Faraday society* (1950), vol. 9: pp. 14–19 (cit. on p. 25).

79. Klán, P. and J. Wirz: *Photochemistry of Organic Compounds: From Concepts to Practice*. Wiley, 2009 (cit. on p. 25).

80. Kasha, M.: 'Collisional Perturbation of Spin-Orbital Coupling and the Mechanism of Fluorescence Quenching. A Visual Demonstration of the Perturbation'. *The Journal of Chemical Physics* (1952), vol. 20(1): p. 71 (cit. on p. 26).

81. Kronenberger, A. and P. Pringsheim: 'Über das Absorptionsspektrum des festen Benzols bei 180°'. *Zeitschrift für Physik* (1926), vol. 40(1-2): pp. 75–91 (cit. on p. 27).

82. Kasha, M., H. R. Rawls, and M. Ashraf El-Bayoumi: 'The exciton model in molecular spectroscopy'. *Pure and Applied Chemistry* (Jan. 1965), vol. 11(3-4) (cit. on p. 28).

83. Frenkel, J.: 'On the Transformation of light into Heat in Solids. I'. *Physical Review* (Jan. 1931), vol. 37(1): pp. 17–44 (cit. on p. 31).

84. Davydov, A S: 'The Theory of Molecular Excitons'. *Soviet Physics Uspekhi* (Feb. 1964), vol. 7(2): pp. 145–178 (cit. on p. 31).

85. Wolf, H. C: 'Die niedersten elektronischen Anregungszustände des Anthracen-Kristalls'. *Zeitschrift für Naturforschung* (1958), vol. 13a: pp. 414–419 (cit. on p. 31).

86. Klingshirn, C.: *Semiconductor Optics*. Springer-Verlag Berlin Heidelberg, 2006 (cit. on pp. 34, 40).

87. Nitsche, R. and T. Fritz: 'Determination of model-free Kramers-Kronig consistent optical constants of thin absorbing films from just one spectral measurement: Application to organic semiconductors'. *Physical Review B* (Nov. 2004), vol. 70(19) (cit. on pp. 34, 55, 119).

88. Demtröder, W.: *Experimentalphysik 2; Elektrizität und Optik*. 6th ed. 2. Springer-Verlag Berlin Heidelberg, 2013 (cit. on p. 35).

89. Stenzel, O.: *The Physics of Thin Film Optical Spectra*. Vol. 44. Springer Series in Surface Sciences. Springer-Verlag Berlin Heidelberg, 2016 (cit. on pp. 36, 38, 39).

90. Demtröder, W.: *Laser Spectroscopy*. Springer-Verlag Berlin Heidelberg, 2008 (cit. on p. 36).

91. D.S. Meneses, D., G. Gruener, M. Malki, and P. Echegut: 'Causal Voigt profile for modeling reflectivity spectra of glasses'. *Journal of Non-Crystalline Solids* (Jan. 2005), vol. 351(2): pp. 124–129 (cit. on pp. 36, 37).

92. Brendel, R. and D. Bormann: 'An infrared dielectric function model for amorphous solids'. *Journal of Applied Physics* (Jan. 1992), vol. 71(1): pp. 1–6 (cit. on p. 38).

93. Kim, C. C., J. W. Garland, H. Abad, and P. M. Raccah: 'Modeling the optical dielectric function of semiconductors: Extension of the critical-point parabolic-band approximation'. *Physical Review B* (May 1992), vol. 45(20): pp. 11749–11767 (cit. on p. 38).

94. Nitsche, R.: 'Optical properties of organic semiconductors - From (sub-)monolayers to crystalline films'. PhD thesis. Dresden, 2005 (cit. on pp. 39, 57, 128, 129).

95. Choy, T. C.: *Effective Medium Theory: Principles and Applications*. Clarendon Press, 1999 (cit. on p. 39).

96. Hecht, E.: *Optics*. Ed. by Black, Adam. 4th. Addison-Wesley, 2002 (cit. on pp. 39, 40).

97. Heavens, O. S.: *Optical Properties of Thin Solid Films*. Dover Publications, 1955 (cit. on pp. 41, 42).

98. Born, M. and E. Wolf: *Principles of Optics*. Elsevier Ltd., 1980 (cit. on p. 42).

99. Sadofev, S., S. Blumstengel, J. Cui, J. Puls, S. Rogaschewski, P. Schäfer, Yu G. Sadofyev, and F. Henneberger: 'Growth of high-quality ZnMgO epilayers and ZnO/ZnMgO quantum well structures by radical-source molecular-beam epitaxy on sapphire'. *Applied Physics Letters* (Aug. 2005), vol. 87(9): p. 091903 (cit. on p. 45).

100. Sadofev, S., S. Blumstengel, J. Cui, J. Puls, S. Rogaschewski, P. Schäfer, and F. Henneberger: 'Visible band-gap ZnCdO heterostructures grown by molecular beam epitaxy'. *Applied Physics Letters* (Nov. 2006), vol. 89(20): p. 201907 (cit. on pp. 45, 103).

101. Sadofev, S., P. Schäfer, Y.-H. Fan, S. Blumstengel, F. Henneberger, D. Schulz, and D. Klimm: 'Radical-source molecular beam epitaxy of ZnMgO and ZnCdO alloys on ZnO substrates'. *Applied Physics Letters* (2007), vol. 91(20): p. 201923 (cit. on p. 45).

102. Sadofev, S.: 'Radical-source molecular beam epitaxy of ZnO-based heterostructures'. PhD thesis. Humboldt-Universität zu Berlin, 2009 (cit. on p. 45).

103. Broglie, L. de: 'Recherches sur la théorie des Quanta'. PhD thesis. Paris University, 1924 (cit. on p. 45).

104. Oura, K., V. G. Lifshits, A. A. Saranin, A. V. Zotov, and M. Katayama: *Surface Science - An Introduction*. Springer-Verlag Berlin Heidelberg, 2003 (cit. on p. 46).

105. Braun, W.: *Applied RHEED: Reflection High-Energy Electron Diffraction During Crystal Growth*. 1st. Springer-Verlag Berlin Heidelberg, 1999 (cit. on pp. 47, 48).

106. Gajdardziska-Josifovska, M. and Cowley, J.M.: 'Brillouin Zones and Kikuchi Lines for Crystals Under Electron Channeling Conditions'. *Acta Crystallographica* (Mar. 1991), vol. 47(2): pp. 74–82 (cit. on p. 48).

107. Bai, C.: *Scanning Tunneling Microscopy and Its Applications*. 1st ed. Vol. 32. Springer-Verlag Berlin Heidelberg, 2000 (cit. on p. 49).

108. Binnig, G., H. Rohrer, Ch. Gerber, and E. Weibel: 'Tunneling through a controllable vacuum gap'. *Applied Physics Letters* (1982), vol. 40(2): p. 178 (cit. on p. 49).

109. Binning, G., H. Rohrer, Ch. Gerber, and E. Weibel: 'Surface Studies by Scanning Tunneling Microscopy'. *Physical Review Letters* (July 1982), vol. 49(1): p. 57 (cit. on p. 49).

110. Binnig, G. and H. Rohrer: 'Scanning Tunneling Microscopy'. *IBM J. Res. Dev.* (July 1986), vol. 30(4): pp. 355–369 (cit. on p. 49).

111. Lang, N. D.: 'Vacuum tunneling current from an adsorbed atom'. *Physical review letters* (1985), vol. 55(2): p. 230 (cit. on p. 49).

112. Chen, J.: *Introduction to Scanning Tunneling Microscopy*. Oxford University Press, 1993 (cit. on pp. 49, 50).

113. Bardeen, J.: 'Tunnelling from a Many-Particle Point of View'. *Physical Review Letters* (Jan. 1961), vol. 6(2): pp. 57–59 (cit. on p. 50).

114. Binnig, G., C. F. Quate, and Ch. Gerber: 'Atomic Force Microscope'. *Physical Review Letters* (Mar. 1986), vol. 56(9): pp. 930–933 (cit. on p. 51).

115. Eaton, P. and P. West: *Atomic Force Microscopy*. Oxford University Press, 2010 (cit. on p. 51).

116. Morita, S., F.J. Giessibl, E. Meyer, and R. Wiesendanger: *Noncontact Atomic Force Microscopy*. Vol. 3. Springer-Verlag Berlin Heidelberg, 2015 (cit. on p. 51).

117. Nonnenmacher, M., M. P. O'Boyle, and H. K. Wickramasinghe: 'Kelvin probe force microscopy'. *Applied Physics Letters* (June 1991), vol. 58(25): pp. 2921–2923 (cit. on p. 52).

118. Sadewasser, S. and T. Glatzel: *Kelvin Probe Force Microscopy*. 48 1. Springer-Verlag Berlin Heidelberg, 2012 (cit. on p. 52).

119. Melitz, W., J. Shen, A. C. Kummel, and S. Lee: 'Kelvin probe force microscopy and its application'. *Surface Science Reports* (Jan. 2011), vol. 66(1): pp. 1–27 (cit. on p. 54).

120. Hansen, Wilford N and Galen J Hansen: 'Standard reference surfaces for work function measurements in air'. *Surface Science* (June 2001), vol. 481(1): pp. 172–184 (cit. on p. 54).

121. Nečas, D. and P. Klapetek: 'Gwyddion: an open-source software for SPM data analysis'. *Central European Journal of Physics* (Feb. 2012), vol. 10(1): pp. 181–188 (cit. on p. 54).

122. Forker, R. and T. Fritz: 'Optical differential reflectance spectroscopy of ultrathin epitaxial organic films'. *Physical Chemistry Chemical Physics* (2009), vol. 11(13): p. 2142 (cit. on pp. 54, 119).

123. Forker, R., M. Gruenewald, and T. Fritz: 'Optical differential reflectance spectroscopy on thin molecular films'. *Annual Reports Section "C" (Physical Chemistry)* (2012), vol. 108: p. 34 (cit. on pp. 54, 119).

124. McIntyre, J.D.E. and D.E. Aspnes: 'Differential reflection spectroscopy of very thin surface films'. *Surface Science* (Feb. 1971), vol. 24(2): pp. 417–434 (cit. on pp. 54, 55).

125. Weinert, H. L.: 'Efficient computation for Whittaker-Henderson smoothing'. *Computational Statistics & Data Analysis* (Oct. 2007), vol. 52(2): pp. 959–974 (cit. on p. 57).

126. Erni, R., M. D. Rossell, C. Kisielowski, and U. Dahmen: 'Atomic-Resolution Imaging with a Sub-50-pm Electron Probe'. *Physical Review Letters* (Mar. 2009), vol. 102(9): p. 096101 (cit. on p. 58).

127. Rauch, E. F., J. Portillo, S. Nicolopoulos, D. Bultreys, S. Rouvimov, and P. Moeck: 'Automated nanocrystal orientation and phase mapping in the transmission electron microscope on the basis of precession electron diffraction'. *Zeitschrift für Kristallographie - Crystalline Materials* (2010), vol. 225(2-3): pp. 103–109 (cit. on p. 59).

128. Moeck, P., S. Rouvimov, E. F. Rauch, M. Véron, H. Kirmse, I. Häusler, W. Neumann, D. Bultreys, Y. Maniette, and S. Nicolopoulos: 'High spatial resolution semi-automatic crystallite orientation and phase mapping of nanocrystals in transmission electron microscopes'. *Crystal Research and Technology* (June 2011), vol. 46(6): pp. 589–606 (cit. on p. 59).

129. Williams, D. B. and C. B. Carter: *Transmission Electron Microscopy*. 2nd ed. Springer US, 2009 (cit. on p. 61).

130. O'Keefe, M. A.: '"Resolution" in high-resolution electron microscopy'. *Ultramicroscopy* (Nov. 1992), vol. 47(1-3): pp. 282–297 (cit. on p. 61).

131. Scherzer, O.: 'The Theoretical Resolution Limit of the Electron Microscope'. *Journal of Applied Physics* (Jan. 1949), vol. 20(1): pp. 20–29 (cit. on p. 61).

132. Kirmse, H., E. Oehlschlegel, F. Polzer, S. Blumstengel, M. Sparenberg, and F. Henneberger: 'Cross-sectional TEM preparation of hybrid inorganic/organic materials systems by ultramicrotomy'. *Journal of Physics: Conference Series* (2013), vol. 471(1): p. 012034 (cit. on pp. 62, 102, 103).

133. Sparenberg, M., A. Zykov, P. Beyer, L. Pithan, C. Weber, Y. Garmshausen, F. Carlà, S. Hecht, S. Blumstengel, F. Henneberger, and S. Kowarik: 'Controlling the growth mode of *para*-sexiphenyl (6P) on ZnO by partial fluorination'. *Phys. Chem. Chem. Phys.* (2014), vol. 16(47): pp. 26084–26093 (cit. on pp. 63, 80, 83, 88).

134. Blumstengel, S., H. Kirmse, M. Sparenberg, S. Sadofev, F. Polzer, and F. Henneberger: 'Texture and morphology of ZnO grown on nanocrystalline p-sexiphenyl thin films'. *Journal of Crystal Growth* (Sept. 2014), vol. 402: pp. 187–194 (cit. on pp. 63, 102, 110).

135. Kirmse, H., M. Sparenberg, A. Zykov, S. Sadofev, S. Kowarik, and S. Blumstengel: 'Structure of *p*-Sexiphenyl Nanocrystallites in ZnO Revealed by High-Resolution Transmission Electron Microscopy'. *Crystal Growth & Design* (May 2016), vol. 16(5): pp. 2789–2794 (cit. on pp. 63, 102, 103).

136. Megow, J., T. Körzdörfer, T. Renger, M. Sparenberg, S. Blumstengel, F. Henneberger, and V. May: 'Calculating Optical Absorption Spectra of Thin Polycrystalline Organic Films: Structural Disorder and Site-Dependent van der Waals Interaction'. *The Journal of Physical Chemistry C* (Feb. 2015), vol. 119(10): pp. 5747–5751 (cit. on pp. 63, 119, 120, 122–124).

137. Resel, R.: 'Crystallographic studies on hexaphenyl thin films - a review'. *Thin Solid Films*. Proceedings from the 12th International Conference on Thin Films (June 2003), vol. 433(1-2): pp. 1–11 (cit. on p. 64).

138. Resel, R.: 'Surface induced crystallographic order in sexiphenyl thin films'. *Journal of Physics: Condensed Matter* (May 2008), vol. 20(18): p. 184009 (cit. on p. 64).

139. Rubahn, H.-G., H. Sitter, and K. Horowitz G. Al-Shamery, eds.: *Interface Controlled Organic Thin Films*. 129. Spr, 2009 (cit. on p. 64).

140. Sitter, H., C. Draxl, and M. Ramsey: *Small Organic Molecules on Surfaces*. Vol. 173. Springer Series in Materials Science. Spr, 2013 (cit. on p. 64).

141. Graupner, W., G. Grem, F. Meghdadi, C. Paar, G. Leising, U. Scherf, K. Müllen, W. Fischer, and F. Stelzer: 'Electroluminescence with Conjugated Polymers and Oligomers'. *Molecular Crystals and Liquid Crystals Science and Technology. Section A. Molecular Crystals and Liquid Crystals* (Nov. 1994), vol. 256(1): pp. 549–554 (cit. on p. 64).

142. Gundlach, D. J., Y.-Y. Lin, T. N. Jackson, and D. G. Schlom: 'Oligophenyl-based organic thin film transistors'. *Applied Physics Letters* (Dec. 1997), vol. 71(26): pp. 3853–3855 (cit. on p. 64).

143. Balzer, F., V. G. Bordo, A. C. Simonsen, and H.-G. Rubahn: 'Optical waveguiding in individual nanometer-scale organic fibers'. *Physical Review B* (Mar. 2003), vol. 67(11): p. 115408 (cit. on p. 64).

144. Quochi, F., F. Cordella, A. Mura, G. Bongiovanni, F. Balzer, and H.-G. Rubahn: 'Gain amplification and lasing properties of individual organic nanofibers'. *Applied Physics Letters* (2006), vol. 88(4): p. 041106 (cit. on pp. 64, 79).

145. Witte, G. and C. Wöll: 'Growth of aromatic molecules on solid substrates for applications in organic electronics'. *Journal of Materials Research* (July 2004), vol. 19(7): pp. 1889–1916 (cit. on pp. 64, 66).

146. Andreev, A., F. Quochi, H. Sitter, H. Hoppe, S. Sariciftci, A. Mura, and G. Bongiovanni: 'Blue emitting self-assembled nano-crystals of *para*-sexiphenyl grown by hot wall epitaxy'. *Microelectronics Journal* (Mar. 2005), vol. 36(3-6): pp. 237–240 (cit. on p. 64).

147. Simbrunner, C., G. Hernandez-Sosa, E. Baumgartner, G. Hesser, J. Roither, W. Heiss, and H. Sitter: '*Para*-sexiphenyl-CdSe/ZnS nanocrystal hybrid light emitting diodes'. *Applied Physics Letters* (Feb. 2009), vol. 94(7): p. 073505 (cit. on pp. 64, 102).

148. Baker, K. N., A. V. Fratini, T. Resch, H. C. Knachel, W. W. Adams, E. P. Socci, and B. L. Farmer: 'Crystal structures, phase transitions and energy calculations of poly(*p*-phenylene) oligomers'. *Polymer* (Apr. 1993), vol. 34(8): pp. 1571–1587 (cit. on pp. 64, 81).

149. Baker, K. N., H. C. Knachel, A. V. Fratini, and W. W. Adams: 'Structural Transformations in Crystalline Oligomers of Polyparaphenylene'. *Symposium J - Materials Science and Engineering of Rigid-Rod Polymers*. Vol. 134. MRS Online Proceedings Library. 1988 (cit. on p. 64).

150. Resel, R., N. Koch, F. Meghdadi, G. Leising, L. Athouel, G. Froyer, and F. Hofer: 'A Polymorph Crystal Structure of Hexaphenyl Observed in Thin Films'. *Crystal Research and Technology* (Jan. 2001), vol. 36(1): pp. 47–54 (cit. on pp. 64, 81).

151. Blumstengel, S., H. Glowatzki, S. Sadofev, N. Koch, S. Kowarik, J. P. Rabe, and F. Henneberger: 'Band-offset engineering in organic/inorganic semiconductor hybrid structures'. *Physical Chemistry Chemical Physics* (2010), vol. 12(37): p. 11642 (cit. on pp. 64, 65, 73–75, 77–79, 112).

152. Nabok, D., P. Puschnig, and C. Ambrosch-Draxl: 'Cohesive and surface energies of π-conjugated organic molecular crystals: A first-principles study'. *Physical Review B* (June 2008), vol. 77(24) (cit. on pp. 65, 74, 76).

153. Ried, W. and D. Freitag: 'Oligophenyls, Oligophenylenes, and Polyphenyls, a Class of Thermally Very Stable Compounds'. *Angewandte Chemie International Edition in English* (Nov. 1968), vol. 7(11): pp. 835–844 (cit. on p. 65).

154. Grem, G., V. Martin, F. Meghdadi, C. Paar, J. Stampfl, J. Sturm, S. Tasch, and G. Leising: 'Stable poly(*para*-phenylene)s and their application in organic light emitting devices'. *Synthetic Metals* (Apr. 1995), vol. 71(1): pp. 2193–2194 (cit. on p. 65).

155. Kobin, B., L. Grubert, S. Blumstengel, F. Henneberger, and S. Hecht: 'Vacuum-processable ladder-type oligophenylenes for organic/inorganic hybrid structures: synthesis, optical and electrochemical properties upon increasing planarization as well as thin film growth'. *Journal of Materials Chemistry* (2012), vol. 22(10): p. 4383 (cit. on pp. 65, 66).

156. Bianchi, F., S. Sadofev, R. Schlesinger, B. Kobin, S. Hecht, N. Koch, F. Henneberger, and S. Blumstengel: 'Cascade energy transfer versus charge separation in ladder-type oligo(*p*-phenylene)/ZnO hybrid structures for light-emitting applications'. *Applied Physics Letters* (Dec. 2014), vol. 105(23): p. 233301 (cit. on pp. 65, 66, 126, 133).

157. Höfner, M., B. Kobin, S. Hecht, and F. Henneberger: 'Strong Coupling and Laser Action of Ladder-Type Oligo(*p*-phenylene)s in a Microcavity'. *Chem Phys Chem* (Dec. 2014), vol. 15(17): pp. 3805–3808 (cit. on pp. 65, 66).

158. Alonso, M. I., M. Garriga, N. Karl, J. O. Ossó, and F. Schreiber: 'Anisotropic optical properties of single crystalline PTCDA studied by spectroscopic ellipsometry'. *Organic Electronics* (Mar. 2002), vol. 3(1): pp. 23–31 (cit. on p. 66).

159. Gisslén, L. and R. Scholz: 'Crystallochromy of perylene pigments: Interference between Frenkel excitons and charge-transfer states'. *Physical Review B* (Sept. 2009), vol. 80(11) (cit. on pp. 66, 124).

160. Tojo, K. and J. Mizuguchi: 'Refinement of the crystal structure of 3,4:9,10-perylene-bis(dicarboximide), $C_{24}H_{10}N_2O_4$, at 263 K'. *Zeitschrift für Kristallographie - New Crystal Structures* (2002), vol. 217(1): pp. 45–46 (cit. on p. 66).

161. Blackburn, A. C., L. J. Fitzgerald, and R. E. Gerkin: '1,4,5,8-Naphthalenetetracarboxylic Acid Cyclic 1,8-Anhydride Bis(dimethyl sulfoxide) Solvate and 1,4,5,8-Naphthalenetetracarboxylic 1,8:4,5-Dianhydride'. *Acta Crystallographica Section C: Crystal Structure Communications* (Dec. 1997), vol. 53(12): pp. 1991–1995 (cit. on p. 66).

162. Liang, G., T. Cui, and K. Varahramyan: 'Electrical characteristics of diodes fabricated with organic semiconductors'. *Microelectronic Engineering* (Mar. 2003), vol. 65(3): pp. 279–284 (cit. on p. 67).

163. Hiramoto, M., M. Kubo, Y. Shinmura, N. Ishiyama, T. Kaji, K. Sakai, T. Ohno, and M. Izaki: 'Bandgap Science for Organic Solar Cells'. *Electronics* (June 2014), vol. 3(2): pp. 351–380 (cit. on p. 67).

164. Slootsky, M., X. Liu, V. M. Menon, and S. R. Forrest: 'Room Temperature Frenkel-Wannier-Mott Hybridization of Degenerate Excitons in a Strongly Coupled Microcavity'. *Physical Review Letters* (Feb. 2014), vol. 112(7) (cit. on pp. 67, 133).

165. Holmes, R. J. and S. R. Forrest: 'Strong Exciton-Photon Coupling and Exciton Hybridization in a Thermally Evaporated Polycrystalline Film of an Organic Small Molecule'. *Physical Review Letters* (Oct. 2004), vol. 93(18) (cit. on p. 67).

166. Forrest, S. R. and R. Holmes: 'United States Patent: 7889774 - Organic polariton laser'. 7889774. Feb. 2011 (cit. on p. 67).

167. Tonner, R., P. Rosenow, and P. Jakob: 'Molecular structure and vibrations of NTCDA monolayers on Ag(111) from density-functional theory and infrared absorption spectroscopy'. *Phys. Chem. Chem. Phys.* (2016), vol. 18(8): pp. 6316–6328 (cit. on p. 67).

168. Tietze, M. L., L. Burtone, M. Riede, B. Lüssem, and K. Leo: 'Fermi level shift and doping efficiency in p-doped small molecule organic semiconductors: A photoelectron spectroscopy and theoretical study'. *Physical Review B* (July 2012), vol. 86(3): p. 035320 (cit. on p. 67).

169. Menke, T., D. Ray, H. Kleemann, M. P. Hein, K. Leo, and M. Riede: 'Highly efficient p-dopants in amorphous hosts'. *Organic Electronics* (Feb. 2014), vol. 15(2): pp. 365–371 (cit. on p. 67).

170. Koech, P. K., A. B. Padmaperuma, L. Wang, J. S. Swensen, E. Polikarpov, J. T. Darsell, J. E. Rainbolt, and D. J. Gaspar: 'Synthesis and Application of 1,3,4,5,7,8-Hexafluorotetracyanonaphthoquinodimethane (F6-TNAP): A Conductivity Dopant for Organic Light-Emitting Devices'. *Chemistry of Materials* (July 2010), vol. 22(13): pp. 3926–3932 (cit. on p. 67).

171. Lüssem, B., M. L. Tietze, H. Kleemann, C. Hobach, J. W. Bartha, A. Zakhidov, and K. Leo: 'Doped organic transistors operating in the inversion and depletion regime'. *Nature Communications* (Nov. 2013), vol. 4: p. 2775 (cit. on p. 67).

172. Christodoulou, C., A. Giannakopoulos, G. Ligorio, M. Oehzelt, M. Timpel, J. Niederhausen, L. Pasquali, A. Giglia, K. Parvez, K. Müllen, David B., N. Koch, and M. V. Nardi: 'Tuning the Electronic Structure of Graphene by Molecular Dopants: Impact of the Substrate'. *ACS Applied Materials & Interfaces* (Sept. 2015), vol. 7(34): pp. 19134–19144 (cit. on pp. 67, 138).

173. Schultz, T., R. Schlesinger, J. Niederhausen, F. Henneberger, S. Sadofev, S. Blumstengel, A. Vollmer, F. Bussolotti, J.-P. Yang, S. Kera, K. Parvez, N. Ueno, K. Müllen, and N. Koch: 'Tuning the work function of GaN with organic molecular acceptors'. *Physical Review B* (Mar. 2016), vol. 93(12): p. 125309 (cit. on pp. 67, 132, 138, 139, 141, 142).

174. King, S. T., S. S. Parihar, K. Pradhan, H. T Johnson-Steigelman, and P. F. Lyman: 'Observation of a $\sqrt{3}x\sqrt{3}$-R30°-reconstruction on O-polar ZnO surfaces'. *Surface Science* (2008), vol. 602(22): pp. L131–L134 (cit. on p. 69).

175. Henzler, M.: 'LEED studies of surface imperfections'. *Applications of Surface Science* (July 1982), vol. 11-12(Supplement C): pp. 450–469 (cit. on p. 69).

176. El Helou, M., E. Lietke, J. Helzel, W. Heimbrodt, and G. Witte: 'Structural and optical properties of pentacene films grown on differently oriented ZnO surfaces'. *Journal of Physics: Condensed Matter* (2012), vol. 24(44): p. 445012 (cit. on p. 73).

177. Palczynski, K. and J. Dzubiella: 'Anisotropic Electrostatic Friction of *para* -Sexiphenyl on the ZnO($10\bar{1}0$) Surface'. *The Journal of Physical Chemistry C* (Nov. 2014), vol. 118(45): pp. 26368–26376 (cit. on pp. 73, 75, 86).

178. Kleppmann, N. and S. H. L. Klapp: 'A scale-bridging modeling approach for anisotropic organic molecules at patterned semiconductor surfaces'. *The Journal of Chemical Physics* (Feb. 2015), vol. 142(6): p. 064701 (cit. on p. 73).

179. Sun, L. D., M. Hohage, P. Zeppenfeld, S. Berkebile, G. Koller, F. P. Netzer, and M. G. Ramsey: 'Online measurement of the optical anisotropy during the growth of crystalline organic films'. *Applied Physics Letters* (Mar. 2006), vol. 88(12): p. 121913 (cit. on pp. 74, 76, 119).

180. Ivanco, J., B. Winter, F.p. Netzer, and M.g. Ramsey: 'Substrate-Mediated Electronic Structure and Properties of Sexiphenyl Films'. *Advanced Materials* (Nov. 2003), vol. 15(21): pp. 1812–1815 (cit. on pp. 74, 76, 77).

181. Yanagi, H. and S. Okamoto: 'Orientation-controlled organic electroluminescence of p-sexiphenyl films'. *Applied Physics Letters* (Nov. 1997), vol. 71(18): pp. 2563–2565 (cit. on pp. 74, 76, 79).

182. Yoshida, Y., H. Takiguchi, T. Hanada, N. Tanigaki, E.-M. Han, and K. Yase: 'Control of growth mechanism and optical properties of p-sexiphenyl thin films on ionic crystal substrates'. *Journal of Crystal Growth* (Mar. 1999), vol. 198-199: pp. 923–928 (cit. on p. 75).

183. Winkler, A.: 'On the nucleation and initial film growth of rod-like organic molecules'. *Surface Science* (Oct. 2016), vol. 652: pp. 367–377 (cit. on pp. 75, 85, 92).

184. Andreev, A. Yu., C. Teichert, G. Hlawacek, H. Hoppe, R. Resel, D. -M. Smilgies, H. Sitter, and N. S. Sariciftci: 'Morphology and growth kinetics of organic thin films deposited by hot wall epitaxy'. *Organic Electronics*. Current Trends in Crystalline Organic Semiconductors: Growth Modelling and Fundamental Properties (Mar. 2004), vol. 5(1-3): pp. 23–27 (cit. on p. 75).

185. Teichert, C., G. Hlawacek, A.Yu. Andreev, H. Sitter, P. Frank, A. Winkler, and N.S. Sariciftci: 'Spontaneous rearrangement of *para*-sexiphenyl crystallites into nano-fibers'. *Applied Physics A* (Mar. 2006), vol. 82(4): pp. 665–669 (cit. on p. 75).

186. Balzer, F. and H.-G. Rubahn: 'Dipole-assisted self-assembly of light-emitting p-nP needles on mica'. *Applied Physics Letters* (Nov. 2001), vol. 79(23): pp. 3860–3862 (cit. on p. 75).

187. Frank, P., G. Hlawacek, O. Lengyel, A. Satka, C. Teichert, R. Resel, and A. Winkler: 'Influence of surface temperature and surface modifications on the initial layer growth of *para*-hexaphenyl on mica (001)'. *Surface Science* (May 2007), vol. 601(10): pp. 2152–2160 (cit. on pp. 75, 82, 88).

188. Tumbek, L., C. Gleichweit, K. Zojer, and A. Winkler: 'Origin of the bimodal island size distribution in ultrathin films of *para*-hexaphenyl on mica'. *Physical Review B* (Aug. 2012), vol. 86(8) (cit. on pp. 75, 82, 86).

189. Wrana, D., M. Kratzer, K. Szajna, M. Nikiel, B. R. Jany, M. Korzekwa, C. Teichert, and F. Krok: 'Growth of *para*-Hexaphenyl Thin Films on Flat, Atomically Clean versus Air-Passivated TiO_2(110) Surfaces'. *The Journal of Physical Chemistry C* (July 2015), vol. 119(29): pp. 17004–17015 (cit. on p. 75).

190. Kankate, L., F. Balzer, H. Niehus, and H.-G. Rubahn: 'From clusters to fibers: Parameters for discontinuous *para*-hexaphenylene thin film growth'. *The Journal of Chemical Physics* (2008), vol. 128(8): p. 084709 (cit. on pp. 76, 82).

191. Berkebile, S., G. Koller, G. Hlawacek, C. Teichert, F. P. Netzer, and M. G. Ramsey: 'Diffusion versus sticking anisotropy: Anisotropic growth of organic molecular films'. *Surface Science* (Dec. 2006), vol. 600(24): pp. L313–L317 (cit. on p. 76).

192. Sun, L., S. Berkebile, G. Weidlinger, G. Koller, M. Hohage, F. P. Netzer, M. G. Ramsey, and P. Zeppenfeld: 'Revealing the buried interface: *para*-sexiphenyl thin films grown on TiO_2(110)'. *Physical Chemistry Chemical Physics* (2010), vol. 12(13): p. 3141 (cit. on pp. 76, 77, 82).

193. Schlesinger, R.: 'Energy-Level Control at Hybrid Inorganic/Organic Semiconductor Interfaces'. PhD thesis. Humboldt-Universität zu Berlin, 2017 (cit. on p. 76).

194. Elkinani, I. and J. Villain: 'Le paradoxe de zenon d'elee'. *Solid State Communications* (July 1993), vol. 87(2): pp. 105–108 (cit. on p. 76).

195. Koller, G., S. Berkebile, J. R. Krenn, G. Tzvetkov, G. Hlawacek, O. Lengyel, F. P. Netzer, C. Teichert, R. Resel, and M. G. Ramsey: 'Oriented Sexiphenyl Single Crystal Nanoneedles on TiO2 (110)'. *Advanced Materials* (Dec. 2004), vol. 16(23-24): pp. 2159–2162 (cit. on p. 77).

196. Ishii, H., K. Sugiyama, E. Ito, and K. Seki: 'Energy Level Alignment and Interfacial Electronic Structures at Organic/Metal and Organic/Organic Interfaces'. *Advanced Materials* (June 1999), vol. 11(8): pp. 605–625 (cit. on pp. 78, 100).

197. Garmshausen, Y., J. Schwarz, J. Hildebrandt, B. Kobin, M. Pätzel, and S. Hecht: 'Making Nonsymmetrical Bricks: Synthesis of Insoluble Dipolar Sexiphenyls'. *Organic Letters* (June 2014), vol. 16(11): pp. 2838–2841 (cit. on p. 80).

198. Yang, J., T. Wang, H. Wang, F. Zhu, G. Li, and D. Yan: 'Ultrathin-Film Growth of *para* -Sexiphenyl (I): Submonolayer Thin-Film Growth as a Function of the Substrate Temperature'. *The Journal of Physical Chemistry B* (July 2008), vol. 112(26): pp. 7816–7820 (cit. on pp. 82, 83, 85, 87, 88, 94, 95).

199. Sun, L., G. Weidlinger, M. Denk, R. Denk, M. Hohage, and P. Zeppenfeld: 'Stranski-Krastanov growth of *para*-sexiphenyl on Cu(110)-(2x1)O revealed by optical spectroscopy'. *Physical Chemistry Chemical Physics* (Nov. 2010), vol. 12(44): pp. 14706–14709 (cit. on pp. 82, 119).

200. Scherwitzl, B., W. Lukesch, A. Hirzer, J. Albering, G. Leising, R. Resel, and A. Winkler: 'Initial Steps of Rubicene Film Growth on Silicon Dioxide'. *The Journal of Physical Chemistry C* (Feb. 2013), vol. 117(8): pp. 4115–4123 (cit. on pp. 83, 88).

201. Trofimov, V. I.: 'Morphology evolution in a growing film'. *Thin Solid Films.* Proceedings of Symposium J on Growth and Evolution of Ultrathin Films: Surface and Interface Geometric and Electronic Structure, of the E-MRS Spring Conference (Mar. 2003), vol. 428(1-2): pp. 56–65 (cit. on p. 83).

202. Zykov, A.: 'On the understanding of organic thin film growth and the changes in structure formation induced by molecular chemical tuning'. PhD thesis. Humboldt-Universität zu Berlin, 2016 (cit. on pp. 83, 94, 98, 101).

203. Einstein, T. L., A. Pimpinelli, and D. Luis González: 'Analyzing capture zone distributions (CZD) in growth: Theory and applications'. *Journal of Crystal Growth* (Sept. 2014), vol.: pp. 61–71 (cit. on p. 85).

204. Lorbek, S., G. Hlawacek, and C. Teichert: 'Determination of critical island size in *para* -sexiphenyl islands on SiO_2 using capture-zone scaling'. *The European Physical Journal Applied Physics* (Aug. 2011), vol. 55(2): p. 23902 (cit. on p. 86).

205. Scott, D. W.: 'On optimal and data-based histograms'. *Biometrika* (Jan. 1979), vol. 66(3): pp. 605–610 (cit. on p. 86).

206. Winkler, A. and L. Tumbek: 'Nucleation of Organic Molecules via a Hot Precursor State: Pentacene on Amorphous Mica'. *The Journal of Physical Chemistry Letters* (Dec. 2013), vol. 4(23): pp. 4080–4084 (cit. on pp. 88, 94, 95, 98).

207. Fleming, A. J., F. P. Netzer, and M. G. Ramsey: 'Nucleation and 3D growth of *para* -sexiphenyl nanostructures from an oriented 2D liquid layer investigated by photoemission electron microscopy'. *Journal of Physics: Condensed Matter* (Nov. 2009), vol. 21(44): p. 445003 (cit. on p. 88).

208. Zhang, X., E. Barrena, D. Goswami, D. de Oteyza, C. Weis, and H. Dosch: 'Evidence for a Layer-Dependent Ehrlich-Schwoebel Barrier in Organic Thin Film Growth'. *Physical Review Letters* (Sept. 2009), vol. 103(13) (cit. on p. 89).

209. Kowarik, S., A. Gerlach, S. Sellner, F. Schreiber, L. Cavalcanti, and O. Konovalov: 'Real-Time Observation of Structural and Orientational Transitions during Growth of Organic Thin Films'. *Physical Review Letters* (Mar. 2006), vol. 96(12) (cit. on p. 89).

210. Frank, C., J. Novák, R. Banerjee, A. Gerlach, F. Schreiber, A. Vorobiev, and S. Kowarik: 'Island size evolution and molecular diffusion during growth of organic thin films followed by time-resolved specular and off-specular scattering'. *Physical Review B* (4 July 2014), vol. 90: p. 045410 (cit. on pp. 89, 98).

211. Macdonald, J. Ross and C. A. Barlow: 'Work Function Change on Monolayer Adsorption'. *The Journal of Chemical Physics* (July 1963), vol. 39(2): pp. 412–422 (cit. on p. 98).

212. Kedem, N., S. Blumstengel, F. Henneberger, H. Cohen, G. Hodes, and D. Cahen: 'Morphology-, synthesis- and doping-independent tuning of ZnO work function using phenylphosphonates'. *Physical Chemistry Chemical Physics* (2014), vol. 16(18): pp. 8310–8319 (cit. on p. 98).

213. Wood, C., H. Li, P. Winget, and J.-L. Brédas: 'Binding Modes of Fluorinated Benzylphosphonic Acids on the Polar ZnO Surface and Impact on Work Function'. *The Journal of Physical Chemistry C* (Sept. 2012), vol. 116(36): pp. 19125–19133 (cit. on p. 98).

214. Hofmann, O. T., J.-C. Deinert, Y. Xu, P. Rinke, J. Stähler, M. Wolf, and M. Scheffler: 'Large work function reduction by adsorption of a molecule with a negative electron affinity: Pyridine on ZnO($10\bar{1}0$)'. *The Journal of Chemical Physics* (Nov. 2013), vol. 139(17): p. 174701 (cit. on p. 98).

215. Lange, I., S. Reiter, M. Pätzel, A. Zykov, A. Nefedov, J. Hildebrandt, S. Hecht, S. Kowarik, C. Wöll, G. Heimel, and D. Neher: 'Tuning the Work Function of Polar Zinc Oxide Surfaces using Modified Phosphonic Acid Self-Assembled Monolayers'. *Advanced Functional Materials* (Nov. 2014), vol. 24(44): pp. 7014–7024 (cit. on p. 98).

216. Koch, N.: 'Energy levels at interfaces between metals and conjugated organic molecules'. *Journal of Physics: Condensed Matter* (2008), vol. 20(18): p. 184008 (cit. on p. 100).

217. Mishima, R., N. T. Loan, and H. Tada: 'Electrostatic Properties of Organic Monolayers on Silicon Oxides Studied by Kelvin Probe Force Microscopy'. *Japanese Journal of Applied Physics* (Apr. 2012), vol. 51: p. 045702 (cit. on p. 100).

218. Kirmse, H., M. Sparenberg, S. Sadofev, S. Blumstengel, and C. T. Koch: 'Visualization of ordering phenomena in di-fluorinated sexiphenyl by HRTEM'. *European Microscopy Congress 2016: Proceedings*. Wiley-VCH Verlag GmbH & Co. KG, 2016 (cit. on p. 100).

219. Schlesinger, R., F. Bianchi, S. Blumstengel, C. Christodoulou, R. Ovsyannikov, B. Kobin, K. Moudgil, S. Barlow, S. Hecht, S.R. Marder, F. Henneberger, and N. Koch: 'Efficient light emission from inorganic and organic semiconductor hybrid structures by energy-level tuning'. *Nature Communications* (Apr. 2015), vol. 6: p. 6754 (cit. on pp. 102, 126).

220. Smith, R., B. Liu, J. Bai, and T. Wang: 'Hybrid III-Nitride/Organic Semiconductor Nanostructure with High Efficiency Nonradiative Energy Transfer for White Light Emitters'. *Nano Letters* (July 2013), vol. 13(7): pp. 3042–3047 (cit. on p. 102).

221. Loos, J., J. K. J van Duren, F. Morrissey, and R. A. J Janssen: 'The use of the focused ion beam technique to prepare cross-sectional transmission electron microscopy specimen of polymer solar cells deposited on glass'. *Polymer* (Dec. 2002), vol. 43(26): pp. 7493–7496 (cit. on p. 102).

222. Dürr, A. C., F. Schreiber, M. Kelsch, and H. Dosch: 'Optimized preparation of cross-sectional TEM specimens of organic thin films'. *Ultramicroscopy* (Dec. 2003), vol. 98(1): pp. 51–55 (cit. on pp. 102, 107).

223. Schaffer, B., C. Mitterbauer, A. Schertel, A. Pogantsch, S. Rentenberger, E. Zojer, and F. Hofer: 'Cross-section analysis of organic light-emitting diodes'. *Ultramicroscopy* (Nov. 2004), vol. 101(2-4): pp. 123–128 (cit. on p. 102).

224. Pacher, P., A. Lex, V. Proschek, H. Etschmaier, E. Tchernychova, M. Sezen, U. Scherf, W. Grogger, G. Trimmel, C. Slugovc, and E. Zojer: 'Chemical Control of Local Doping in Organic Thin-Film Transistors: From Depletion to Enhancement'. *Advanced Materials* (Aug. 2008), vol. 20(16): pp. 3143–3148 (cit. on p. 102).

225. Fladischer, S., A. Neuhold, E. Kraker, T. Haber, B. Lamprecht, I. Salzmann, R Resel, and W. Grogger: 'Diffusion of Ag into Organic Semiconducting Materials: A Combined Analytical Study Using Transmission Electron Microscopy and X-ray Reflectivity'. *ACS Applied Materials & Interfaces* (Oct. 2012), vol. 4(10): pp. 5608–5612 (cit. on p. 102).

226. Blumstengel, S., S. Sadofev, J. Puls, and F. Henneberger: 'An Inorganic/Organic Semiconductor "Sandwich" Structure Grown by Molecular Beam Epitaxy'. *Advanced Materials* (Dec. 2009), vol. 21(47): pp. 4850–4853 (cit. on p. 103).

227. Katsia, E., N. Huby, G. Tallarida, B. Kutrzeba-Kotowska, M. Perego, S. Ferrari, F. C. Krebs, E. Guziewicz, M. Godlewski, V. Osinniy, and G. Luka: 'Poly(3-hexylthiophene)/ZnO hybrid pn junctions for microelectronics applications'. *Applied Physics Letters* (Apr. 2009), vol. 94(14): p. 143501 (cit. on p. 107).

228. Obuchovsky, S., I. Deckman, M. Moshonov, T. Segal Peretz, G. Ankonina, T. J. Savenije, and G. L. Frey: 'Atomic layer deposition of zinc oxide onto and into P3HT for hybrid photovoltaics'. *Journal of Materials Chemistry C* (Oct. 2014), vol. 2(42): pp. 8903–8910 (cit. on p. 107).

229. Stadelmann, P. A.: *JEMS: Java Electron Microscopy Software. Version 3.5707U2010*. http://www.jems-saas.ch/. 2010 (cit. on p. 107).

230. Drift, A. van der: 'Evolutionary selection, a principle governing growth orientation in vapour-deposited layers'. *Philips Research Reports* (1967), vol. 22: pp. 267–288 (cit. on p. 116).

231. Kajikawa, Y.: 'Texture development of non-epitaxial polycrystalline ZnO films'. *Journal of Crystal Growth* (Mar. 2006), vol. 289(1): pp. 387–394 (cit. on p. 116).

232. Wander, A., F. Schedin, P. Steadman, A. Norris, R. McGrath, T. S. Turner, G. Thornton, and N. M. Harrison: 'Stability of Polar Oxide Surfaces'. *Physical Review Letters* (Apr. 2001), vol. 86(17): pp. 3811–3814 (cit. on p. 116).

233. Choi, J. H., H. Tabata, and T. Kawai: 'Initial preferred growth in zinc oxide thin films on Si and amorphous substrates by a pulsed laser deposition'. *Journal of Crystal Growth* (Aug. 2001), vol. 226(4): pp. 493–500 (cit. on p. 116).

234. Claeyssens, F., C. L. Freeman, N. L. Allan, Y. Sun, M. N. R. Ashfold, and J. H. Harding: 'Growth of ZnO thin films - experiment and theory'. (Dec. 2005), vol. 15(1): pp. 139–148 (cit. on p. 116).

235. Diebold, U., L. Vogel Koplitz, and O. Dulub: 'Atomic-scale properties of low-index ZnO surfaces'. *Applied Surface Science*. Proceedings of the Seventh International Symposium on Atomically Controlled Surfaces, Interfaces and Nanostructures (Oct. 2004), vol. 237(1-4): pp. 336–342 (cit. on p. 116).

236. Proehl, H., T. Dienel, R. Nitsche, and T. Fritz: 'Formation of Solid-State Excitons in Ultrathin Crystalline Films of PTCDA: From Single Molecules to Molecular Stacks'. *Physical Review Letters* (Aug. 2004), vol. 93(9) (cit. on pp. 119, 120, 129).

237. Proehl, H., R. Nitsche, T. Dienel, K. Leo, and T. Fritz: 'In situ differential reflectance spectroscopy of thin crystalline films of PTCDA on different substrates'. *Physical Review B* (Apr. 2005), vol. 71(16): p. 165207 (cit. on pp. 119, 129).

238. Forker, R., T. Dienel, T. Fritz, and K. Müllen: 'Optical evidence for substrate-induced growth of ultrathin hexa-peri-hexabenzocoronene films on highly oriented pyrolytic graphite'. *Physical Review B* (Oct. 2006), vol. 74(16) (cit. on p. 119).

239. Dienel, T., C. Loppacher, S. Mannsfeld, R. Forker, and T. Fritz: 'Growth-Mode-Induced Narrowing of Optical Spectra of an Organic Adlayer'. *Advanced Materials* (2008), vol. 20(5): pp. 959–963 (cit. on pp. 119, 121).

240. Forker, R., C. Golnik, G. Pizzi, T. Dienel, and T. Fritz: 'Optical absorption spectra of ultrathin PTCDA films on gold single crystals: Charge transfer beyond the first monolayer'. *Organic Electronics* (2009), vol. 10(8): pp. 1448–1453 (cit. on pp. 119, 132).

241. Gruenewald, M., K. Wachter, M. Meissner, M. Kozlik, R. Forker, and T. Fritz: 'Optical and electronic interaction at metal-organic and organic-organic interfaces of ultra-thin layers of PTCDA and SnPc on noble metal surfaces'. *Organic Electronics* (Sept. 2013), vol. 14(9): pp. 2177–2183 (cit. on p. 119).

242. Forker, R., D. Kasemann, T. Dienel, C. Wagner, R. Franke, K. Müllen, and T. Fritz: 'Electronic Decoupling of Aromatic Molecules from a Metal by an Atomically Thin Organic Spacer'. *Advanced Materials* (Dec. 2008), vol. 20(23): pp. 4450–4454 (cit. on p. 119).

243. Gruenewald, M., L. K. Schirra, P. Winget, M. Kozlik, P. F. Ndione, A. K. Sigdel, J. J. Berry, R. Forker, J.-L. Brédas, T. Fritz, and O. L. A. Monti: 'Integer Charge Transfer and Hybridization at an Organic Semiconductor/Conductive Oxide Interface'. *The Journal of Physical Chemistry C* (Mar. 2015), vol. 119(9): pp. 4865–4873 (cit. on pp. 119, 132, 133).

244. Navarro-Quezada, A., M. Aiglinger, E. Ghanbari, Th. Wagner, and P. Zeppenfeld: 'Polarization-dependent differential reflectance spectroscopy for real-time monitoring of organic thin film growth'. *Review of Scientific Instruments* (Nov. 2015), vol. 86(11): p. 113108 (cit. on p. 119).

245. Li, H. H.: 'Refractive index of alkali halides and its wavelength and temperature derivatives'. *Journal of Physical and Chemical Reference Data* (Apr. 1976), vol. 5(2): pp. 329–528 (cit. on pp. 119, 132).

246. Sellmeier, W. von: 'Zur Erklärung der abnormen Farbenfolge im Spectrum einiger Substanzen'. *Annalen der Physik* (Jan. 1871), vol. 219(6): pp. 272–282 (cit. on p. 119).

247. Ludwig, C., B. Gompf, J. Petersen, R. Strohmaier, and W. Eisenmenger: 'STM investigations of PTCDA and PTCDI on graphite and MoS_2. A systematic study of epitaxy and STM image contrast'. *Zeitschrift für Physik B Condensed Matter* (Sept. 1994), vol. 93(3): pp. 365–373 (cit. on p. 120).

248. Uder, B., C. Ludwig, J. Petersen, B. Gompf, and W. Eisenmenger: 'STM characterisation of organic molecules on H-terminated Si(111)'. *Zeitschrift für Physik B Condensed Matter* (Sept. 1995), vol. 97(3): pp. 389–390 (cit. on p. 120).

249. Guillermet, O., M. Mossoyan-Déneux, M. Giorgi, A. Glachant, and J. C. Mossoyan: 'Structural study of vapour phase deposited 3,4,9,10-perylene tetracarboxylicacid diimide: Comparison between single crystal and ultra thin films grown on Pt(100)'. *Thin Solid Films* (Aug. 2006), vol. 514(1-2): pp. 25–32 (cit. on p. 120).

250. Topple, J. M., S. A. Burke, W. Ji, S. Fostner, A. Tekiel, and P. Grütter: 'Tailoring the Morphology and Dewetting of an Organic Thin Film'. *The Journal of Physical Chemistry C* (Jan. 2011), vol. 115(1): pp. 217–224 (cit. on pp. 120, 122).

251. El-Nahhas, M. M., H. Abdel-Khalek, and E. Salem: 'Structural and Optical Properties of Nanocrystalline 3,4,9,10-Perylene-Tetracarboxylic-Diimide Thin Film'. *Advances in Condensed Matter Physics* (2012), vol. 2012. DOI: 10.1155/2012/698934: p. 7 (cit. on pp. 120, 124).

252. Renger, T., B. Grundkötter, M. El-Amine Madjet, and F. Müh: 'Theory of solvatochromic shifts in nonpolar solvents reveals a new spectroscopic rule'. *Proceedings of the National Academy of Sciences* (Sept. 2008), vol. 105(36): pp. 13235–13240 (cit. on pp. 122, 123).

253. Bayliss, N. S.: 'The Effect of the Electrostatic Polarization of the Solvent on Electronic Absorption Spectra in Solution'. *The Journal of Chemical Physics* (Mar. 1950), vol. 18(3): pp. 292–296 (cit. on p. 123).

254. Megow, J.: 'Computing dispersive, polarizable, and electrostatic shifts of excitation energy in supramolecular systems: PTCDI crystal'. *The Journal of Chemical Physics* (Sept. 2016), vol. 145(9): p. 094109 (cit. on p. 124).

255. Megow, J., T. Körzdörfer, T. Renger, M. Sparenberg, S. Blumstengel, F. Henneberger, and V. May: 'Reply to "Comment on 'Calculating Optical Absorption Spectra of Thin Polycrystalline Organic Films: Structural Disorder and Site-Dependent van der Waals Interaction'"'. *The Journal of Physical Chemistry C* (Aug. 2015), vol. 119(32): pp. 18818–18820 (cit. on p. 124).

256. Megow, J., T. Renger, and V. May: 'Mixed Quantum-Classical Description of Excitation Energy Transfer in Supramolecular Complexes: Screening of the Excitonic Coupling'. *ChemPhysChem* (Feb. 2014), vol. 15(3): pp. 478–485 (cit. on p. 124).

257. Karl, N. and Ch. Guenther: 'Structure and Ordering Principles of Ultrathin Organic Molecular Films on Surfaces of Layered Semiconductors Organic-on-Inorganic MBE'. *Crystal Research and Technology* (Feb. 1999), vol. 34(2): pp. 243–254 (cit. on p. 133).

258. Piersimoni, F., R. Schlesinger, J. Benduhn, D. Spoltore, S. Reiter, I. Lange, N. Koch, K. Vandewal, and D. Neher: 'Charge Transfer Absorption and Emission at ZnO/Organic Interfaces'. *The Journal of Physical Chemistry Letters* (Feb. 2015), vol. 6(3): pp. 500–504 (cit. on p. 133).

259. Blossey, D. F.: 'Wannier Exciton in an Electric Field. I. Optical Absorption by Bound and Continuum States'. *Physical Review B* (Nov. 1970), vol. 2(10): pp. 3976–3990 (cit. on p. 135).

260. Blossey, D. F.: 'Wannier Exciton in an Electric Field. II. Electroabsorption in Direct-Band-Gap Solids'. *Physical Review B* (Feb. 1971), vol. 3(4): pp. 1382–1391 (cit. on p. 135).

261. Aspnes, D. E.: 'Third-derivative modulation spectroscopy with low-field electroreflectance'. *Surface Science* (June 1973), vol. 37(Supplement C): pp. 418–442 (cit. on p. 135).

262. Dow, J. D., B. Y. Lao, and S. A. Newman: 'Differential Electroabsorption'. *Physical Review B* (Apr. 1971), vol. 3(8): pp. 2571–2581 (cit. on p. 136).

263. Neumann, M. D., C. Cobet, N. Esser, B. Laumer, T. A. Wassner, M. Eickhoff, M. Feneberg, and R. Goldhahn: 'Optical properties of MgZnO alloys: Excitons and exciton-phonon complexes'. *Journal of Applied Physics* (July 2011), vol. 110(1): p. 013520 (cit. on p. 136).

264. Schlesinger, R., Y. Xu, O. T. Hofmann, S. Winkler, J. Frisch, J. Niederhausen, A. Vollmer, S. Blumstengel, F. Henneberger, P. Rinke, M. Scheffler, and N. Koch: 'Controlling the work function of ZnO and the energy-level alignment at the interface to organic semiconductors with a molecular electron acceptor'. *Physical Review B* (Apr. 2013), vol. 87(15): p. 155311 (cit. on pp. 138, 141).

265. Heinhold, R., G. T. Williams, S. P. Cooil, D. A. Evans, and M. W. Allen: 'Influence of polarity and hydroxyl termination on the band bending at ZnO surfaces'. *Physical Review B* (Dec. 2013), vol. 88(23): p. 235315 (cit. on p. 138).

266. Kingston, R. H. and S. F. Neustadter: 'Calculation of the Space Charge, Electric Field, and Free Carrier Concentration at the Surface of a Semiconductor'. *Journal of Applied Physics* (June 1955), vol. 26(6): pp. 718–720 (cit. on p. 141).

List of Figures

List of Tables

Publications

Publication List

1. Meisel, T., **M. Sparenberg**, M. Gawek, S. Sadofev, E. List-Kratochvil, and S. Blumstengel: 'Revealing Charge Redistribution at Hybrid Interfaces by DRS'. (2018), vol. in preparation.
2. Kirmse*, H., **M. Sparenberg***, A. Zykov, S. Sadofev, S. Kowarik, and S. Blumstengel: 'Structure of *p*-Sexiphenyl Nanocrystallites in ZnO Revealed by High-Resolution Transmission Electron Microscopy'. *Crystal Growth & Design* (May 2016), vol. 16(5). *Equal contribution: pp. 2789–2794.
3. Megow, J., T. Körzdörfer, T. Renger, **M. Sparenberg**, S. Blumstengel, F. Henneberger, and V. May: 'Calculating Optical Absorption Spectra of Thin Polycrystalline Organic Films: Structural Disorder and Site-Dependent van der Waals Interaction'. *The Journal of Physical Chemistry C* (Feb. 2015), vol. 119(10): pp. 5747–5751.
4. Blumstengel, S., H. Kirmse, **M. Sparenberg**, S. Sadofev, F. Polzer, and F. Henneberger: 'Texture and morphology of ZnO grown on nanocrystalline p-sexiphenyl thin films'. *Journal of Crystal Growth* (Sept. 2014), vol. 402: pp. 187–194.
5. **Sparenberg*, M.**, A. Zykov*, P. Beyer, L. Pithan, C. Weber, Y. Garmshausen, F. Carlà, S. Hecht, S. Blumstengel, F. Henneberger, and S. Kowarik: 'Controlling the growth mode of *para*-sexiphenyl (6P) on ZnO by partial fluorination'. *Phys. Chem. Chem. Phys.* (2014), vol. 16(47). *Equal contribution: pp. 26084–26093.
6. Heinen, B., T.-L. Wang, **M. Sparenberg**, A. Weber, B. Kunert, J. Hader, S.W. Koch, J.V. Moloney, M. Koch, and W. Stolz: '106 W continuous-wave output power from vertical-external-cavity surface-emitting laser'. *Electronics Letters* (2012), vol. 48(9): p. 516.
7. Heinen, B., F. Zhang, **M. Sparenberg**, B. Kunert, M. Koch, and W. Stolz: 'On the Measurement of the Thermal Resistance of Vertical-External-Cavity Surface-Emitting Lasers (VECSELs)'. *IEEE Journal of Quantum Electronics* (July 2012), vol. 48(7): pp. 934–940.

8. Wang, T.-L., B. Heinen, J. Hader, C. Dineen, **M. Sparenberg**, A. Weber, B. Kunert, S.w. Koch, J.v. Moloney, M. Koch, and W. Stolz: 'Quantum design strategy pushes high-power vertical-external-cavity surface-emitting lasers beyond 100 W'. *Laser & Photonics Reviews* (Sept. 2012), vol. 6(5): pp. L12–L14.

Conference contributions

1. **DPG Frühjahrstagung***: 'Controlled UHV growth of organic-inorganic hybrid structures: Conjugated molecules on ZnO'*. Regensburg, 2016.
2. **DPG Frühjahrstagung***: 'All-UHV growth of organic/ZnO hybrid structures'*. Dresden, 2014.
3. **HIOS Young Researcher Workshop***: 'Controlled UHV growth of polycyclic aromatic hydrocarbons on ZnO'*. Rheinsberg, 2013.
4. **HIOS Young Researcher Workshop***: 'All-UHV growth of organic hybrid structures on ZnO'*. Wittensee, 2012.

Acknowledgments

As a scientific work is never the product of a single person I want to express my gratitude to everyone who has contributed to the completion and achievement of this thesis and supported me throughout.

First of all I want to thank the late Prof. Dr. Fritz Henneberger who gave me the opportunity to work on the exciting field of inorganic/organic hybrid structures, impart his vast knowledge and write this thesis in his group. In this context a great thanks also goes to Prof. Dr. Benson, who took over supervision after the sudden death of Prof. Henneberger and made it possible to continue my thesis and bring it to an end. Also, I would like to thank Prof. Dr. Stefan Kowarik and Prof. Dr. Gregor Witte for taking the time to review this work. Next, I especially have to thank Dr. habil. Sylke Blumstengel, who supported and advised me throughout my thesis with many productive discussions and input, as well as the assistance given by Dr. Sergey Sadofev, who helped to solve all the emerging problems in the MBE lab. Thereby I also want to thank Dr. Matthias Brandt, who introduced me in the secrets of MBE growth.

Further, I am particularly grateful for fruitful collaborations with numerous members of the collaborative research centre 951 - Hybrid Inorganic/Organic Systems for Opto-Electronics: From the TEM group especially Dr. Holm Kirmse, with his impressive knowledge of the TEM and Eva Öhlschegel whose preparation just made the TEM investigations possible, the X-ray team around Prof. Dr. Stefan Kowarik with Dr. Anton Zykov, Dr. Linus Pithan and Dr. Christoph Weber, who provided valuable insights into the molecular growth. Moreover, I also want to thank Dr. Jörg Megow, Prof. Dr. Thomas Körzdörfer, Prof. Dr. Thomas Renger and Prof. Dr. Volkhard May for their theoretical input to interpret the DR spectra. Then I further have to thank Dr. Björn Kobin and Yves Garmshausen from the group of Prof. Dr. Stefan Hecht for providing fancy molecules. In addition, I want to express my thanks for stimulating discussions with Dr. Nikola Kleppmann.

Also I wish to acknowledge the great help provided by my student workers for setting up the DRS and making the amazing results possible (in alphabetic order): David Augustin, Marcel Gawek, Josef Kaliski, Paul Korbach and Viola Schmidt.

Apart from this a special thanks goes to my fellows Francesco Bianchi and Dr. Michael Höfner, for having a great time together, the technical support by Christian Kremer, the administrative support by Beatrix Matthes, Dagmar Fahnauer for her crafting skills and Elfriede Renger for helping out with chemicals. Furthermore, I want to thank all my other colleagues and friends, all former and current members of the Photonics/Hybrid Devices group for creating a nice atmosphere (in alphabetic order): Mario Bomers, Moritz Eyer, Dr. Simon Halm, Dr. Sascha Kalusniak, Sebastian Kickhöfel, Dr. Juangtaek Kim, Dr. Alexander Kuznetsov, Tino Meisel, Hala Memmi, Niklas Mutz, Laura Orphal, Dr. Joachim Puls, Dr. Maurizio Roczen, Dr. Peter Schäfer, Dr. Sylvia Schikora, Evgenji Travkin and Dr. Hans-Jürgen Wünsche.

Finally I want to deeply thank my whole family for their guidance and tremendous support through good and bad times and heartly thank my sunshine Laura Bogula for her love, moral support and patience.

Thank you all

Selbständigkeitserklärung

Ich erkläre, dass ich die Dissertation selbständig und nur unter Verwendung der von mir gemäß § 7 Abs. 3 der Promotionsordnung der Mathematisch-Naturwissenschaftlichen Fakultät, veröffentlicht im Amtlichen Mitteilungsblatt der Humboldt-Universität zu Berlin Nr. 126/2014 am 18.11.2014 angegebenen Hilfsmittel angefertigt habe.

Ort, Datum Unterschrift